DOCTOR OF PHILOSOPHY

Seismic performance of vegetated slopes

Liang, Teng

Award date:
2015

College of Art, Science & Engineering
School of Engineering, Physics & Mathematics
Department of Civil Engineering

Seismic performance of vegetated slopes

Teng Liang

A dissertation submitted for the degree of Doctor
of Philosophy to the University of Dundee

March 2015

天下事有难易乎？

为之

则难者亦易矣；

不为

则易者亦难矣！

i. Declaration

This is to certify that, except where specific reference to other investigation is made, the work described in this dissertation is the result of the investigation of the candidate. Neither this dissertation, nor any part of it, has been presented or is currently submitted in candidature for any degree at any other university.

Mr Teng Liang (Candidate), Dundee / /2015

Dr Jonathan Knappett (Supervisor), Dundee / /2015

ii. Acknowledge

It cannot be argued with that the most influential person during my PhD study has been my supervisor, Dr. Jonathan Knappett. His strong encouragement and patience to students, great enthusiasm to research, strong abilities to inspire people and enormous knowledge on this area have been indispensable to my growth as a scientist and as a person. I have been extremely fortunate to have such a supervisor. I am extremely grateful to him for his devotion to his students' education and success.

Sincere thanks are given to Prof. David Muir Wood as co-supervisor to help me get the opportunity to start my PhD research; Dr. Glyn Bengough, for helping me get access to James Hutton Institute to conduct part of my research; Dr. Andrew Brenan, Dr. Anthony Leung, Dr Michael Brown for helping me better understand the geotechnical issues.

Sincere thanks are given to all of the technicians, Dr. Gary Callon, Colin stark, David Husband, Mark Truswell, John Anderson, Willie Henderson, Alex Anderson, Callum Moore, Chris Walker within the Department of Civil Engineering of the University of Dundee who were always ready to provide technical assistance as well as a good laugh from time to time.

Sincere thanks are given to all my colleagues in the Dundee geotechnical group, with special thanks to Dr. Natasha Duckett for showing me how everything works and providing the Microsoft Excel spreadsheet file for establishing BNWF model; Dr. Asad Hafudh Humaish Al-Defae and Ke Wang for showing me how to use centrifuge; Scott Robinson for showing the opterartion of triaxial testing system and universal testing machine, and orginsing parties in the research group; Therar Al-Baghdadi for recommending me some excellent softwares to make my research more efficient; David Boldrin and Davide Vitali for sharing new ideas frequenctly.

Sincere thanks are given to all my Chinese friends in Dundee, Chunyang Xu, Heng Lu, Huan Wang, Jian Gou, Jian Liu, Dr. Kai Fu, Ke Wang, Dr. Qinqin Gui, Xiaojing Zhong, Dr. Xu Xiao, Dr. Yiqiang Chen, Dr. Yang Kuang, Yiming Jin, Dr. Zhengtian Song. It is all your guys that make me feel I am not alone in UK. Thank you. Here I want to express special thanks to

the girl I have the biggest crush on. Every time I see her, I will feel comfortable and achieve inner peace. It is such a strange feeling. But it is just so amazing. How good it is to meet her in Dundee and almost see her every day.

I would also like to acknowledge the financial supporter of my PhD study from the China Scholarship Council and special thanks to my supervisor and tutor in China, Prof. Xibing Li and Prof. Diyuan Li and my University, Central South University.

Last, but not least, my support group, my family, for their love, support and encouragement.

iii. Abstract

Vegetation (grasses, shrubs and trees) as an environmental-friendly approach has been widely used in many natural and man-made slopes. And it is generally recognized that this can increase the stability of slopes under static condition. There is anecdotal evidence that vegetated slopes also perform better than fallow slopes during earthquakes. However, the study of the dynamic behaviour of slopes planted with dichotomous ('woody') roots is relatively rare owing to the extreme expense and difficulty involved in conducting full scale dynamic testing on shrubs and trees.

In the thesis, the seismic performance of such slopes in non-liquefiable granular soils has been investigated and an extensive programme of centrifuge testing was conducted to quantify the improvements to global slope performance. The key indicators of slope performance considered herein are acceleration response and permanent crest settlement, which are key parameters for slope design. Supporting numerical (finite element) and analytical (sliding-block) models were also developed to better understand the behaviour and reveal the mechanism. Four major contributions are made in this thesis.

Firstly, a scaled model root clusters having a tap root system was designed, and then fabricated in ABS plastic using 3-D printing to simulate the fibrous structure of root. The printed ABS plastic was firstly used to represent real roots and was shown to effectively simulate the mechanical behaviour of real roots through element tests. A series of large direct shear (DS) tests were then conducted to investigate the root and soil interaction and reveal how RAR and root morphology may influence the root contribution to shear strength and stiffness. The distinct behaviours between the tap root system (3D root cluster) and the plate / heart root type (straight root group) were demonstrated. The common root reinforcement estimation methods were also compared with the measured root cohesion from the DS tests and inferred values from the centrifuge tests and generally resulted in an over estimation of root contribution.

Secondly, a total of 8 centrifuge tests were designed and performed at different scales (1:10 and 1:30) and corresponding centrifugal acceleration fields (10-g and 30-g, respectively) under a sequence of earthquake ground motions. The presence of roots significantly reduced the permanent crest movement of the slope compared to the fallow case, but had a limited influence on the general propagation and amplification of earthquake motion from the toe to the crest of the slope. Input motion frequency content and slope height, which are often considered to be the key factors influencing the seismic behaviour of slopes were also revealed in this study.

Thirdly, the supporting numerical models which could highly simulate the seismic performance of rooted slope were developed separately for different roots systems. For the plate/heart root system, the analytical modelling consisted of a two-stage process. Firstly, a beam-on-a–nonlinear-Winkler-foundation (BNWF) approach using existing *p-y* curves developed from piling engineering was used to develop a computationally efficient macro-element for individual soil-root interaction. The second stage was to add the force resistance contributions from roots of different diameters with different mechanical properties to produce a smeared zone of continuum material properties (e.g. additional representative cohesion) in place of the roots. While for the tap root system, strength properties of the smeared zone were derived from Large DS tests rather than BNWF. Two models was shown to be effective in predicting the seismic performance of vegetated slopes through validation against centrifuge test data and can be used in the detailed study of the seismic hazard posed to such slopes and any infrastructure located at the slope crest. Following validation, a parametric study was conducted to investigate the influence of different potential characteristics of rooted soil on the overall seismic performance of slope with different size.

Finally, an improved sliding-block procedure was developed to predict the seismic performance of vegetated slopes as a complimentary simplified procedure in preliminary design, particularly for identifying key configurations for further detailed study via FEM. The procedure consisted of two components. Firstly, an analysis using Discontinuity Layout Optimisation (DLO) was used to detect the slope failure mechanism (i.e. find the lowest upper-bound mechanism using a virtual work approach) and predict the yield acceleration of a given slope configuration, accounting for the presence of the roots. The derived yield

acceleration from DLO was then incorporated into a modified limit equilibrium formulation for sliding block to further account for the geometric hardening of the slope as it flattened with slip allowing the permanent settlement at the crest of the slope to be estimated. The procedure was then validated against the centrifuge test results and revealed further insights into the seismic behaviour of vegetated slopes.

iv. Notations and abbreviations

a	adhesion between root and soil
a_{slip}	acceleration of the sliding mass
$a(t)$	shaking induced acceleration
a_r	cross–sectional area
A	area of plane
A_r	total root cross sectional area
ABS	Acrylonitrile Butadiene Styrene
ACC	Accelerometers
ARS	Acceleration Response Spectra
A_s	empirical coefficient for sand, static loading
A_c	empirical coefficient for sand, cyclic loading
b	width of slope
BNWF	Beam-on-non-linear-Winker-foundation
B_s	empirical coefficient for sand, static loading
B_c	empirical coefficient for sand, cyclic loading
c	cohesion of soil
c_k	stiffness proportional, Rayleigh damping coefficient
c_m	mass proportional, Rayleigh damping coefficient
c_r	cohesion due to reinforcement
c_u	undrained shear strength of the soil
C	coefficient related to stress level
CAD	Computer-aided design
CNC	Computer numerically controlled
CRZ	Critical root zone
CSL	Critical state line
C_u	coefficient of uniformity
C_z	coefficient of curvature

D	diameter of pile
d	diameter of root
d_{eq}	equivalent thickness of the plate
DAQ	data acquisition
DBH	Diameter at breast height
DLO	Discontinuity Layout Optimisation
DSA	Direct Shear Apparatus
D_{10}	particle diameter at which 10% is smaller
D_{30}	particle diameter at which 30% is smaller
D_{60}	particle diameter at which 60% is smaller
E	Young's modulus
E_{Al}	Young's modulus the Aluminium
E_r	Young's modulus of the rubber
EC	Euro code
EQ	Earthquake
EQS	Earthquake simulator
ESB	Equivalent Shear Beam
e	void ratio
e_{max}	Maximum void ratio
e_{min}	minimum void ratio
E_{50}^{ref}	triaxial secant stiffness (at 50% of deviatoric failure stress in drained triaxial compression
E_{oed}^{ref}	oedometric tangent stiffness (in compression)
E_{ur}^{ref}	unloading-reloading stiffness
f_0	natural frequency
F	force
FBM	Fibre bundle model
FE	Finite element
FEM	Finite element modelling
FELA	Finite element limit analysis
FoS	Factor of safety

$F_{dynamic}$	dynamic sliding loading
F_p	force against pile group
F_{Pd}	forces required to pull a reinforcement bar from drained soil
F_{Pu}	forces required to pull a reinforcement bar from undrained soil
F_r	force for a single root
F_R	resistance force against sliding
F_s	factor of safety
F_{static}	static sliding force
G_r	shear modulus rubber layer
G_s	specific gravity
G_0	maximum shear modulus
G_0^{ref}	small strain modulus
$\boldsymbol{g}$	acceleration due to gravity(=9.81m/s^2)
H	soil layer height
h_m	total model height
I	second moment of area
I_D	relative density
I_R	relative dilation index
k	coefficient for group efficient
k'	coefficient for the shape of the soil layer
k_h	horizontal pseudo-static acceleration coefficients
k_v	vertical pseudo-static acceleration coefficients
k_{hy}	horizontal yield acceleration
$k_{hy(fallow)}$	horizontal yield acceleration of fallow slope
$k_{hy(rooted)}$	horizontal yield acceleration of rooted slope
$k_{hy(fallow)}^{DLO}$	horizontal yield acceleration of fallow slope derived from DLO
$k_{hy(rooted)}^{DLO}$	horizontal yield acceleration of rooted slope derived from DLO
Δk_{hy}	increase of yield acceleration due to the presence of roots
k_{py}	initial modulus of subgrade reaction
K_0	coefficient of earth press at rest

K_a	coefficient of active earth press at rest
K_a'	coefficient of active earth press at rest for sloping ground
K_p	coefficient of passive earth pressure
l	span of root in material testing
L	length of pile
L_a	anchorage length of the reinforcement bar
L_{pile}	length of the pile
LE	Limiting Equilibrium
LVDT	Liner variable differential transformers
m	slope of *p-y* curve
m'	power-law index for stress-level
MEMS	Micro-Electro-Mechanical Systems
M_s	surface wave magnitude
M_w	Moment magnitude
n	code of model root
n_i	number of roots in root *i*
n_T	total number of roots
N	quantity
NCL	Normal compression line
NMR	Nuclear magnetic resonance
PGA	Peak Ground Acceleration(at soil surface)
PS	Pseudo-static
PSD	Particle size distribution
p	reaction from soil due to the deflection of pile
$p_0^{'}$	initial mean effective confining stress
p_k	a specific soil reaction on *p-y* curves for sand
p_m	a specific soil reaction on *p-y* curves for sand
$p_m^{'}$	overall *p*-multiplier
$p_{mi}^{'}$	*p*-multiplier in root *i*
p_u	a specific soil reaction on *p-y* curves for sand

q	soil reaction
q_y	bearing pressure at yield of the soil
r	radius of soil and root matrix
r_u	errors of maximum under-stress
r_0	errors of maximum over-stress
R	radius of root
R_e	effective centrifuge radius
R_f	root orientation factor
RAR	Root area ratio
RAR_n	root area ratio of each single root n
RPZ	Root protection zone
RSA	Root system architecture
R_f	ratio of deviatoric failure stress to asymptotic limiting deviator stress
s	pile spacing (centre to centre)
s/d	pile spacing/pile diameter
S	soil factor describing the site effect
SH	Strain hardening
SS	Strain softening
S_{amp}	spectral amplification factor
S_{red_ARS}	spectral reduction factor
S_T	topographic amplification factor
S_{pk_amp}	peak acceleration amplification factor
T_r	ultimate tensile strength
T_{rn}	tensile strength of root n
u	lateral displacement
UTS	ultimate tensile strength
v	velocity
V_s	shear wave velocity
w	unit weight of plate
w_{Al}	weight of the aluminium frame plate

W_i	total weight of the strip of material laying vertically above discontinuity *i*
WWM	Wu & Waldron model
y	deflection
y_k	a specific deflection on *p-y* curves for sand
y	a specific deflection on *p-y* curves for sand
y_u	a specific deflection on *p-y* curves for sand
Y	cumulative root fraction
z	depth of soil
z_{silp}	Slip depth
z/H	normalised elevation
ZRT	Zone of rapid taper
α	angle to define geometry
α_i	horizontal direction cosines of the discontinuity
β	angle to define geometry/slope angel
β_0	a depth coefficient
β_{i+1}	instantaneous slope angle
ε_f	flexure strain
$\varepsilon_{s,0.7}$	shear strain
γ	unit weight
γ_r	threshold shear strain γ_r
γ_{unsat}	unsaturated unit weight
γ_{sat}	saturated unit weight
ψ	angle of the root at rupture relative to the failure plane
ψ'	effective angle of dilation
τ	shear stress
$\tau_{applied}$	applied down slope shear stress
τ_{ult}	ultimate soil resistance
θ	slope angle
Δ	deflection
ν	Poisson's ratio

v_r	Poisson's ratio of rubber
v_{Al}	Poisson's ratio of Aluminium
v_{ur}	Poisson's ratio(unload-reload)
ρ	density of the soil
σ	normal stress
σ_f	flexure stress
ϕ'	effective angle of friction
ϕ'_{crit}	critical angle of friction
ϕ'_{mob}	the mobilised friction angle
ϕ'_{pk}	(secant) peak angle of friction
ϕ^*	equivalent angle of friction accounting for non-associative flow
ζ_{add}	additional Rayleigh damping ratio
χ_i	vertical direction cosines of the discontinuity

v. Table of content

vi. List of Figures

vii. List of Tables

Chapter 1 Introduction

1.1 Background

Earthquakes have been historically perceived as one of the most damaging natural hazards. In the past ten years, several catastrophic earthquakes have been reported, including the Kashmir (Pakistan) earthquake (2005, M_w=7.6); the Java (Indonesia) earthquake (2006, M_w=6.3); the Peru earthquake (2007, M_w=8); the Wenchuan (China) earthquake (2008, M_w=7.9); the Southern Sumatra earthquake (2009, M_w=7.5); the Haiti earthquake (2010, M_w=7.0); the Tōhoku earthquake(2011,M_w=9.0) and the Christchurch earthquake (2011, M_w=6.3).

The primary hazard to the built environment associated with earthquakes is the strong shaking of the ground caused by the passage of seismic waves, which induces inertial forces and relative displacements in structures that can lead to structural damage. The ground vibrations can also trigger secondary geotechnical hazards, including liquefaction and the settlement of loose deposits. These can greatly increase the human, social and economic impact of an earthquake. Amongst the secondary geotechnical hazards associated with earthquakes, tsunami and landslides (see Fig 1.1) are potentially the most destructive (Rodríguez et al. 1999).

As an example, in the 2008 Wenchuan earthquake, 69,227 lives were lost and 374,643 people injured, with a further 17,923 listed as missing. Tens of thousands of landslides were triggered over a broad area, some of which buried large sections of some towns, blocked transport links and dammed rivers (Dai et al. 2011). It was estimated that the total losses exceeded £80 billion, and the losses from the earthquake-triggered landslides accounted for over a third of the total earthquake losses (Chen et al. 2008).

Considering such catastrophic destruction due to earthquake-induced landslides, research ranging from modelling and understanding the mechanism of landslides (Terzaghi 1951; Leroueil 2001; Gabet & Mudd 2006; Changwei et al. 2014), monitoring of some trigger factors (such as premonitory small displacement) (e.g. Reid et al. 2008;Tofani et al. 2013),

improvements in risk management (mainly through hazard zonation and forecasting) (e.g. Refice & Capolongo 2002; Li et al. 2012; Umar et al. 2014), to improvements in slope stability (e.g. Abramson et al. 2002), have been widely undertaken.

Fig 1.1 Earthquake induced landslides in recent years (After Evans & Bent 2004; Dai et al. 2011; www.eathquake-report.com; Harp et al. 2013; Miyagi et al. 2011; Aydan et al. 2012)

The use of vegetation (grasses, shrubs and trees) as an effective and environmentally-friendly approach to improving slope stability under static conditions has been widely recognized (Coppin & Richards 1990; Stokes et al. 2008). There is anecdotal evidence that vegetated slopes also performs better than fallow slopes during earthquakes. However, no research has yet been reported on the dynamic behaviour of slopes planted with vegetation due to the extreme expense and difficulty involved in conducting full scale dynamic testing on shrubs and trees.

Moreover, although a number of analytical and numerical models have been introduced to understand and quantify the root and soil interaction, these models are far from ideal in practical application, because they either over-simplify the problem or are time consuming (Wu 2013).

Recent studies that focus on mechanical soil-root interaction (e.g. Schwarz et al. 2010; Mickovski et al. 2010) suggest that plant roots respond in a similar way to inert soil inclusions, such as soil nails or pile foundations, when subjected to loading. Duckett (2013) employed existing pile analysis techniques to develop numerical models to quantify individual root soil interactions under very low effective stress and the model was validated by laboratory direct shear (static) tests to be accurate and time-efficient. Whether this model can be used for dynamic loading and higher confining stresses still requires investigation and methods for incorporating such soil-root interaction within engineering analysis and design are still required.

1.2 Aims and objectives

This thesis will describe the results of an investigation into the dynamic performance of slopes planted with trees/containing tree roots from individual root-soil interaction to global slope behaviour. Centrifuge modelling, numerical and analytical modelling will be employed in this study alongside supporting novel element testing of rooted soil, and the aim will be met through the following key objectives:

i. *Design and fabricate scaled models/analogues of tree root systems for use in centrifuge modelling*: The plate and heart root system (See Fig 2.2) of trees planted in slopes will be simulated by groups of individual straight root analogues. A more complex 3-D tap root system (see Fig 2.2) is also designed in SolidWorks 2012. Both classes of root model are fabricated using a Stratesys Inc.uPrint SE Acrylonitrile Butadiene Styrene (ABS) rapid prototyper (also known as a 3-D printer). The strength and stiffness of model roots will be validated against data of real roots collected from previous studies.

ii. *Observe and quantify root-soil interaction during shear loading*: A serious of large direct shear tests are described which show the behaviour of the 3-D model roots and straight root groups within a soil matrix during monotonic shear loading. The effects of root area ratio, root morphology and root anchorage depth are investigated. The most widely used existing root reinforcement analytical models are compared against the testing results, alongside recently-developed beam-and-spring models (after Duckett, 2013).

iii. *Develop a computationally-efficient numerical model to quantify root soil interaction during shear loading*: A Beam-on-non-linear-Winker-foundation (BNWF) model using existing *p-y* formulations from piling engineering is employed to produce a macro-element describing the individual root and soil interaction pre- and post-failure. The model is validated against the direct shear testing results from (ii) and is then used to forward-predict the root soil interaction within centrifuge models at prototype scale.

iv. *Centrifuge modelling of rooted slopes under earthquake loading*: 8 dynamic centrifuge tests are designed and performed to investigate the seismic performance of rooted slopes. Factors which may affect the performance of rooted slopes, including root morphology, input motion frequency content and slope height are investigated through the comparison of different centrifuge tests.

v. *Develop a numerical modelling approach which can simulate the complete global dynamic performance of rooted slopes during centrifuge tests:* A continuum Finite Element Modelling (FEM) approach incorporating appropriately-sized zones of smeared rooted soil properties derived from the BNWF macro elements (ii) or direct shear tests (iii) is developed and validated against the centrifuge modelling results from (iv).

vi. *Develop a simplified method for predicting permanent deformations of rooted slopes to complement FEM (v) for engineering application*: A simplified procedure for preliminary design based on a combination of Newmark sliding block analysis and Discontinuity Layout Optimisation (DLO) for determining yield acceleration is developed to predict the seismic performance of fallow and rooted slope. The procedure is again validated against the centrifuge modelling results from (iv).

1.3 Structure of thesis

The thesis is presented in eight chapters, and the contents of each chapter are described in this section:

Chapter 2 firstly reports an literature review of the basic properties of roots related to engineering practice. Then a detailed state-of -the-art of seismic slope stability analysis will be given, with a particular emphasis on vegetated slopes. Finally, calculation models used for root and soil interaction will be illustrated.

Chapter 3 describes the experimental method used in this work and explains the principles of centrifuge testing and scaling laws. The centrifuge machine, model material, instruments, input motion and preparation procedure are presented in detail.

Chapter 4 considers the design and fabrication of representative 3-D scaled root models which represent a tap root system in full detail. The material used to fabricate model roots is tested and validated against data collected from a body of literature for real roots. A series of large direct shear (DS) tests are then reported which investigate root and soil interaction and reveal how RAR and root morphology may influence the root contribution to shear strength and stiffness. The results of three 1:10 scale dynamic centrifuge tests containing multiple 3-D root clusters and having the same root diameter to soil particle size ratio as the DS tests are then used to investigate the global performance of rooted slopes during earthquake-induced sliding, and the root morphology effect. Existing root reinforcement estimation methods are also compared with the measured root cohesion from the DS tests and inferred values from the centrifuge tests.

Chapter 5 presents the dynamic performance of slopes planted with roots with relatively simple geometry representing plate/ heart root system in centrifuge modelling. Supporting numerical modelling is conducted and validated against the centrifuge data to further study the problem. The numerical modelling work consists of two parts: (i) A computationally-efficient BNWF model using *p-y* springs is employed to observe and quantify the individual root and soil interaction relative soil-root displacement; (ii) A fully dynamic plane-strain continuum Finite Element (FE) model using an appropriately-sized zone of smeared rooted

soil properties derived from the BNWF macro elements is performed to show the global slope behaviour.

Chapter 6 gives further insight into the seismic performance of rooted slope reinforced with tap root system. Results of a total of 5 centrifuge tests at different scales (1:10 and 1:30) under a sequence of strong earthquake motions are reported and compared. Input motion frequency content and slope site effect, which are always considered as the key factors influencing the seismic behaviour of slope will be studied. The seismic response preshocks and aftershocks will also be revealed.

Chapter 7 illustrates the numerical modelling approach which can be used for a tap-root system following the procedures developed in Chapter 5 and validated against the centrifuge models performed in Chapter 6. A small parametric study to isolate the effects of different root-soil matrix properties (e.g. root cohesion, rooted zone, matrix stiffness and additional damping) on the overall response will also be performed.

Chapter 8 focuses on developing a simplified procedure for preliminary design to predict the seismic slip of a vegetated slope. The whole procedure consists of two components. Firstly, DLO analysis is used to detect the slope failure mechanism and the corresponding yield acceleration of a vegetated slope. The second stage is to incorporate the derived yield acceleration from DLO into modified limit equilibrium equations to further account for the geometric hardening response of slope and predict the permanent settlement at the crest of the slope via a slip-dependent Newmark sliding block approach. This procedure is then validated against the centrifuge test results reported in Chapter 6 and used to provide further insight into the controlling mechanisms behind the seismic behaviour of rooted slopes.

Chapter 9 summaries the results of the work and suggestions for future work are made.

Chapter 2 Literature review

2.1 Introduction

Earthquakes are one of the major triggering causes for landslides (Malamud et al. 2004). Keefer (1984) established a database on earthquake induced landslides from 1811 to 1980 and performed statistical analysis on the correlations between landslides and the magnitude of earthquake. It was found that the minimum earthquake magnitude to generate landslides was 4.0 according to US specification. Such correlations varied in different geological, topographical and climatic conditions. Following this study, Bommer et al. (1999) renewed the database from 40 to 76, adding worldwide earthquakes between 1980 and 1997. There was no significant difference in the findings between these two studies, which offers an effective way to initially assess the hazard of earthquake induced landslides. As for the case in the past twenty years, no similar study has been performed. Given the active crustal activity in recent years (see Fig 2.1), the threat of earthquakes to slope stability should be highlighted.

Damage from seismically induced landslides and other ground failures sometimes exceeds the damage directly caused by the ground shaking and fault rupture. Minimising this damage has been one of the major concern to geotechnical engineers (Kokusho & Ishizawa 2006).

To evaluate seismic slope stability, based on limiting equilibrium (LE) slope stability analysis and finite element (FE) analysis a variety of techniques have historically been developed (Duncan 1996), which generally fall into three categories: (i) force based pseudo-static methods; (ii) displacement based methods (also known as the Newmark sliding block method) and (iii) stress-deformation analysis through numerical methods. The advantages and limitations of these three methods will be discussed later.

In order to decrease failure of slopes, various types of traditional geotechnical methods have been used, including soil nailing, piling and retaining walls, but these traditional geo-techniques are not the focus of this project. Vegetation as an environmental-friendly approach

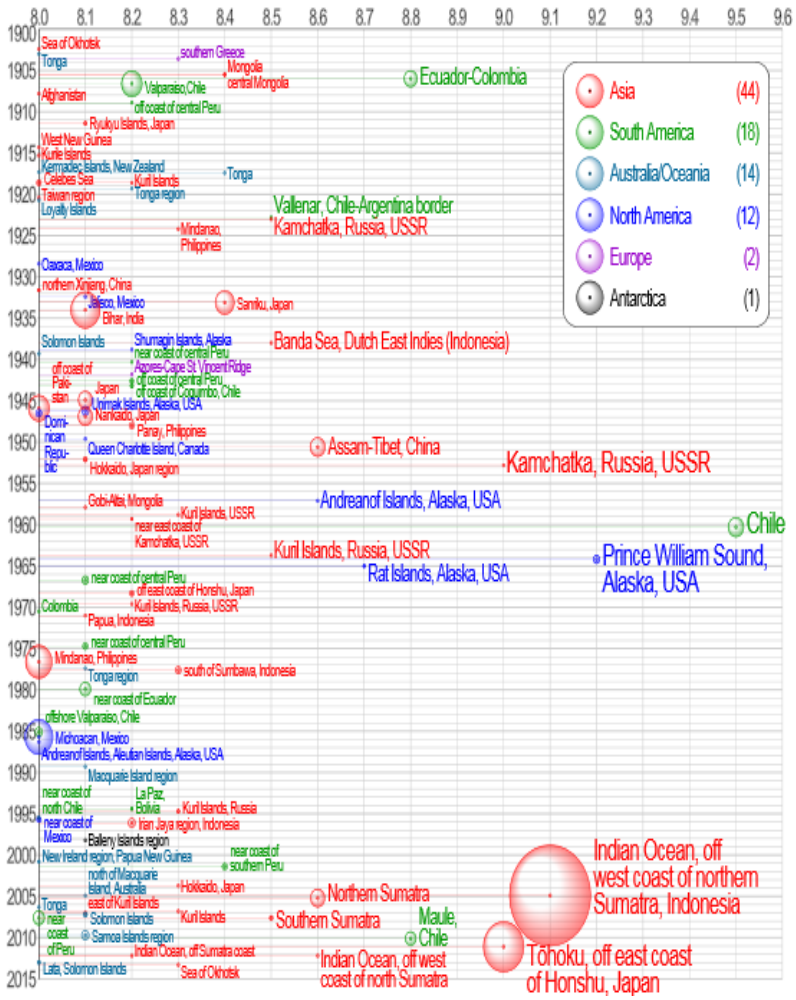

Fig 2.1 Earthquake of magnitude 8.0 and greater since 1900. The apparent 3D volumes of the bubbles are linearly proportional to their respective fatalities (http://en.wikipedia.org/wiki/List of 21st century earthquakes)

has been widely used in many natural and man-made slopes, and it has been generally recognized that this can increase the stability of slopes under static conditions. There is anecdotal evidence that vegetated slopes also perform better than fallow slopes during earthquakes.

This literature review will start with a review of the fundamental properties of roots related to use in engineering practice. Then a detailed state-of-the-art of seismic slope stability analysis review will be given, with a particular emphasis on vegetated slopes. Finally, calculation models used for root-soil interaction will be illustrated.

2.2 Fundamental characteristics of roots

To appreciate how roots are mobilized to stabilize slope during slippage and should be managed in practice, a better understanding of the basic properties of roots is essential. This section reviews those aspects which are relevant to the performance and use of vegetation in an engineering context.

2.2.1 Root system

Plant root systems are of particular interest to engineers because of their fundamental importance to most of the functions that vegetation can perform. Root systems vary from very fine fibrous systems (herbaceous plants) through branched systems to tap root systems depending on the species of the plant. Controlled laboratory experiments have shown that the size, plasticity and branching pattern of a plant root system is highly dependent upon the genes within the plant and the surrounding soil condition (e.g. Norris et al. 2008; Hodge et al. 2009; Smith & De Smet 2012; Jung & McCouch 2013; Rich & Watt 2013). For herbaceous plants, which have highly flexible stems, transmit mainly tensile force to their roots. As a result, they produce shallow, fine, fibrous root systems. While for shrub and trees, on the other hand, which have stiff stems that transmit both tensile and overturning forces to their root systems, are consequently stiffer, deeper and more favourable for slope stability applications (Reubens et al. 2007; Duckett 2013).

Tree root systems are generally categorized into three groups (Lal 1998), depending on their basic three-dimensional structure. A heart system is the most common type of root system found in angiosperms, where horizontal and vertical laterals develop from the base of the tree (Fig 2.2a). Plate systems are often found in gymnosperms such as spruce and consist of horizontal lateral roots spreading out from the base of the tree stem (Fig.2.2b). Vertical sinker roots develop and grow downwards from the main lateral roots. A third type of root system found in tree species is one where a large tap root anchors the tree directly, like a stake in the ground (Fig 2.2c) and horizontal lateral roots act like guy ropes (Ennos 1993). However, the shape of a root system is largely determined by site conditions and external mechanical loading (Danjon et al. 2013).

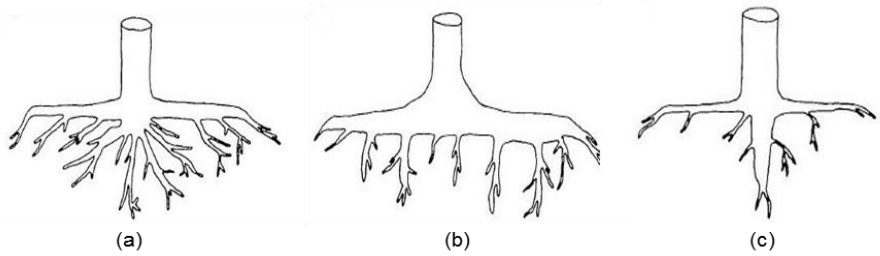

Fig 2.2 Three basic types of tree root system: (a) Heart root system with many branches; (b) Plate root system with large horizontal lateral roots and sinkers; (c) Tap root system with a large central vertical root and small lateral roots (Lal 1998)

The mechanical behaviour of two types of tree system (heart and plate), of which individual roots resist overturning or uprooting force separately due to the wind or soil movement, is well recognized (Stokes & Mattheck 1996). In terms of the tap root system, many uncertainties still exist and it is has been of much interest to researchers recently (Danjon et al. 2013).

2.2.1.1 Root architecture

Root system architecture (RSA) is a result of a sequence of formation processes including branching, elongation, gravitational response, thickening and turnover (Thaler & Pagès 1998). Root morphology and root density have been considered to contribute more than root mechanical traits to the additional root cohesion (Docker & Hubble 2008; Fan & Chen 2010; Ghestem et al. 2013). Research related to RSA has concentrated on two aspects: i) measurement and statics; ii) modelling and development prediction.

An up to date review of state-of-the-art techniques used for RSA measurement and analysis is given by Danjon & Reubens (2007). The majority of the available RSA data is from the invasive method (e.g. excavation and uprooting). Non-invasive techniques such as high resolution X-ray computed tomography (see Mooney et al. 2012) and nuclear magnetic resonance (NMR) imaging (Stingaciu & Schulz 2013; Liu et al. 2014) can only be used on very small potted plants for specific geometry properties. Measurements can be recorded in the form of XYZ coordinates or specific root segment features (length, orientation and dimension).

Topological arrangement of component and geometric characteristics are two major concerns involved in the establishment of RSA. Two main types of models are generally used to quantify the topology in previous studies: (1) the static Fractal branching model (e.g. Fitter & Stickland 1992; Spek & Noordwijk 1994; Ozier-Lafontaine et al. 1999; Walk et al. 2004; Dannowski & Block 2005; Wang et al. 2009) and (2) Dynamic 3-D developmental models (Jourdan & Rey 1997; Pagès et al. 2004; Collet et al. 2006). These models successfully capture the developmental rules and growth rhythm of root systems and can provide an accurately simulated output of 3-D root systems compared with the natural case (Tobin et al. 2007). It should be noted that in this project the essential simplification of RSA for small scale investigation at printable sizes will generate a slight misfit with the topology functions, but the overall trend will be followed. In terms of geometry, shape, size, orientation and spatial location are all important. Existing analytical models on quantifying root soil interaction (e.g. Wu 1976; Pollen & Simon 2005) derive mechanical properties from root geometry (specifically diameter). Root size properties including root length, root density, root diameter will be discussed in the following section.

2.2.1.2 Root size

Classifying roots into different categories is a practical tool to make measurement and analysis of RSA easier and more effective. For this reason, a variety of attempts have been performed on the basis of differences in morphology and physiological parameters observed between roots. The most common division is the one distinguishing coarse roots from fine roots, which highlights the difference in diameter assuming a functional difference then exists. Coarse roots play an important role in anchorage while fines roots act in reinforcement and soil fixation (Reubens et al. 2007; Danjon et al. 2013). However, there is no consensus on the critical value of diameter to distinguish fine roots and coarse roots. Reubens et al. (2007) suggests fines roots usually are root biomass with diameter less than 3mm. Values of 0.5 mm, 2mm and 5mm are given by Bohm (1979); Watson et al. (1995) and Sonnenberg (2008), respectively. This variation is associated with the objective of the study and should be used with caution. Within this two category range, sub-categories can be defined (Tobin et al. 2007). Here the classification (Table 2.1) of Watson et al. (1995) is shown for illustration as such study has a similar research objective with this project.

Root length and root number vary with species, plant age and season. Main structural roots are perennial structures whereas fine fibrous roots are subject to annual cycles of decay and renewal (Danjon et al. 2005). The root distribution (Fig 2.3) of two white oak trees growing on sloping ground reported by Danjon et al. (2008) is shown here for a general understanding of root size properties. The two trees were located in the University of Georgia's Warnell School of Forest Resources Whitehall research forest (33°56'00"N, 83°22'00"W). This area is a seismically sensitive zone (http://earthquaketrack.com/r/georgia-usa/recent). It is assumed that the growth of root systems more or less has some relationship with earthquake motions.

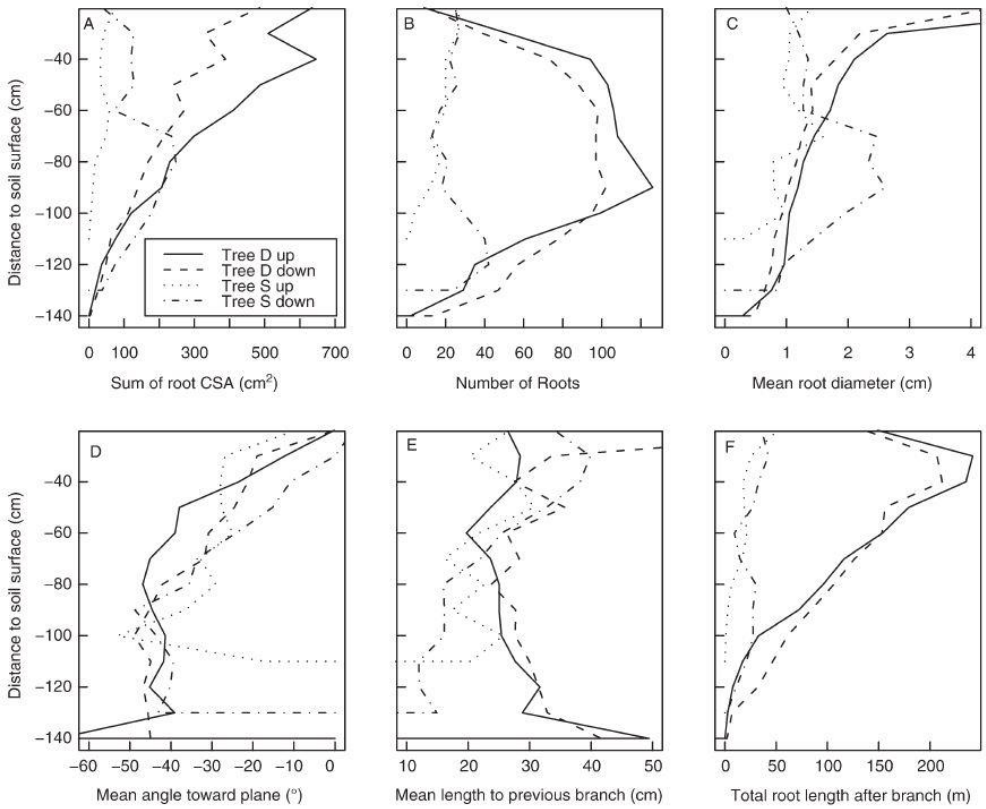

Fig 2.3 Vertical distributions of roots where roots intersect planes parallel to the slope (Danjon et al. 2008)

Table 2. 1 Root diameter classes for structural roots (Watson et al. 1995)

Root diameter :mm	Structural root class
<2	Not consider
2-10	Small
10-20	Medium
20-50	Large
50-100	Very large
>100	Coarse

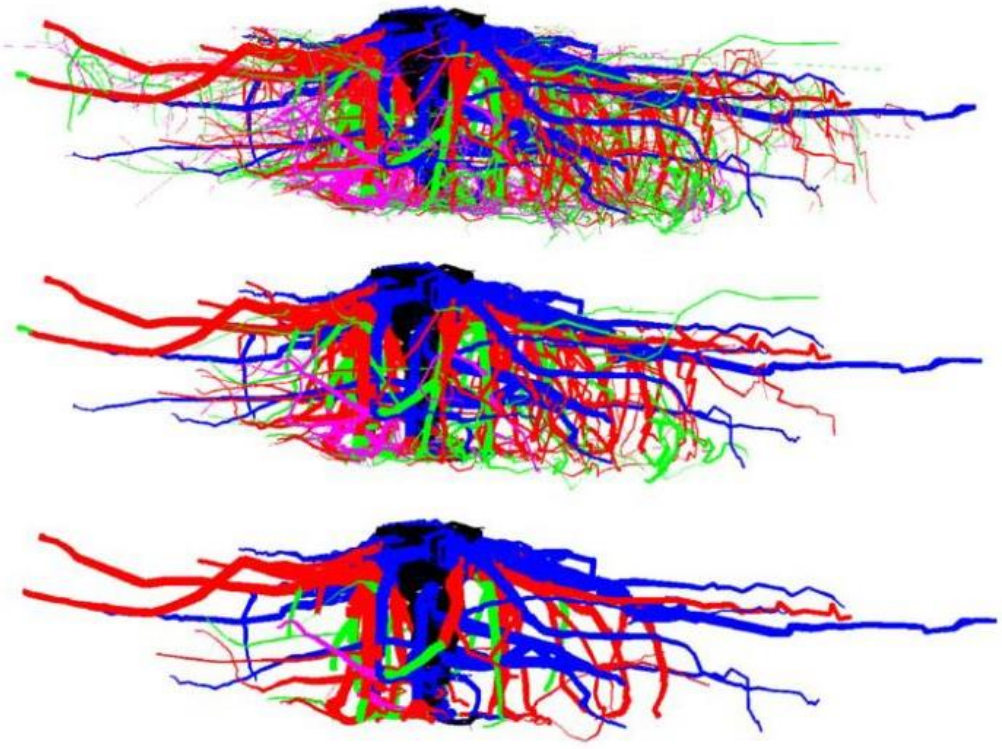

Fig 2.4 Graphic reconstruction of a mature showing a mature P.pinaster root system ,showing how the sampling threshold affects the architecture (Danjon & Reubens 2008)

The average diameter of tree roots is generally small, which is related to the composition of root system. Abernethy & Rutherfurd (2001) found that 96% of riparian tree roots were less than 1cm in diameter. 60% of all roots in three hardwood species were found to be smaller than 0.5mm in diameter by Abdi et al. (2010). But this does not mean the quantity of fine roots (<5mm) is always higher than that of coarse roots. A study by Parr & Cameron (2004) observed that a spruce tree had a total of 82500 roots. Among them, coarse roots (>5mm) comprised 62%. Root number and diameter composition are species dependent.

Danjon & Reubens (2008) illustrated a change of RSA (Fig.2.4) if eliminating roots with fine diameter. When the minimum root diameter is varied from 5mm through 20mm to 40mm, the number of root segments decreases from 6700 to 4000 to 1600. A large portion of fine roots leads to a small average diameter, so it may be not suitable to use the average root diameter to indicate the cross section of roots. In despite of low quantity, only 3 to 10, the dominant structural roots of the tree were found to occupy 80% of the total root mass and play a significant role in tree anchorage (Coutts et al. 1999).

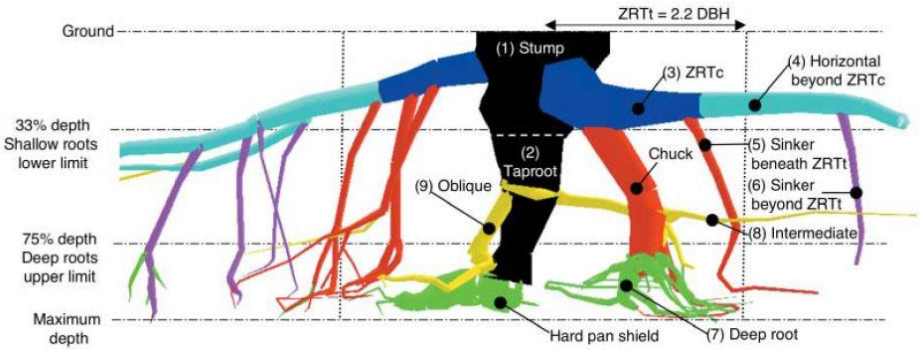

Fig 2.5 A typical tap root system of mature Pinus pinaster, showing the zone of rapid taper (Danjon et al. 2005)

2.2.1.3 Root plate

One important concept of a root system related to tree anchorage is the root plate. This provides a simple approach to understand and work with tree anchorage in the field (Coder 2010). Tree anchorage has been estimated as a function of root plate size, tree mass and external loading by some researchers (e.g. Coutts et al. 1999; Koizumi et al. 2007; Moore 2000; Fourcaud et al. 2008). It is also an indicator of root influence zone used for analytical models and numerical models.

A tree root plate is composed of large structural roots generated at the base of the stem. Such structural roots usually taper rapidly away from the stem base (see Fig 2.5). The tapering structure will make the dominant behaviour of the root segment transform from bending to tension. The boundary of the root plate is defined by the critical point of behaviour transformation. Given such a definition, a root plate is a stiff, shallow, horizontal disk-shaped rooting area.

A root plate can be the same as or much larger than zone of rapid taper (ZRT) (Coder 2010), depending on the study. The typical shape of a root plate suggested by Koizumi et al. (2007) is an oval with a ratio of 0.8 between the long and short axes as viewed from above. A circular shape with a side cross section of a cone or half an ellipse was reported by Peltola (2006) and Lundström & Jonas (2007), respectively.

Tree anchorage was commonly observed to increase with the depth of root plate, and two approaches have been introduced : i) 3.6 times the tree diameter at breast height (DBH)

(Coder 2010); ii) 1/3 of the maximum rooting depth (Danjon et al. 2005) . However, debates also exist on the impact of root plate depth on root anchorage. Koizumi et al. (2007) found that root plate depth was not a significant factor in anchorage after a study of tree failures.

2.2.2 Root spread

The lateral extent of root systems, especially of trees, can be considerable, with the majority of trees spreading by several metres. Measurements of root distributions around individual isolated trees revealed that root biomass decreases with increasing distance from the stem (Gilman 1988; Schenk & Jackson 2002; Göttlicher et al. 2008). It is therefore important to consider root systems as a function of influence zone. Two types of root zone have previously been defined, namely: critical root zone (CRZ) and zone of rapid taper (ZRT).

CRZ extends to approximately one third to half of the zone the roots really occupy (known as the root protection zone RPZ)(Johnson 1999). One common method used to identify the CRZ is to define it as the "drip line"—the area directly below the branches of the tree. However, when dealing with trees that have been growing in the forest or that naturally have a narrow growth habit, an approach using "critical root radius" is more accurate than the drip line method. This is particularly true for columnar trees and for those where competition has reduced the canopy spread. The critical root radius is calculated by the relationship with the diameter at breast height (DBH). For each 1 cm of DBH, 18 cm of critical root radius is allowed for sensitive, older, or unhealthy trees, or 12 cm for tolerant, younger, healthy trees(Johnson 1999).

The ZRT is more closely related to the mechanical behaviour of roots as this concept defines the zone of dominant structural roots, which have been found to provide more than 80% of total root mass (Coutts et al. 1999). A tree will be vulnerable to wind throw if it produces very few structural roots (Nicoll et al. 2006). It is evident that most coniferous tress are supported by 3 to 11 large structural roots (Coutts et al. 1999; Mickovski & Ennos 2003; Tobin et al. 2007). Eis (1974) studied the growth rhythm of tap root systems of various species of distinct ages. During the early seedling stage, a rapidly developing tap root penetrates into the soil and plays a dominant role in early stability. Oblique lateral roots originated from the tap root in the early seeding stage, followed by oblique sinkers which

originated from the main laterals. Some of these oblique roots increased in size in the late stage and the whole root system formed a bell-shaped form. Lateral roots taper rapidly until a maintained diameter of 10-20 mm, by which stage they have lost much of their rigidity and physical strength. Beyond the ZRT, lateral roots extend outwards in a broad zone for many meters, without further decrease in size. The three types of structural roots comprise a functional cage, in which the tap root acts as a main pole in the soil to mobilise the whole system to resist external loading, oblique laterals contribute to wind firmness and sinkers hamper the lateral movement of the whole system.

The volume of sinker roots was mainly located within twice the DBH radial distance according to Danjon et al. (2005), which provides a quantitative indication for physical modelling. For quantifying ZRT, Danjon et al. (2008) introduced three approaches,

i) Defining a standard, fixed radial distance of the main tree axis or of the stump bark.
ii) Defining the ZRT by a radial distance function of the tree size. In Danjon et al. (2005), this limit was set to 2.2×DBH to determine the radius of ZRT.
iii) Directly from the definition of ZRT, as function of root taper or ovality.

2.2.3 Rooting depth

Plant root systems can penetrate to depths of several metres if unconstrained by soil conditions (Canadell et al. 1996; Jackson et al. 1996; Zeng 2001; Schenk & Jackson 2002; Schenk & Jackson 2005; Schenk 2008) . Most species have roots at least of 2 m length, as shown in Fig 2.6 (Schenk & Jackson 2002; Kleidon 2004). This structural trait has developed mainly for the function of water up-taking, as well as carbon and nutrient cycling. The benefit of such a structure compared with the shallow root system for slope stability applications has been highlighted. The presence of root system deep within the soil increases the safety factor of the slope and hence prevents potential slip.

Despite rooting so deep, the majority of root biomass is concentrated in the top soil, and shows exponential reduction of root density with increasing depth. An asymptotic equation introduced by Gale & Grigal (1987) has been used by most authors to model the cumulative root fraction with regard to depth for most species:

$$Y = 1 - \beta_0^{100d} \qquad \textbf{Eq 2. 1}$$

where Y is the cumulative root fraction from the surface to depth d (m) and β_0 is a depth coefficient, which depends upon vegetation type. The approximate distribution of tree, shrub and grass roots as a function of soil depth across the major biomes is shown in Fig 2.7.

The downward growth of roots can be limited by a variety of factors, such as soil bulk density, seeding method or shallow bed rock, but probably the most efficient barriers are horizontally stratified layers of shale or clay, permafrost, and the water table (Varney & Canny 1993;Grant 1998; Yanagisawa & Fujita 1999;Laio et al. 2006; Osman & Barakbah 2006; Guswa 2008; Ibrahim et al. 2011) .

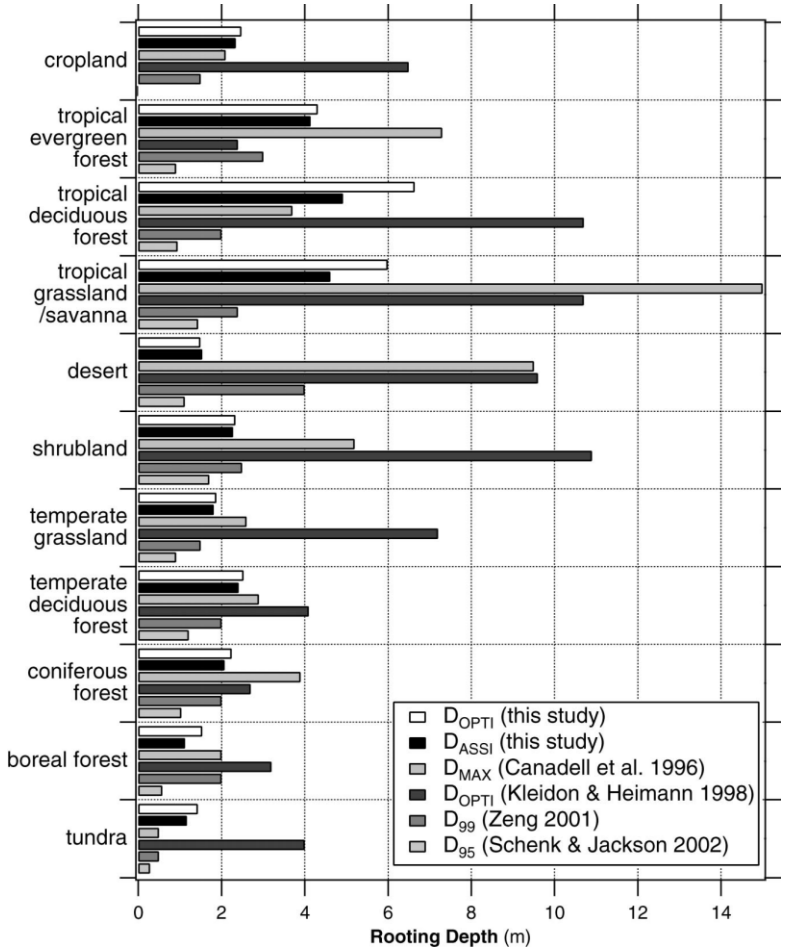

Fig 2.6 Maximum rooting depth compiled from various authors (Kleidon 2004)

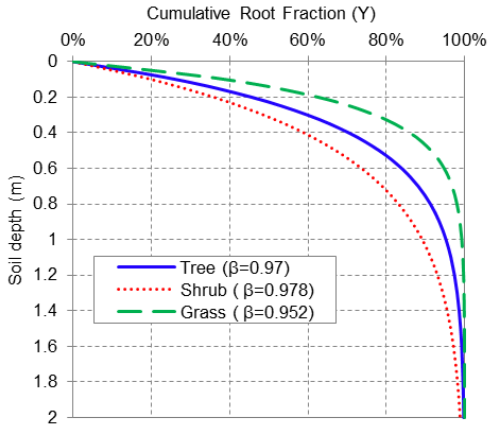

Fig 2.7 The distribution of grass, tree and shrub roots as a function of soil depth (After Jackson et al., 1996)

Plants show a variety of root types through which they have access to deep soil layers. The majority are tap roots, sinker roots and obliquely descending lateral roots, all of which are important adaptions for reaching deep soils. The phenotypic expression of these root types is species dependent, but environmental conditions may completely change root structure, architecture, and the depth to which roots are able to descend (Schenk & Jackson 2005; Kroon & Hendriks 2012; Pinheiro et al. 2013).

2.2.4 Root mechanical properties

Tree roots, which have a cellular structure with a number of overlying layers of tissue, have evolved to an optimum balance of stiffness and strength (Bischetti et al. 2005). Among them, the xylem and cambium layers play a significant role on mechanical behaviour, driving the characterisation of tensile strength and stiffness, respectively. The xylem tissue runs through the core of the root and consists of long, cylindrical cells that are joined from end to end and provide unidirectional fibre orientation (Karam 2005). The main function of the xylem tissue is to transport minerals, nutrients and water throughout the plant. Such biomechanical function requires strong walled cells which are constituted of cellulose. The cambium layer sits between the xylem and phloem tissues and generates layers of cork as the plant ages (Karam 2005). It should be noted here that herbaceous species do not have the cambium layer.

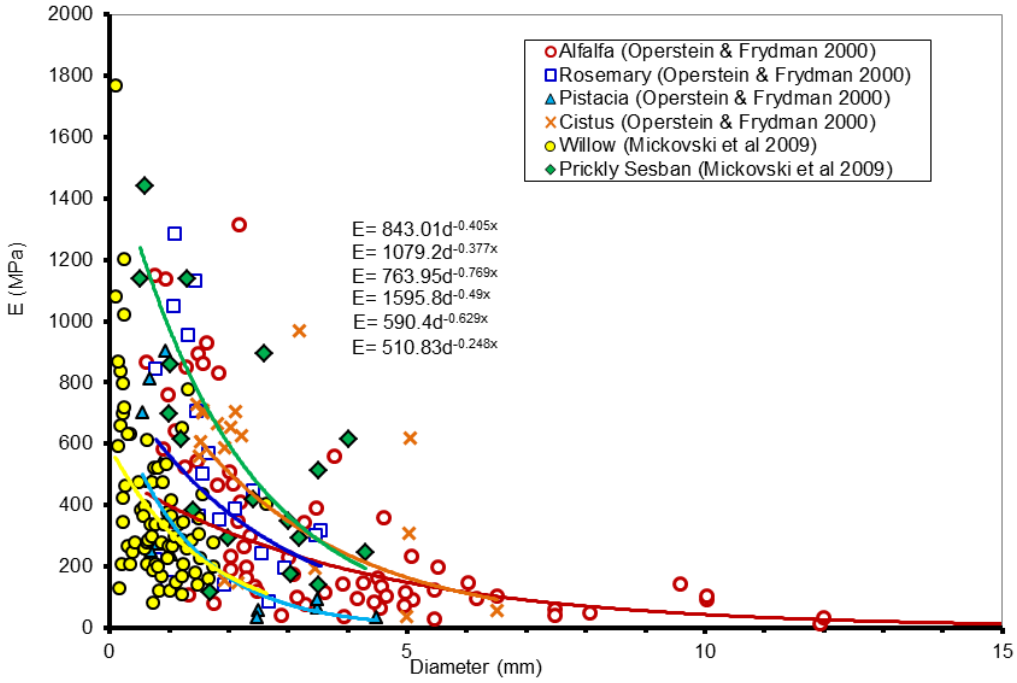

Fig 2.8 Effect of root diameter on Young's modulus

2.2.4.1Root stiffness

The response of structural roots under lateral loading (such as from moving soil or wind) conforms to beam theory (Tobin et al. 2007). The elastic flexural stiffness of the beam is *EI*, where *E* is the Young's Modulus (MPa) of the material and demonstrates a declining power-law trend with diameter (Fig 2.8), i.e. $E \sim d^a$, where a is typically -0.5 to -2 (Mickovski et al. 2009). *I* is the second moment of area; if the beam is circular in cross section (of diameter *d*), *I* can be calculated using:

$$I = \frac{\pi d^4}{64} \qquad \textbf{Eq 2. 2}$$

The above equation clearly demonstrates that the bending stiffness decreases rapidly with diameter, which explains why the structural roots with large diameter play a dominant role in tree anchorage. When a root branches, even when the cross section of the branching roots remains the same as the 'parent' root, there is still a considerable reduction in stiffness of the system, and as a result root always fails at the point of branch.Resistance to bending also

occurs through the development of the shape of structural roots. In response to wind movement, trees with shallow structural roots have been reported to develop root cross-sectional shapes comparable in appearance to 'I-beams' and 'T-beams' (Fig 2.9) used by engineers, to maximize resistance to bending while using a minimum of material.

Fig 2.9 Typical spruce I-beam and T-beam root cross sectional shape (Tobin et al. 2007)

2.2.4.2 Root tensile strength

When an individual root is under tension loading, the root will present an approximation of conventional elasto-plastic behaviour until the root breaks. Failure occurs in two stages: i) breakage of the stiffer outer root structure; then ii) breakage of the inner root structure (Hamza et al. 2006). The failure tensile force is observed to vary with root geometry, plant species and root age (Sonnenberg et al. 2010).

The ultimate tensile strength (UTS) of roots is also found to be a function of root diameter:

$$T_r = k * d^m \qquad \textbf{Eq 2. 3}$$

From Genet et al. (2005) the value of k and the exponent m varied within ranges of 23 to 64, and -1.0 to -0.5, respectively, where d is in mm and T_r is in MPa. There is a trend for angiosperms to have an exponent value near -1.0, and for gymnosperms to have an exponent value near "-0.75" (Bischetti et al. 2005); however, it should be noted that many exceptions exist (Coder 2010).

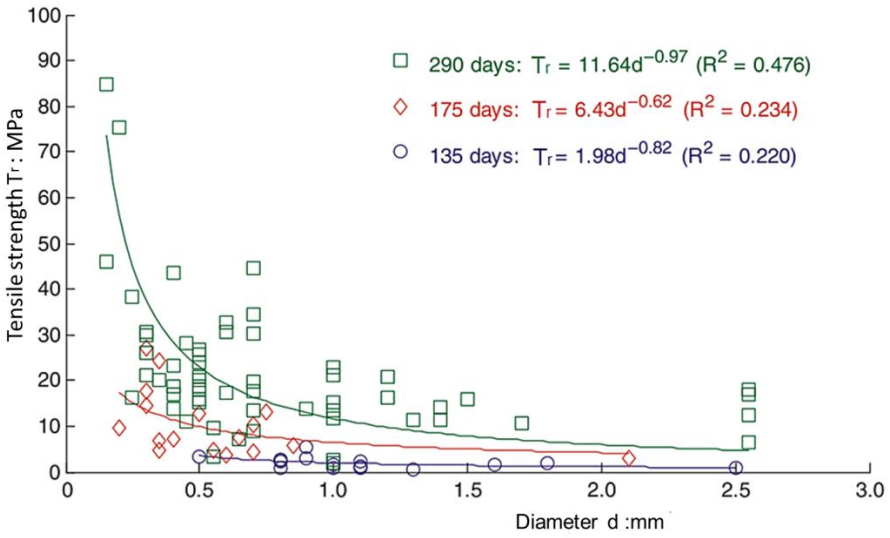

Fig 2.10 Relationship between tensile strength and diameter for roots of different ages (Sonnenberg et al. 2010)

Mao et al. (2012) compiled a comprehensive database (Appendix I) of the value of *k* and *m* from the literature. One-way analysis of variance (ANOVA) was employed to distinguish the difference between herbaceous plants, shrubs and trees. It was found that the effect of plant functional group was significant on both *k* (F=6.34, p=0.003) and *m* (F=18.38, p<0.001). Mean *k* was 21.05±16.81, 29.23±22.87, 39.63±20.84 and mean *m* was -1.15±0.42, -0.69±0.3, -0.70±0.23 for herbaceous plants, shrubs and trees, respectively. Values of *k* and *m* for trees were significant differently to those for herbaceous plants, but not when compared to shrubs.

As a root grows, its cell walls develop reinforcement, which increases its cellulose content. As a result, tensile strength has been observed to increase with root age. The evidence was presented by Sonnenberg et al. (2010), as shown in Fig 2.10. However, this study only considered very young roots. As for mature roots, whether tensile strength increases with age is still uncertain (Duckett 2013).

2.2.4.3 Root anchorage

When the subaerial component of woody plant subject to external loadings (e.g. strong wind loading, earthquake shaking and animal grazing), various axial and lateral loadings are transferred to the root system. In order to resist such multiple loadings, root requires a combination of fibrous and rigid elements (Coutts et al. 1999; Nicoll et al. 2006; Reubens et

al. 2007). The location, scale and quantity of these elements are highly affected by the magnitude and frequency of external loading during root growth as well as genetic factors.

In response to these multiple loadings, root system may overturn or be uprooted from the soil. Overturning is the most common failure mechanism for woody plants. Resistance to overturning is generally considered as a function of root stiffness, soil confining stress and root soil interaction (Coutts et al. 1999; Gregory 2006). Gregory (2006) investigated the most likely overturing mechnisms for different types of tree root system (Fig 2.2) and considered the tap root system as pile foundation to assess the capacity of tap root system against lateral loading. It was found that the ability of tap root system against moving soil illustrated a positive relationship with the dimension of the tap root (diameter and length). Such derivation was further validated by Duckett (2013) through numerical modelling.

In terms of the uprooting behaviour, it is more likely to occur in herbaceous plants due to their supple nature. While for woody plants, uprooting will mainly be observed in lateral roots and deep individual roots below the slip plane (Mickovski et al. 2005; Mickovski et al. 2010). The resistance of these individuals root to uprooting is highly dependent on the surrounding root soil interaction (Mickovski et al. 2007). During uprooting, root may break or be pulled out, which performance occurs is dominated by that which requires a lesser force (i.e. the lesser of pull out force and root tensile strength). Further discussion on uprooting and overturning behaviour will be presented in Section 2.4 under the view of traditional geotechnical structure.

2.3 Slope stability analysis

2.3.1 Classification of seismic failure of natural slopes and earth dams

Natural slopes and embankments have a tendency to slip as a result of gravity and other forces, but this slip trend is counteracted by the soil resistance. During an earthquake, the increase of the shear force because of the additional seismic load, or the decrease of the soil resistance results from strength loss may lead to failure. A variety of residual deformations have been observed in past earthquakes; basically, these failures can be classified into the following types, as shown in Fig 2.11:

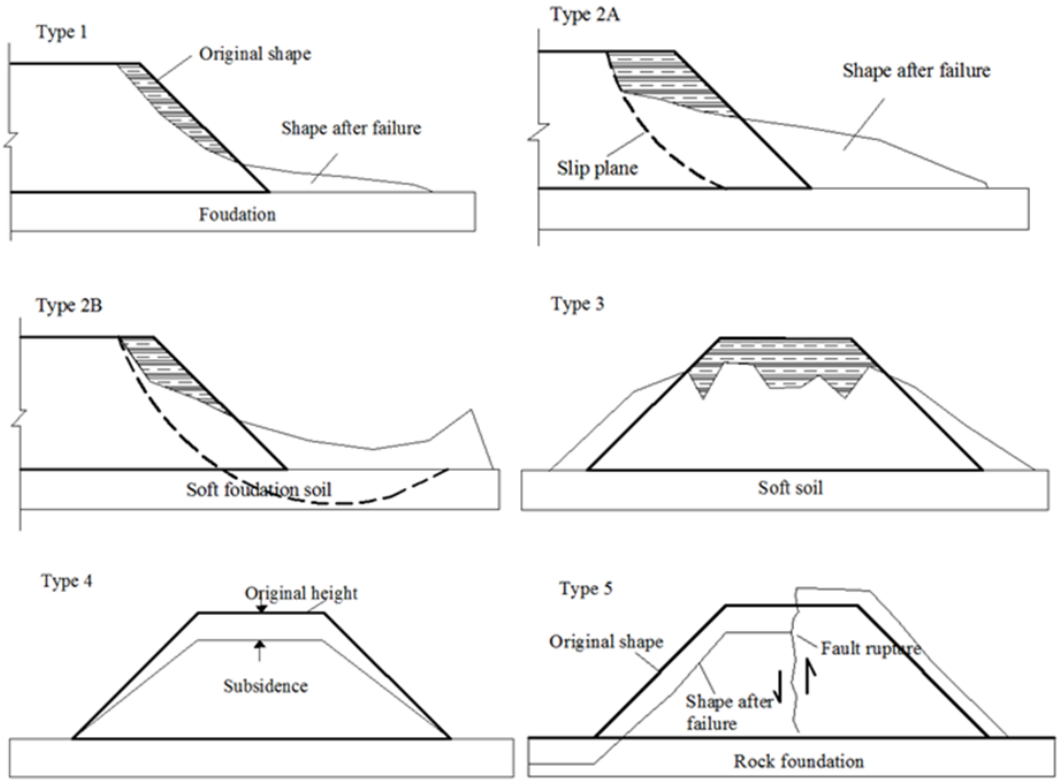

Fig 2.11 Types of failure of earth fills during past earthquakes (after Towhata 2008)

1) Shallow surface sliding of the slope;
2) Development of a slip surface within the body of an embankment or passing through the soft foundation soil,
3) Slumping
4) Densification
5) Fault rupture

2.3.2 Static slope stability analysis

Slope stability is the resistance of an inclined surface to failure by sliding or collapsing. The main objectives of slope stability analysis are identifying endangered areas, investigation of potential failure mechanisms, determination of the slope sensitivity to different triggering mechanisms, designing of optimal slopes with regard to safety, reliability and economics, or designing possible remedial measures, e.g. barriers and stabilisation (Towhata 2008). Static

slope analysis is mentioned here for completeness and as a basis for the better understanding of seismic slope analysis.

Problems associated with the stability of slopes are very complicated, varying between natural and man-made slopes. Basic features that should be considered in slope stability analysis include: geological conditions, site topography, soil properties, groundwater condition, external loading and slope reinforcement technique (Jaeger 1981).

A number of approaches have been developed for the analysis of slope stability, basically these approaches can be classified into two types: limit analysis approaches and numerical solution based on elasto-plastic theory (Duncan 1996). It should be noted here that the Limit Equilibrium (LE) technique overlooks the plastic flow rule of the soil and investigates the global stability only; as a result, the calculated safety factor will be dependent with the fundamental assumptions. However, LE analysis can provide a satisfactory result when considering slopes composed of homogenous soil.

The most popular LE models are Bishop (1955), Spencer (1967) and Janbu (1975) due to their accuracy on both circular and non-circular failure surfaces. When a non-homogenous soil is considered, the LE models may not be ideal due to the difficulty in identifying the position of the slip plane (Duncan 1996). In these cases more sophisticated numerical modelling techniques should be utilised. Numerical solution commonly uses advanced soil constitutive models and therefore a more detailed data input, i.e. advanced soil testing (Al-Defae et al. 2013), is generally required.

2.3.3 Seismic slope stability analysis

2.3.3.1 Seismic safety factor

The conventional method to evaluate the dynamic slope stability is the seismic factor of safety, which is calculated by Towhata (2008):

$$FoS = \frac{F_R}{F_{static} + F_{dynamic}} \qquad \textbf{Eq 2. 4}$$

where *FoS* is seismic safety of factor; F_R is resistance force against sliding; F_{static} is static sliding force; $F_{dynamic}$ is dynamic sliding loading.

The ground vibrations caused by the seismic waves may lead to an increase of the shear stresses in geotechnical structures and reduction of soil resistance. The slope will come to a hazardous condition resulting in possible failure if the *FoS* becomes ≤1.

2.3.3.2 Pseudo-static (PS) method

The pseudo-static method is an extension of the limit equilibrium (LE) slope stability analysis method from a conventional static situation to the dynamic state. Terzaghi (1951) is often cited with the first development of the PS method. Terzaghi (1951) proposed that the effect of an earthquake could be represented by a seismic force acing on the mass of the slope. In order to keep consistency with the static forces, the mathematical formulation of the seismic force was illustrated as a product of a seismic coefficient *k* and the weight of potential sliding mass.

For the application of the PS method, selection of the seismic coefficient *k* is one of the major concerns. Terzaghi (1951) suggested that *k*=0.1 for severe earthquakes, *k*=0.25 for violent-destructive earthquakes, and *k*=0.5 for catastrophic earthquakes. In all cases he suggested that the design safety factor with respect to strength (i.e. *FoS*) may be close to 1 (Baker et al. 2006).

Seed (1979) proposed that the PS approach was useful in evaluating the performance of embankments through combination with the displacement based Newmark model, and recommended the adoption of *k* = 0.1 for earthquake magnitude 6.5, and *k* =0.15 for earthquake magnitude 8.5, together with a required factor of safety of 1.15.

Hynes-Griffin & Franklin (1984) conducted similar research to Seed on dams and found that using an adequate seismic coefficient *k*, dams were not likely to generate the failure if there was no large strength loss (such as liquefaction and strain softening) in the soil. They provided a proposal of using a *k* value equal to one-half of the peak bedrock acceleration, and requiring a design safety factor of 1.0. They also recommend the PS method as a screening technique in the evaluation of seismic induced slope stability. Only if the *FoS* is below 1,

more analysis is required. This has been accepted as a philosophy of design in numerous guidelines and specifications (Shukha & Baker 2008).

The California Division of Mines and Geology summarised various recommendations about the determination of seismic coefficient *k* into a single figure (Fig 2.12). These recommendations cover different kinds of situations as observed in past earthquakes, and it can provide an adequate basis for design.

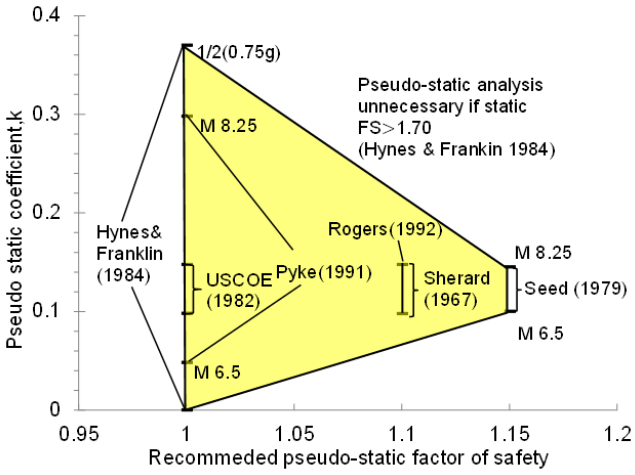

Fig 2.12 Criteria for slope Pseudo-Static slope stability analysis given by the California Division of Mines and Geology (after Baker et al. 2006)

The PS method is an extension of LE methods, which are based on various static and kinetic assumptions. Baker (2003) pointed out that these assumptions would tend to result in non-conservative results, which should be avoided. Through minimizing the safety function in regard to the potential slip surface and the normal stress, Baker & Garber (1978) presented an approach which does not require these assumptions. Based on this formulation, Baker et al. (2006) developed a design chart for pseudo-static analysis of homogeneous slopes which would be applicable for a wide range of input parameters. However, the PS method cannot predict the deformations when slope failure occurs. In the hazard analysis of slopes during earthquakes, it is important to evaluate not only the safety factor, but also how far the deformation will develop, and the area covered by the slip surface in the resulting movement (Newmark 1965).

2.3.3.3 Newmark sliding block method

Newmark (1965) assumed that the mechanism of earthquake induced slope displacement is regarding sliding along a well-defined slope surface. The dynamic behaviour of the sliding mass could be simulated by modelling the mass as a rigid block sliding on an inclined base. The concept of yield acceleration or critical acceleration was introduced to represent the acceleration required to overcome the friction resistance of the slope material and thus initiate sliding. The sliding occurs when the shaking induced acceleration exceeds the yield acceleration, resulting in a slip acceleration which can be calculated as follows:

$$a_{slip} = a(t) - k_{hy} \qquad \textbf{Eq 2. 5}$$

where a_{slip} is the acceleration of the sliding mass; $a(t)$ is the shaking induced acceleration and k_{hy} is the yield acceleration.

In practice, the value of k_{hy} is typically estimated by using a trial and error approach to identify the failure mechanism along with a conventional PS LE slope stability method. Explicit equations have also been developed for the relatively uniform slopes and simple failure mechanism (e.g. Bray & Rathje 1998; Jibson et al. 2000) and non-circular failure mechanisms (e.g. Sarma 1973) as a function of critical input parameters such as slope geometry, the unit weight of the soil mass, the frictional angle and the cohesion of the soil.

Slip displacement can be determined by integration everywhere of the relative velocity of sliding while this is greater than zero. Some empirical formulas have also been introduced, e.g. Jibson (2007).

Since the first introduction of the sliding block method by Newmark (1965), numerous displacement based slope stability analysis methods have been developed (Meehan & Vahedifard 2013), ranging from improving the accuracy of the standard sliding block model, to simplifying its use, to the expansion of its application, to the estimation of uncertainties and spatial variability of input parameters associated with the yield acceleration. Meanwhile, considering that the sliding block method is based on a number of simplifying assumptions, a significant amount of research has been conducted to examine the sensitivity of predicted displacements to these assumptions.

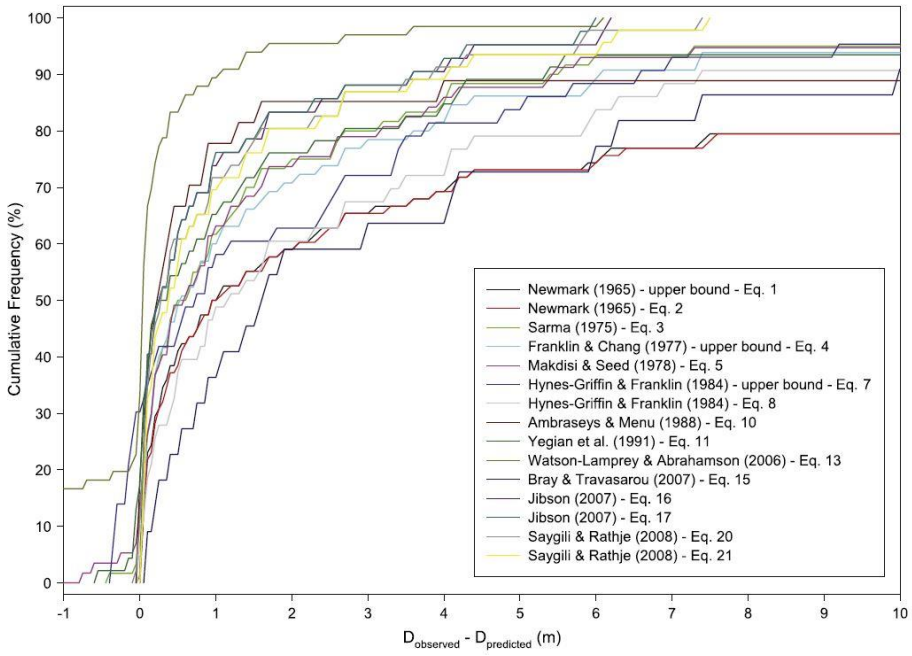

Fig 2.13 Cumulative distribution of difference between predicted and observed displacements for each of the simplified sliding block models (Meehan & Vahedifard 2013)

Meehan & Vahedifard (2013) compared the recorded displacement during earthquakes with the predicted displacement of 15 simplified sliding block models (Fig.2.13) and found that the existing sliding block methods resulted in smaller deformations for a large majority of the case histories. The reason for this is because of the assumptions that the sliding soil mass is rigid and soil strength is fixed. In actual slope failures, sliding soil may not always act as a rigid block but deforms continuously without a distinct slip surface. Once the soil strength decreases drastically after the initiation of failure, the velocity of the sliding mass will increase very quickly and cause destructive damage.

2.3.3.4 Improved sliding block method

An improved sliding block method for granular slopes proposed by Al-Defae et al. (2013) is illustrated here in detail for better understanding of a combined displacement based and LE slope stability analysis for engineering use. Compared with the initial sliding block model introduced by Newmark (1965), this model incorporates soil strain softening and slope geometric hardening behaviour into the formulation to calculate the yield acceleration and

permanent deformation. The predicated permanent crest settlement showed a good match with values from centrifuge and numerical models.

In this procedure, the slope is assumed to be of infinite length and width and the soil is sliding as a block, parallel to the slope surface, as shown in Fig 2.14. For a slope plane at depth z beneath the slope surface under uniaxial horizontal shaking (plane strain), the applied down slope shear stress is:

$$\tau_{applied} = \gamma z \sin\beta \cos\beta + k_h \gamma z \cos^2\beta \qquad \textbf{Eq 2. 6}$$

where the first term relates to the static shear stress due to the ground slope, and the second term relates to the additional peak dynamic shear stress induced by the earthquake (ref Eq 2.4).

The shear strength of the soil along the slip plane, assuming that the soil failure can be described by the Mohr-Coulomb failure criterion, is given by

$$\tau_{ult} = c' + (\gamma z \cos^2\beta - k_h \gamma z \sin\beta \cos\beta - u)\tan\phi' \qquad \textbf{Eq 2. 7}$$

The soil yields when $\tau_{applied} = \tau_{ult}$ .Then the yield acceleration k_{hy} can then be determined,

$$k_{hy} = \frac{c' + (\gamma z \cos^2\beta - u)\tan\phi' - \gamma z \sin\beta \cos\beta}{\gamma z \cos^2\beta + \gamma z \sin\beta \cos\beta \tan\phi'} \qquad \textbf{Eq 2. 8}$$

where c' is soil cohesion, γ is the soil unit weight, β is the slope angle and ϕ' is the effective angle of friction.

In a dry cohesionless soil, $c' = 0$, $u = 0$, and γz cancel in Eq 2.8, resulting in a yield acceleration k_{hy} which is independent of the depth of the slip plane:

$$k_{hy} = \frac{\cos\beta \tan\phi' - \sin\beta}{\cos\beta + \sin\beta \tan\phi'} \qquad \textbf{Eq 2. 9}$$

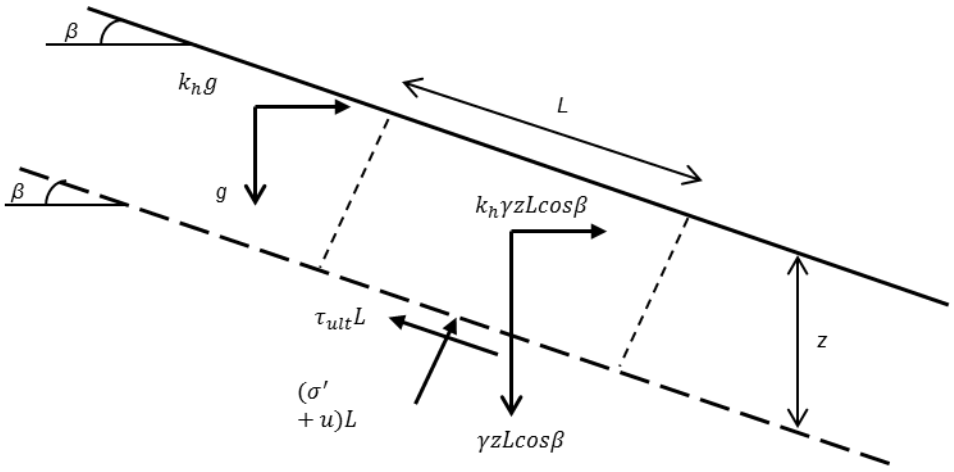

Fig 2.14 Forces acting within infinite slope under horizontal shaking

In a standard sliding block analysis, β and ϕ' are constant, but in reality, strain softening behaviour is always observed for dense soil. A simplified model for strain softening is given by Matasovic et al. (1997) as shown in Fig 2.15. The variation of ϕ' with shear strain is incorporated in the improved model. In terms of the slope angle, it will decrease with slippage as crest settlements make the slope shallower, which is called re-grading. A simplified model for re-grading is shown schematically in Fig 2.16. The instantaneous slope angle β_{i+1} can be estimated by the following equation,

$$\beta_{i+1} = \tan^{-1}\left(\frac{H_i - d_i \sin\beta_i}{H_i \cot\beta_i + d_i \cos\beta_i}\right) \qquad \textbf{Eq 2. 10}$$

where H_i is the height of the slope at the previous step; d_i is an increment of slip; for the initial time step, d_0=0, H_i=H and β_i=β_0 (initial slope angle).

When the horizontal component of the ground acceleration exceeds the yield acceleration in the downslope direction, the slope will start to slip under the slip acceleration a_{slip}; this acceleration is numerically integrated with respect to time to obtain the slip velocity, which is then itself integrated to obtain the slip displacement.

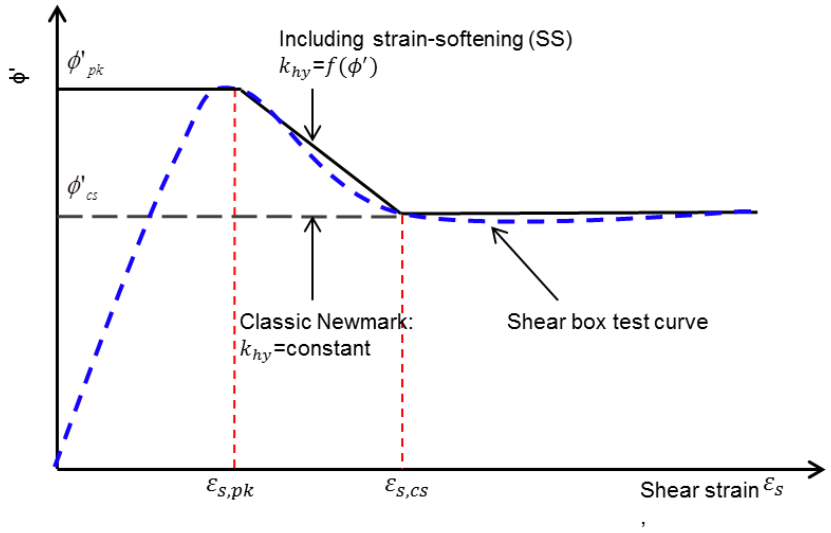

Fig 2.15 Effect of strain-softening (After Matasovic et al. 1997)

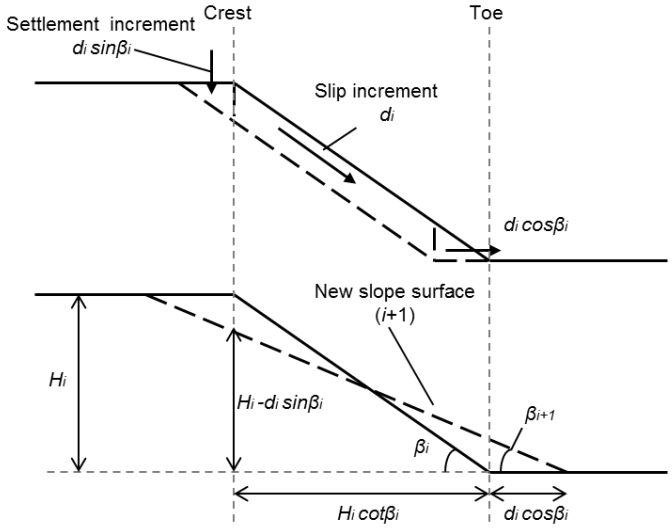

Fig 2.16 Incremental slope re-grading mechanism (Al-Defae et al. 2013)

2.3.3.5 Dynamic response amplification in slopes

Amplification of seismic waves in the presence of topographic irregularities is often advocated as one of the possible causes of concentration of damage during earthquakes. The term topographic amplification is used to describe the amplification due to the slope

geometry (i.e. the response at the slope crest divided by the ground surface response in the free-filed).

Many studies (Paolucci et al. 1999; Bouckovalas & Papadimitriou 2005; Yu et al. 2008; Brennan & Madabhushi 2009; Massa et al. 2010) have been conducted on different types of slopes to investigate the dynamic amplification within the slope. It was found that topographic factor varies with the slope geometry, frequency and duration of earthquake motions, as well as soil dynamic properties. However, most of these studies are using either physical modelling approach or numerical simulation, which are a simplification of the field case due to the simplified topographic irregularities.

Typically instrumented field studies (e.g. LeBrun et al. 1999; Sepúlveda et al. 2005; Buech et al. 2010) on topographic effects during earthquakes measure earthquake motion on the surface of the topography (e.g. slope or hill) relative to a base station. The magnitude of topographic factor reported from these studies varies, with some studies reporting amplification in the range of 2–3 times (Pedersen et al. 1994), whilst other studies observed amplifications of up to 30 times (Geli et al. 1988). However, it should be noted that the recorded amplifications are generally higher than those predicted in the analytical studies (Geli et al. 1988). The discrepancy may be partly blamed to the difficulty in identifying a good 'reference' station for calculating amplification ratios, but also to the way site amplification functions are computed. However, as indicated by Paolucci (2002), the large differences between field observation and theoretical predictions probably depend upon a combination of other factors, such as source directivity effects, stratigraphic irregularities, insufficient knowledge of local geology.

In other words, filed topographic factors tend to be concealed in stratigraphic amplification effects. As a result, in most seismic codes surface topography effects are disregarded. One of the few exceptions is included in Part 5 of Eurocode 8, that provides amplification factors ranging from 1.2 to 1.4, as a function of the slope angle and of the topographic feature. For slope angles <15°, the topography effects can be neglected, while the highest values apply near the top of the slopes of ridges with crest width significantly less than the base width and average slope angles >30°, the amplification factor can be assumed to linearly decrease towards the base, where it becomes unity.

However, most published results and parametric solutions, including the previous topographic amplification factors of the EC8, are mainly derived from 2D numerical wave propagation analyses (Paolucci 2002). Due to the lack of an adequate set of filed observations or 3D numerical results, the EC8 factors should in preference be applied when the slope belongs to 2D topographic irregularities (Tripe et al. 2013).

2.3.3.6 Numerical solution

The most rigorous approach to analysis of the behaviour of slopes during earthquakes is numerical solution of the relevant dynamic boundary value problem, adopting suitable elasto-plastic constitutive laws in the framework of continuum mechanics. However, this approach suffers from two basic limitations (Kokusho & Ishizawa 2006):

i) Insufficiently reliable constitutive information of the various materials at the site.
ii) It is impossible to predict the future time history of acceleration, which is essential in the definition of the boundary conditions of the dynamic problem.

These difficulties limit the application of this rigorous dynamic approach, particularly in conventionally (small and medium) sized projects.

2.4 Slopes reinforced with inert inclusions

Compared with traditional inert inclusions, vegetation is a more environmentally friendly reinforcing material. To better understand the mechanical effect of roots on slopes, it is useful to recognise the reinforcement mechanism of inclusions made of inert materials, in particular soil nails, dowels and piles.

Commonly, a slope is thought to be divided into moving and retaining soil masses. The inclusions retain the moving soil mass and enhance the shear strength of the slope. The enhancement of the shear strength induced by the presence of inclusions is a function of the forces in the inclusions, which are the direct results of soil-inclusion interaction. There are two modes of interaction between soil and reinforcement: (a) friction, which leads to axial tension and compression; (b) bearing, which leads to shear forces and bending moments

(Pedley 1990). The magnitude of the induced forces is principally dependent on the relative inclusion stiffness and strength, and deformation occurring in the inclusion. The mechanisms of friction and bearing are illustrated in Fig.2.17.

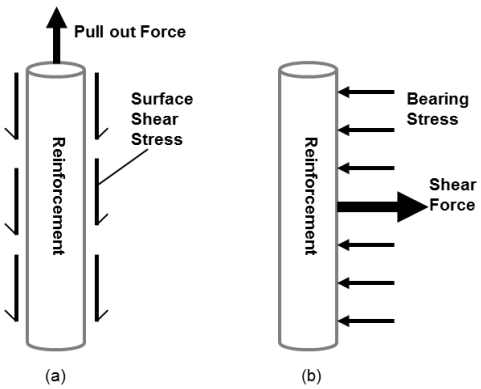

Fig 2.17 Mechanism of soil inclusion interaction: (a) Friction; (b) Bearing (Pedley 1990)

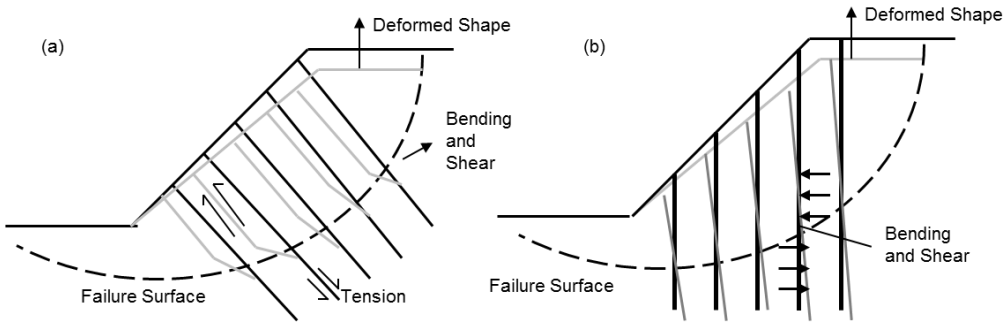

Fig 2.18 Mechanism of soil reinforcement interaction used by different reinforcing technique :(a) Soil nailing reinforcement; (b) Dowelling and piling reinforcement (After Duckett 2013)

Soil nails predominantly mobilise the friction mechanism while soil dowels and piles behave in bearing. This is related to their orientation and cross section (Pedley 1990). As shown in Fig 2.18, soil nails always have a low slenderness and are always installed perpendicular to the slope surface. These structural properties mean limited resistance to bending and shearing force, but with a high axial resistance along the nails. In terms of the soil dowels and piles, they penetrate into the soil vertically and are much stiffer and stronger than soil nails, hence

with a high bearing capacity. Better understanding the two interaction modes could help to distinguish the mechanical behaviour of fine roots and structural roots during shear loading.

2.4.1 Soil nails

2.4.1.1Seismic performance of nailed slopes

In the past decades, soil nailing has been widely used in slope remediation, and it can improve the soil shear strength significantly through the use of steels or other high strength strip materials. This has been proved a versatile and cost effective technique in reinforcing soil or soft rock slopes (Martin 1997). The process of soil nailing includes installation of nails in excavated cuts or in slopes either by driving or grouting in predrilled holes. The stability of the slope face between nails is ensured by providing thin layers of shot-crete reinforced with wire mesh. The nails are generally steel bars, metal tubes or other metal rods that can resist not only tensile force but also a very limited amount of shear stress and bending moment. The nailing method has been used in both granular and cohesive soils and in relatively heterogeneous deposits. Considering nailed soil structures are coherent and flexible, they can present inherent advantages of withstanding larger deformation with high resistance to dynamic loading (Giri & Sengupta 2009). So the general consensus among practising engineers is that soil nailed structures perform reasonably well under seismic conditions. However, documented performance of soil-nailed systems is relatively rare in the literature (Sengupta & Giri 2011).

Studies on soil nail reinforced slopes have concentrated on the mechanisms of the reinforcement (e.g. Chu & Yin 2005; Pradhan & Tham 2006; Zhou & Yin 2008; Kim et al. 2013) and the design of structures under static loading (e.g. Gassler 1988; Martin 1997; Tan & Chow 2004; Patra & Basudhar 2005; Turner & Jensen 2005; Lees et al. 2013). The failure mechanism of such a slope under seismic loading was investigated using pseudo-static approach (e.g. Babu & Singh 2008; Rabie 2014) and using a kinematic limit approach (e.g. He et al. 2011; Sengupta & Giri 2011). These analytical parametric studies indicated that the strength and geometry of the slope as well as characteristic parameters of the soil nails have a significant effect on the critical seismic yield acceleration coefficient and the permanent displacement of the soil nail reinforced slope. However, only a handful of full-scale and

model tests in the laboratory have been conducted on soil nailed system (Tufenkjian & Vucetic 2000; Hong & Chen 2005; Giri & Sengupta 2009) to validate these models.

2.4.1.2 Soil nail and soil interaction

Experimental and analytical studies have led to better understanding of the interaction between soil nails and the surrounding soil masses (Giri & Sengupta 2009). A detailed literature review about the behaviour of soil nails can be found in Sonnenberg (2008) and Duckett (2013). In the past few years, no relatively new ideas have been proposed and so there is no need to update these. Therefore, this part will be presented here in brief to ensure completeness.

In practise, soil nails are generally installed either horizontally or normal to the slope face and parallel to each other (Patra & Basudhar 2005). This will result in tension for the toe nails and compression for the crest nails (Fig 2.19). Johnson et al. (2002) suggested that the optimum inclination of the nails is 35° to horizontal in an anticlockwise direction, with an effective drop to 0% improvement when the inclination tends toward 125°.This is supported by the laboratory shear tests (Fig 2.20) conducted by Jewell & Wroth (1987) .

Powell & Watkins (1990) proposed three failure modes for soil nailed structures, namely: local failure of material, failure of bonds and development of external failures. Sonnenberg (2008) suggested that failure of bonds (nail pull out) will be most likely to occur considering current design strategies. The pulling out force can be estimated using the following equations, which account for undrained and drained soil condition, respectively:

$$F_{Pu} = \pi \cdot d \cdot L_a \cdot \alpha \cdot c_u \qquad \textbf{Eq 2. 11}$$

$$F_{Pd} = \pi \cdot d \cdot L_a \cdot (K \cdot \sigma' \cdot \tan\phi' + c') \qquad \textbf{Eq 2. 12}$$

where F_{Pu}/F_{Pd} are the forces required to pull a reinforcement bar from undrained and drained soil; d is the diameter of reinforcement bar; L_a is the anchorage length of the reinforcement bar; α is an adhesion factor; c_u is the undrained shear strength of the soil; K is the earth pressure coefficient (typically 1.4 to 2.3 for medium-dense to dense sandy gravel ; 1.4 for dense sand, ;1.0 for fine sand and slits of high relative density; 0.5 for fine sand and silts of

low relative density); σ' is the normal effective stress at the slip plane; ϕ' is the effective angle of internal soil friction; c' is the effective soil cohesion.

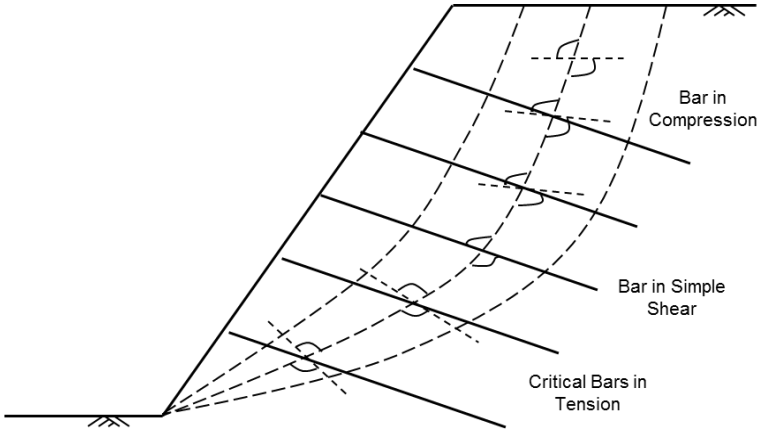

Fig 2.19 Effects of maintaining an inclination angle through the slope (Bush et al. 1991)

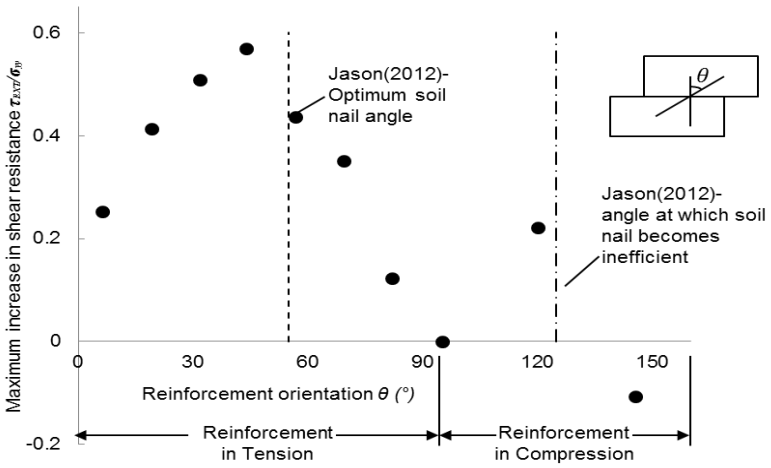

Fig 2.20 Effect of inclination angle to an inclusion contribution to shear resistance (After Jewell & Wroth 1987)

2.4.2 Soil dowels and piles

Piles are one of the most widely used foundation elements in geotechnical design and widely used by geotechnical engineers to stabilize slopes against environmental effects (Al-Defae et al. 2013). Research related to piled slope design has generally focussed on two aspects. The first is to find the optimum pile properties including diameter, length, location and spacing in order to achieve the desired slope improvement with the least construction cost. The second is to ensure the induced bending moment and shear force are within the structural capacity of the pile. As individual roots have been considered as a type of frictional pile (e.g. Mickovski et al. 2007; Duckett 2013), it will be essential to fully understand the behaviour of piles under lateral kinematic loading and distinguish the factors that may influence the performance of the piles and the piled slope.

2.4.2.1 Failure mechanisms of pile

The typical failure mechanism of piles observed in theoretical analysis performed by Poulos (1995) is shown in Fig 2.21 . The following observations can be made from Fig 2.21:

(i) The maximum shear force in the pile is generated at the level of slip plane ;
(ii) For the flow mode, the maximum bending moment occurs in the stable soil (below the shear plane). Compared with the soil movement, the pile movement is relatively small.
(iii) For the short-pile mode, the maximum bending moment is recorded in the unstable soil (above the shear plane). The pile movement is very similar to the soil movement.
(iv) For the intermediate mode, the maximum moments are observed both below and above the shear plane. The pile head movement exceeds the soil movement.
(v) The maximum shear force of the intermediate mode is higher than the other two modes.

In reality, the failure mode will be a combined function of pile length, pile cross section, pile mechanical properties, pile spacing and soil properties. However, piles can provide its maximum resistance to stabilize the slope when the intermediate mode was mobilized (Mahdī et al. 2004; Phanikanth et al. 2010; Duckett 2013).

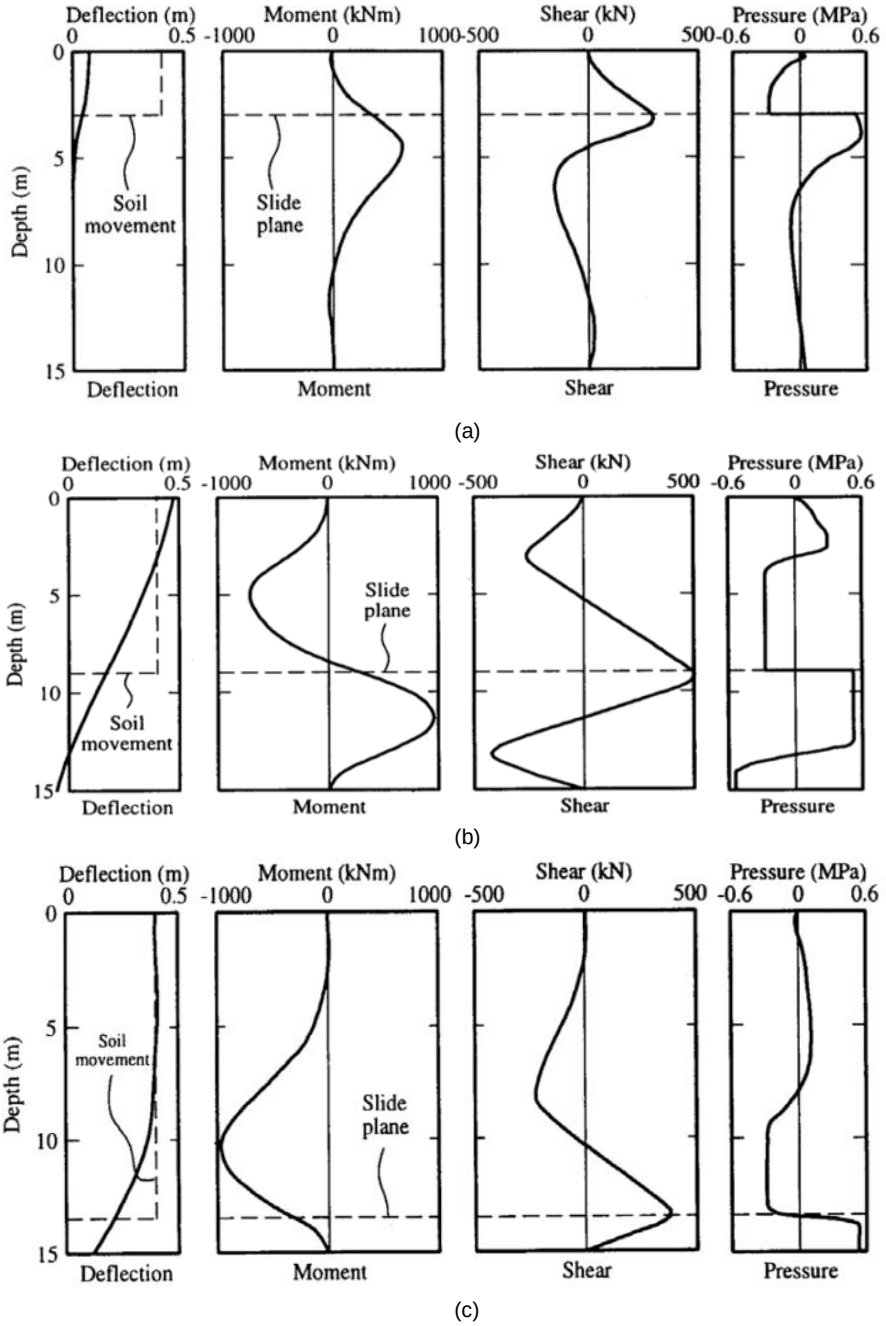

Fig 2.21 The typical failure mechanism of pile (Poulos 1995): (a) flow mode; (b) intermediate mode; (c) short pile model

2.4.2.2 Pile position effect

The optimum pile position on slope stabilisation depends on a variety of factors, including site topography, soil type and the infrastructure located at the crest of the slope. As a result, debates always exist on the best pile positions. Some researches (e.g. Lee et al. 1995; Ausilio et al. 2001) observed that piles near the toe of the slope gave the highest factor of safety. While other researches (e.g. Cai & Ugai 2003; Won et al. 2005; Wei & Cheng 2009; Ellis et al. 2010) reported the maximum factor of safety is found when the piles are installed at the middle of the slope. But it should be noted here these studies varied in the slope geometry and pile types.

2.4.2.3 Pile length effect

Recent studies (e.g. Akl et al. 2014) on piling design suggested that the reinforcing capacity of piles was highly dependent on the pile length with respect to the depth of failure surface. This was backed up by the pile failure mechanism mentioned above by Poulos (1995). Basically, piles can be classified into short, intermediate and long by considering their stiffness, length and surrounding soil, as shown below (after Mahdī et al. 2004):

Short pile,

$$\frac{L_{pile}}{\left[\left(EI\right)_{pile} / k_{py}\right]^{1/5}} < 2 \qquad \textbf{Eq 2. 13}$$

Intermediate pile,

$$2 \le \frac{L_{pile}}{\left[\left(EI\right)_{pile} / k_{py}\right]^{1/5}} \le 4 \qquad \textbf{Eq 2. 14}$$

Long flexible pile,

$$\frac{L_{pile}}{\left[\left(EI\right)_{pile} / k_{py}\right]^{1/5}} > 4 \qquad \textbf{Eq 2. 15}$$

where, L_{pile} is the length of the pile; E is the Young's modulus of the pile; I is the moment of inertia the pile; k_{py} is the modulus of sub-grade reaction for the soil.

2.4.2.4 Pile group effect

In practice, piles are most often used in groups. The difference between single piles and pile groups is that pile group response is additionally influenced by the nonlinear pile-soil-pile interaction, the spacing of piles and the arrangement of piles with respect to the direction of applied force. If these piles are distributed at wider spacing, the pile will behave individually and no arching will be generated between piles. But if piles are installed closely to each other, the group effect should be considered. Two problems are always addressed for the group effect: the efficiency of closely-spaced piles under lateral loading or axial loading; and the distribution of the loading to each of the piles in the group.

The pile spacing was always presented as a function of pile diameter. Extensive studies have been conducted to find the minimum spacing without group effect. Mokwa (1999) proposed that the group effect is negligible when the piles spaced at more than 6 times the pile diameter. This observation was supported by the full scale lateral load tests conducted by Ng et al. (2001). A critical spacing of 8*d* with no group effect was also suggested by Carder (2009).

Other researchers (e.g. McVay et al. 1998; Rollins & Olsen 2006) suggested that the efficiency of piles depended on the location of pile row with respect to the direction of applied force. A spacing of 6.5*d* for leading row piles and 7-8*d* for tailing row piles was given, as illustrated in Fig 2.22. Ellis et al. (2010) proposed a simple equation to define the critical pile spacing based on the centrifuge modelling under monotonic loading conditions, that is,

$$\left[\frac{s}{d}\right]_{\max} = \frac{K_p^2}{K_p - K_a} \qquad \textbf{Eq 2. 16}$$

where s is the pile spacing (centre to centre), d is the pile diameter, K_p is the passive earth pressure coefficient; and K_a is the active earth coefficient.

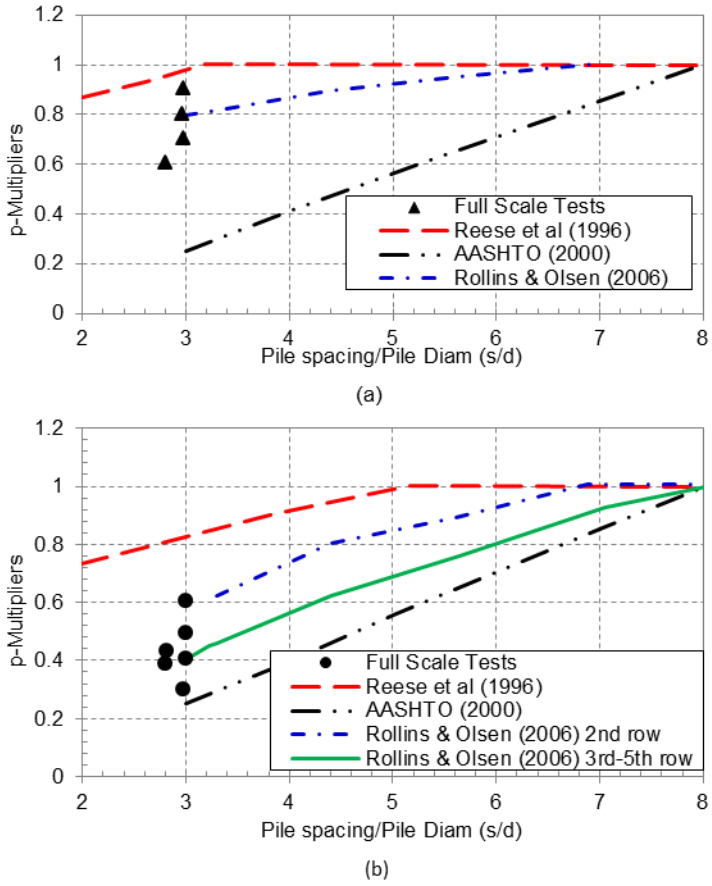

Fig 2.22 Back calculated p-multipliers for : (a) leading row; (b) trailing rows piles from previous full scale tests along with recommended design curve (after Rollins et al. 2005)

In terms of the group efficiency when piles are spaced closely, the *p*-multiplier concept originally proposed by Brown et al. (1988), is widely used. This method accounts for the loss of soil resistance due to the group "shadowing " effect, and different values of *p*-multipliers are assigned to each row within the group to reduce the pile loads at a given relative soil-pile displacement , as shown in the following equation (adapted for a group of roots) (Duckett 2013):

$$p_m^{'} = \sum_{i=1}^{T} p_{mi}^{'} \cdot n_i \Big/ n_T \qquad \textbf{Eq 2. 17}$$

where, $p_m^{'}$ is the overall *p*-multiplier; $p_{mi}^{'}$ is the *p*-multiplier in root *i*; n_i is the number of roots in root *i*; n_T is the number of roots.

Location with respect to the loading direction, and pile head connection (Ng et al. 2001) also influence response. But it should be mentioned here, full-scale pile load tests are relatively rare due to the extreme expense of the tests. Only tests in sand (Brown et al. 1988; Ruesta & Townsend 1997), clay (Brown et al. 1987) and clayey silt (Rollins et al. 1998) have been reported. A detailed summary of the *p*-multipliers value from in-situ and centrifuge tests on pile groups in sand is given in Table 2.2 and Table 2.3, respectively (after Rollins et al. 2005).

Table 2. 2 *P*-Multiplier values from tests on full-scale pile groups in sand (after Rollins et al. 2005)

Soil properties	Pile properties-driving details (Arrangement)	Spacing	Deflection range(mm)	1st row	2nd row	3rd row	4th row
Sand to silty sand(SP,SP-SM) D_r=50%,ϕ=38° (Rollins et al. 2005)	324 mm O.D. steel pipe pile-driven open ended to 11.3m (3×3)	3.29	15-40	0.8	0.4	0.4	-
Loose fine sand (SP) D_r=30%,ϕ=32° (Ruesta & Townsend 1997)	760 mm square pre-stressed concrete pile-driven 15.25m into 6m jetted hole(4×4)	3.0	25-75	0.8	0.7	0.3	0.3
Clean medium sand(SP) D_r=50%,ϕ=38° (Brown et al. 1988)	272 mm O.D. steel pipe filled with grout-sand compacted around existing pile group (3×3)	3.0	25-40	0.8	0.4	0.3	-
Silty sand to silt(SM,ML) D_r=40-60%,ϕ unknown (Huang et al. 2001)	800 mm O.D. ,560 I.D. precast concrete pipe pile-driven closed ended to 33m (3×4)	3.0	20-130	0.89	0.61	0.61	0.66

Table 2. 3 *P*-Multiplier values from centrifuge tests on pile groups in sand (after Rollins et al. 2005)

Investigator(s)	Soil density	Pattern	Spacing (diameters)	*p*-multipliers by row						
				1	2	3	4	5	6	7
Kotthaus (1992)	D_r=97%	1×3	3	0.75	0.42	0.45	-	-	-	-
		1×3	4	0.95	0.60	0.65	-	-	-	-
McVay et al. (1995)	D_r=55%	3×3	3	0.80	0.40	0.30	-	-	-	-
(Remaud et al. 1998)	D_r=33%	3×3	3	0.65	0.45	0.35	-	-	-	-
	D_r=33%	3×3	5	1.0	0.85	0.70	-	-	-	-
	Dense	1×2	2	1.0	0.52	-	-	-	-	-
McVay et al. (1998)	D_r=36% and D_r=55%	1×2	4	1.0	0.82	-	-	-	-	-
		1×2	6	1.0	0.93	-	-	-	-	-
		3×3	3	0.80	0.40	0.30	-	-	-	-
		3×4	3	0.80	0.40	0.30	0.30	-	-	-
		3×5	3	0.80	0.40	0.30	0.20	0.30	-	-
		3×6	3	0.80	0.40	0.30	0.20	0.20	0.30	-
		3×7	3	0.80	0.40	0.30	0.20	0.20	0.20	0.30

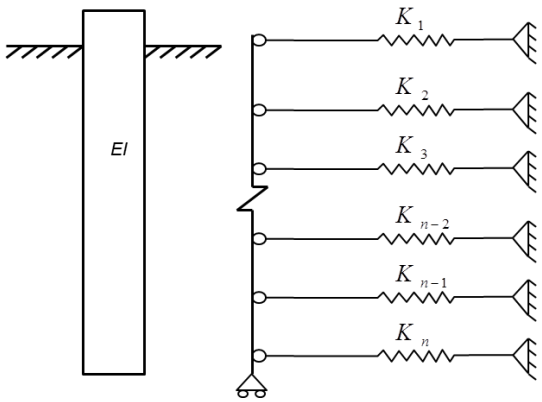

Fig 2.23 The Winkler approach with the pile modelled as a beam element supported by non-liner uncoupled springs. *K* is the stiffness corresponding to E_{py}

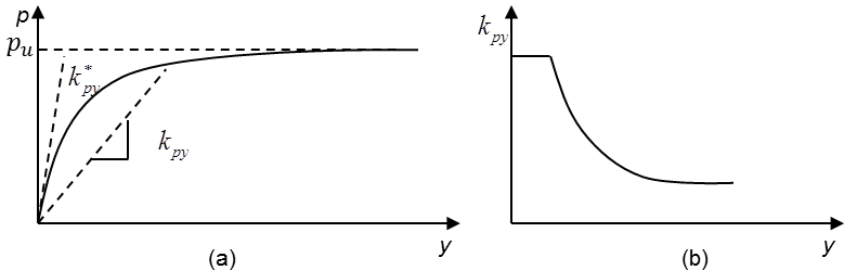

Fig 2.24 Typical *p-y* curve and variation of the modulus of subgrade reaction at given point along the pile (after (Reese & Van Impe 2000)

2.4.2.5 Piles under lateral loading

A number of methods have been used for the analysis of piles under lateral loading. Among these, the most widely used is Beam-on-non-linear-Winkler-foundation (BNWF) model using published *p-y* formulations, also known as the *p-y* method. This approach was originally proposed by Winkler (1867) and treats the pile as an elasto-plastic beam loaded through a series of springs that sit along its length, as shown in Fig 2.23. The springs are given specific *p-y* properties (see Fig 2.24) to model the soil reaction with relative soil-pile displacement. Commonly used rules and recommendations for using *p-y* method for the design of piles are presented by the American Petroleum Institute (1987). The *p-y* curve for single piles and pile groups subject to different loading in different soils can been found in Reese & Van Impe (2000) . Details about the *p-y* curve used in this project will be illustrated in Chapter 5 and it will not be discussed further here.

2.4.2.6 Seismic performance of piled slope

The benefit of piles on slope performance during static condition has been well recognized, but research specific to the seismic performance of pile-reinforced slopes is relatively rare. Al-Defae & Knappett (2014) performed an extensive program of dynamic centrifuge tests on pile reinforced slope models and found that the presence of pile row highly improved the global performance of slopes under a sequence of earthquake motions. When piles were spaced at s/d=3.5, which is quite close to the most cost effective pile spacing (s/d=4) suggested by Kourkoulis et al. (2010), the permanent deformation at the slope crest was observed to reduce by up to 35%, and the dynamic ground motions at the crest were also found to decrease by 20%. The highest reduction was observed during the first motion, and this phenomenon was explained by the mobilization of pile-pinning forces during the first motion. After that, the pile would keep on deforming, but the change of the bending moment was relatively small compared that of the first motion. The other findings in this study are in accordance with previous suggestions based on static tests.

2.5 Slope reinforced with roots

The role of vegetation in slope stability and erosion has been well recognized and incorporated in soil-bioengineering practise (Coppin & Richards 1990; Stokes et al. 2008; Khalilnejad et al. 2012). There are many possible advantages to planting trees, shrubs or grasses on slopes, including preventing surface erosion and improving aesthetic appearance; however the two most significant influences of vegetation are in (i) controlling water within the slope (e.g. Smethurst et al. 2006) and (ii) directly increasing the shear strength of the rooted soil through the roots acting like miniature anchors/ piles.

2.5.1 Performance of rooted slopes

The importance of roots and their influence on slope stability has gradually been realized from consideration of the failures of many natural slopes because of the removal of the roots, such as in the Alps in the early 19th century, it has been recorded that extensive slope failures occurs as roots decay (Sonnenberg 2008). To investigate the global performance of rooted

slopes and verify the contribution of roots on the behaviour of slope, some trials (e.g. Brown 1991; Dalton 1995; Winter et al. 2005) have been conducted on real or 1:1 scaled slope models. The statistical survey found that recorded slope failures showed significantly more slope movement in fallow slopes in comparison with slopes coved with large trees and extensive grasses. Rickli and Buncher (2003) found that more than 75% of all landslides occur on bare slopes, rather than in forested areas. It may not be rigorous to compare these slopes directly considering varied slope geometry, inclination and hydraulic conditions, but these investigations indicate the good performance of vegetated slopes qualitatively. However, such large trials are expensive and time consuming, and therefore relatively rare. Moreover, it is impossible to quantify the root contribution on slope performance due to the lack of root data in these studies.

Another approach is to collect the root properties (e.g. root tensile strength, root architecture, root cohesion) from stable slopes in situ and perform back-calculations of slope behaviour employing existing analytical models or computational models (e.g. Abernethy & Rutherfurd 2000; Danjon et al. 2008; Ji et al. 2012; Mao et al. 2014). This approach highly depends on the accuracy of the analytical models or soil constitutive models selected (Wu 2013). It may be useful to detect the characteristics that impact the global performance of rooted slope, but for accurately quantifying the root contribution on slopes, it is not the case, as a number of these analytical models lack experimental evidence.

Geotechnical centrifuge modelling is an approach which can simulate the global performance of a full-scale soil slope prototype to a high level of fidelity, by achieving similitude of stresses at homologous points within the model and prototype. Compared with full scale investigations, centrifuge tests are cheaper and easier to perform. Meanwhile, the slope failure can be achieved and displayed in process. Despite such popularity in geotechnical engineering, few centrifuge model tests (Sonnenberg et al. 2010; Sonnenberg et al. 2011; Eab et al. 2014) have been performed on vegetation reinforced slopes. This is likely associated with limited access to a centrifuge for most bioengineering scientists.

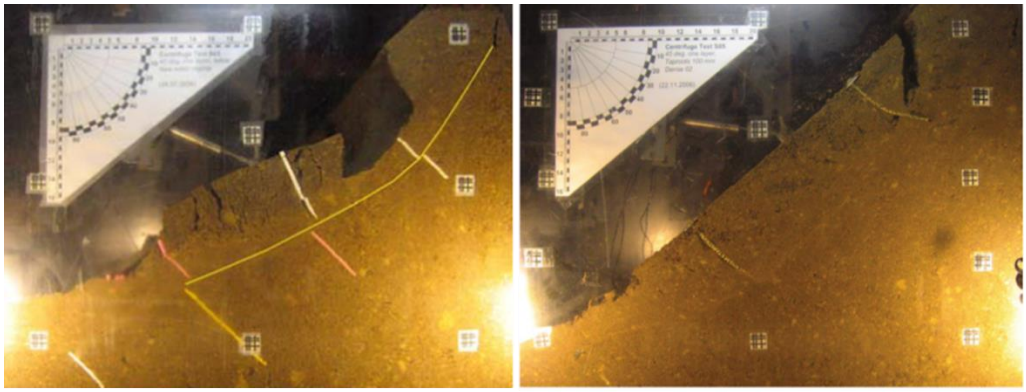

Fig 2.25 Image of slope failure captured in flight : (a) fallow slope; (b)slope reinforced with wooden tap root analogues (after Sonnenberg et al. 2011)

The presence of roots was observed to transform the failure mode of slope from progressive block failure to translational failure (Fig 2.25), which highly improved the stability of the natural slope. The drawback of this study lies in the root analogues which were used to model real roots. Straight rods, occasionally with some highly simplified branching patterns following the procedure introduced by Mickovski et al. (2007) were employed to represent highly simplified tap root, herringbone pattern and dichotomous pattern systems. Such simplified structures may mask the effects of more complicated (and realistic) morphologies (Mickovski & Van Beek 2009; Fourcaud et al. 2008; Ghestem et al. 2013). Additionally, the analogues used were typically made of either rubber or wood as materials with low and high stiffness and strength respectively. While these bracket the stiffnesses of typical root systems, neither of their properties are ideal. Eab et al. (2014) found that roots delay the ground infiltration of rainfall and delay the rise in groundwater table hence delay the soil movement and the slope failure. However, this study overlooked the particle size effect and scale effect in centrifuge modelling. In terms of the seismic performance of rooted slopes, no documented evidence has been found.

2.5.2 Hydrological mechanisms

The hydrological mechanism of vegetation plays a significant role in modifying soil moisture content and hence increasing the soil strength. The reduction of the pore water pressure due to the presence of vegetation is mainly achieved in two ways: rainfall interaction by leaves and organic cover in the subsoil; evapotranspiration through the plant during its growth process

(Chok & Kaggwa 2004). Eab et al. (2014) reported that rainfall was also intercepted by the deeper root biomass significantly apart from leaves in the subsoil.

The seasonal variation of pore pressures within an embankment slope is controlled by the climatic conditions and is exaggerated by the effects of the vegetation present. Perry & Pedley (2003) observed that the suction effect for deciduous trees near the surface was higher than that for grass system. Similar behaviour was reported by Scott et al. (2007), as shown in Fig 2.26. This study also found that a grass covered area dissipated suctions more rapidly than a tree covered area.

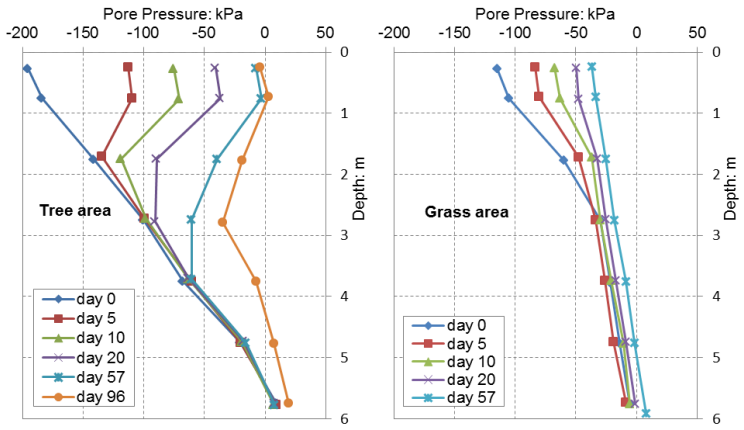

Fig 2.26 Negative pore water due to the presence of roots for tree area (a) and grass area (b) (after Scott et al. 2007)

Sonnenberg (2008) proposed that root suction hydrological effects were usually not considered in slope stability analysis due to its unreliable and minimal contribution to an unstable soil based on a body of literature. However, some researchers (e.g. Ng & Yu 2014) insisted on the role of water uptake to slope stability and developed a new technique to model the water uptake behaviour through centrifuge modelling.

2.5.3 Mechanical mechanisms

Tree roots penetrate into the soil to form a composite material consisting of fine roots of high tensile strength for reinforcement and structural roots of high flexural resistance for anchorage within a matrix of lower strength (Nilaweera & Nutalaya 1999; Sinnett et al. 2008). This is analogous to a reinforced soil system, where the soil mass is enhanced by the

reinforcement (e.g. geo-grids, geotextiles, soil nails or soil anchors). The shear strength of the rooted soil mass is enhanced due to the presence of the root matrix. This effect varies with species and root architecture and can extend to several metres, both in depth (Canadell et al. 1996) and spread (Danjon & Reubens 2008) for the case of trees. Understanding and quantifying the mechanical effect of vegetation on steep slopes started approximately 40 years ago with direct shear tests performed on soil blocks containing roots (as reported in Wu 2013). Since then, many shear tests have been conducted both in the field (Wu & Watson 1998; Simon & Collison 2002; Greenwood et al. 2004; Van Beek et al. 2005; Docker & Hubble 2008; Schwarz et al. 2010; Comino & Druetta 2010) and in the laboratory (Waldron 1977; Operstein & Frydman 2000; Fan & Su 2008; Fan & Chen 2010; Loades et al. 2010).

These studies have provided insight into the strength of vegetated soil and revealed possible factors that affect the root contribution (e.g. root density, root architecture, root tensile strength and root stiffness). Few studies, however, report shear tests on well-developed mature trees rather than young trees due to the large size of whole tree root systems and the limited size of available shearing apparatus (Sonnenberg 2008).

Roots as a type of reinforcement act in two separate ways to improve the shearing resistance of soil: reducing the disturbing shear forces on the soil and increasing the available shearing resistance of the soil (Stokes et al. 2008; Khalilnejad et al. 2012). To express this effect within engineering calculations, the expression of root cohesion c_r was introduced, as an additional strength term to the fallow component of the Mohr-Coulomb failure criterion (Coppion & Richards 1990), as shown in Fig.2.27.

Fig.2.28 considered that the roots only affected the cohesion of the soil, without any change to the internal friction angle of the soil. But this point is not always agreed. In most publications, research consistently suggests that there was no increase of the internal friction angle of the soil. However, some researchers (e.g. Frei et al. 2003 ; Chen 2006 ; Mickovski et al. 2007; Graf et al. 2009) observed a change in magnitude of 1° to 5° increase of the internal frictional angle of the soil from the test. Meanwhile, Yetimoglu & Salbas (2003) reported that there was no change of the cohesion of the soil for fibre-reinforced soil based on the results of a series of direct shear box tests.

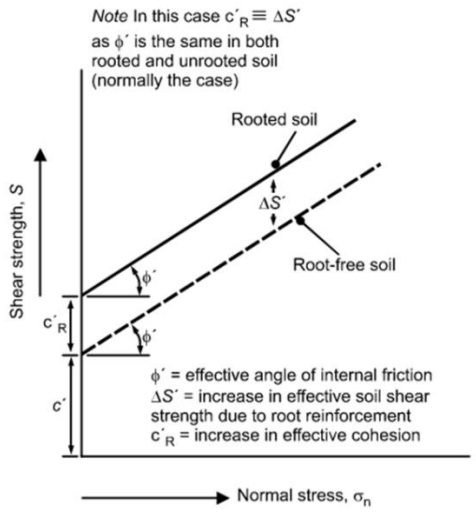

Fig 2.27 Effect of root reinforcement on the shear strength of soil (Coppion & Richards 1990)

The increase of shear strength of the rooted soil was always considered as a function of root properties itself including root strength, root concentration, branching pattern and spatial distribution of the root system, and has no relationship with the surrounding soil properties (e.g. Wu 1976; Wu et al. 1979; Thomas & Pollen-Bankhead 2010). But this may not be true. A positive relationship was observed between the confining stress and the root cohesion c_r according to a parametric study performed by Duckett (2013) using root analogues.

Jewell & Wroth (1987) proposed that the shear band limits the maximum reinforcement force. Accurate determination of the shear band is essential for better understanding the sliding behaviour of soil. The shear band thickness of fallow soil was estimated to be a function of soil particle size D_{50} (Mühlhaus & Vardoulakis 1987; Oda & Kazama 1998; Wood 2003). The magnitude of shear band thickness of granular sand is generally less than 5mm. However, Duckett (2013) reported a shear band of 20mm for soil reinforced with fibrous root analogues of 150mm in length. The change of shear band thickness should be given attention. The stiffness of the reinforced soil was also observed to increase with the presence of reinforcement (Jewell & Wroth 1987; Shewbridge & Sitar 1989; Michalowski & Cermák 2003).

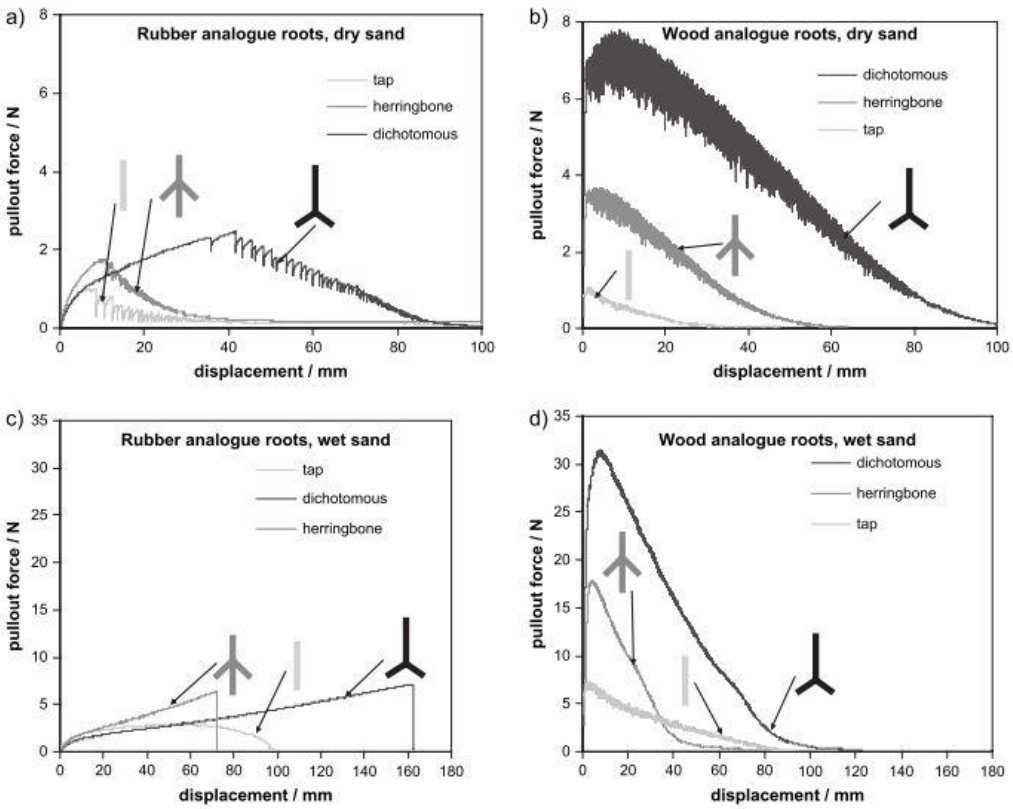

Fig 2.28 Representative of pull out behaviour of rubber and wood model roots with different architecture pulled out from dry and wet sand (after Mickovski et al. 2007)

When direct shear testing technique are used on quantifying the root soil interaction, attentions are always concentrated on the overturning behaviour of root system and very few focus are given to the uprooting behaviour, especially for the deep roots below the slip surface and lateral roots which are subject to axial loading during shearing. Pull out testing as a most widely used approach in pile engineering has been employed to investigate the uprooting behaviour of deep roots during slippage (Greenwood et al. 2004; Mickovski et al. 2007; Docker & Hubble 2008; Lin et al. 2010; Osman et al. 2011) . The pull out resistance of roots was reported to depend on the material stiffness, root architecture and the pore water suction of the sand base in the study of Mickovski et al. (2007), as shown in Fig 2.28. The maximum pull out resistance depended strongly on the presence and position of lateral roots. The deeper these were located, the greater the resistance to pull out.

2.6 Analytical models of root reinforcement

Since the 1970s, a number of analytical models have been introduced to quantify and evaluate the role of vegetation on slope stability (Wu 2013). Generally, these models can be classified into two types:

i) The macro model which considers the root soil matrix as a homogenous material;
ii) The soil-vegetation interaction model which considers the root as a structural element embedded in the soil;

The properties of the macro model were determined by tests on reinforced soil. The strength is represented as a Mohr-Coulomb envelope or a yield surface as for conventional soil (Michalowski & Cermák 2003; Zaimoglu & Yetimoglu 2012; Hassen et al. 2013). This model is convenient where the dimensions and spacing of the reinforcement is small, as otherwise tests are difficult to perform.

As for the latter approach, the soil-root interaction properties can be calculated from axial root properties (e.g. Greenwood et al. 2004; Mickovski et al. 2007; Docker & Hubble 2008; Lin et al. 2010; Osman et al. 2011) which can be determined from pull-out tests and axial tension tests of the roots. The additional forces due to the presence of roots may be introduced into the slope stability equations as boundary forces (Greenwood et al. 2004; Greenwood 2006) or used to evaluate c_r in the Mohr-Coulomb equation (Waldron 1977; Wu et al. 1979). The variety of available root-soil interaction models will be illustrated and reviewed in the following subsections.

2.6.1 Fibre break model

The first attempt to quantify soil reinforcement due to roots was introduced by Waldron (1977), which evaluated root reinforcement as an additional soil strength term. The additional strength c_r was adapted within the Mohr-Coulomb shear strength criterion for unsaturated soil, as mentioned above. Waldron (1977) assumed that all roots were mobilized and broken, which is the reason why the original and improved models are known as the fibre break model. The major difference of these models lies in the sequence that failure occurs, whether simultaneous or progressive (Thomas & Pollen-Bankhead 2010).

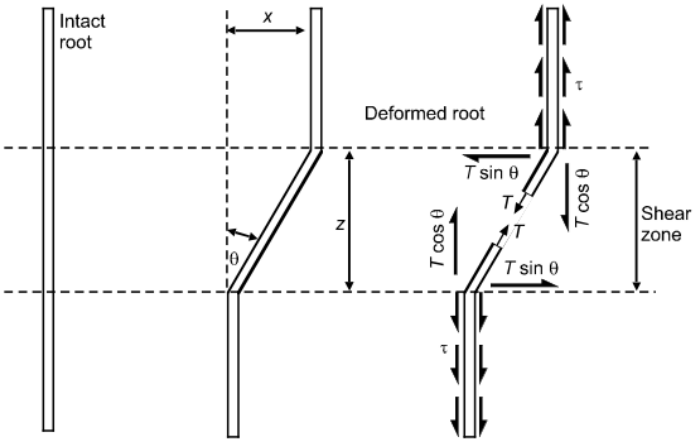

Fig 2.29 Model of flexible elastic root extending vertically across a horizontal shear zone (after Wu et al. 1979)

2.6.1.1 Wu and Waldron's Model (WWM)

Waldron (1977) assumed that all roots extend vertically across a horizontal shear zone, and the roots act like axially loaded piles, so tension is transferred to them as the soil is sheared. The tension developed in each root is resolved into a tangential component that augments the apparent cohesion and a normal component that augments the frictional resistance, as shown in Fig 2.29. The cohesion due to roots is provided by the total tensile strength of all roots per soil unit area:

$$c_{rWWM} = R_f \sum_{n=1}^{N} (T_{rn} \times RAR_n) \qquad \textbf{Eq 2. 18}$$

where T_{rn} is the tensile strength of root n, RAR_n is root area ratio *(RAR)* of each single root n , *RAR* represents the ratio of the area of roots crossing the failure plane to the total area of failure plane, is an indicator of root density properties (Mao et al. 2012) and can be given by:

$$RAR = \sum_{n=1}^{N} (\frac{\pi d_n^2}{4A}) \qquad \textbf{Eq 2. 19}$$

where d_n is the diameter of root n, A is the total area of failure plane.

R_f is a root orientation factor, which can be calculated using the following equation:

$$R_f = \sin\theta + \cos\theta \tan\phi \quad \textbf{Eq 2. 20}$$

where ϕ is the friction angle of the soil and θ is the angle of shear distortion of the root, can be estimated by:

$$\tan\theta = \frac{x}{z} \quad \textbf{Eq 2. 21}$$

where x is shear displacement at failure (peak shear resistance), and z is the thickness of the shear zone. Gray & Leiser (1982) generalized the WWM to the case where roots may be orientated at any angle relative to the failure plane, so that R_f was modified to be,

$$R_f = \cos\psi + \sin\psi \tan\phi \quad \textbf{Eq 2. 22}$$

where ψ is the angle of the root at rupture relative to the failure plane, which can be expressed as:

$$\psi = \tan^{-1}\left(\frac{1}{\tan\theta + 1/\tan i}\right) \quad \textbf{Eq 2. 23}$$

where i is the initial root orientation relative to the failure plane.

Wu (1976) independently developed a perpendicular root model and found that R_f was fairly insensitive to normal variations in θ and ϕ (40-70° and 25-40°, respectively), with R_f values ranging from 0.92 to 1.31. A constant value of 1.15 was therefore selected by Wu et al. (1979) to replace R_f and the simplified equation became :

$$c_{rWWM} = 1.15 \times \sum_{n=1}^{N} (T_{rn} \times RAR_n) \quad \textbf{Eq 2. 24}$$

Considering that Wu et al. (1979) assumed that all roots were perpendicular to the failure plane, the value of 1.15 could provide a reasonable representation of R_f (Thomas & Pollen-Bankhead 2010). However, if root orientation is allowed to vary between 0° to 180°, with distinct shear distortion θ and frictional angle ϕ, it may be not the case. Danjon et al. (2008) reported much larger variability in R_f based on field excavations. Moreover, the shear distortion θ has also been observed to range from 1° to 25°, with R_f values of 0.62-0.98

(Docker & Hubble 2008). Thomas & Pollen-Bankhead (2010) performed a statistical analysis (see Fig 2.30) which simulated different root systems within a Monte Carlo framework by randomly selecting root orientations from appropriate distributions and proposed that an R_f value close to 1.0 was more appropriate than 1.15.

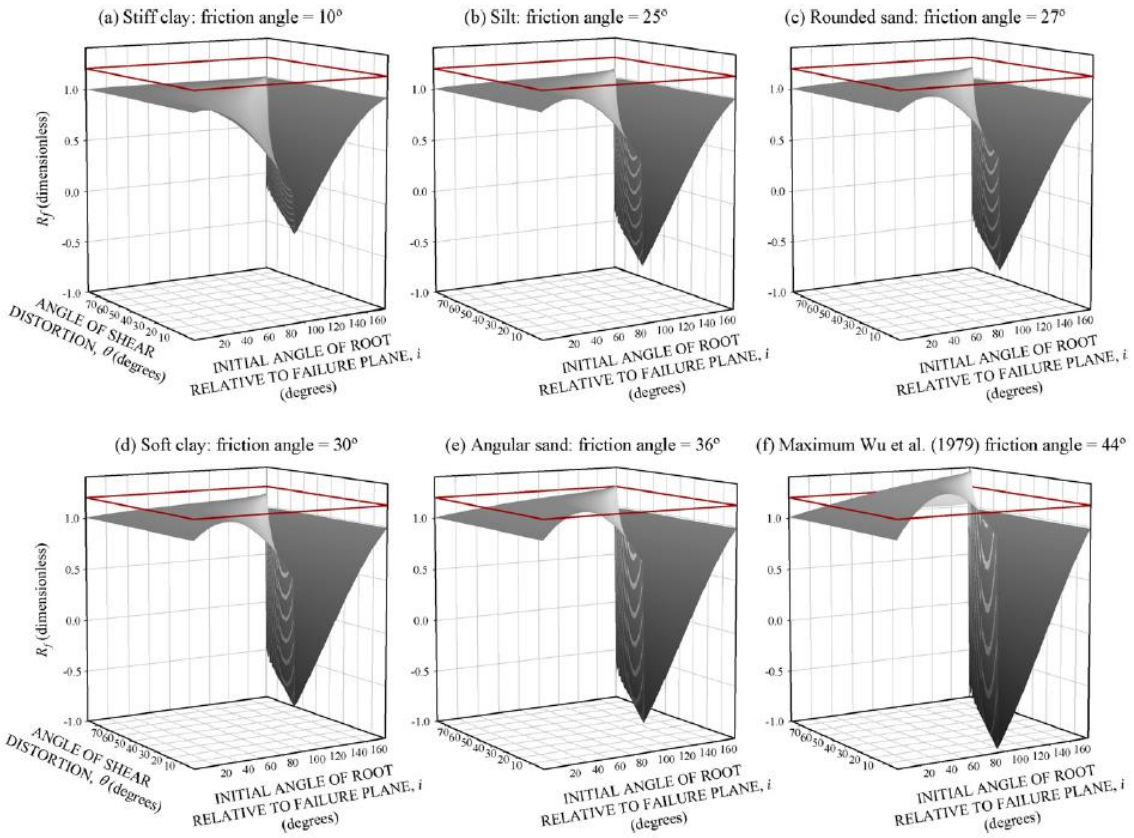

Fig 2.30 Effect of friction angle and shear distortion on reinforcement correcting factor R_f (Thomas & Pollen-Bankhead 2010)

2.6.1.2 Fibre Bundle Model (FBM)

In the FBM, c_r is also a function of *RAR* and tensile strength, but the roots are considered to break progressively rather than simultaneously. When some roots break, the total shear force is redistributed among the remaining roots with the total shear force being apportioned to each root in a bundle according to three assumptions: (i) Equal load applied to individual root regardless of root dimension; (ii) load apportioned by root diameter; or (iii) load apportioned by root cross-sectional area. According to these three assumptions root cohesion c_r can be calculated in the following equations (after Pollen & Simon 2005):

$$c_{r\,FBM,byrootCSA} = R_f \times \max \sum_{n=1}^{j} (T_{rj} \times RAR_n) \quad \textbf{Eq 2. 25}$$

$$c_{r\,FBM,byrootdiameter} = R_f \times \max(T_{rj} RAR_j \frac{\sum_{n=1}^{j} d_n}{d_j}) \quad \textbf{Eq 2. 26}$$

$$c_{r\,FBM,byrootnumber} = R_f \times \max(T_{rj} RAR_j j) \quad \textbf{Eq 2. 27}$$

where n is root number ordered from strongest to weakest, $n \in [1, N]$, j is the weakest root removed at each simulation step, $j \in [1, N]$ and T_{rj} is the tensile strength of the weakest remaining root.

When using different assumptions of load distribution, root breakage occurs in different orders (Thomas & Pollen-Bankhead 2010). For the above three assumptions, the breaking order of each root can be evaluated by T_{rj} , $T_{rj}d_j$, $T_{rj}d_j^2$, as a function of root CSA, root diameter, and root number, respectively (Mao et al. 2012). Mao et al. (2012) compiled a comprehensive literature review on the validation of these models and demonstrated that majority of studies (Pollen & Simon 2005; Hales et al. 2009; Bischetti et al. 2009; Mickovski et al. 2009; Loades et al. 2010) using FBM were based on only one of the assumptions. Few studies (Ji et al. 2012) have been conducted to employ all three assumptions. But in reality, especially in mixed forests with abundant species, the three assumptions may all exist. Mao et al. (2012) showed that the predicted c_r varied significantly depending on the model used, among them, c_r (FBM, root number) < c_r (FBM, root diameter) < c_r (FBM, root CSA) < c_r (WWM). However, no field or laboratory tests were performed in this study to validate which model is more realistic.

2.6.2 Fibre slippage/ pull out model

Waldron & Dakessian (1981) further developed the Waldron (1977) fibre break model, assuming root will slip or pull out from the root soil matrix, rather than break, to simulate the uprooting behaviour during slippage of the slope. Root cohesion c_r was then calculated using the following equations:

$$c_r = R_f \times \left(\frac{a\pi nLD}{2A} \right) \quad \textbf{Eq 2. 28}$$

where n is the root number, L is the anchorage length of the root; D is the diameter of root; A is the area of shear plane; a is adhesion, which is usually not well known (Wu 2013). An approximation is to assume that failure occurs in the soil within a thin soil layer around the root, then

$$a = c \quad \textbf{Eq 2. 29}$$

$$a = \sigma_0 \tan\delta = K\gamma z \tan\delta \quad \textbf{Eq 2. 30}$$

for cohesive and cohesionless soils, respectively; where c is cohesion of soil; K is coefficient of lateral earth pressure; σ_0 is the average normal stress on reinforcement; δ is the friction between soil and root. Limited studies show that a conservative estimate is (Wu 2013):

$$\tan\delta = 0.5\tan\phi \quad \textbf{Eq 2. 31}$$

Mickovski (2010) observed that K and δ are a function of several parameters including stress distribution, root diameter and stiffness. Compared with the fibre break model, this model is seldom used by researchers in practice. The reason for this may be associated with the difficulties in determining the anchorage length of roots and root soil adhesion in the field. Other pull out models in recent years can be found in Schwarz et al. (2010) and; Schwarz et al. (2011) and will not discussed further here.

2.6.3 Axial force and bending moment in reinforcement

Another more widely used approach to calculate the reinforcing effect is to consider the axial force and bending moment in the reinforcement (Wu 2013). This approach is presented here only for illustration. Full detail about this section can be found in Wu (2013). For the deformed segment of root shown in Fig 2.31, the following equation can be obtained,

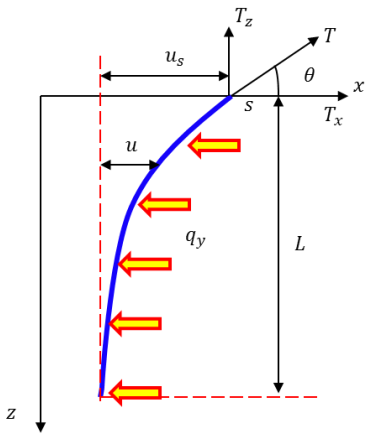

Fig 2.31 Schematic of forces on the deformed bar (Wu 2013)

$$EI\frac{d^4u}{dz^4} - T_z\frac{d^2u}{dz^2} = qd \qquad \textbf{Eq 2. 32}$$

where E and I are the Young's modulus and moment of inertia of the reinforcement; u is lateral displacement; L is the length of the root (deformed portion of reinforcement); d is the diameter of the root; q is soil reaction, and can be estimated using the equation:

$$q = ku \qquad \textbf{Eq 2. 33}$$

where k is a measure of soil stiffness, also called the coefficient of subgrade reaction; the limit of q is q_y (bearing pressure at yield of the soil). Beyond this point, passive failure occurs in the soil. As displacement increases, the zone of passive failure (L) increases until tension failure or pull-out occurs. It is assumed that the bending moment is zero at $z=0$. The shear stress between the reinforcement and soil is ignored.

2.6.3.1 Flexible cable solution

The reinforcement can be regarded to be a flexible cable when T_z is relative large relative to EI, or ηL >2.5, where

$$\eta = \sqrt{T_z/EI} \qquad \textbf{Eq 2. 34}$$

The cable solution is

$$T_z(0) = T(L) = T(0)\sin\psi \quad \textbf{Eq 2. 35}$$

$$T_x(0) = q_y dL = T(0)\cos\psi \quad \textbf{Eq 2. 36}$$

$$u(0) = \frac{q_y dL^2}{2T_z(0)} \quad \textbf{Eq 2. 37}$$

If any two of *u(0)*, θ or *L* are known , *T(0)* can be calculated. At any point, T cannot exceed the in situ strength of the reinforcement or root.

2.6.3.2 Beam or pile solution

The reinforcement can be regarded to be a beam (pile) subjected to horizontal or lateral loading when T_z is small relative to *EI*, or ηL <1.5. A number of solutions and equations have been developed for better understanding pile and soil interaction (Reese & Van Impe 2011):

i) Elastic pile and elastic soil
ii) Elastic pile and finite elements for soil
iii) Rigid pile and plastic soil
iv) Non-linear pile and *p-y* model for soil

Among them, the most widely used model is the *p-y* model (e.g. Boulanger et al. 2003; Allotey & Foschi 2005; Knappett & Madabhushi 2009; Duckett 2013) and this will be employed later in this project, full details about *p-y* model will be illustrated in detail in the Chapter 5.

2.6.4 Finite element method (FEM)

The highly developed calculating ability of computers allows researchers to make solutions more rapidly and accurately in recent years. FEM has been widely used for understanding the root soil interaction, and investigating the global performance of rooted slopes. In general, these FE models have been explored from three different perspectives (Duckett 2013). The first looks into modelling of root system development: a detailed review of state of art on this aspect can be found in Danjon & Reubens (2007) and Tobin et al. (2007). The second is interested in the simulation of root and soil interaction as a function of external loading, root

architecture and root/soil properties (e.g. Dupuy et al. 2005; Mickovski et al. 2011; Duckett 2013). The third simulates the global performance of slope, either through simulating the rooted zone as a macro soil with additional cohension c_r (e.g. Frydman & Operstein 2001;Mao et al. 2014), or through treating roots as beam elements or conventional geo-structure embedded into the continuum elements of the slope (e.g. Genet et al. 2008; Lin et al. 2010).

For the macro soil model, it is generally considered that the root cohesion is uniformly distributed along the slope surface. This may be not the case, especially for highly spaced tree rooted slopes. The main stucture of tree root systems is concentrated within the ZRT horizontally. Beyond this zone, roots still extend to several metres, but the density will be relatively low (Gilman 1988; Schenk & Jackson 2002; Göttlicher et al. 2008). Tiwari et al. (2013) reported a new approach which permits the use of a transitional discontinuous function in finite element modelling to simulate the progressive failure of roots, and evaluate the behaviour of vegetated slopes. However, this model can still be regarded as a type of root–soil interaction model as it based on the fundamental theory of the fibre breakmodel.

2.7 Research requirement

The use of vegetation to reinforce soil on landslide-prone slopes is an ecological and economical alternative to traditional civil engineering techniques. The mechanical benefit of roots on slope stabilty has been commonly accepted (e.g. Norris et al. 2008; Wu 2007; Stokes et al. 2014). Quantifying this benefit is of great importance for engineering application and has attracted much research interest. Many analytical models have been developed based on small site in-situ investigation and laboratory tests. However, the majority of validation work has concentrated on grasses owing to the extreme expense and difficulty involved in conducting full-scale field tests on shrubs and trees.

Geotechnical centrifuge modelling offers an opportunity to investigate in detail the engineering performance of vegetated slopes and provide a database for the validation work of these models, but its application has been restricted due to the lack of availability of suitable root analogues that can replicate appropriate mechanical properties (stiffness and strength) and realistic 3-D geometry. This thesis aims at designing a repeatable scaled 3-D

tree root model and investigating its behaviour subject to earthquake-induced landslips. The factors that will influence the root soil interaction during slippage will be revealed by performing large direct shear tests using the same root analogues.

Moreover, previous research on vegetation reinforced slope focus on the static condition. Whether vegetated slopes also perform better than fallow slopes during earthquakes is still uncertain. Given the fact that earthquakes are one of the major triggering causes for landslides, understanding the seismic behaviour of rooted slopes and understanding the additional factors influencing rooted slopes design to resist seismic loading is essential. So in this thesis the dynamic centrifuge modelling approach will be employed.

In terms of the assesment of slope stablity, the stabiliy of a grassed slope is generally estimated in 2D assuming that the additional cohesion provided by roots is homogenous in the soil layer. However, this is not suitable for forested slopes mainly consisting of trees because of the heterogeneous distribution of woody roots (Kokutse et al. 2006). New analytical and computational processes for analysing forested slopes under earthquake action will also be explored in this thesis and these will be validated against the centrifuge test data.

Chapter 3 Physical Modelling Methodology

3.1 Introduction

Geotechnical centrifuge modelling is an approach which can simulate the global performance of a full-scale soil slope prototype to a high level of fidelity, by achieving similitude of stresses at homologous points within the model and prototype. Despite such popularity in geotechnical engineering, only relatively few centrifuge model tests (Sonnenberg et al. 2010; Sonnenberg et al. 2011; Eab et al. 2014) have been performed on vegetation reinforced slopes. This chapter will introduce the principles of centrifuge modelling, and present the modelling procedures used in the subsequent chapters of this thesis.

3.2 Principles of centrifuge modelling

It is well recognised that in situ soil stresses change with depth and soil behaviour is highly dependent on the stress level and stress history (Knappett 2012). In the physical modelling of geotechnical problems, scale models of field prototypes are generally involved. But the main drawback of 1 g testing of scale models is that it reduces the stress level and results in a greatly different soil response. An example is illustrated in Fig 3.1, a soil sample A is located below the critical state line (CSL) (Schofield & Wroth 1968), when it is subject to shear loading under a relatively low confining stress (1g testing) , it will dilate towards CSL. As a comparison, a soil sample B with same density but located between CSL and normal compression line (NCL) (Wood 1990), will contract when it is sheared under a higher mean effective stress. The unrealistic dilation behaviour observed in 1g model testing cannot easily represent the soil response in the field. This particular shortcoming of 1g testing of scale models can be overcome by spinning the scale model on a geotechnical centrifuge to increase the gravitational factor N and generating the same stress level with the prototype in the field (Taylor 2003; Wood 2003).

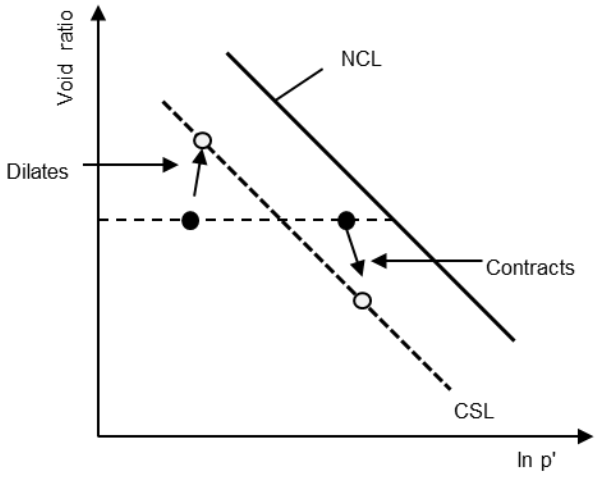

Fig 3.1 Distinct response of two soil samples at the same density sheared under different confining stress

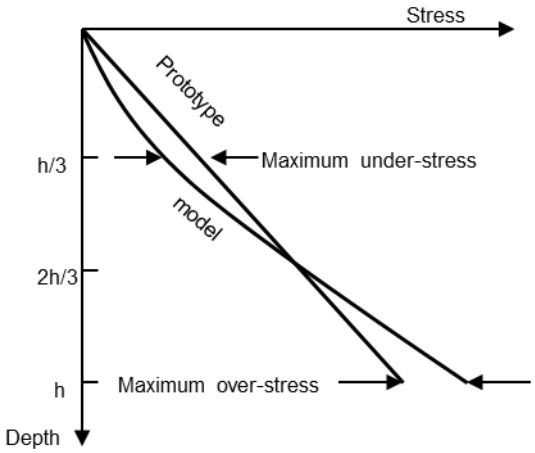

Fig 3.2 Comparison of stress variation with depth in a centrifuge model and its corresponding prototype (Taylor 2003)

Table 3.1 shows a summary of the principal scaling laws used in geotechnical modelling. A typical derivation of the most fundamental scaling laws for centrifuge modelling can be found in Taylor (2003). There is a gravitational distortion within centrifuge models that can be minimised by setting the exact match in stress between model and prototype at two thirds of the model depth (see Fig 3.2). The maximum error in stress can be estimated using the following equation,

$$r_u = r_o = \frac{h_m}{6R_e} \quad \textbf{Eq 3. 1}$$

where r_u and r_o are errors of maximum under-stress and over-stress, respectively. h_m is the total model height, and R_e is the effective centrifuge radius, which is measured from the central axis to one-third the depth of the model.

From Eq 3.1, it is clear that the maximum error in the stress profile for most geotechnical centrifuges is minor and generally less than 3% given the fact that in most cases the ratio of model height to effective centrifuge radius is less than 20%. In practice, three other types of distortion which affect the similitude between model and prototype are generally considered, that is, angular distortion, radial distortion, and Coriolis distortions. Full detail of these distortions and aspects of dynamic centrifuge modelling related to simulation of earthquake effect can be found in Taylor (2003), Kutter (1995) and will not be illustrated here.

Table 3. 1. Scaling laws for centrifuge testing (After Schofield, 1981; Kutter, 1995)

Parameter	Scaling law: Model/Prototype	Dimensions*
Length	1/N	L
Area	$1/N^2$	L^2
Volume	$1/N^3$	L^3
Density	1	M/L^3
Mass	$1/N^3$	M
Stress	1	M/LT^2
Strain	1	-
Force	$1/N^2$	ML/T^2
Bending moment	$1/N^3$	ML^2/T^2
Young's modulus	1	M/LT^2
Second moment of area	$1/N^4$	L^4
For dynamic events		
Time (Dynamic)	1/N	T
Frequency	N	1/T
Displacement	1/N	L
Velocity	1	L/T
Acceleration	N	L/T^2

* L = length; M = mass; T = time.

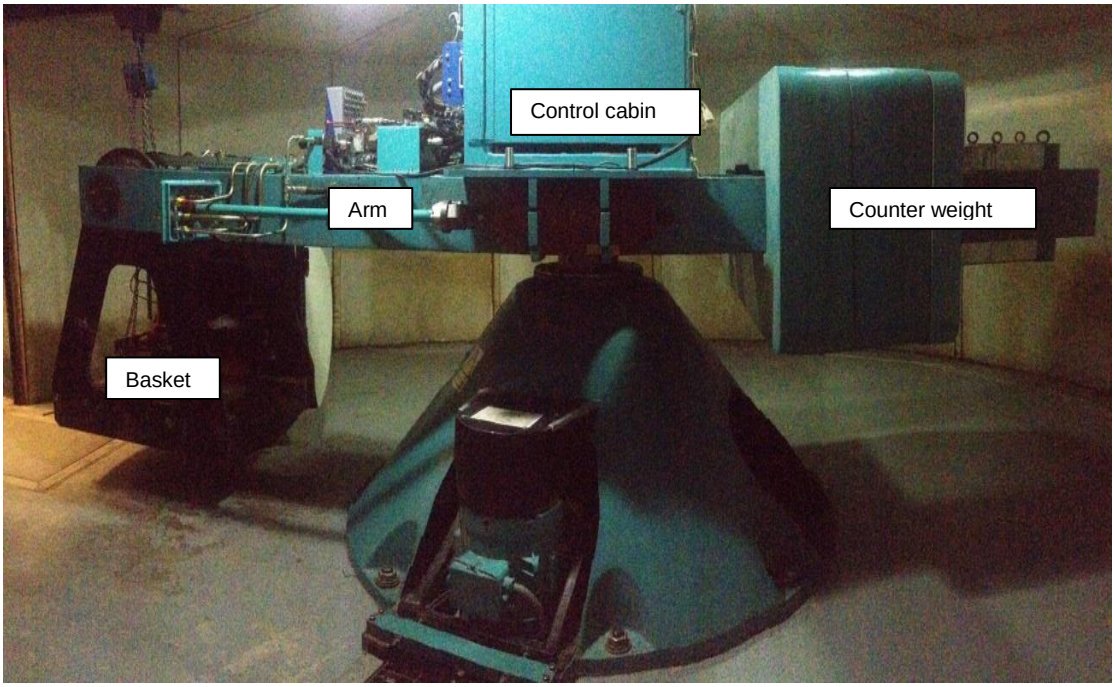

(a)

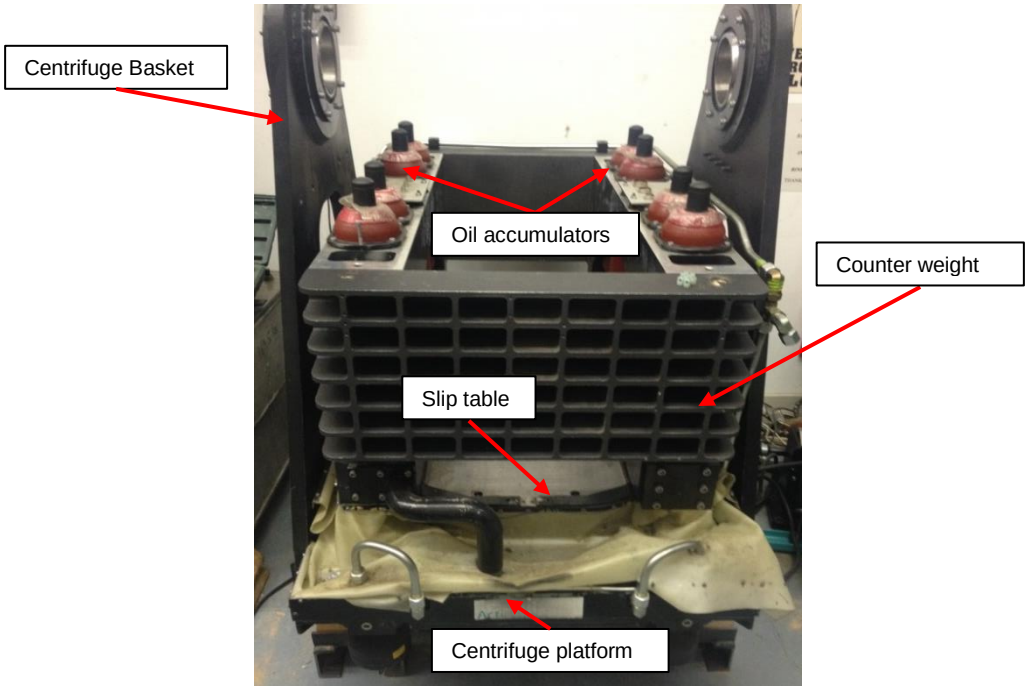

(b)

Fig 3.3 (a) University of Dundee *Actidyn Systems C67-2* geotechnical centrifuge ; (b) *Actidyn QS67-2* earthquake simulator

For reinforced slope modelling, the particle size effect should be given particular attention (Kutter 1995). If the geotechnical problem only involves soil and water, then using the same soil in both model and prototype should not give any unwanted grain size effects. But if the structure (e.g. fine roots in this study) is relatively small compared to the size of the grains (e.g. D_{50}) then the soil may no longer behave as a continuum but more as a set of discrete particles. Ovesen (1979) proposed that there was some deviation from continuum behaviour in centrifuge modelling when the ratio of foundation diameter to grain size was less than about 15. In fact, the diameter of fine model roots used in this study will be very similar to D_{50}, as a result, grain size effects should not be overlooked in this study and these will be discussed in further detail in Chapter 7.

3.3 University of Dundee Centrifuge

An *Actidyn Systèmes* C67-2 geotechnical centrifuge was installed at the University of Dundee Civil Engineering Department in 1996 (Fig 3.3 (a)). In June 2011 the centrifuge was equipped with an *Actidyn Systèmes* QS67-2 in-fight earthquake simulator (EQS), becoming one of four facilities with earthquake simulation capabilities under *N.g* field in Europe. It is a 3 m radius beam type centrifuge, capable of maximum accelerations ranging between 100 and 130 *g* depending on the payload. Loads may vary from 0 to 1500 kg with a maximum payload force of 150 kN.

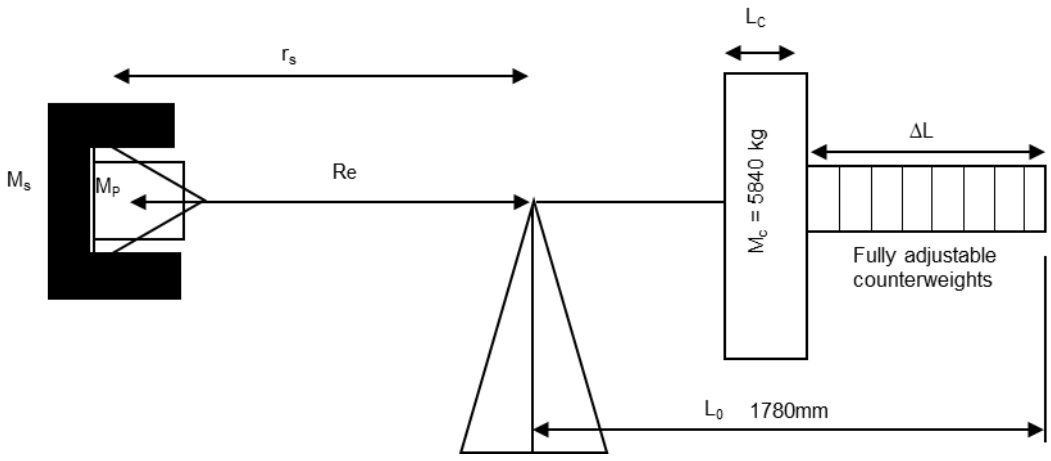

Fig 3.4 Mechanism of centrifuge balancing

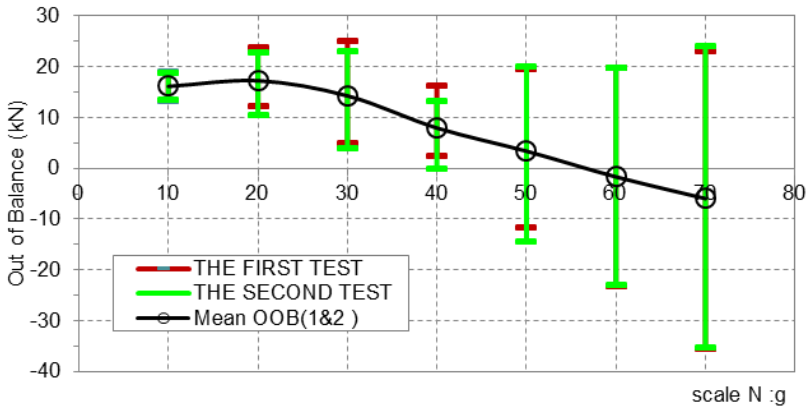

Fig 3.5 Measured out of balance as a function of g level

The self-aligning swing basket can accommodate a model with maximum dimensions of 0.8×1×0.8 m^3 (which reduce to 0.4×0.9×0.5 m^3 for earthquake simulation). And it requires for proper positioning, a platform surface orthogonal to the resultant centrifugal acceleration field and with the payload centre of mass is aligned with the platform mounting surface geometrical centre. This is quite important especially when the load is not fastened to the platform and caution must be employed at any time to ensure the proper load centring.

A set of fully adjustable counterweights (see Fig 3.4) are located at the opposite side of the arm to the swing basket. For proper operation the centrifuge must be balanced. When this condition is not satisfied the control system detects the unbalance and stops the centrifuge when the unbalance reaches a maximum limit. Fig 3.5 shows the magnitude of out-of-balance (OOB) as a function of g level when the counterweights were initially set for 60 g acceleration field. The error bars indicate the change in OOB due to the oil for the EQS moving on and off the centrifuge.

Centrifuge balancing is possible from no to full load condition by simple manual adjustment of the built-in counterweight position. A spreadsheet has been developed to calculate the required counterweight position based on the model mass, the position of its centre of mass and the desired *g*-level (*N*). The centrifuge is spun by two electrical motors having a speed range of 340 to 1800 rpm, which transmit the motion to the centrifuge spindle through a belt drive (with a 9:1 transmission ratio).

Table 3. 2 C67-2 geotechnical centrifuge specifications

Platform radius	3 m
Nominal radius	2.7 m
Max usuable height	1.5 m
Max payload	1500 kg
Centrifugal acceleration at max payload	100 g
Payload at max centrifugal acceleration	850 kg
Max centrifugal acceleration	130 g
Centrifugal acceleration range	5-130 g
Boom rate	38-208 rpm
Max operational unbalance	±40kN

The centrifuge is installed in a circular chamber. The chamber walls are made of reinforced concrete encased by steel plates in order to present good geometrical tolerance and smooth finish. The main specifications of the centrifuge are surmised in Table 3.2.

3.3.1 Earthquake simulator (EQS)

The *Actidyn* Q67-2 mono-directional servo-hydraulic earthquake simulator (EQS) (see Fig 3.3 (b)) is mounted on the centrifuge and is used to simulate a one-dimensional prescribed base input earthquake motion. This device is based on the dynamic self-balancing technique developed by *Actidyn* to eliminate a large portion of undesired reaction forces and vibrations transmitted during earthquake shaking to the centrifuge main body (Perdriat et al. 2002). It has a maximum payload of 400 kg, with a maximum table displacement of 2.5 mm and a peak operation of 80 g. The motion can be exerted to a maximum acceleration value of 40 g, with model scale frequency of 40 to 400 Hz. The EQS allows users to select the earthquake frequency, magnitude and duration if harmonic motions are to be used. The EQS can also simulated recorded earthquake time histories once they have been band-pass filtered to ensure frequency content (at model scale) in the range of 40 to 400 Hz. More details about this equipment can be found in Brennan et al. (2014).

3.3.2 Data acquisition

The data acquisition (DAQ) system consisted of a number of components as shown in Fig 3.6. Before the spinning of centrifuge, all of the instruments are plugged into two junction boxes, which provide the necessary supply voltage (5 V or 10 V DC depending on the instrument).

Table 3.3 QS67-2 earthquake simulator specifications

Max payload moving mass	400 kg
Payload at full shaker acceleration	300 kg
Centrifugal acceleration range	10-80 g
Max shaking force	150 kN
Peak table displacement	2.5 mm
Peak table velocity	0.75 m/s
Frequency response	40-400Hz
Peak full load acceleration	40g
Peak acceleration with no payload	60g

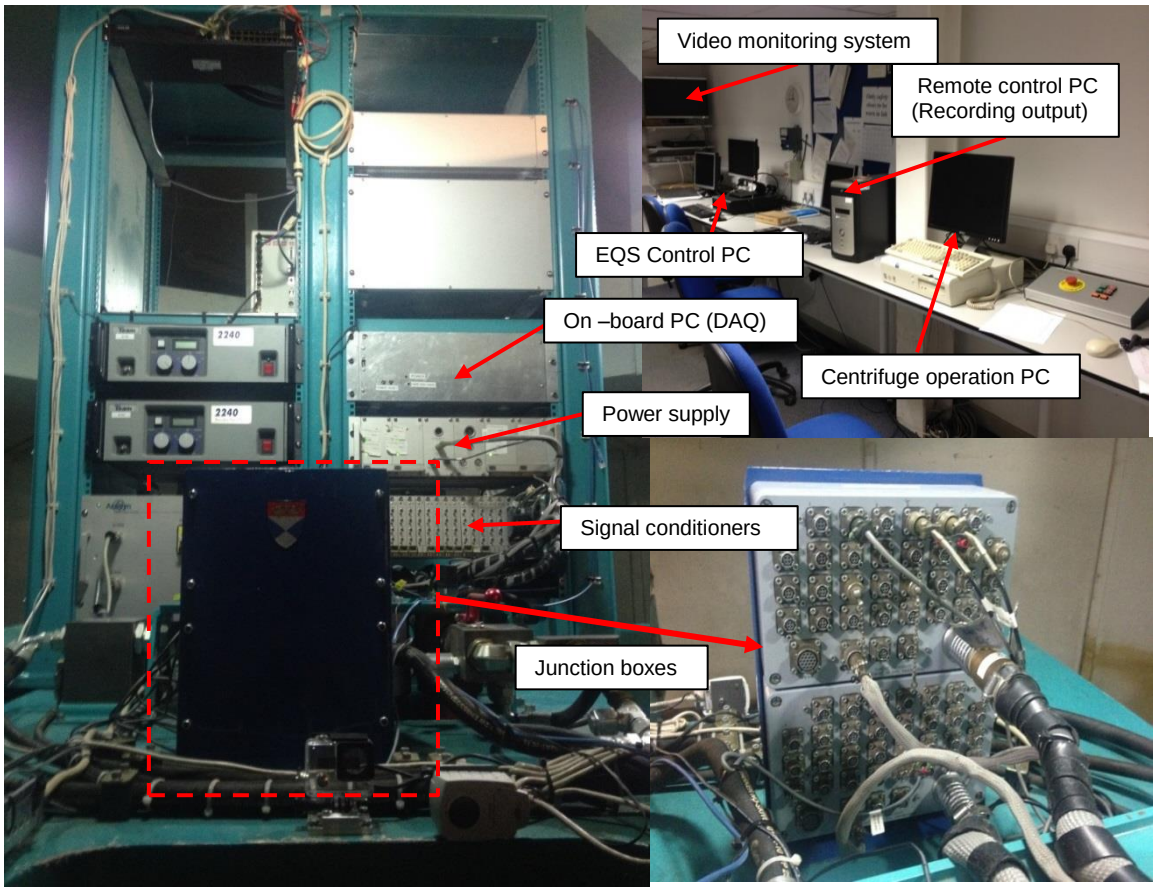

Fig 3.6 Data acquisition (DAQ) system

During spinning, the instruments' signals were collected by the junction boxes and transferred to a signal conditioning unit, where they can be filtered or amplified if necessary. Once processed, the signals are sent to the on-board PC via four 16 channel *Adlink NuDAQ*

2204 high frequency PCI data acquisition cards. Table 3.3 summarizes the main features of the DAQ system used.

The data acquisition process is controlled by a *LabVIEW* routine originally developed by Bertalot (2013). *LabVIEW* runs on the on-board PC which, in turn, is controlled remotely from the centrifuge control room. Further detail about the operation interface for the *LabVIEW* programme used in this study can be found in Al-defae (2013).

3.4 Model preparation

3.4.1 Soil

HST 95 Congleton silica sand was used in model construction, having the basic properties shown in Table 3.4 (Lauder 2010). This sand has been widely used in geotechnical research(e.g. Lauder 2010; Al-Defae et al. 2013; Bertalot 2013) at the University of Dundee. It is a specific fraction of the sand extracted at Bent Farm, Congleton, Cheshire. It can be classified as a uniformly graded fine sand with the particle size distribution (PSD) shown in Fig 3.7. Lauder (2010) observed the sand particle shape with an electron microscope and found that the material roundness index (R) for this sand is 0.53, which classifies it as rounded in shape. This is important for the determination of an analytical model to estimate soil dynamic properties and will be discussed in detail in Chapter 4.

Al-Defae et al. (2013) summarised shear box data from total of 38 tests (see Table 3.4) conducted over a range of relative densities and confining normal effective stresses between 5kPa and 200kPa based on the literature and proposed that the critical state friction angle of HST 95 sand is ϕ_{cs}'=32°. This conforms to results from the Large DSA tests reported later in this study. A straight-line fit for the variation of the dilation angle and peak friction angle as a function of relative density I_D is also given,

$$\phi_{pk}' = 20I_D + 29 \qquad \textbf{Eq 3. 2}$$

$$\psi' = 25I_D - 4 \qquad \textbf{Eq 3. 3}$$

Table 3.4 State-independent physical properties of sand used in DSA testing (after Byrne et al. 2012; Al-Defae et al. 2013)

Property	HST 95 silica sand
D_{50}:mm	0.16
C_u	1.9
C_c	1.06
γ_{max}: kN/m^3	17.6
γ_{min}: kN/m^3	14.3

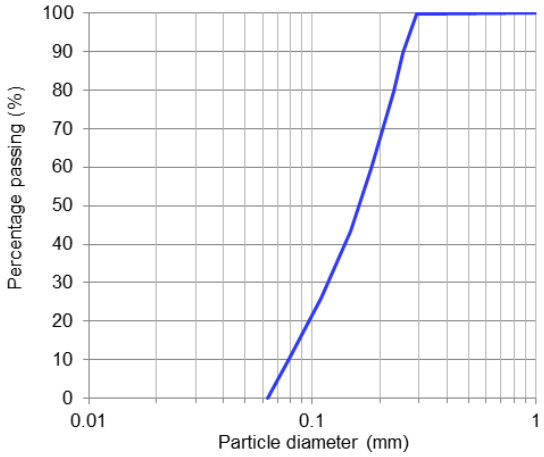

Fig 3.7 Particle size distribution for HST95 silica sand

These simple linear fits satisfy the dilation model given by Bolton (1986), but it should be mentioned here that they have been calibrated for this particular sand of HST 95. Considering the repeatability of this study, the more common dilation model of Bolton (1986) rather than the linear fits given above will be used in the Chapter 7 and Chapter 8.

3.4.2 Soil preparation techniques

For all the centrifuge tests discussed in this thesis, slopes were constructed by air pluviation of dry sand through a predetermined height using a slot pluviator (see Fig 3.8) to level, followed by vacuum removal of excess sand to form the required slope. The slot pluviator was mounted on wheels running on two tracks parallel to the model container longitudinal direction, and was swept back and forth over the container length during pluviation until the desired model height was reached. The width of the pluviator was 540 mm along the slot, which was enough to cover the full width of the container during the pluviation process. The guide track was fixed at a height of 1.9 m from the ground surface, which allowed a falling

height of 1.5 m. This falling height could guarantee the sand particle falling through air nearly at a constant speed near the model surface and ensure minimum fluctuation of density in the vertical plane. The slopes were constructed as a uniform deposit at a relative density of I_D =55%-60%. The desired relative density can be achieved by adjusting the slot width through moving the two plates up or down the inclined side of the container. Apart from the predetermined falling height and the slot width, the sweeping rate was also found to influence the relative density (Bertalot 2013). A faster sweeping rate is preferred to keep the pouring rate for a given location, however, if the sand is dropping too fast, then local wind currents will be generated and lead to non-uniform loose density zones (Ueno 1998). Before constructing the formal slope model, density tests were performed to determine the width of the slot. Four density pots were placed within the ESB container, with one sitting at the centre of the container, one sitting near the root cluster and the other two sitting adjacent to the boundary and side wall of the container. No more than 5% differences were detected between these four sample points. And this indicates the uniformity of soil density across the model. Fig 3.9 shows the measured density as a function of slot width. It can be clearly seen from this figure, that 3 mm can reliably provide a relative density of 55%-60% for the use of this study.

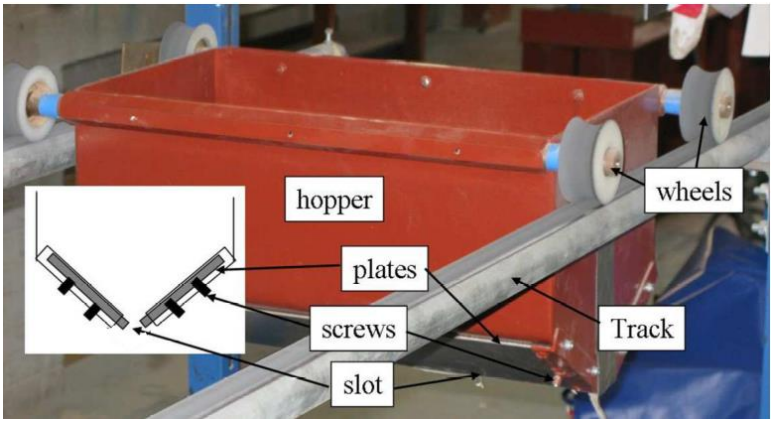

Fig 3.8 Slot pluviator with cross section (inset) for preparing all centrifuge models (Lauder 2010)

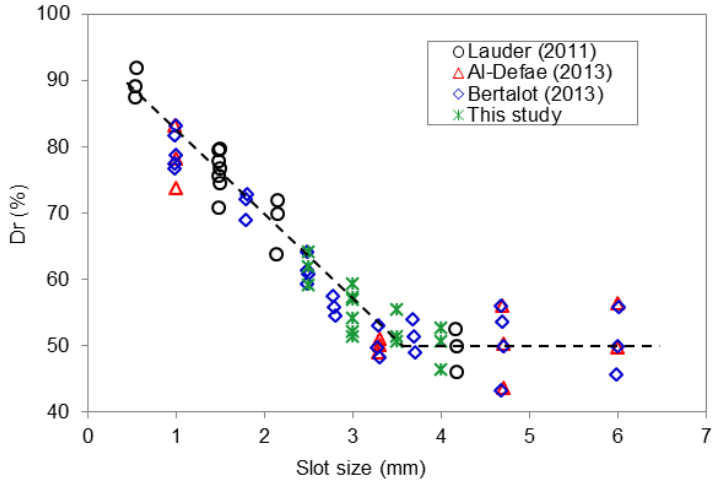

Fig 3.9 Correlation between slot size and relative density D_r

3.4.3 Root analogue installation

Two types of root analogues were used in this study: i) a straight root group which was designed to represent plate/ heart root system (see Fig 2.2 (a) (b)); ii) a tap root cluster with deep roots which was designed to represent a tap root system (see Fig 2.2 (c)). Full details about the design, fabrication and testing of these root analogues will be presented in the Chapter 4.

During pluviation, the tap root clusters were attached using double-sided adhesive tape and cyanoacrylate adhesive (super glue) to plastic drinking straws with varied length, as shown in Fig 3.10.

The length of the straw depended on the distance between the root cluster and the ESB container upper surface. Then the straws were attached to a steel support using duct tape (or transparent adhesive tape) so that the root clusters could be hung at pre-defined positions. When the lower part of the root clusters were embedded in the soil, the supporting straws were cut off and removed. This approach can maintain the root clusters' verticality and prevent any damage or wedging of the root analogues during installation.

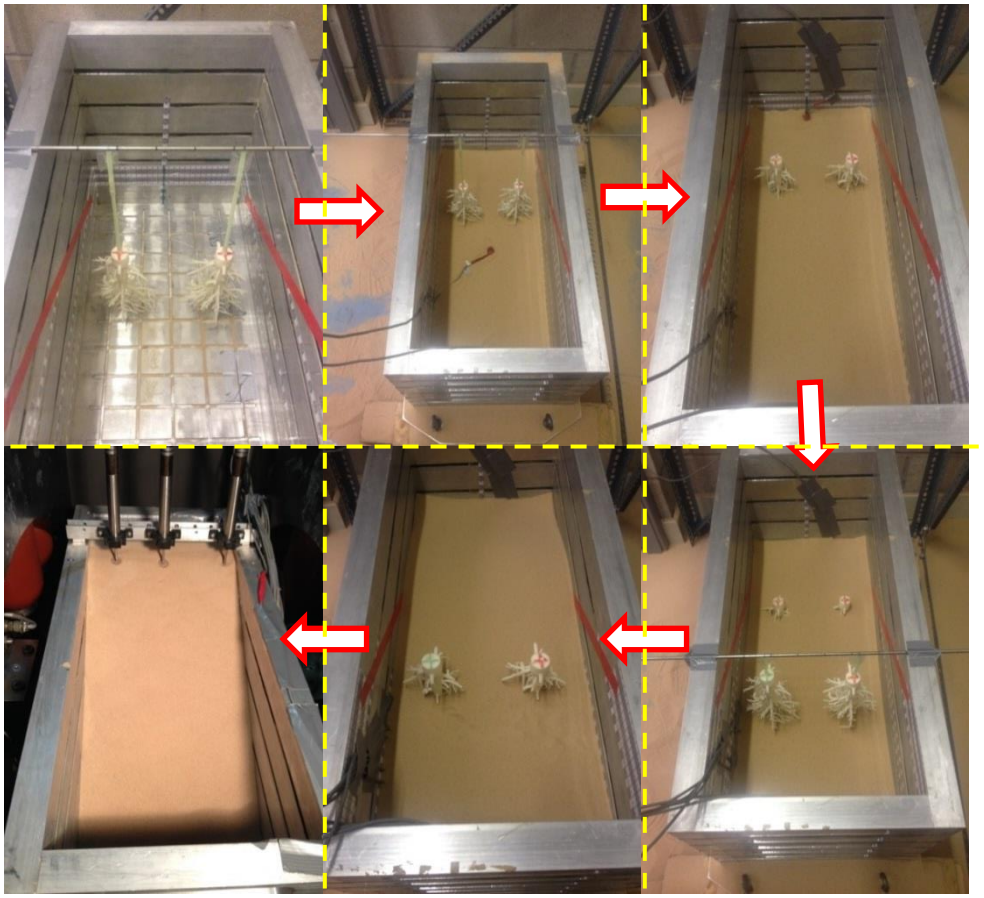

Fig 3.10 Procedure of 1:10 scale root cluster installation

In terms of straight root group, a penetration technique, rather than the hanging technique described above was used because the latter could not maintain the individual straight roots vertically due to the light weight of these roots. When the soil layer was 20mm higher than the tips of the root analogues, they were inserted into the soil and arranged vertically.

3.4.4 Equivalent Shear Beam (ESB) container

Models were constructed within an Equivalent Shear Beam (ESB) container with internal dimension of 669mm × 279mm× 338mm. This type of container could provide the equivalent dynamic shear stiffness as the adjacent soil and simulate the infinite soil condition for the model. Such containers have been extensively used and tested for different soil types; detailed information about the performance of such container can be found in Zeng & Schofield

(1996), Teymur & Madabhushi (2003), Brennan et al. (2006), Lee et al. (2013) and Bertalot (2013).

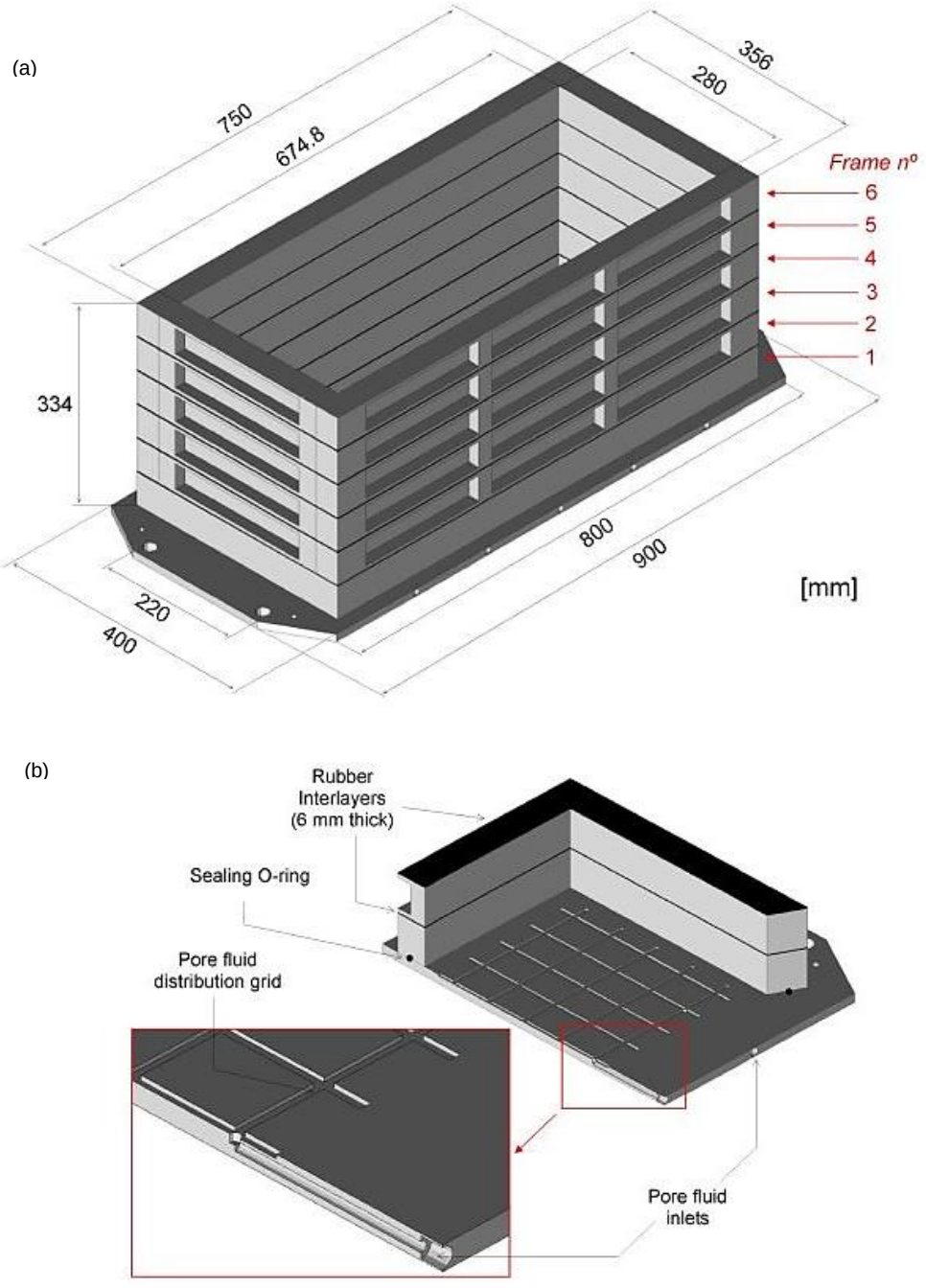

Fig 3.11 ESB container layout : a) Outline and dimensions; b) Base plate detail (Bertalot 2013)

Table 3.5 Design parameters used for the evaluation of the ESB container dynamic behaviour (Bertalot 2013)

Box Parameter	
Number of frames	6
Number of rubber layers (DOF)	5
Frame mass ,M_f (kg)	7
Frame thickness, t_f (mm)	50.1
Rubber thickness, t_r (mm)	6
Rubber shear stiffness, $G_{r,0}$ (kPa)	1374
Small-strain shear stiffness, $G_{r,ss}$ (kPa)	177
Confining stress coefficient, m	14.6

Here $G_{r,0}$ is the value estimated under zero confining stress condition; m represents the increase in shear stiffness for 1 kPa increase of vertical confining stress

The ESB container used in this study was originally designed, fabricated and tested by Bertalot (2013). The box was constituted of a stack of 6 solid aluminium frames mounted on a rigid, 12 mm thick, aluminium base. The bottom frame was rigidly bolted to the base, accommodating a rubber O-ring that runs along an indentation carved in its bottom surface in order to provide fluid sealing, while the five top frames were glued to rubber interlayers positioned in between them. The empty ESB container had an overall mass of approximately 70 kg, with other properties shown in Table 3.5. A typical layout of this container is shown in Fig 3.11.

Uniform slope conditions were modelled across the slope width within the container. Given the boundary condition of the container, the effect of side friction from the container wall should be considered. Taylor (2003) suggested establishing the plane strain model wide enough to eliminate this effect. In practice, this was achieved by a minimum container width to model height ratio. The ratio between the container width to the slope height was approximately 0.875, which was very close to the optimal ratio of 1 suggested by Davies & Parry (1985)

3.5 Instrumentation

The centrifuge models tested were instrumented with a number of transducers in order to document their behaviour during shaking. Two main categories of transducers were used: MEMS accelerometers and linear variable differential transformers (LVDT). Table 3.6 lists the specific type of instrument used.

Table 3.6 Type of transducers used in the centrifuge tests

Transducer	Manufacturer	Physical variable	Supply voltage (V)	Cable length (m)
ADXL78	Analog Device	Acceleration	5	3.5
LDC1000A	RDP Group	Displacement	5-18	3

3.5.1 ADXL78 MEMS Accelerometers

ADXL78 MEMS accelerometers (ACC) manufactured by Analog Devices Inc. were embedded within each model to measure the horizontal accelerations within the soil specimen. Micro-Electro-Mechanical Systems (MEMS) is a technology defined as miniaturized mechanical and electro-mechanical elements that are made using the techniques of microfabrication used in the integrated circuit industry. The ADXL78 (see Fig 3.12) is the fourth-generation surface micro-machined *iMEMS* accelerometer manufactured by Analog Devices Inc. It is a single-axis accelerometer with signal conditioned voltage outputs that are on a single monolithic integrated circuit. This product measures acceleration with a full-scale range of $\pm 70g$. It can measure both dynamic acceleration and static acceleration (gravity). The sensing element of this device consists of several differential capacitor unit cells. Each cell is composed of fixed plates attached to the instrument body and movable plates attached to a moving frame. Displacement of the frame changes the differential capacitance, which is measured by the on-chip circuitry. The output signal is conditioned by means of a built-in 400 Hz 2-pole Bessel filter which smoothes out high-frequency response. These devices are widely used in the automotive industry (Bertalot 2013), specifically for use in front and side impact airbag applications, thus they are designed to be stable over vibration and temperature ranges found in such applications. A simple calibration procedure has been followed: each instrument was aligned with the earth gravity field (i.e. perpendicular to the ground surface, +1g) and its output voltage recorded, the same operation was then repeated after rotating the instrument through 180◦ in the vertical plane (i.e. opposite direction,-1g) and its sensitivity calculated by:

$$Sensitivity(V/g) = \frac{|Voltage(+1g) - Voltage(-1g)|}{2} \qquad \textbf{Eq 3. 4}$$

Given the fact that the ADXL78 accelerometer is very small and delicate, they were attached using cyanoacrylate adhesive (super glue) to a 20mm diameter circular PVC disk and then

coated by a plastic-dip flexible emulsion. The purpose of this disk was to keep the accelerometer in a horizontal plane during placement within the soil models, increasing the movement sensitivity during earthquake shaking through better coupling with the surrounding soil, and to make them waterproof with neutral buoyancy for use in saturated tests.

3.5.2 LDC 1000A Differential Transformers

Three external linear variable differential transformers (LVDTs), with one installed at the centre of the crest and the other two placed adjacent to the side walls at different distances along the crest (see Fig 3.13), were used to measure the settlement of the slope crest and detect any boundary effects on this. The LDC1000A type manufactured by RDP electronics Ltd. was selected. This instrument is a spring return type LVDT, thus the measuring rod is constantly pushed in contact with the moving object, exerting on it a force of 2 N at its mid-run. This characteristic allows the instrument to accurately measure both downward and upward vertical movements. The measuring range of the LDC1000A is 50 mm. The LVDTs used in the tests were calibrated using a micrometer and their calibration factor is shown in Fig 3.13(b). A circular disc with a diameter of 32mm was placed between the surface of the slope and the tip of LVDT to prevent the LVDT penetrating into the soil. The presence of such a disc may affect the ability of the LVDTs to record settlement at a single point. Further discussion of the disc effect will be discussed in the Chapter 4.

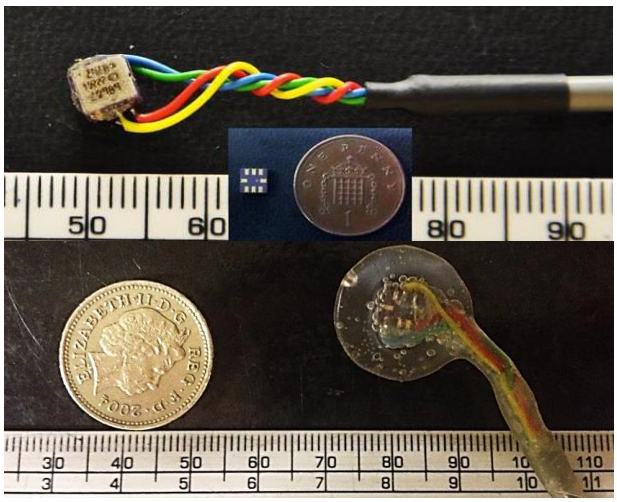

Fig 3.12 ADXL78 MEMS Accelerometers: a) without coating; b) with coating

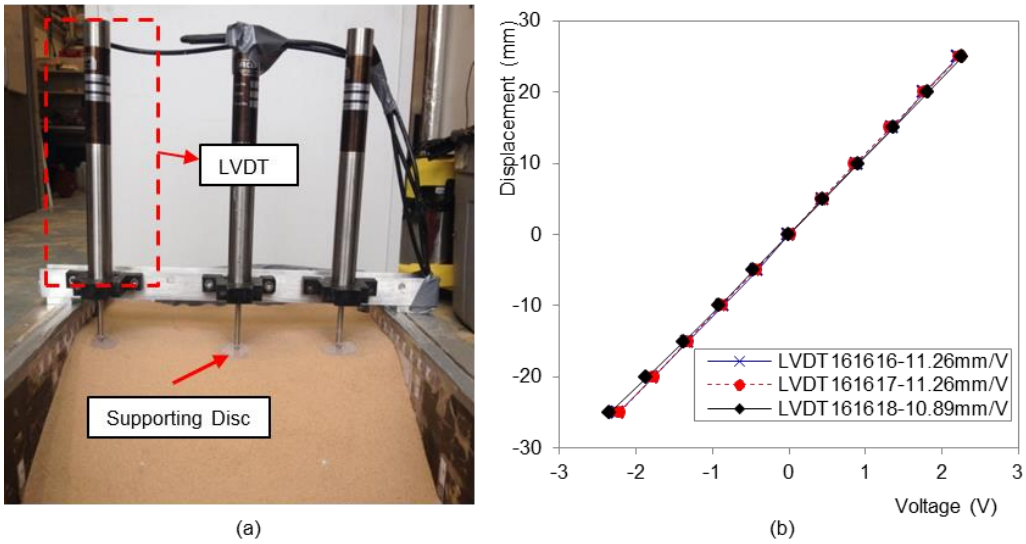

Fig 3.13 LDC 100A differential Transformers: a) Arrangement in centrifuge model; b) Calibration

3.6 Input ground motions

Eight successive earthquake motions were applied to each model at different g level, comprised of three types with distinct peak ground acceleration (PGA), duration and frequency content. The sequence of motions is summarised in Table 3.7. The first motion was taken from the 1995 Aegion earthquake (M_s 6.2) and was predicted to cause only a small amount of slip and predominantly acts to characterise the elastic dynamic behaviour of the slope. This initial motion was followed by three nominally identical stronger motions from the 1994 Northridge earthquake (M_s 6.8) and a further three from the 2009 L'Aquila earthquake (M_s 6.3), followed by a final Aegion motion to allow the changes in the elastic dynamic response to be determined following the sequence of larger motions. The three motions were downloaded from the PEER (Pacific Earthquake Engineering Research) Next Generation Attenuation model database and are shown as acceleration response spectra (ARS), normalized by the peak acceleration for the case of a system with 5% structural damping, in Fig 3.14. The motions were each band-pass filtered using 512 point filter to obtain demand motions which were within the controllable range of the EQS. Considering the distinct frequency range between models, the actual input motions for each model will be presented separately in Chapter 4 and Chapter 6.

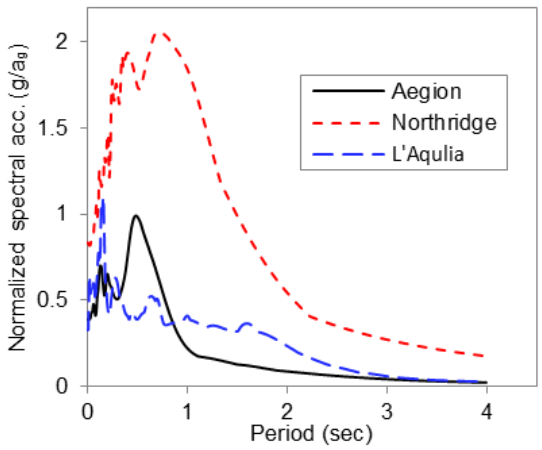

Fig 3.14 Normalised acceleration response spectra (ARS) of input motions, as recorded in the field

Table 3. 7. Sequence of input motions

Motion ID	Input motion	M_s
EQ1	Aegion,1995	6.2
EQ2	Northridge,1994	6.8
EQ3	Northridge,1994	6.8
EQ4	Northridge,1994	6.8
EQ5	L'Aquila,2005	6.3
EQ6	L'Aquila,2005	6.3
EQ7	L'Aquila,2005	6.3
EQ8	Aegion,1994	6.2

3.7 Centrifuge model layout

A total of 8 identical slopes at model scale were tested, with varied g level and motion frequency as indicated in Table 3.8. All of the centrifuge models were constructed as a uniform deposit at a relative density of I_D =55%-60%, and had a height of 0.24m (at model scale) from toe to crest, with a further 0.08m (at model scale) underneath. The slope angle was 27° (1:2), and it has been shown by Al-Defae et al. (2013) that a slope of similar angle was statically stable, yet with a low enough factor of safety (or yield acceleration) to maximise the magnitude of slip displacement during strong ground motion. The model configuration and instrumentation for a typical fallow case (at model scale) is shown in Fig 3.14. The test series was subdivided into three groups:

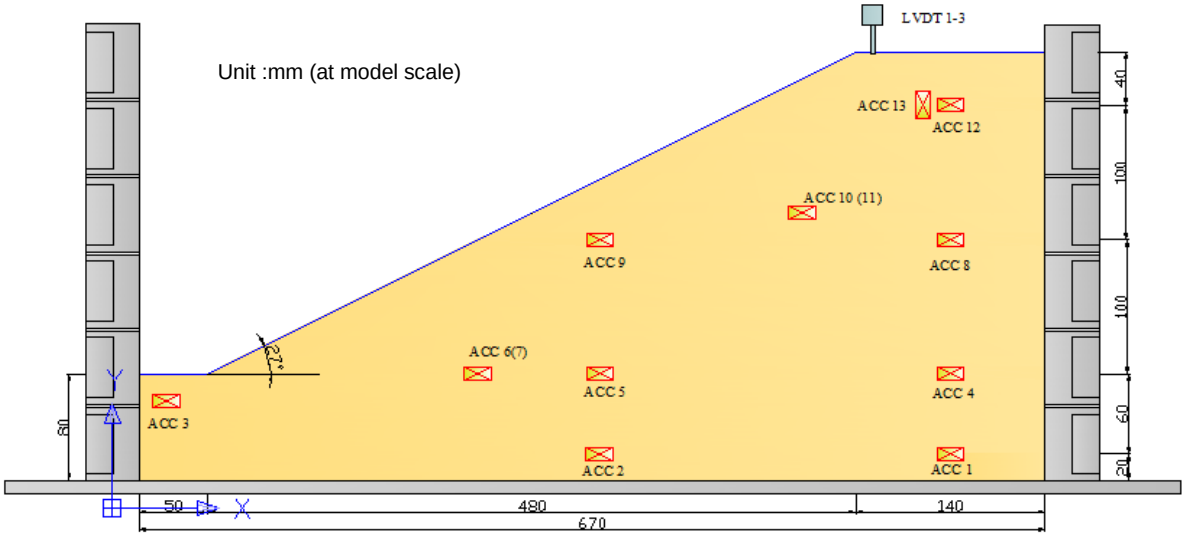

(a)

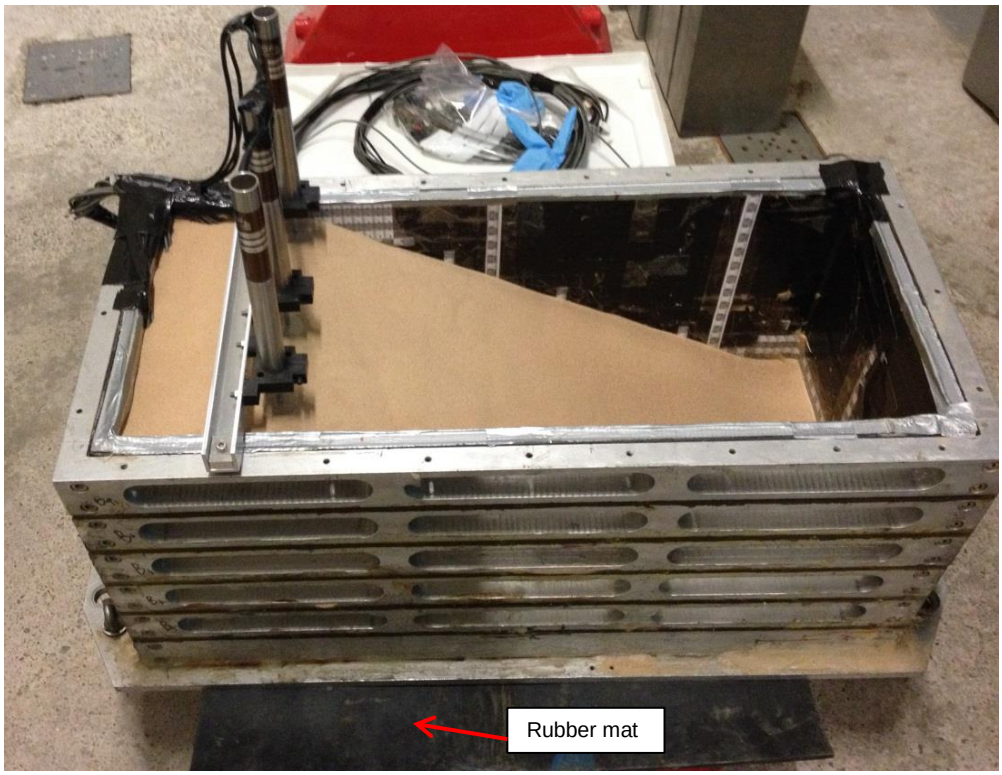

(b)

Fig 3.15 Centrifuge model layout and instrumentation (at model scale): (a) schematic; (b) photo before loading

Table 3. 8. Summary of Centrifuge models tested

Test identification number	Test scale	Slope height	Root type	root quantity	Motion frequency content(Hz)
TL01	1:10	2.4m	Fallow	0	4-30
TL02	1:10	2.4m	1:10 scale straight root group	4	4-30
TL03	1:10	2.4m	1:10 scale root cluster	4	4-30
TL 04	1:10	2.4m	Fallow	0	4-30
TL 05	1:30	7.2m	Fallow	0	1.33-10
TL 06	1:30	7.2m	1:30 scale root cluster	36	1.33-10
TL 07	1:10	2.4m	1:10 scale root cluster	4	4-30
TL 08	1:30	7.2m	Fallow	0	4-10

- Group 1- consisted of four fallow (non-reinforced) slopes, which were designed and performed as reference cases for rooted slopes. Additionally, comparisons between these tests could be used to reveal the influence of slope height and input motion frequency on seismic slope performance; further details will be presented in Chapter 6.
- Group 2- consisted of three 1:10 scale rooted slopes. Among them, model TL 03 was reinforced with a straight root group and designed to model plate / heart root systems, of which most of the individual roots behave independently. Further details of this model will be discussed in Chapter 4 and 5. Tests TL 02 and TL 07 were designed to model a tap root system. These tests will be discussed in Chapter 4.
- Group 3- consisted of one 1:30 scale rooted slope, which was designed to investigate the potential difference of root contribution on different sized slopes. Details of this model will be presented in Chapter 7.

3.8 Summary

In this chapter, the general programme for centrifuge modelling has been presented and characterised. This involved presenting the background of centrifuge modelling and describing the centrifuge machine, model materials, instruments and preparation procedures. However, detailed discussion of the modelling procedure for the tree roots are not shown here and will be discussed in detail in Chapters 4 and 5.

Chapter 4 Small scale modelling of plant root systems using 3-D printing

Contents of this chapter have been submitted as:

Liang, T., Knappett, J.A., Bengough, A.G.& Ke.Y.X, 201X. Small scale modelling of plant root systems using 3-D printing, with applications to centrifuge modelling of root-reinforced slopes. Canadian Geotechnical Journal, under review

4.1 Introduction

Geotechnical centrifuge modelling offers an opportunity to investigate in detail the engineering performance of vegetated slopes, but its application has been restricted due to the lack of availability of suitable root analogues that can replicate appropriate mechanical properties (stiffness and strength) and realistic 3-D geometry. This chapter aims at designing a repeatable 1:10 scaled 3-D tree root cluster model and investigating its behaviour within a slope subject to slip. A scaled model root cluster having a tap root system will be designed, and then fabricated in ABS plastic using 3-D printing to simulate the fibrous structure of root. The suitability of the model roots will be identified through performing axial tensile testing on straight rods fabricated using the same method. Large direct shear tests will then be conducted with these root models in fine sand to measure additional root cohesion and this data will be compared to Wu & Waldron model (WWM) and Fibre bundle model (FBM) predictions using the parameters from the mechanical tests. Finally, some example results using the model roots in centrifuge tests of slopes under earthquake loading as a way of inducing soil slip will be presented to demonstrate the potential impact of tree roots on slope performance.

4.2 Root modelling

4.2.1 Overview of modelling technique

The 3-D root models considered in this study were designed following the procedure demonstrated in Fig 4.1. The initial architecture was based on the tap root system of a white oak tree located at the Warnell School for Forestry and Natural Resources, University of Georgia (after Danjon et al. 2008). It should be noted that the check of ZRT before detailed modelling was conducted to ensure that the root models fitted within the centrifuge container or direct shear apparatus (DSA), and also within the build volume of the 3-D printer. The apparatus used in the later testing is shown in Fig 4.2 (DSA) and Fig 4.3 (centrifuge). The diameter of structural roots has tapered to less than 5 mm beyond the range of 0.5 m for most species (e.g. see Table 4.1), and these fine components cannot in any case be resolved within the 3-D printer (see below) and were therefore not modelled. XYZ coordinates were input manually into the Solidworks 2012 3-D computer-aided design (CAD) software and spline functions were employed to link these coordinates and generate each root segment. The output file (Fig 4.4) was directly input to the uPrint SE 3-D printer used (discussed in more detail below).

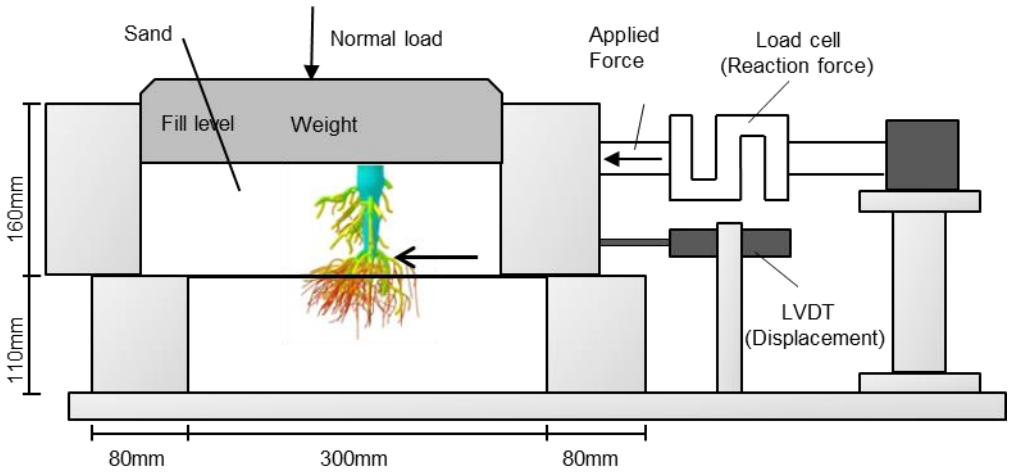

Fig 4.1 Schematic of large direct shear apparatus (DSA)

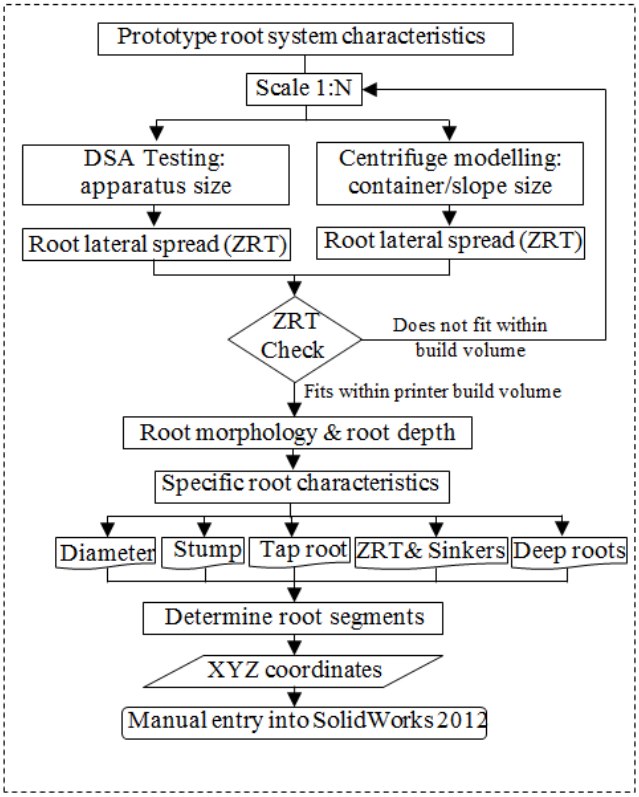

Fig 4.2 Design procedure for 3-D root model

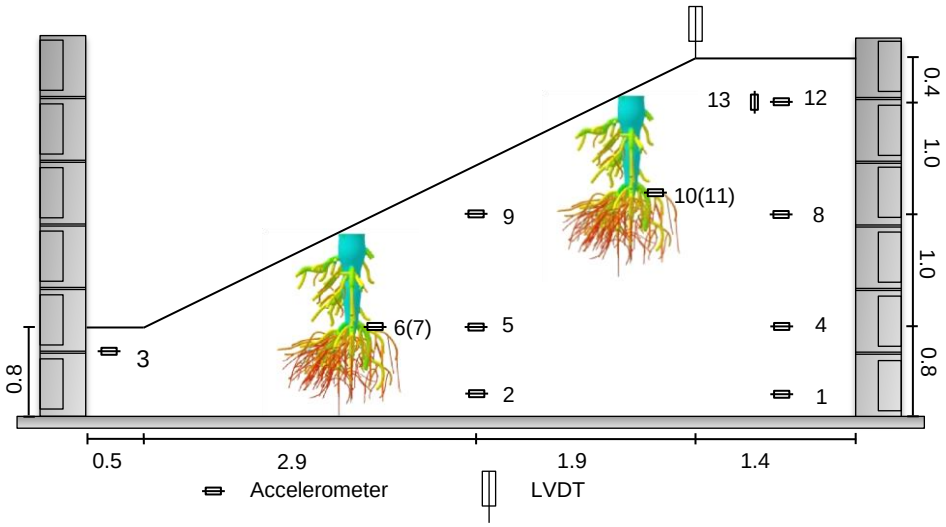

Fig 4.3 Schematic of centrifuge model geometry, instrumentation and position of root analogues (Dimensions at prototype scale in metres)

Table 4.1 Mean lateral structural root diameter estimates at different distances from tree trunk and the maximum lateral root spread at Ibadan, Nigeria (After Akinnifesi et al. 1999)

Species	Distance from tree trunk (cm)					
	10	50	100 (mm)	150	200	Mean maximum spread(m)
Albizia niopoides	19.3±1.7	3.4±1.3	-	-	-	0.6±0
Alchronea cordifolia	14.8±4.7	5.9±1.2	4.7±1.4	4.7±2.7	4.2±0	2.2±0.4
Dialium guineese	7.3±1.2	3.3±0.7	-	-	-	0.9±0.2
Enterolobium cyclocarpum	27.3±7.0	17.3±6.9	12.4±7.5	3.6±0.8	-	1.5±0.3
Grewia pubescens	10.2±1.8	4.5±0.9	3.3±0.6	3.2±0.6	1.6±0.2	2.5 ±0.7
Lonchocarpus sericeus	13.1±2.0	9.3±2.9	-	-	-	0.8±0.2
Milletia thonningii	7.2 ±0.8	4.8±0.6	2.3±0.8	1.5±0.1	-	1.6±0.3
Nauchlea latifolia	23.4±6.4	13.1±4.9	12.3±3.4	11.1±3.5	7.4±1.2	3.5±0.6
Pterocarpus erinaceus	11.8±2.1	-	-	-	-	0.4±0
Pterocarpus mildbraedii	5.1±0	-	-	-	0.1±0	0.1±0
Pterocarpus santalinoides	18.9±8.3	8.4±2.7	6.6±2.2	3.6±4.2	-	1.5±0.5
Tetrapleura tetraptera	13.2±4.7	10.2±0.9	8.1±4.2	-	-	1.0±0.1
Triplochotion scleroxylon	5.7±0.5	3.9±0.9	3.9±0.9	3.2±1.1	3.0±1.1	2.5±0.6

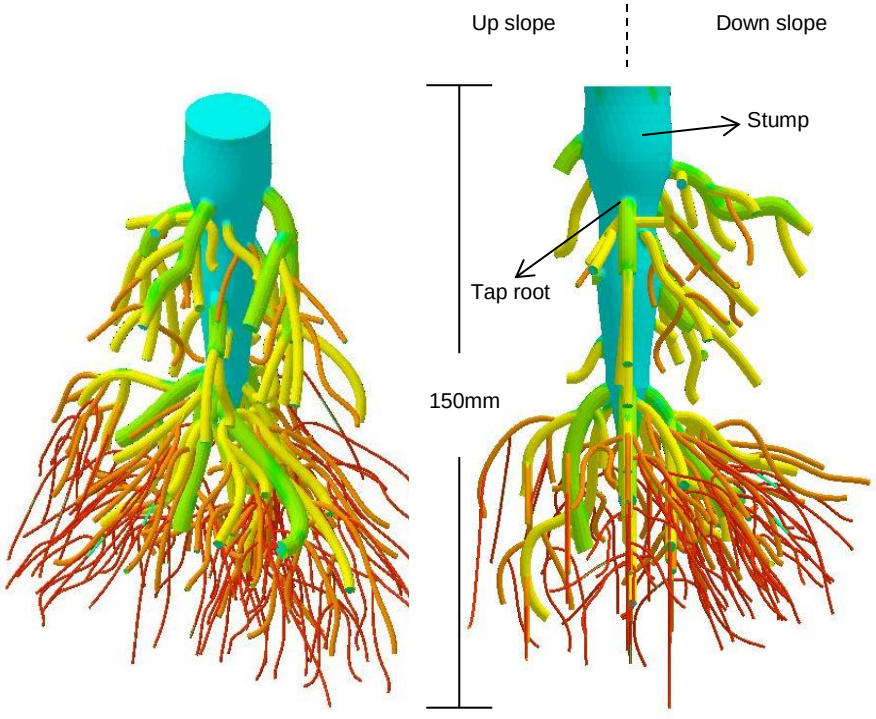

Fig 4.4 Model tree root cluster in SolidWorks; different root diameter classes are represented by different colours

A scale of 1:10 was ultimately decided upon as a suitable compromise given the competing effects of the size of the centrifuge container (see later), the need to maintain a suitably frequency-rich input earthquake motion (see later) and the minimisation of any root diameter – particle size scale effects. Typical scaling laws between model and equivalent prototype are shown in Table 3.1 (after Schofield 1981; Kutter 1995) – these relate to a model which is scaled purely geometrically, with model material properties (e.g. T_r, E) scaled 1:1. Because of the geometric scaling, the model will not be distorted in shape and so the root architecture was the same between model and prototype.

The reduced scale combined with the threshold dimension that could be resolved within the 3-D printer (0.75mm), meant that roots < 7.5 mm at prototype scale were not considered. However, roots with the diameter in the range of 5-7.5 mm at prototype scale were catalogued into the 7.5 mm range. The fine roots below this size are highly flexible and always break when subject to soil slippage (Stokes et al. 2009) as their area reduces more rapidly than the tensile strength increases as diameter reduces, meaning they have a lower force contribution at break. As a result, the effect of fine roots on slope stability could be investigated separately without considering them to be connected to the structural roots.

4.2.2 The stump

The stump, especially in older and mature trees, integrates various root segments to a coherent whole and plays a specific role in stability. Danjon & Reubens (2007) suggested defining the stump as the portion with a fixed depth of the first–order roots in trees. A value of 0.25 m was employed for real trees planted in slopes by (Danjon et al. 2008). The same value was used in this study at prototype scale. The tree component above the ground surface was simplified to be a circular rod. Following this criterion, the radial dimension of the stump was equal to Diameter at breast height (DBH) which was 23 mm at model scale (full details are presented in the following section).

4.2.3 Root diameter and length

All of the roots except the tap root were simplified to circular rods of uniform diameter along their length. The sectional dimension of these roots were grouped into four classes, as shown

in Table 4.2 (After Watson et al. 1995), with each class being represented by a single diameter which was approximately the mid-point in the class range. These diameters were selected as representative of each class to be similar to those used in previous studies (Sonnenberg *et al.* 2010; Duckett 2013) and use of only a few representative diameters also simplified the quantification of the mechanical properties. Considering that the shear zone thickness was approximately 20 mm in similar previous DSA tests (see Duckett 2013), if fine roots are held in tension principally (Stokes et al. 2009), roots over 20 mm in length will behave similarly and root length will have no significant effect on root contribution.

Tap roots are very common across species and they have been observed in up to 75% of tropical trees (Klinge 1973) and in 73% of Mediterranean woody species (Canadell et al. 1996). In Khuder et al. (2007), the largest vertical root was classified as the tap root. Typical tap root penetrations are within a range of 0.5 to 1.4 m based on limited literature (Eis 1974 ; Systems & Agrzcultl 1992; Crook & Ennos 1999 ; Danjon et al. 2008). A series of taproot morphologies were recorded by Danjon & Reubens (2007), based on twenty-two 12-year old *P.pinaster*. These patterns can be regarded as a taper varying with root inclination and branching rate. The pattern of taper will affect the bending moment capacity of the tap root (Goodman 2001). A tap root penetration depth of 1.0 m at prototype scale was selected here. A taper pattern, the diameter of which was 0.12 m (prototype) at the midpoint was selected.

Table 4. 2 Root diameter class for medium and structural roots (not including tap root)

Diameter range at prototype scale (mm)	Root class at prototype scale (after Watson et al. 1995)	Diameter at model scale (mm)	Number of roots
<5	fine	-	-
5-10	small	0.8	109
10-20	medium	1.6	81
20-40	large	3	43
>40	coarse	5	13

The ZRT was determined as a function of DBH, following the procedure introduced by Danjon & Reubens (2007a). In Danjon et al. (2005), the radius of ZRT was set to be 2.2 times DBH. This ZRT can be approximately achieved within the threshold of 50 mm for the model scale DBH of 23 mm (ZRT = 2.17 × DBH).

4.2.4 Upslope /downslope distribution

Trees on slopes tend to develop a specific asymmetrical architecture in the root system compared with trees growing in level ground. Various factors, that may be related to the growth of root, e.g. soil strength (Kirby & Bengough 2002), slope angle (Abdi 2014), vegetation layout (Fan & Lai 2014) and static loading (Chiatante et al. 2003; Genet et al. 2008), have been reported. It is generally believed that roots growing upslope develop to a greater extent than roots growing downslope (see Nicoll et al. 2005; Di Iorio et al. 2005; Sun et al. 2008; Danjon et al. 2013) despite some exceptions (e.g. McIvor et al. 2007; Sonnenberg et al. 2011; Ji et al. 2012). This phenomenon appears related to the orientation of the aerial part of the plant which may be vertical or perpendicular to the slope surface (Saez et al. 2014). More roots develop and thicken in the up-down direction of the slope in response to the turning moment induced by the combination of the inclination and the weight of the stem interacting with the root morphology of a particular species (Danjon et al. 2013). Apart from the inclination and weight of the stem, wind also contributes to the development of root morphology on the slope (Danjon & Reubens 2008). However, wind effects are highly site-dependent and will not be considered further in this thesis. The asymmetrical architecture in the root system at the shallow depth was here modelled by reducing the ZRT and number of sinkers on one side in the model (see Fig 4.4). During the laboratory testing, the model roots were tested with the most heavily rooted side towards the downslope direction (e.g. as illustrated for a tree with a vertical trunk in Saez et al. 2014).

4.2.5 Fabrication

3-D printing techniques (also known as ‘rapid prototyping’ and ‘stereo-lithography’) (Cima et al. 1995) were used to fabricate the model roots using a Stratesys Inc. uPrint SE Acrylonitrile Butadiene Styrene (ABS) prototyper at the University of Dundee. This machine takes a continuous spool of plastic which is melted and injected into place, a process known as fused deposition modelling. In this way, the machine may be thought of as a 3-D inkjet printer that uses molten plastic rather than ink. The machine is computer numerically controlled (CNC) and once given an input file containing the 3-D geometry (exported directly from the 3-D CAD model), will operate entirely automatically. This is useful as the root models described

herein took approximately 22 hours to fabricate. Given the complex geometry of the model, the rapid prototyper automatically generated a scaffold (Fig 4.5) of a contrast material to support the model roots as they hardened. The scaffold material was subsequently dissolved in a bath of caustic soda.

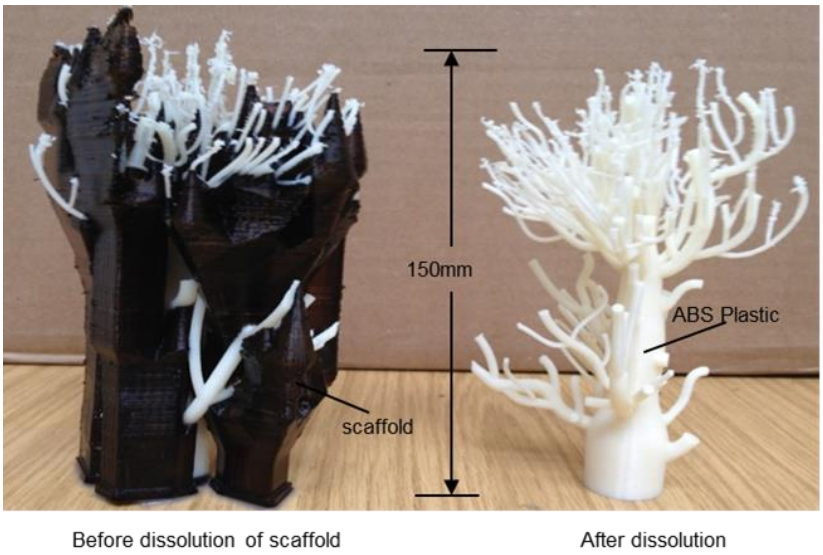

Fig 4.5 ABS plastic root model from 3-D printer showing the temporary support scaffold (left) during printing, and the final model (right), after this has been dissolved

Multiple 2-D maps showing where roots intersect potential slip planes at different prototype scale depths (Fig 4.7) provide an overview of the spatial structure of root reinforcement. Planes at shallow depth showed intersections with the main tap root; above the depth of 100 mm, despite the low number of roots (Fig 4.6a) the root cross sectional area (CSA) is high (Fig 4.6b) for this reason. Deeper planes demonstrated abundant medium and fine roots, but the corresponding CSA is relatively low. Root CSA is directly related to RAR and root biomass, which indicates that the major part of the root model is still concentrated in the upper layers of soil.

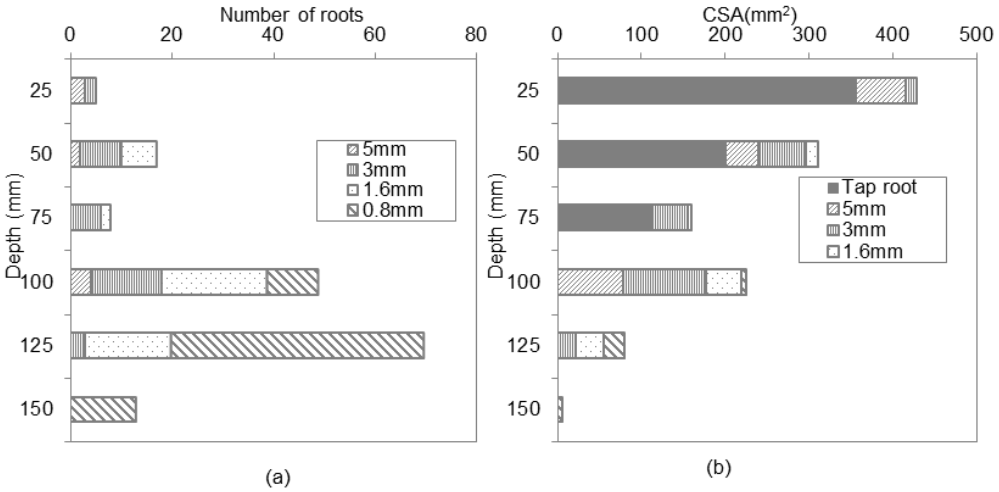

Fig 4.6 Vertical distribution of model roots: (a) number of roots; (b) root cross sectional area (CSA)

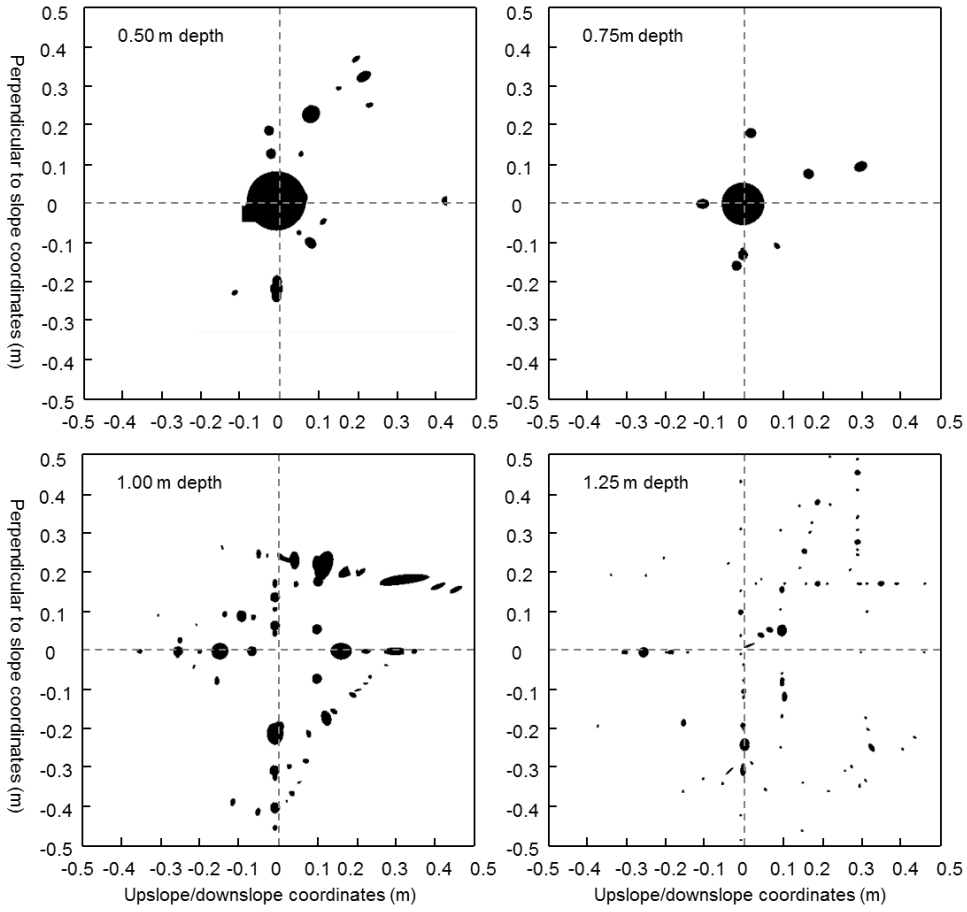

Fig 4.7 Multiple 2D distribution of roots intersecting four planes at different soil depth for 3D root model at prototype scale (downslope positive).

4.3 Testing

4.3.1 Material testing of individual roots

The root mechanical properties (stiffness and strength) were characterised by performing axial tensile tests in an Instron 4204 loading frame. Straight root samples were required for these tests and were fabricated using the same method described above but with much simple geometry (Fig 4.8 a). All the test roots were 200 mm long, but with varied diameter (0.8 mm–16 mm).

The ultimate tensile strength (UTS) of a root, T_r is calculated as a measure of the force F in tensile testing required to induce failure of the root divided by its cross–sectional area a_r:

$$T_r = \frac{F}{a_r} \qquad \textbf{Eq 4. 1}$$

Young's modulus was determined as the slope of stress–strain curve within the elastic deformation region.

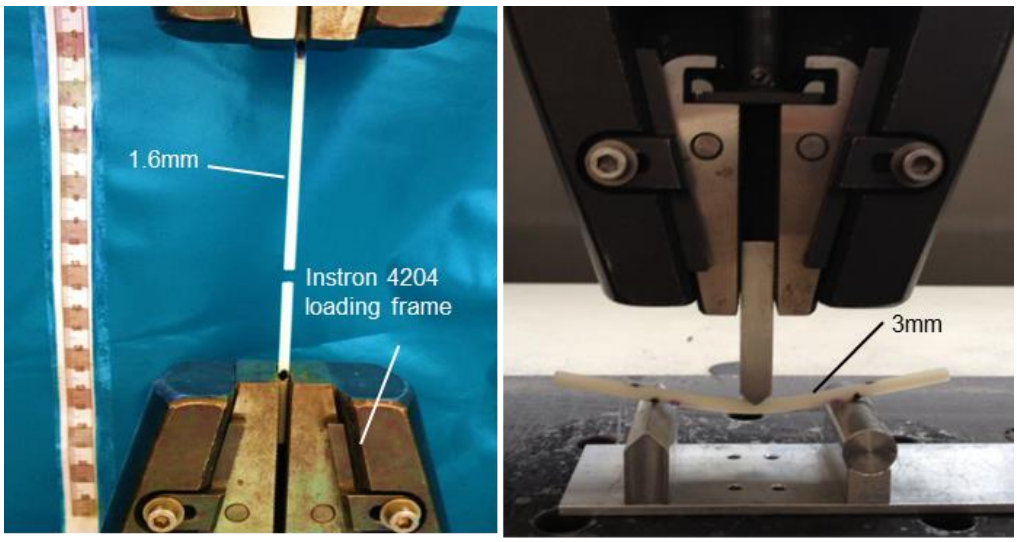

Fig 4.8 Element testing on printed ABS plastic straight root samples: a) Axial tensile tests; b) Three point bending tests

4.3.2 1-g large shear test with additional confining stress

Direct shear tests on the buried root model with a free soil surface have previously been conducted using a modified conventional DSA at the James Hutton Institute, Invergowrie, Dundee. Further details about this series of tests can be found in Liang et al. (2014) (see Appendix B) and will not be discussed further in this Chapter. This Chapter reports further tests in a larger purpose-built DSA that were conducted at the University of Dundee (Fig 4.2). Compared with a conventional DSA mentioned above, this apparatus has three main advantages:

a) A larger maximum shear displacement can be achieved (75 mm, compared to 20 mm), so that soil containing ductile root analogues could be sufficiently deformed to mobilise the full capacity of the rooted soil and break the roots, if required;

b) The top half of the shear box has a depth of 160 mm, which allows the shear plane to be located at different depths along the 150 mm deep model by varying the amount of fill in the upper half and applying a suitable surcharge;

c) The cross section of the DSA is large compared with the ZRT of the model root clusters to model low RAR conditions, and is similar in total area to the slope face in the subsequent centrifuge tests.

The model root cluster was suspended within the centre of the DSA from thin wire attached on the boundary of DSA. Dry HST95 Congleton silica sand was then pluviated in air around the model roots to a uniform relative density of I_D = 55%-60%. The basic properties of this sand are shown in Chapter 3. Varied confining stress at the shear plane was obtained by changing the weights applied on the top of the sample to be able to represent the full range of stress levels expected at different depths around the roots in the centrifuge tests.

4.3.3 10-g centrifuge modelling

Three models, referred to herein as TL03, TL04 and TL07 are presented in this chapter. The model slope TL07 included the 3-D model root analogues (Fig 4.3) while model TL03 was

reinforced with straight roots having the same RAR and spatial distribution at the level of the middle of the 3-D root cluster to investigate the root morphology effect. Further detail about the design of model TL03 can be found in chapter 5. Model TL04 was a fallow reference case for the two rooted models. A dry soil model was selected to eliminate hydrological effects (specifically any liquefaction) to focus on the pure mechanical reinforcement effect. Full details of the model preparation, instrumentation and input motions can be found in Chapter 3.

4.4 Results and Discussion

4.4.1 Root mechanical properties

The tensile strength of model roots demonstrated a negative power-law relationship when plotted against root diameter, which conforms with typical relationships for real roots. The tensile strength, T_r *(*MPa*)* , and Young's modulus, *E (*GPa*)*, as a measurement of the root diameter at the point of rupture, *D*, were found to be:

$$T_r = 57.886D^{-0.523} \quad \textbf{Eq 4. 2}$$

$$E = 3.24D^{-0.55} \quad \textbf{Eq 4. 3}$$

Further detail about such relationship is illustrated in chapter 5. Plotting these values for various root diameters on a material selection chart (Fig 4.9) shows that printed analogues fall within the range of real roots collected from the literature (Mora et al., 2009; Warren, 2009; Mickovski et al., 2009; Mao et al., 2012) and that they are superior to wood and rubber root analogues used previously (results from Duckett (2013) are shown in Fig 4.9).

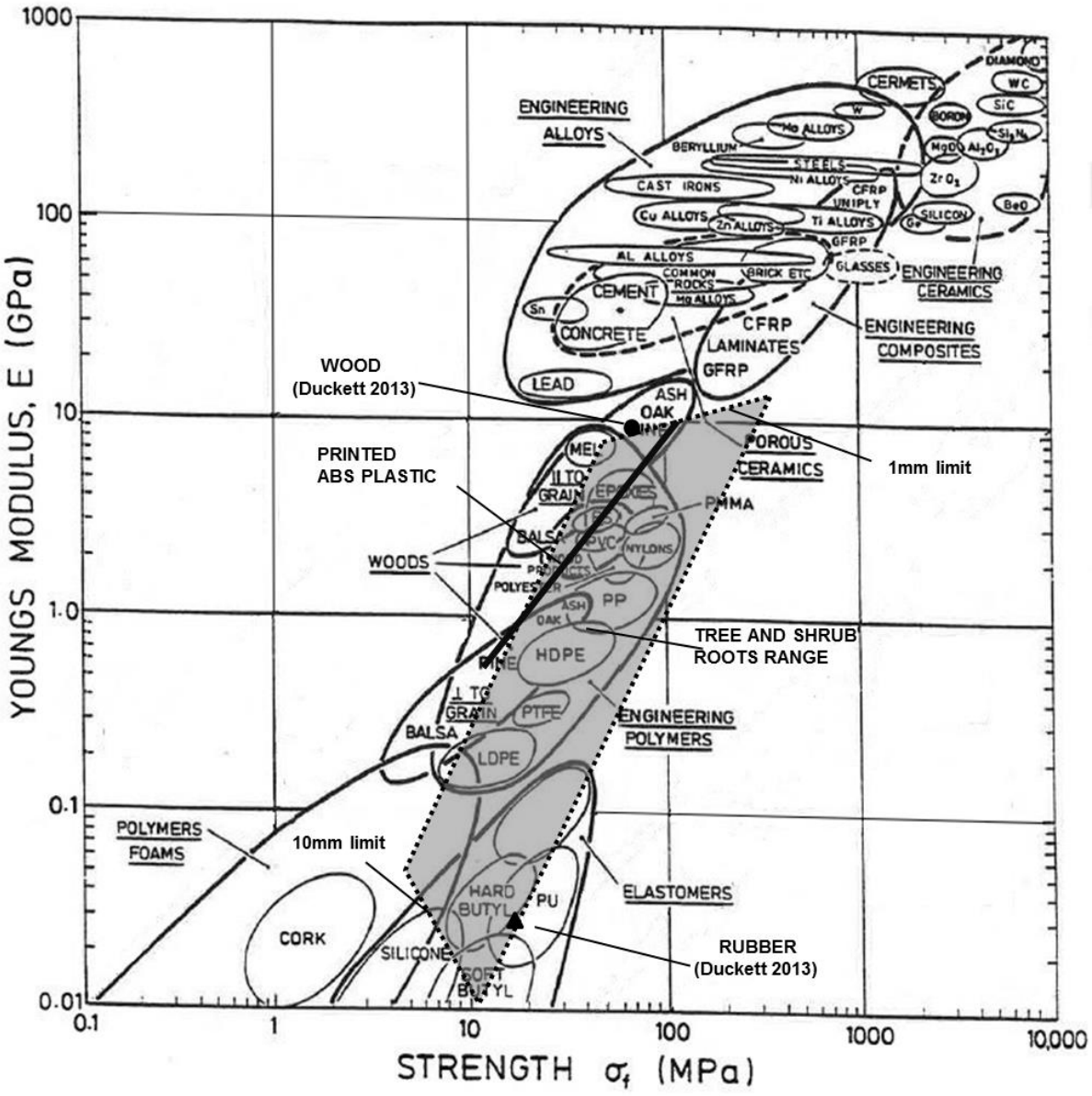

Fig 4.9 Comparison of material properties between trees roots and root analogues based on material selection chart

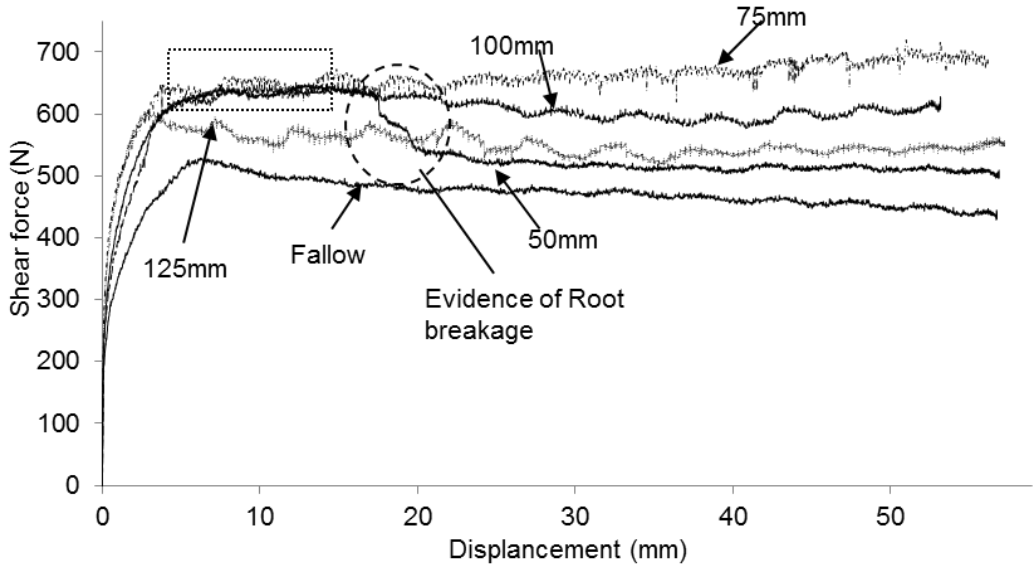

Fig 4.10 Results of large DSA tests on 3D root cluster reinforced soil with constant confining stress along different potential slip planes

4.4.2 Direct shear tests: RAR effects within tap root system

To investigate the RAR effect of the tap root system, the confining stress at the shear plane was kept constant at 8 kPa (geostatic stress at a shear plane depth of 0.5 m in the centrifuge prototype slope). This is important to keep the dilative component of the soil shear strength at the shear plane the same for comparison (low confining stresses result in excessive amounts of dilation – Bolton, 1986). However, the shear plane was made to pass through the root models at different depths (50 mm, 75 mm, 100 mm and 125 mm) so that the RAR could be varied (3.99%, 2.03%, 2.86%, 1.03% respectively), as shown in Fig 4.10. Here RAR was defined using the following equation,

$$RAR = A_r / A \qquad \textbf{Eq 4. 4}$$

where, A_r is the total root cross sectional area and A is the area of CRZ (CRZ and ZRT is the same for model root cluster) rather than the total cross sectional area of the DSA. This was selected based on the observation of numerical studies presented in chapter 5: that is, roots influenced the slope performance in a certain area, but beyond this area the root influence is limited.

The resulting shear resistance of rooted and fallow soil is plotted against shear displacement in Fig 4.10. As demonstrated, with different RAR, the additional shearing force was very similar when the shear plane was at the depth of 50 mm, 75 mm or 100 mm. Given RAR varied significantly for these three planes, 3.99%, 2.03% and 2.86% respectively, the additional shear force should be quite different according to the general understanding. The main difference of these three cases to the 125 mm case was that the tap root crossed the shear plane in the former, but not in the latter. This indicated that the presence of the tap root was very important in mobilizing the whole 3-D root system to resist shear loading. This would be of great interest for engineering application, especially as a guide to the planting approach for improving slope stability in terms of the importance of selecting a type of vegetation that has a deep taproot, but has not been reported previously. The reason for this may lie with the difficulties in generating an identical tap root system for comparison and the general non-repeatability of shear testing on samples *in-situ*. The ability to produce repeatable model root systems (yet of realistically complex 3-D geometry) is therefore a significant benefit of the 3-D printing approach described in this paper to future studies on root-soil interaction.

In general, roots below the tap root broke in quantity (Fig 4.11) when the root cluster was subject to moving soil; however, whether the tap root broke or not varied with the test conditions and could be classified into two types of failure.

Type 1 tests were those in which the root cluster broke at the fork of the tap root (e.g. the 50 mm case). For this test, the lower part disconnected from the upper component and contributed no more to the additional shear resistance. Following the disconnection (at ~17 mm displacement, see Fig 4.10), the shear resistance decreased rapidly, but there was still some remaining resistance compared with the fallow case. It is interesting to note that this lower resistance after tap root breakage is approximately the same as in the 125 mm case where the tap root does not cross the shear plane.

Type 2 tests were those in which the whole structure continued to work, despite some root breakage of individual deep roots. This is also evident in the resistance-displacement curve (compare the 75 mm and 50 mm cases in Fig 4.10 – both initially have the same resistance, but the 75 mm case retains this throughout the test, even with the substantial root breakage

(Fig 4.11)). The load displacement data also suggested that deep roots were mobilized and destroyed in sequence rather than simultaneous (see the sudden drops on the 75 mm curve, Fig 4.10).

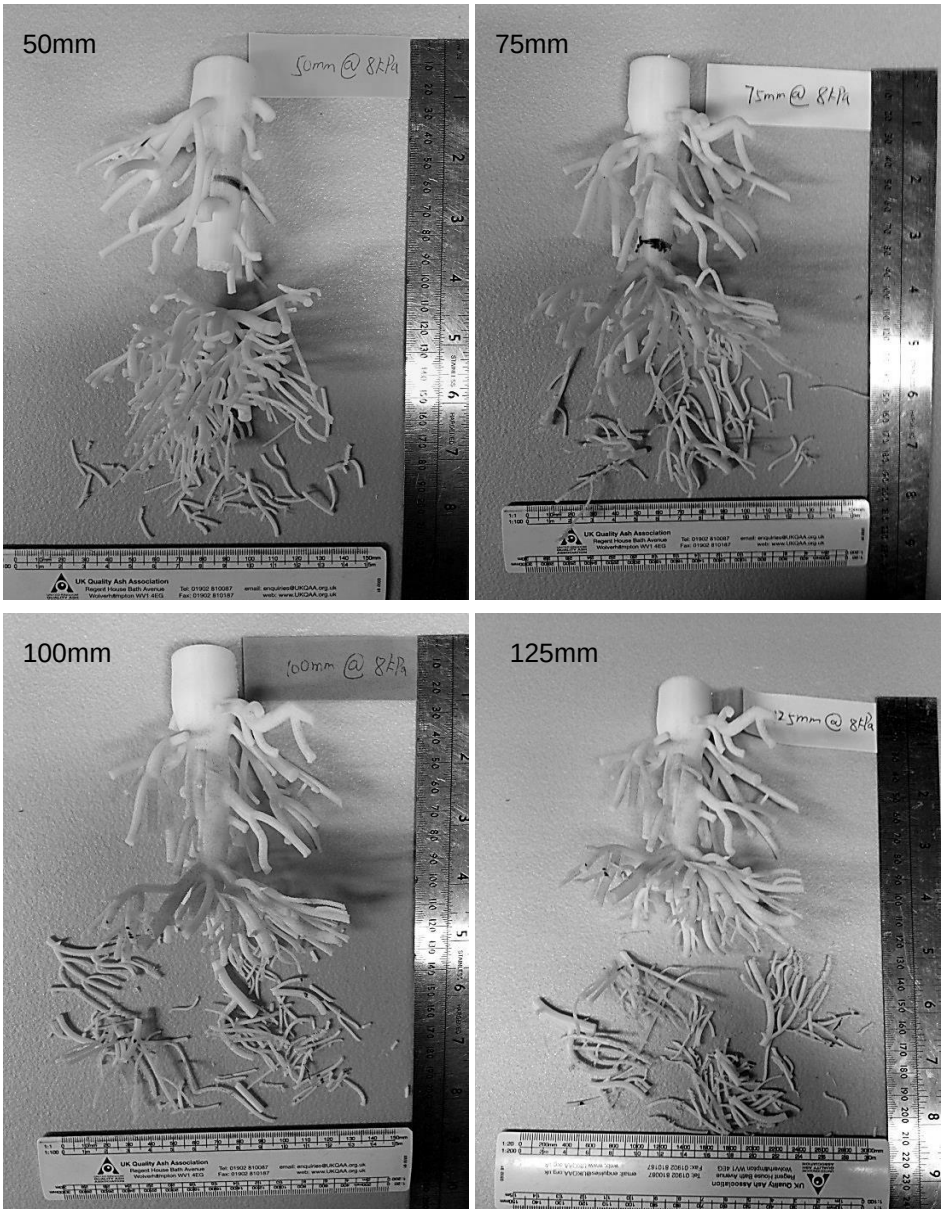

Fig 4.11 Breakage of root clusters under constant confining stress following careful post-test exhumation

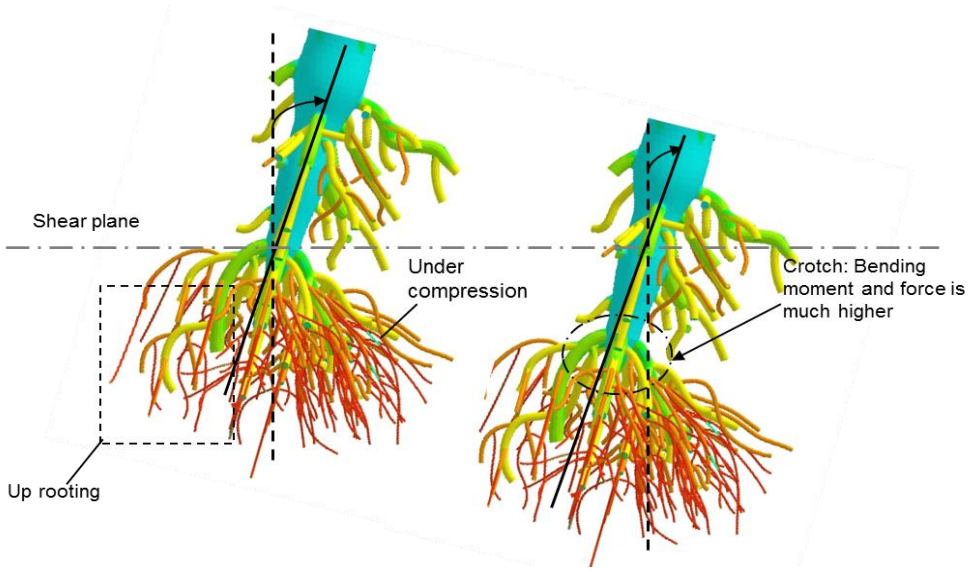

Fig 4.12 Comparison of inferred root behaviour as a function of slip plane depth

The distinct difference between type 1 and type 2 can be related to the position of shear plane, as shown in Fig 4.12. As the upper part of the root cluster rotated against the moving soil, the tap root acted mechanically as a lever-arm. Commonly, 'lever–arm' structural roots failed at a point where they branch (Tobin et al. 2007), as shown in type 1 test. The fulcrum of the lever depended on the depth of the shear plane. As the shear displacement of the top soil was fixed, the shallower of shear plane, the higher the bending moment transferred to the point of branch.

4.4.3 Direct shear tests: Root morphology effect

In the preceding section it was indicated that the additional root contribution to shear resistance was principally associated with the presence (or not) of the tap root. To better understand the effect of the 3-D geometry compared to straight root assumptions typically made in prediction models, further large DSA tests with a simpler group of straight root analogues at the same confining stress (8 kPa) were conducted. The straight analogues were 150 mm in length and were installed to provide the same RAR and spatial distribution of roots of different diameter on the shear plane as the 3-D root cluster at the different depths (50 mm, 75 mm, 100 mm and 125 mm). The shear plane was made to pass through the same depth with 3-D Root cluster. The resulting shear resistance of rooted and fallow soil is plotted against shear displacement in Fig 4.13.

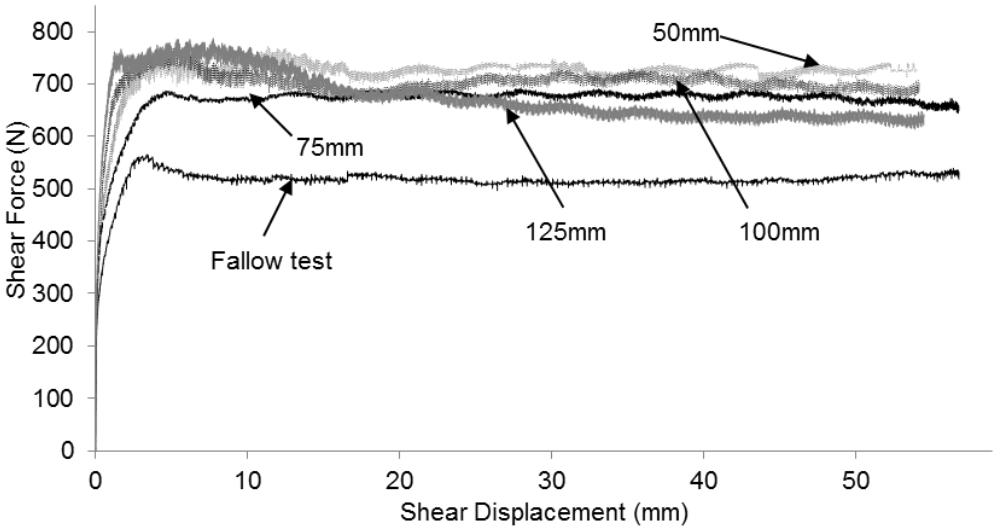

Fig 4.13 Results of large DSA tests on straight roots reinforced soil with constant confining stress along different potential slip planes

A comparison of the root cohesion between the 3D root cluster and straight root analogues is shown in Fig 4.14. Root cohesion c_r' was determined by dividing the additional shear resistance force by the area of the CRZ of 3D root cluster (which is 50 mm in diameter) such that the values can be fairly compared. The variation of c_r' with depth for the straight analogues is, unsurprisingly, highly similar in shape to the root CSA distribution (Fig 4.6b). The effect of the interconnection of roots in the 3-D cluster, however, can be seen to 'smooth-out' the zone of low CSA around the 75 mm depth shear plane, due to the ability to transfer load between roots in the 3-D case. Fig 4.14 also shows that c_r' of the 3-D root cluster is consistently lower than that of straight analogues. This is not unexpected as the individual roots of the straight analogue group had higher anchorage length (each root was of identical length). The observations made in this section suggest that it may not be suitable to apply theories based on straight vertical rods (such as the WWM and FBM) directly to tap root systems of trees.

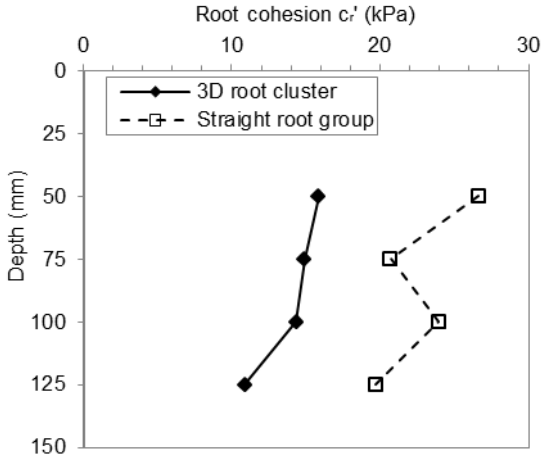

Fig 4.14 Comparison of 3-D root cluster and equivalent straight root shear tests, constant confining stress at slip plane (8 kPa)

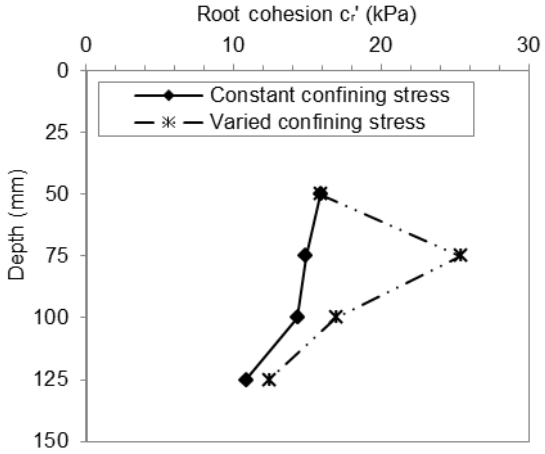

Fig 4.15 Effect of confining normal stress at slip plane on measured root cohesion

4.4.4 Direct shear tests: Confining stress effect

In this section, DSA tests with varied confining stress at the shear plane are presented. As in the previous sections, the position of the shear plane was varied, but the confining stress was also varied to match the centrifuge stress levels at the prototype depths of 0.5m, 0.75m, 1.0m and 1.25m. These tests therefore simulate the conditions on various potential translational shear plane locations in test TL07. The results are compared to the earlier tests with the same RAR but constant confining stress at all depths (8 kPa) in Fig 4.15. There was an initial

positive correlation between c_r' and the slip plane normal stress within the soil from 50 mm to 75 mm. This was consistent with the behaviour of straight root analogue group reported by Duckett (2013) . However, as the shear plane moves closer to the bottom of the root cluster and the anchorage length reduces, c_r' reduces. In fact, Fig 4.15 suggests that for this geometry of roots, confining stress is perhaps the more significant controlling parameter down to half the rooting depth, but that it is RAR that is the principal control as the anchorage length reduces.

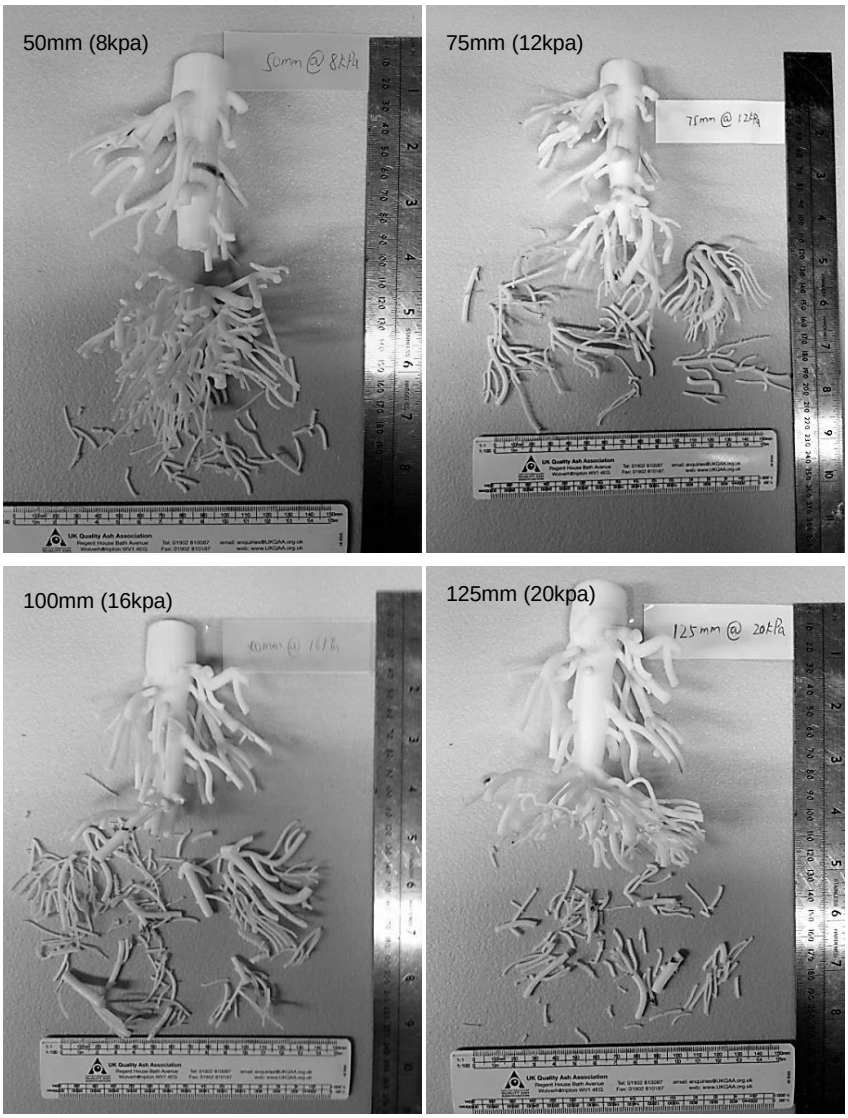

Fig 4.16 Breakage of root clusters under varied confining stress following careful post-test exhumation

These observations would again suggest that current c_r' prediction models which assume the root cohesion is independent of soil type may not provide suitable predictions of root contribution to soil strength. Fig 4.16 shows the breakage of roots during the varied confining stress test series following careful post-test exhumation. Compared with Fig 4.11, more roots broke at the higher confining stresses. This was not surprising as the frictional restraint between root and soil will be higher and hence it is much more likely that the roots will break, rather than pulling out.

4.4.5 Global performance of rooted slope in 10g centrifuge modelling

The key indicator of slope performance considered herein is the crest settlement (proportional to permanent slip) and the acceleration response spectra at the crest. A comparison of the crest settlement between the three slope models is shown in Fig 4.17. The interesting aspects of behaviour were as follows:

a) For both root reinforced slopes and the unreinforced slope, a decreasing trend of settlement was observed when the slope was subjected to successive identical motions (e.g. aftershocks). This can be associated with slope geometry change (re-grading), as previously reported for fallow and pile reinforced slopes by Al-Defae et al. (2013) and Al-Defae & Knappett (2014), respectively.
b) The presence of root analogues results in a significant reduction (by 61% and 85%, for straight roots and 3-D root cluster, respectively) in permanent slope movement compared with the fallow case, especially in the first two motions (EQ1 and EQ2). This can be interpreted as the rapid mobilization of root-soil interaction due to the initial soil slip under dynamic loading.
c) After the first two motions, relatively smaller reductions in permanent settlement (in total 14% and 27%, for straight roots and 3-D root cluster, respectively) were observed, which indicates that the additional restive force of the root is largely constant after the initial mobilization.
d) No roots were observed to have broken following careful post-test exhumation, which would infer that the maximum root-soil resistance was mobilised after EQ2 and that this was either associated with (i) yielding of the soil around the root analogues, or (ii) the strengthening effect of the roots forcing the slip plane deeper within the slope.

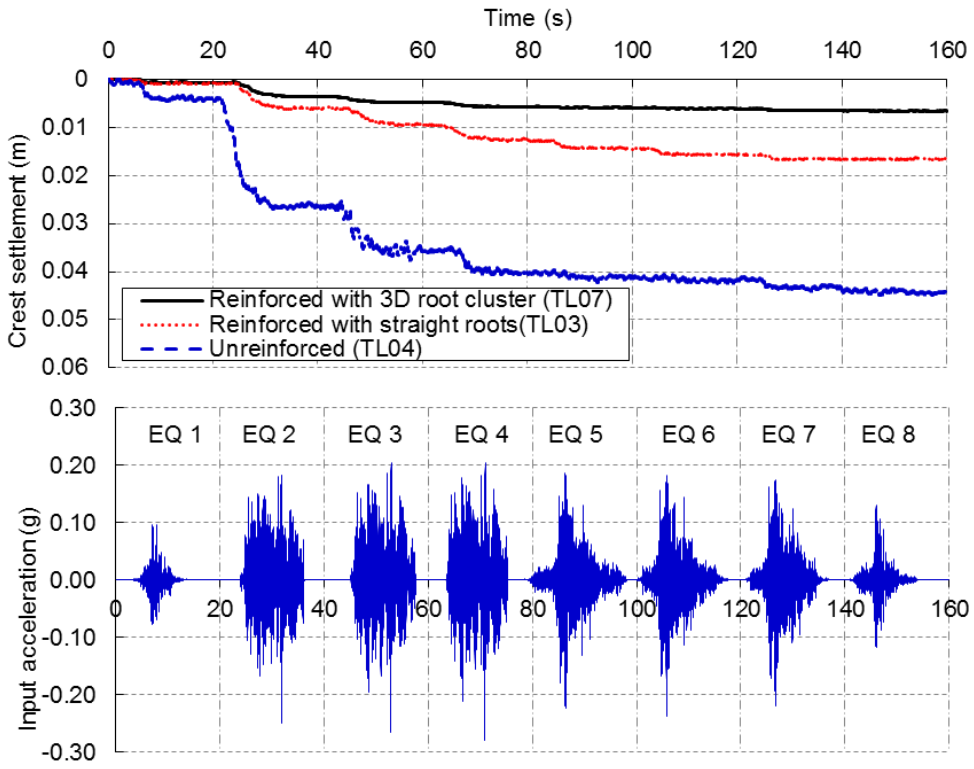

Fig 4.17 Comparison of permanent crest settlement of fallow and root-reinforced slopes from centrifuge testing

Fig 4.18 (a) shows a comparison of acceleration response spectra (ARS) measured at the crest of the slope (instrument 12) between the slope containing the 3-D root clusters and the fallow slope. ARS was normalized by the peak acceleration of the input motion and determined for the case of nominal 5% damping. The ARS for the root-reinforced slope was similar to that of the fallow slope and no significant reductions due to the root presence were observed in any of the three distinct motions. The ARS of EQ1 for the rooted slope was even slightly higher than that of the fallow slope over a limited range of periods. This indicates that the presence of the roots had a very limited influence on the general propagation and amplification of earthquake motion from the toe of the slope to the crest of the slope, in contrast to the very significant effect they had on slip displacements (Fig 4.17). Some reductions in ARS magnitude were observed in the near-field of the root analogues, as shown in Fig 4.18 (b), which may have had some effect in reducing settlement at the slope crest. The difference of ARS measured at instrument 11 and instrument 12 suggests that roots can only influence the slope's dynamic cyclic performance over a very limited area close to the roots (i.e. the ZRT).

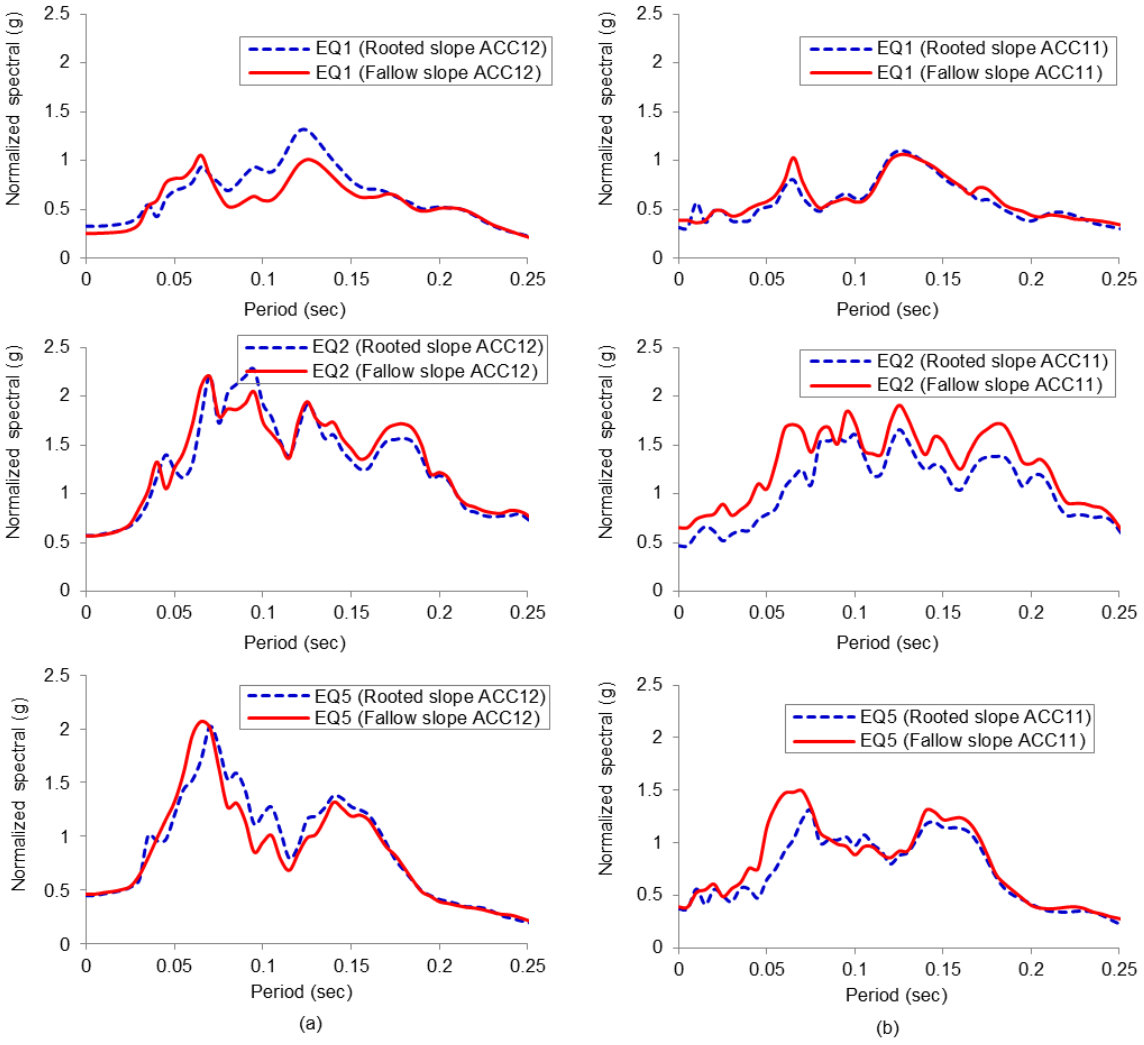

Fig 4.18 Normalized acceleration response spectra (ARS) of three distinct motions between rooted slope (TL07 – 3-D clusters) and fallow slope: (a) at the crest of the slope; (b) at the location of a root analogue.

4.4.6 Root morphology effect observed in centrifuge modelling

Fig 4.17 also shows that the slope reinforced by 3-D root cluster provides a similar reduction in slope movement compared to the straight root case. However, the root cohesion c_r' of the straight root case was much higher for the same confining stress, shear plane location and RAR from the DSA tests (see Fig 4.14). It may therefore not be suitable to relate the reduction of permanent settlement (i.e. the reinforcing effect) solely to a change in c_r'. Given, also the observation of no root breakage in either rooted test, it may be true that in both cases,

the $c_r^{'}$ is high enough to force the slip plane into a new (similarly deeper) position, and that this is both the reason for the similarity in settlements between TL07 and TL03 and the mechanism by which the roots reinforce the slope. The ARS was also determined (see Fig 4.19) and there was no considerable difference between 3-D and straight root cases in the near-field of the root analogues, with the exception of EQ5.

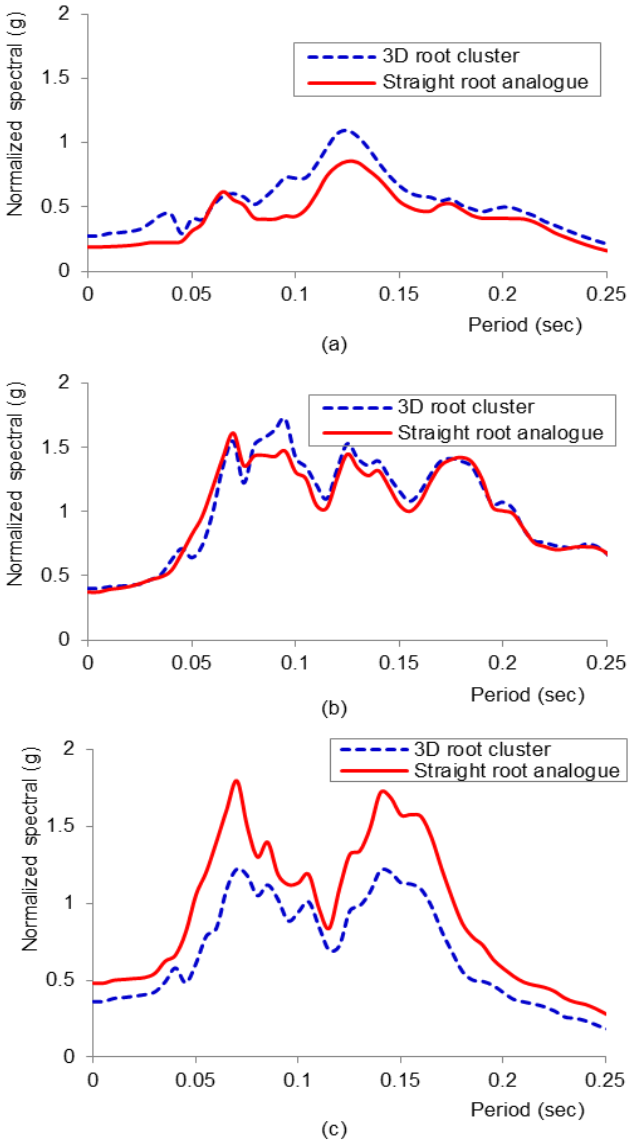

Fig 4.19 Comparison of normalized acceleration response spectra (ARS) of three distinct motions at the location of the root analogue (ACC11) between slopes reinforced with 3-D root clusters and straight root groups: (a) EQ1; (b)EQ2; (c)EQ5.

4.5 Implications for use of existing 'straight root' models

The additional shear resistance provided by the roots was estimated using the WWM and FBM using the tensile strength relationship given by Eq 4.2. In the FBM all three assumptions of breaking order were considered as defined by Eq 2.24-Eq 2.26. When the load was apportioned by root CSA, the maximum contribution to root cohesion was provided by the largest root (5 mm). While the maximum contribution was provided by the finest root (0.8 mm) when the load was distributed by root diameter and root number. The calculated additional root cohesion c_r' from the WWM and FBM compared with those measured from the large DSA tests considering the shear plane at different depth (with change of confining stress) is shown in Fig 4.20. The root cohesion c_r' for the straight root case with varying confining stress was not measured directly in the DSA but was calculated using the validated Beam-on-non-linear-Winkler-foundation (BNWF) model presented in Chapter 5. This calculated distribution used within a continuum finite element model was shown to be consistent with the centrifuge test results of TL03. It should be noted here this should be higher than that of 3-D root cluster case as mentioned above.

The shear displacement at failure and size of the related shear zone used in the WWM and FBM calculations are shown in Table 4.3. The tap root with a diameter > 10 mm was not included in the calculation of c_r' in consideration of their bending behaviour during soil slip (Genet et al. 2008; Stokes et al. 2009). Despite ignoring the anchoring mechanism of the tap root, WWM and FBM still over-estimated the contribution of root. This significant overestimation may come from the following aspects:

Table 4.3. WWM and FBM parameters

Prototype shear plane depth	Confining stress (kPa)	Peak displacement x (mm)	Shear zone thickness z (mm)	Shear distortion angle θ(°)	Soil effective friction angle ϕ'(°)	Root orientation factor R_f
0.50 m	8	7.3	20	20	32	0.93
0.75 m	12	7.7	20	21	32	0.94
1.00 m	16	4.4	20	18	32	0.83
1.25 m	20	2.9	20	8	32	0.76

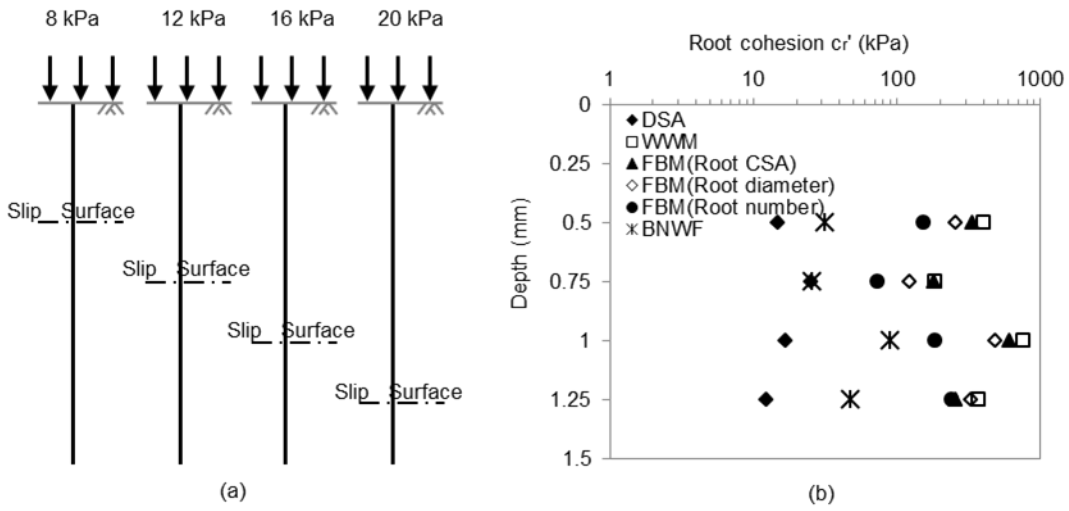

Fig 4.20 Comparison of the measured and predicted root cohesion: (a) position of assumed slip surface; (b) variation of root cohesion with depth

a) Many of the roots in the 3-D cluster were not distributed perpendicular to the shear plane; though this cannot be the principle reason as the models also overestimated the straight root values;
b) During tests, only some of the roots were observed to break and these roots varied in diameter. This indicated that the rupture of roots would not be simultaneous or rigorously progressive in the order from weakest to strongest, which was inconsistent with the assumptions of WWM and FBM. In actuality, most of the roots were not mobilised to their ultimate tensile strength, with many having suffered pull-out at lower load, or behaving principally in bending;

Fig 4.20 also shows that c_r' calculated by the WWM was generally higher than that calculated by the FBM. This has been previously been illustrated and discussed by a body of literature (Pollen & Simon 2005; Hales et al. 2009; Bischetti et al. 2009;Mickovski et al. 2009; Loades et al. 2010;Mao et al. 2012). The calculated c_r' demonstrated a uniform ordinal relation above the depth of 100mm, that is, c_r' (FBM, root number) < c_r' (FBM, root diameter) < c_r' (FBM, CSA) < c_r' (WWM). This relation was in agreement with the one presented by Mao et al. (2012).

4.6 Conclusions

A tree root cluster model that can be used in centrifuge model tests to more realistically model the geometry, spatial distribution and mechanical properties of tree roots was designed and fabricated from ABS plastic using the 3-D printing technique, and subsequently used to investigate the seismic behaviour of rooted slopes. A series of element tests in a large direct shear apparatus were also conducted to investigate the root traits that may affect the root and soil interaction and support the centrifuge tests. These data were used to discuss the suitability of common root reinforcement prediction methods. The following conclusions can be drawn from this study:

1) The common root reinforcement models such as WWM and FBM generally over simplified the behaviour of root and soil interaction and significantly over-estimated the contribution of roots to the rooted soil shear strength. This suggests that improved root reinforcement calculation models should be developed and adopted.
2) When subject to shear loading in soil, the tap root mobilized the whole root system to resist the soil movement. As a result, the conventional RAR dependent root cohesion derived from uniformly distributed straight root systems was not applicable for the highly interlinked root system of a tree.
3) Root reinforcement is not only a function of root mechanical properties, but more significantly on factors including surrounding confining stress (resulting in depth dependency even for the same RAR), depth of the slip plane and root morphology. The repeatability of the printed analogues was particularly useful in identify these effects through like-for-like comparison, which will be of significant benefit for future laboratory studies of root-soil interaction.
4) The presence of root analogues resulted in a significant reduction (by 61% and 76%, for straight roots and 3-D root cluster, respectively) in seismically-induced permanent slope movement (crest settlement) compared with the fallow case in the centrifuge tests. However, the roots had a very limited influence on the general propagation and amplification of earthquake motion from the toe of the slope to the crest of the slope. Reductions of spectral acceleration were only observed in the near-field of the root analogues.

Chapter 5 Seismic performance of rooted slopes from individual root- soil interaction to global slope behaviour

Contents of this chapter have been submitted as:

Liang, T., Knappett, J.A. & Duckett,N., 201X. Modelling the seismic performance of rooted slopes from individual root-soil interaction to global slope behaviour. Geotechnique, under review

5.1 Introduction

Vegetation (grasses, shrubs and trees) as an effective and environmental-friendly approach to improving slope stability, improves slope stability mainly through direct mechanical reinforcement of soil and by modifying groundwater conditions by means of evapotranspiration. The net effect of both of these mechanisms is an increase in shear strength within a defined zone around the roots, though only the mechanical effect is present at all times, the hydrological effects potentially disappearing following heavy rain. In terms of the former direct mechanical effect, many studies have been performed to quantify the increase in soil strength due to roots. Analytical models (e.g. Waldron 1977; Pollen & Simon 2005) and numerical models (e.g. Van Beek et al. 2005; Lin et al. 2010; Mickovski et al. 2011) based around full continuum finite element modelling of small soil-root zones have been introduced and validated against laboratory and in-situ shear tests (Wu 2013). A fibre break model which permits the use of a transitioning discontinuous function in finite element modelling, was also developed to simulate the progressive tensile failure of roots, and evaluate the behaviour of vegetated slope (Tiwari et al. 2012). Despite such attention, the majority of this work focused on static cases. Relatively few, if any, studies have been performed to investigate the dynamic performance of vegetated slopes during earthquakes, which are a perennial threat to slope stability, in contrast to other more traditional reinforcing elements within slopes such as geosynthetic layers (or 'reinforced earth', e.g. Ausilio et al., 2000) and piles (e.g. Kourkoulis et al., 2011).

Geotechnical centrifuge testing using both real plants and simple straight root analogues was reported by Sonnenberg et al. (2011) for the case of a static rise in water table using wood dowels and rubber cord to simulate roots of very high or low stiffness, respectively. However, neither of these materials is a perfect analogue to the mechanical behaviour of real roots, see Liang et al. (2014), and to the best of the authors knowledge, testing under fully dynamic ground motions representative of real earthquake shaking has not previously been conducted. Again, this is in contrast to other potential methods of seismic slope reinforcement which have been investigated using dynamic centrifuge testing, including for geosynthetics (Nova-Roessig & Sitar, 2006) and piles (Al-Defae & Knappett, 2014).

The work presented herein will therefore investigate the dynamic behaviour of slopes reinforced with improved root analogues formed from ABS plastic using 3-D printing under a sequence of successive earthquake motions and develop analysis tools for linking the individual root-soil interactions to the global dynamic behaviour of the slope under a single motion or a series of successive motions. The root analogues will be shown to have mechanical properties more representatives of real roots, and the use of successive motions might represent a sequence of strong motions occurring with insufficient intervening time for slope reinstatement. These tests will indicate the potential improvements to seismic performance of a slope which may be provided by the presence of vegetation.

The analytical modelling will consist of a two-stage process. Firstly, a beam-on-a–nonlinear-Winkler-foundation (BNWF) approach using existing p-y curves developed from piling engineering will be used to develop a computationally efficient macro-element for individual soil-root interaction that is analogous to pile response under lateral loading. The approach has been commonly used in analysing lateral soil-pile interaction, e.g. Boulanger et al.(2003); Allotey & Foschi (2005); and Knappett & Madabhushi (2009). The second stage is to add the force resistance contributions from roots of different diameters with different mechanical properties to produce a smeared zone of continuum material properties (e.g. additional representative cohesion) in place of the roots. The BNWF model is used to determine the soil-root interaction for different potential slip plane depths through the rooted soil, to define the variation of the smeared properties with depth. These smeared properties are finally used within a fully dynamic Finite Element (FE) model in the time domain to simulate the global seismic response of the slope. This will build on procedures for the seismic response of

fallow slopes presented by Al-Defae et al. (2013). The BNWF soil-root macro-elements are validated against a series of large direct shear tests with stress conditions mimicking those in the centrifuge models, and the whole procedure (macro-elements to smeared properties to dynamic FE modelling) will be validated against the centrifuge test data.

5.2 Centrifuge modelling

5.2.1 Model preparation and soil properties

Two tests, referred to herein as TL03 and TL04 are presented here. These two tests were performed at a scale of 1:*N* where $N = 10$. The use of such a low scaling factor was felt to be the best compromise between the competing requirements of minimising grain size effects on the soil-root interaction (due to the generally small root analogue diameters, a lower value of *N* is desirable) and producing a prototype of the order of metres in height with as much low frequency content as possible (both of these factors improve with a larger value of *N*).

The model slope TL03 was reinforced with straight root analogues with a predefined distribution (as shown in Fig 5.1), and was designed to investigate the seismic performance of reinforced vegetated slope under multiple successive earthquakes. The root analogues were 'printed' from Acrylonitrile Butadiene Styrene (ABS) plastic which has mechanical properties which are highly representative of plant root material. This study represents the first use of this material as a root analogue. Further details about the construction and material testing of these root analogues will be presented in the following section. The model TL04 was designed as a reference case for the model TL03, having identical slope geometry and soil properties, but fallow (no roots).

The model configuration and instrumentation is shown in Fig 5.1. In order to maximise the size of the slope, given the low scaling factor, the slope crest and toe were relatively close to the ESB container walls. However, this geometry was carefully chosen following initial limit analyses of the slope which suggested that the seismic failure mechanism would lie within the geometry shown and would not be constrained by the boundaries. This will be confirmed later through the results of the Finite Element (FE) simulations. More details about model preparation and soil properties can be found in Chapter 3.

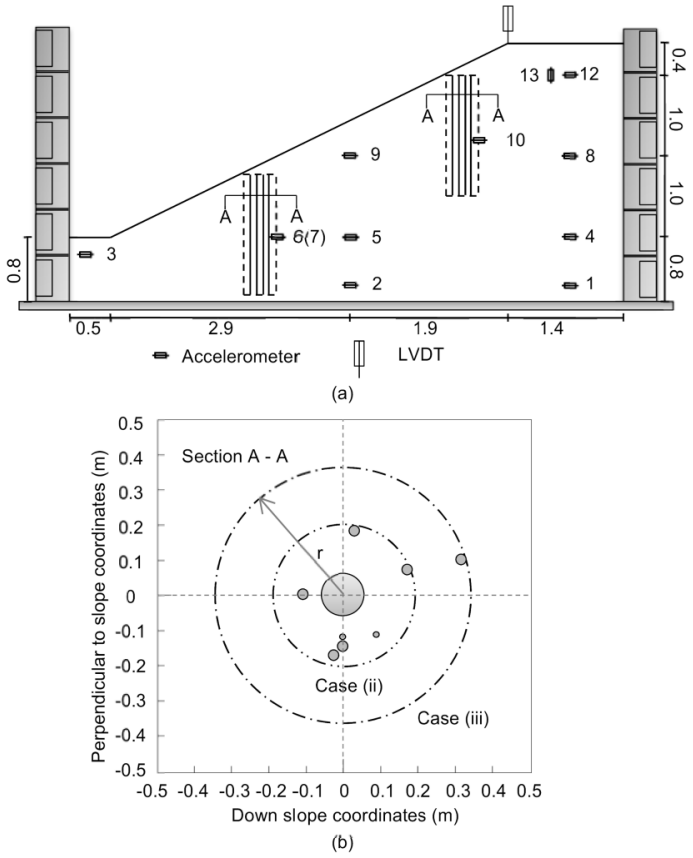

Fig 5.1 Slope configuration: (a) centrifuge model layout and instrumentation (elevation); (b) distribution of root group (plan). All dimensions in m at prototype scale

5.2.2 Model root characterization

A simplified 3-D root model cluster (length of 0.15 m at model scale) with root area ratio (*RAR*), root distribution and root length representative of 1:10 geometrically-scaled tree root clusters for element and centrifuge testing are reported in Chapter 4. These complex 3-D models are not discussed further in this chapter as to develop the analytical models, it was decided to start with a simpler group of straight root analogues (but still having varying diameter) which are designed to represent heart/plate root system, of which most of the individual roots behave independently. The straight analogues were selected to have the same *RAR* and spatial distribution at the level of the middle of the 3-D root cluster; this is shown in Fig 5.1 (b). The middle cross section was selected for two reasons: (i) *RAR* at the middle of the cluster was close to the mean *RAR* of the 3-D cluster, which has in the past generally been

considered as the major factor in root-soil interaction (e.g. Waldron 1977; Pollen & Simon 2005); and (ii) The stump/main central tap-root, which distinguishes tree root systems from herbaceous types extended to 0.1 m depth from the ground surface at the model scale, and the effect of this can therefore be investigated. There were four 'blocks' of root analogues inserted within the centrifuge model slope: two near the crest of the slope and two towards the toe (the position of these two rows in elevation is shown in Fig 5.1).

ABS plastic was selected as a material potentially having a very similar Young's modulus and ultimate tensile strength to real roots. Strength and stiffness were considered to be the most important characteristics in selecting an appropriate material. However, real roots have a cellular structure, with a number of overlying layers of tissue. Among them, the xylem and cambium layers play a significant role on mechanical behaviour, driving the characterisation of tensile strength and stiffness, respectively. The xylem tissue runs through the core of the root and consists of long, cylindrical cells that are joined from end to end and provide unidirectional fibre orientation (Karam 2005). The cellular structure can be idealised as a stack of fibres aligned uni-directionally. To obtain a uni-directionally layered structure to the root analogues, they were fabricated using a Stratesys Inc. uPrint SE Acrylonitrile Butadiene Styrene (ABS) rapid prototyper (also known as a 3-D printer) at the University of Dundee following the procedures outlined in Liang & Knappett (2015). The ABS plastic was delivered into the machine in the form of a spooled rod which was melted and injected in successive layers onto a build platform by a moving print head. The whole printing procedure was controlled by a computer from a digital input file exported directly from the SOLIDWORKS 3-D modelling software.

To characterise the mechanical properties of the layered root analogues, three-point bending flexural tests and uniaxial tensile testing of analogue specimens of various diameters were conducted following the methods described in Liang et al. (2014); the results are shown in Fig 5.2.

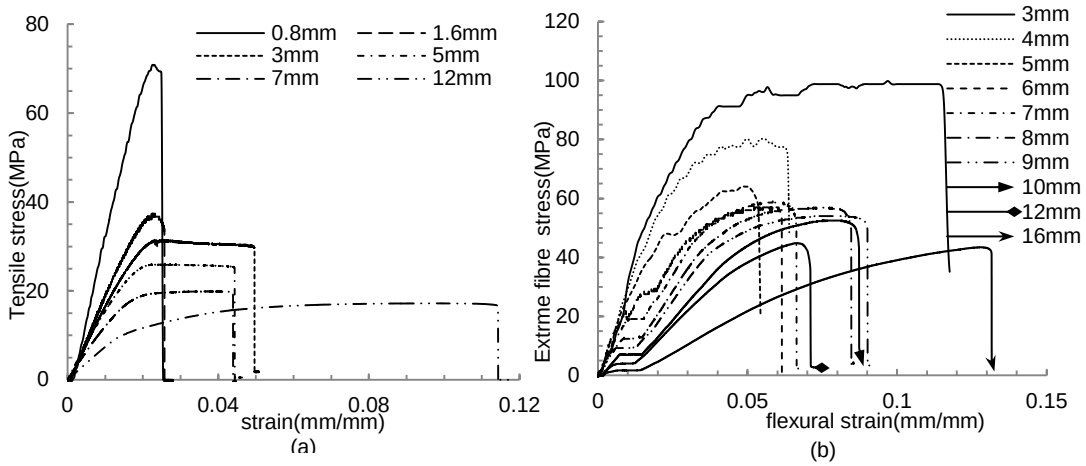

Fig 5.2 Typical stress-strain curves for printed ABS plastic root analogues: (a) from uniaxial tensile testing; (b) from three-point flexural bending test

The extreme fibre stress σ_f versus flexural strain ε_f curve for the bending tests in Fig 5.2 (b) were derived from the applied load at midspan, F, and deflection at this point, Δ, using the following formulation:

$$\sigma_f = \frac{8Fl}{\pi D^3} \qquad \textbf{Eq 5. 1}$$

$$\varepsilon_f = \frac{6\Delta D}{l^2} \qquad \textbf{Eq 5. 2}$$

where l is the root length and D is the root diameter. The value of σ_f at failure was defined as the modulus of rupture (MOR), while the tensile stress at failure in the uniaxial tension tests was defined as the ultimate tensile strength (UTS).

In each case, failure was defined as the point at which the root analogues broke, indicated by the post-peak drop in stress in Fig 5.2. These measures of strength are not necessarily the same due to the different modes of loading (bending and stretching, respectively). Fig 5.3 shows that the new model root analogues perform as suitable substitutions of real roots – the 'real root' data in this figure is collated from the literature (Sonnenberg 2008; Mora et al. 2009 ; Warren, 2009; Mickovski et al., 2009; Mao et al., 2012) from uniaxial tension tests on tree and shrub roots. It should be noted that bending test data was not available for the real roots in the database, and is not routinely collected for real plant roots. The stiffness of the

root analogues is less representative than the strength, but is still a substantial improvement on previously used analogue materials such as rubber and wood, which are also shown in Fig 5.3 (b).

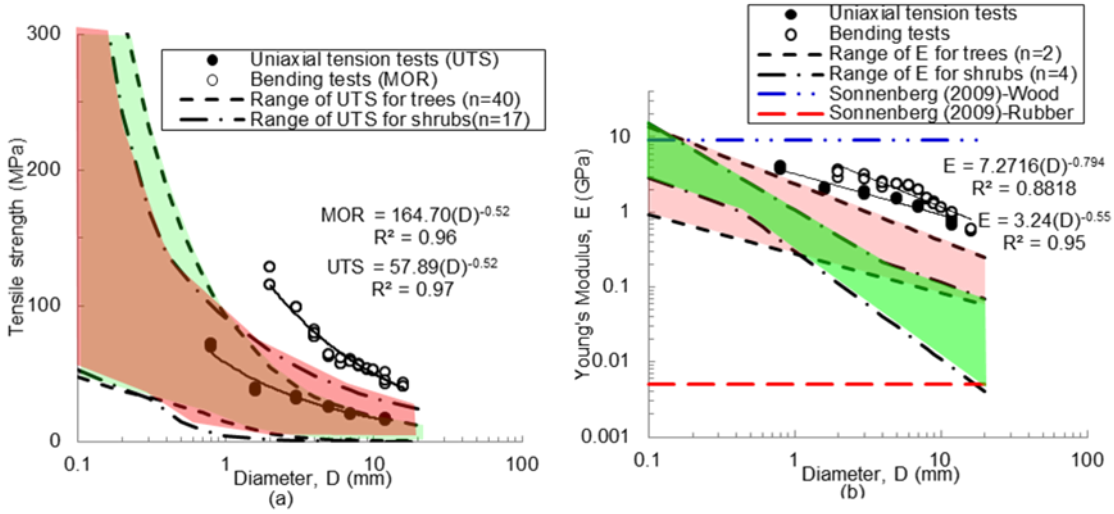

Fig 5.3 Comparison of material properties between typical roots and root analogues:(a) Tensile strength; (b)Young's Modulus

5.2.3 Initial observations of seismic performance of rooted slopes

A comparison of the crest settlement between the root reinforced slope and unreinforced slope is shown in Fig 5.4. Because of the potential effect of the settlement-reducing disc (as mentioned in the previous section), the settlement was confirmed by visual observations and measurements post-test. The presence of root analogues highly reduced the permanent slope settlement (61%) compared with the unreinforced cases, especially for the first two motions (EQ1 and EQ2). This can be interpreted as a result of the rapid mobilisation of root-soil interaction due to the initial soil slip under dynamic loading. Al-Defae & Knappett (2015) have demonstrated that for the case of large vertical piles reinforcing slopes to significant depths, the full lateral restraint of the piles is mobilised within 2% of the pile diameter; applying this analogously to the root analogues here would suggest very rapid mobilisation. After the first two motions, relatively smaller reductions (in total 14%) were observed, which indicates that the additional resistive force of the root is largely constant after the initial rapid increase. The roots were not observed to have broken following careful post-test exhumation,

which would infer that the maximum root-soil resistance was mobilised after EQ2 and that this was associated with yielding of the soil around the root analogues. For both root reinforced and unreinforced slopes, a decreasing trend of settlement was observed when the slope was subjected to successive identical motions. This can be associated with the slope geometry change (re-grading), as previously proposed for fallow slopes by Al-Defae et al. (2013). Dynamic motions observed from the centrifuge tests will be discussed alongside results from numerical simulation later in the paper.

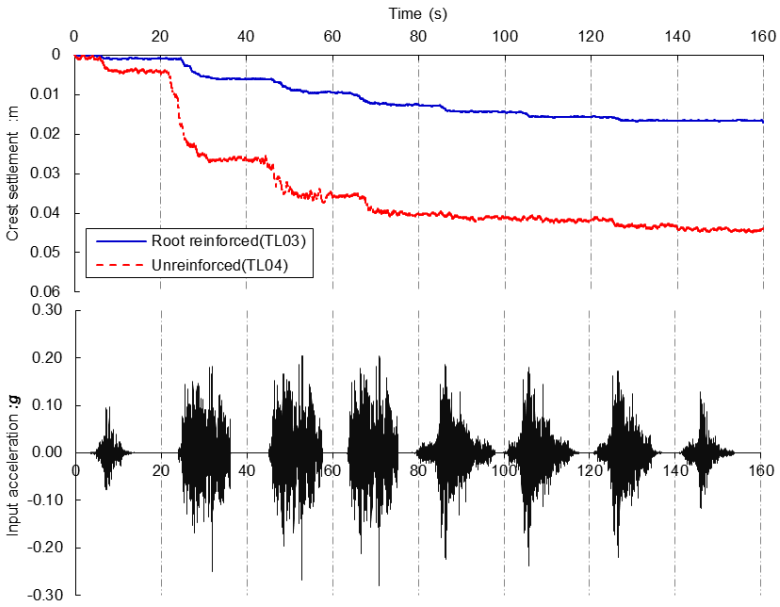

Fig 5.4 Comparison of permanent crest settlement of fallow and root-reinforced slopes from centrifuge testing

5.3 Modelling root-soil interaction using a BNWF approach

The BNWF approach using existing *p-y* curves was conducted using the non-linear FE programme ABAQUS as a convenient method to solve the beam-on-spring problem (though it should be noted that it would also be possible to complete the calculations using a finite difference approach). A BNWF approach has significant advantages in computational efficiency compared to previous continuum FE models of root-soil interaction (e.g. Mickovski et al. 2011), while offering significantly more detail in the response compared to simple models (e.g. Waldron 1977; Pollen & Simon 2005).

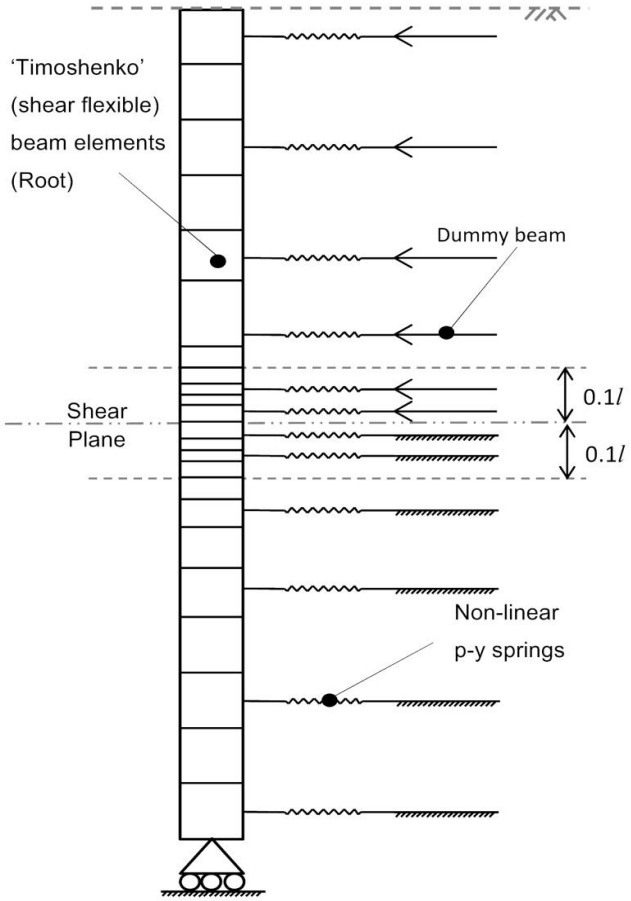

Fig 5.5 Schematic of root-soil system undergoing shear loading

Fig 5.5 presents a schematic of an individual soil root system undergoing shear loading as idealised within the BNWF approach. The root was modelled using deformable 'Timoshhenko' beam elements (which are flexible in both shear and bending) with constitutive behaviour defined by Timoshenko & Goodier (1986). A detailed description of the advantage of this element compared to simpler types may be found in Knappett & Madabhushi (2009).

The root is discretised into elements non-uniformly along the length, with a higher concentration within the deformable zone (0.1l either side of the slip plane) after Randolph (1981). This was designed to provide additional computational efficiency. A linear elastic-perfectly-plastic model was used to model the stress-strain behaviour of the root, which is a very reasonable approximation to the measured behaviour illustrated in Fig 5.2. The Poisson's

ratio of ABS plastic was taken as 0.35. A series of dummy beams which sat at a uniform horizontal offset from the discrete nodes along the root were established to represent the free-field soil movement. A portion of horizontal rigid dummy beams on roller supports allowing horizontal movement (above the location of a potential shear plane) could move past the root without coming into contact. Non-linear *p-y* springs were then connected between roots and dummy beams. A full description of the *p-y* spring properties will be given in the following section. Soil deformation could be simulated by displacing the upper dummy beams laterally while fully restraining the lower beams. By re-meshing and changing the number of beams which were displaced, it was possible to simulate the soil-root interaction for any particular location of the slip plane passing through the rooted soil. A horizontal roller connection was attached at the tip of the root to prevent any unwanted vertical movement while allowing lateral displacement and rotation (as suggested by Duckett (2013)). Other than at this point, axial movement of the root was unrestrained.

5.3.1 p-y modelling framework

The non-linear *p-y* relationship derived by Reese et al. (1974) is employed in the modelling presented herein, which was derived from the results of full-scale pile testing in sands at Mustang Island. The use of this *p-y* modelling framework is beneficial given familiarity with the approach from piling engineering; however, there are a number of differences between root analogues and piles. Firstly, plant roots are much smaller in diameter than piles (by approximately 2 orders of magnitude compared to the Mustang Island tests). Given that mobilised pile-soil resistance is expressed in terms of the diameter of the pile, and the lateral response (including the transition from rigid rotation to bending) is a function of slenderness (i.e. again expressed in terms of diameter), it follows that so long as continuum behaviour is still appropriate at small diameter, then the absolute size of the diameter should not have an effect. Secondly, due to their increased flexibility, the lateral root analogue deformation will be much larger (5-42*D*) than traditionally occurs in laterally loaded piles. However, the *p-y* formulation includes a limiting capacity which is reached at low amounts of deformation, and so if there is no post-peak reduction in this capacity, then it is reasonable to assume that this capacity could be extended to larger deformations.

The Mustang Island tests were performed on steel piles for only one pile diameter and one type of sand. Due to the limitation of the validation data, Brødbæk & Møller (2009) discussed the practicability of this model and emphasised the effect of pile slenderness ratio on the initial stiffness of the *p-y* curve. The feasibility of this model for stiff piles with slenderness of *l/D* <10 still requires investigation as the Mustang Island tests had a slenderness ratio of *l/D* =34.4. A summary of model root properties used in this project is given in Table 5.1, where the quantity column refers to an individual root block as shown in Fig 5.2(a). This indicates that all of the root analogues had l/D > 10.

This model has been successfully used in calculating the contribution of model root analogues made from wood and rubber to soil shear strength at shallow depths (i.e. in low stress 1-g direct shear tests) by Duckett (2013) including validation against a large programme of direct shear tests.

As shown in Fig 5.6, The *p-y* curves consist of four segments: an initial straight line p_1, a following parabolic section p_2 a connecting line p_3 and an upper border line p_4 characterised by the ultimate resistance p_u. Two modes of failure were distinguished which depend on the pile embedded depth. At shallow depths, an unstable mass of soil is pushed upward along the connecting shear plane sitting in front of the pile to form a wedge. Reese et al. (1974) simplified this to be a sharp-edged wedge to analytically calculate the ultimate soil resistance.

Table 5. 1 Summary of root property (model scale)

Root ID	Diameter: mm	Length: mm	Slenderness (L/D)	Quantity
1	12	150	12.5	1
2	3	150	50	6
3	1.6	150	93.75	2

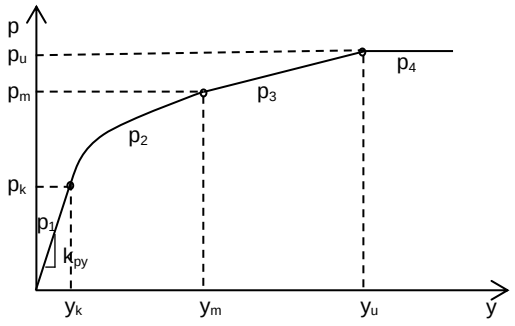

Fig 5.6 *p-y* curve for piles in drained cohesionless soil (Reese et al. 2002)

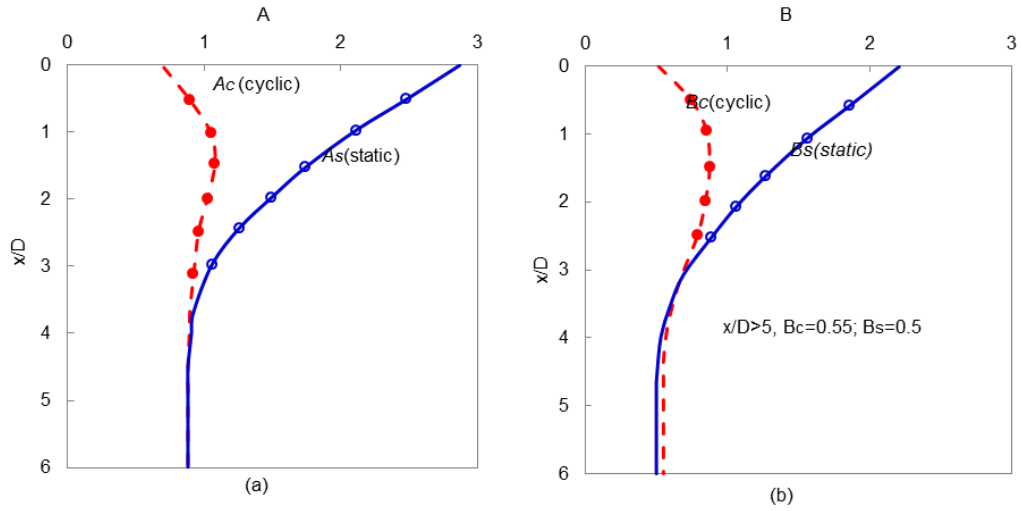

Fig 5.7 Non-dimensional constants used to define: (a) ultimate soil response p_u; (b) soil response p_m (Reese & Van Impe 2011)

The ultimate resistance per unit length of pile can be calculated through equation Eq 5.3. At deeper depths, the sand flows around the pile, with the ultimate capacity of the soil against a flow mechanism being given by equation Eq 5.4.

$$p_{us} = \gamma' x \left[\frac{K_0 x \tan\phi \sin\beta}{\tan(\beta-\phi)\cos\alpha} + \frac{\tan\beta}{\tan(\beta-\phi)}(D + x\tan\beta\tan\alpha) + K_0 x \tan\beta(\tan\phi\sin\beta - \tan\alpha) - K_a D \right] \quad \textbf{Eq 5. 3}$$

$$p_{ud} = K_a D\gamma' x(\tan^8\beta - 1) + K_0 D\gamma' x \tan\phi \tan^4\beta \quad \textbf{Eq 5. 4}$$

In the foregoing equations, $\gamma' x$ represents the effective stress at any given depth x. In the centrifuge tests, $\gamma' x$ is generated by the soil self-weight; to simulate the centrifuge stress conditions in direct shear tests that are reported in the following section, the soil was subjected to an additional vertical surcharge load. In these cases, $\gamma' x$ was adjusted to be the actual normal effective stress in the direct shear test at the given depth. The angles α and β are used to define the geometry of the wedge, K_a and K_0 are the coefficients of active horizontal earth pressure and horizontal earth pressure at rest, respectively; these parameters can be calculated using:

$$\alpha = \frac{\phi}{2} \quad \textbf{Eq 5. 5}$$

$$\beta = 45^\circ + \frac{\phi}{2} \quad \textbf{Eq 5. 6}$$

$$K_a = \tan^2(45^\circ - \frac{\phi}{2}) \quad \textbf{Eq 5. 7}$$

$$K_0 = 0.4 \quad \textbf{Eq 5. 8}$$

At any given depth, the ultimate soil resistance is the most critical of the two potential failure mechanisms, and the transition depth between the two failure modes occurs at the depth where p_{us} (shallow wedge mechanism) is equal to p_{ud} (deep flow mechanism). However, a poor agreement of the theoretical ultimate resistance with the data gathered from the Mustang Island test was observed (Brødbæk & Møller, 2009). A correction parameter A was introduced to fit the field test, that is:

$$p_u = Ap_{us} \quad \textbf{Eq 5. 9}$$

$$p_u = Ap_{ud} \quad \textbf{Eq 5. 10}$$

The variation of the coefficient A with non-dimensional depth x/D is presented in Fig 5.7(a). The soil resistance per unit length p_m at y_m, is determined to be:

$$p_m = Bp_u \quad \textbf{Eq 5. 11}$$

where B is defined as a function of the non-dimensional depth x/D, using Fig 5.7 (b).

Table 5. 2 Initial modulus of subgrade reaction k_{py}: kN/m^3 (after Reese et al. 1974)

Relative density	Loose	Medium	Dense
Unsubmerged	6800	24400	61000
Submerged	5400	16300	34000

The initial straight line portion was influenced by the initial subgrade reaction modulus $k_{py}$and the depth x, and this can be associated with the phenomenon that the in-situ modulus of elasticity increases approximately with depth according to:

$$p = (k_{py}x)y \quad \textbf{Eq 5. 12}$$

Reese (1974) suggests that the value of k_{py} only depends on the relative density of the sand, and the appropriate value can be obtained from Table 5.2. For the dry soil density used in the centrifuge and subsequent shear box tests (see below) k_{py} = 24.4 MN/m^3 was used in all BNWF simulations reported in the paper. The parabolic part of the line can be established as:

$$p = C \cdot y^{1/n_a} \quad \textbf{Eq 5. 13}$$

The value and tangent at point *k* and *m* are equal, according to the criteria; the parameter n_a can be calculated through the following equations:

$$y_m = \frac{D}{60} \quad \textbf{Eq 5. 14}$$

$$y_u = \frac{3D}{80} \quad \textbf{Eq 5. 15}$$

$$m = \frac{p_u - p_m}{y_u - y_m} \quad \textbf{Eq 5. 16}$$

$$n_a = \frac{p_m}{m y_m} \quad \textbf{Eq 5. 17}$$

$$C = \frac{p_m}{y_m^{1/n_a}} \quad \textbf{Eq 5. 18}$$

$$y_k = \left(\frac{C}{k_{py}x} \right)^{n_a/n_a - 1} \quad \textbf{Eq 5. 19}$$

The *p-y* curve described in this section represents the soil response per unit length of pile. To serve as the property of an individual spring in the BNWF approach, the values of *p* are scaled proportionally to the length of the element.

5.4 Validation of BNWF model

5.4.1 Prediction of additional shearing resistance from root analogues

Laboratory shear tests were conducted to verify the BNWF model. The same number and sizes of root analogues and density of soil as used in the centrifuge tests were used in the large DSA, though the model roots were here spaced at $s/D > 8$ to eliminate the group effect (Herndon 1991; Randolph 2003). All measurements were corrected to remove the small force component due to friction between the two halves of the DSA frame, which was independently measured for tests with no soil. Fig 5.8 (a) shows the overall shearing resistance over the shear plane measured in the fallow and rooted tests and Fig 5.8 (b) shows a comparison between the inferred additional shear force provided by the roots from the DSA tests and as predicted by the BNWF simulations. The numerical value was found by integrating up the reaction forces of the *p-y* springs above the shear plane depth, while the experimental value was found as the difference in the shear box load measurement between the rooted and fallow cases (i.e. from Fig 5.8 (a)).

The varied confining stress at the shear plane in the DSA was obtained by maintaining the same spatial distribution of root analogues and soil, and altering the surcharge weight to simulate homologous confining stress for different potential slip plane locations in the centrifuge test. It should be noted that DSA tests mentioned here could not be used directly to evaluate the realistic slip behaviour in centrifuge test due to the largely uniform confining stress along the length of the root analogues in the DSA (in the centrifuge this increases with depth from a value of zero at the ground surface).

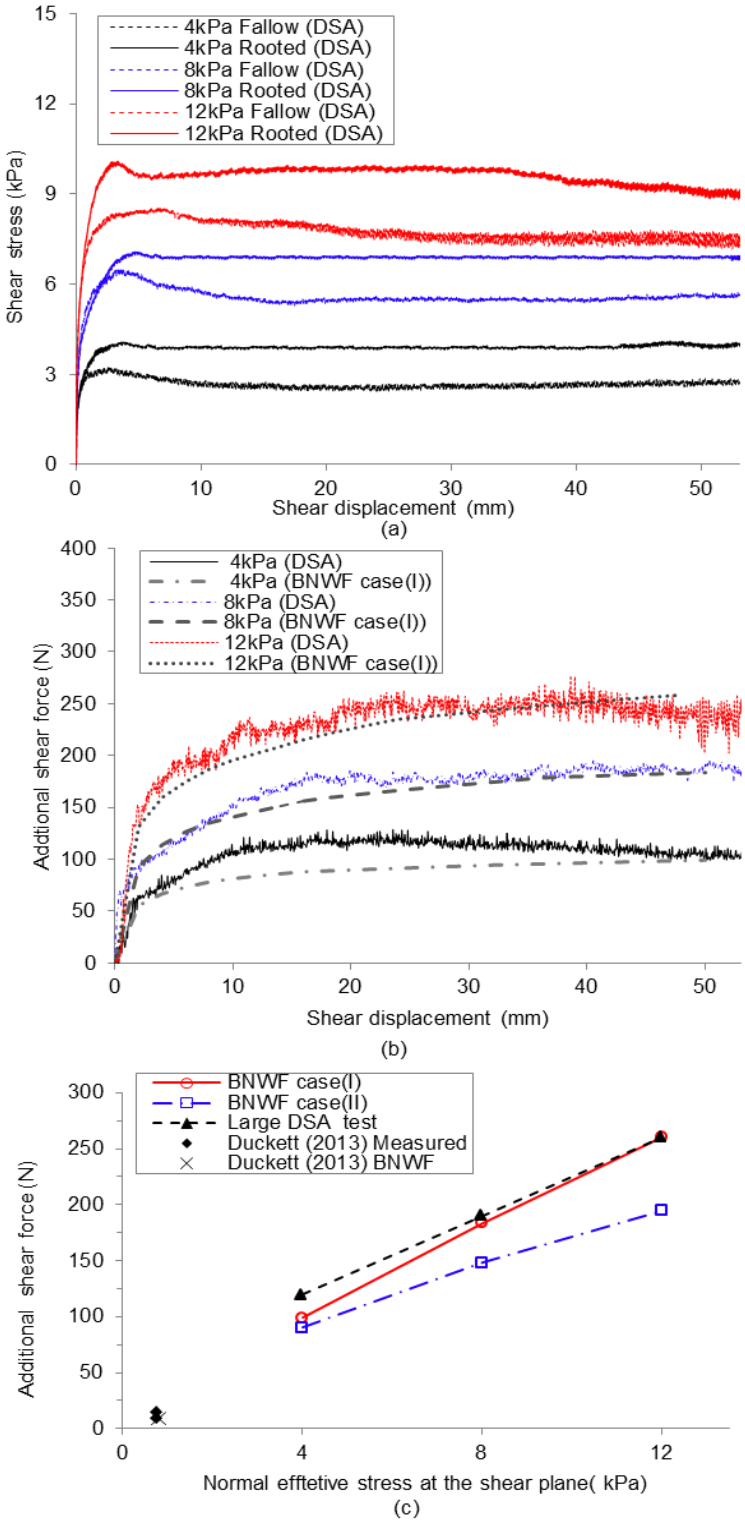

Fig 5.8 (a) Measured shear resistances from DSA tests of fallow and rooted soil; (b) additional shearing resistance provided by root analogues, as measured in DSA and predicted using BNWF; (c) comparison of additional ultimate shear resistance from BNWF approach and laboratory DSA tests

The peak resistive forces in each case are summarised in Fig 5.8 (c). In Fig 5.8 two cases are considered numerically: (I) the use of root analogue material properties from three-point bending tests (i.e. Fig 5.2 (b)); (II) the use of material properties from uniaxial tensile tests (i.e. Fig 5.2 (a)). The comparison is necessary, as most existing analytical formulations of root contribution are based on the results of uniaxial tests which are much easier to conduct on real root specimens exhumed from the ground, particularly for very fine roots, see Wu (2013). Compared with an under-prediction in case (II), a good match was observed in case (I). This could be considered as evidence supporting the need to define root properties (at least for shear cases) through bending rather than uniaxial tests. At low effective stress (4 kPa), case (II) presents a slight under prediction suggesting that enhanced dilation should perhaps be considered at very low effective stress. Fig 5.8 (c) also demonstrates a positive correlation between the root resistive force and the vertical effective confining stress of the soil at the slip plane based on both numerical simulation and the laboratory shear tests. This is consistent with the behaviour of piles within a cohesionless soil and is supported by other recent work e.g. Duckett (2013). However the observations are inconsistent with current implementations of root reinforcement models in which typically a constant amount of additional resistance with depth is used, as it is assumed that this is based only on the properties of the roots and independent of the soil properties, which may vary with depth (Waldron 1977; Pollen & Simon 2005). The use of constant additional resistance with depth may be acceptable for grass root systems which penetrate only to very shallow depths, but for deeper rooting systems, the normal effective stress varies significantly due to the deeper embedding depth.

In each numerical case, critical state properties for the soil were considered (namely $\phi' = 32^\circ$). The reason for this was that the BNWF models are primarily used to obtain the representative additional shear strength of the roots (i.e. at large strain shear displacements of the rooted soil) for use in the later FEM simulations (described below). Given that the diameter of the majority of the roots used is very small, it will only require relatively small global slip of the rooted soil to potentially induce large relative soil-root deformations. Therefore, by the displacement at which the rooted soil globally reaches critical state conditions most of the roots will have relative soil-pile shear strains much higher than this and will therefore be at p_u as defined by the critical state of the local surrounding soil. Fig 5.8 (b) shows the additional

combined resistive force from the root analogues, plotted against global shear displacement of the DSA for both the experiments and the BNWF simulations. Considering the 12 kPa case as an example, there are actually a series of small 'bumps' in the experimental data below 10 mm displacement which would be consistent with individual size classes of roots passing through peak behaviour at different global displacements (due to their different diameters). By the displacement at which the additional root contribution reaches its maximum level (beyond 20 mm or so, which is larger than the strain to critical state of ~8% in fallow soil, after Al-Defae et al. 2013) most, if not all, of the root-soil shearing will be at strains large enough for critical state locally, and this is why the BNWF simulations with critical state parameters generally fit well to the measured data at the larger displacements which is where the additional root strength is defined.

5.4.2 Replication of failure mechanism

Soil–pile response depends on the flexibility of the pile (Augustesen 1901). In terms of the root analogues, the behaviour of a rigid analogue and a flexible one subject to a soil movement of 0.05 m is compared in Fig 5.9. These two analogues have identical root length (l = 150 mm) but different diameters (D = 1.6 mm and 12 mm). For both analyses shown in Fig 5.9, significant difference in soil response was observed.

For the flexible analogue, the root deformation is governed by the soil movement; the upper part of the root moves similarly to the soil and the deformation zone is concentrated around the shear plane (between 0.05 m and 0.1 m depth). This causes stress concentration near the middle part of the root with it just reaching the yield point, as shown in Fig 5.9 (a).

According to Fig 5.9 (b) , the extreme fibre strain is approximately 0.046, which is just above the limiting material flexural strain inferred from the strength and stiffness relationships in Fig 5.2(b) for 1.6 mm diameter ('elastic limit' strain at MOR) but above the strain at UTS (Fig 5.2(a)). As the small analogues were not observed to snap, this suggests that there was some axial pull-through of the small roots at larger deformations which occurred at an axial force lower than that associated with the UTS. This is allowed for in the BNWF models as there is no restraint to axial movement at the top of the root (Fig 5.5).

Combining these observations, the flexible root therefore would therefore be expected to show some irrecoverable bending deformation close to the shear plane when subjected to a soil movement of 0.05 m (which was exceeded within the laboratory DSA tests). Such behaviour corresponds well with the physical observations following the laboratory DSA test, as shown in Fig 5.9 (d). Conversely, the rigid root rotates significantly inside the soil with a translational slip of about 0.02 m and the performance is dominated by the root, which is shown to be well within the elastic range.

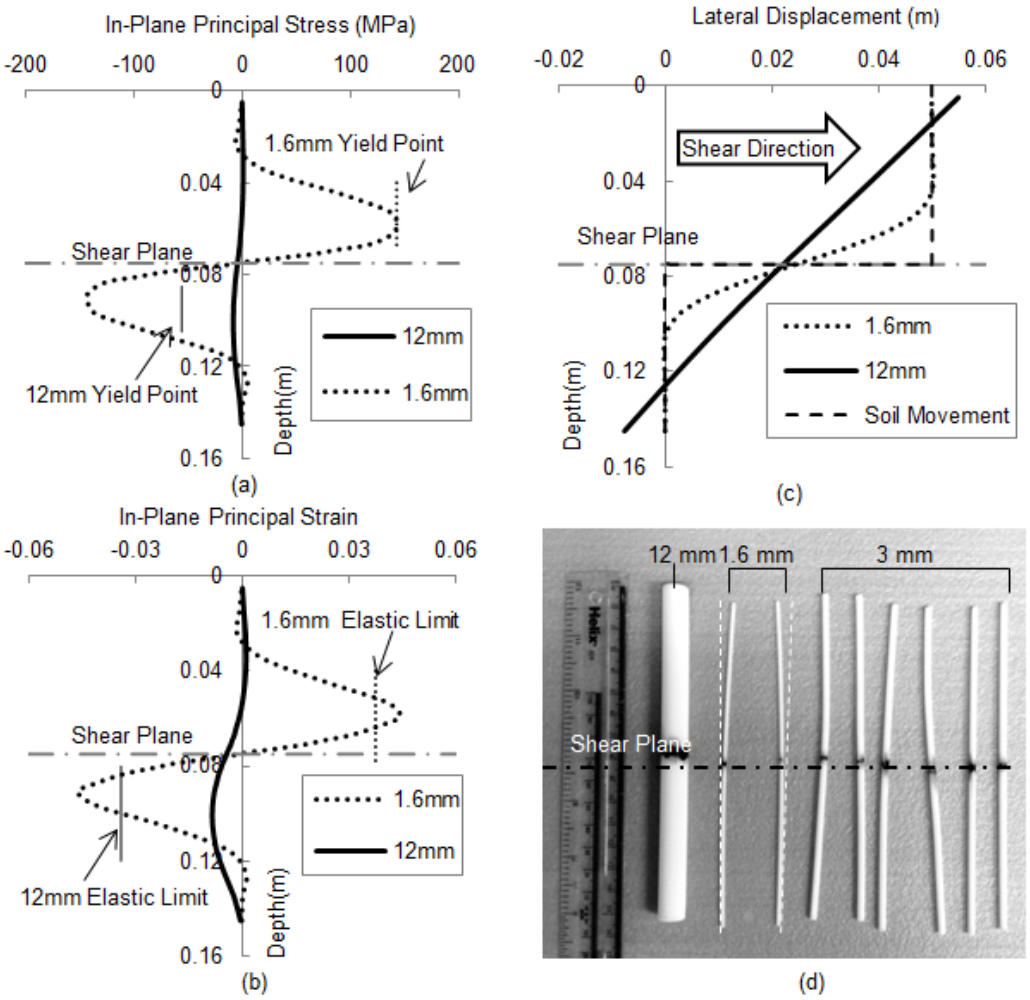

Fig 5.9 Comparison of root analogue response under lateral loading for stiff and flexible roots: (a) in plane principal stress (BNWF); (b) in plane principal strain (BNWF); (c) lateral displacement(BNWF); (d) post-test observation of laboratory DSA tests.

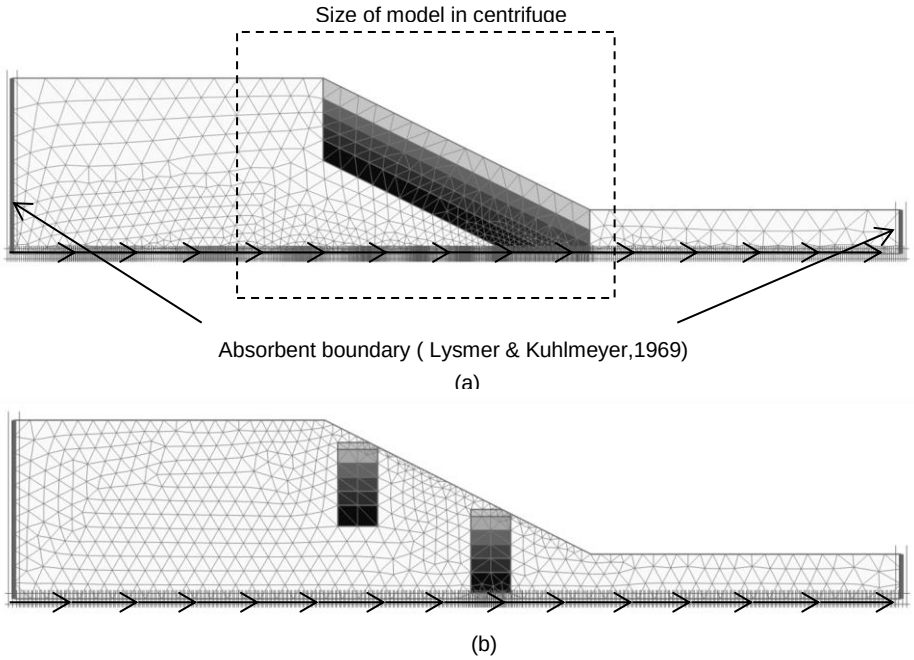

Fig 5.10 Finite element mesh, showing boundary conditions: (a) case (i); (b) cases (ii) and (iii)

5.5 Finite-element modelling

The centrifuge tests were simulated numerically using PLAXIS 2D in this study. 15-noded triangular elements with 12 Gaussian points suitable for stress and collapse simulations were used. This element can simulate accurately the dynamic behaviour of slopes (e.g. Al-Defae et al. 2013). The mesh and boundary conditions are shown in Fig 5.10. The boundary conditions, which allowed lateral deformation while reacting normal stresses and incorporated non-reflecting vertical boundaries, were established based on the theory proposed by Lysmer & Kuhlemeyer (1969) to simulate the semi-infinite soil condition. In this way, the performance of the boundary deformation in the ESB container can be controlled by the adjacent soil. This same procedure has previously been used by Al-Defae et al. (2013). A dynamic ground displacement time history was applied along the bottom of the slope. The input motions were obtained from the measurements at instrument 2 in the centrifuge tests, which represented the actual input motion the slope saw during the centrifuge tests. Before input, the measured motions were band-pass filtered using an 8^{th} order Butterworth filter defined by a zero phase filtering method to eliminate any steady-state offset in the accelerometer recording.

Table 5. 3 Key parameters and properties of HST95 silica sand for HS small strain model (after Al-Defae et al., 2013)

Parameter	value
ϕ'_{pk}(°)	32
ψ'(°)	0
γ_{unsat}(kN/m^3)	16.0
γ_{sat}(kN/m3)	16.0
E_{50}^{ref}(MPa)	42.5
E_{oed}^{ref}(MPa)	34
E_{ur}^{ref}(MPa)	102
ν_{ur}	0.2
G_0^{ref}(MPa)	116.3
m'	0.55
$\varepsilon_{s,0.7}$(%)	0.016
R_f	0.9

5.5.1 Soil constitutive models

The hardening soil model with small-strain stiffness (HS small, (Schanz et al. 1999) is used to model all soil units. This specific constitutive model has been verified to be effective at simulating the dynamic behaviour of HST 95 sand (Al-Defae et al., 2013). Model parameters used in the analyses are summarised in Table 5.3. All of the parameters apart from the cohesion c and damping ratio ζ_{add} (discussed later) could be collected from the aforementioned literature.

5.5.2 Root-soil matrix modelling

To model the dynamic behaviour of a slope with regions of different strength in FE analysis, it is feasible to consider the slope as a composite set of different soil blocks (Fig 5.10 (a) and (b)), with the soil root interaction behaviour from the BNWF approach mentioned previously being used to quantify the additional strength and stiffness in the rooted zones.

The strength of root reinforced soil is typically evaluated from the following equation based on Mohr-Coulomb failure criterion after Waldron (1977) ,

$$\tau = \sigma \tan\phi' + c' + c'_r \qquad (5)$$

where, c'_r represents the additional shear strength contribution due to the presence of roots, with ϕ' and c' representing the strength properties of the fallow soil. Given that the additional

resistance from the roots was found to increase with the depth of the shear plane (Fig 5.8 (c)), this was incorporated through increasing the c' value in the rooted zones above that for the soil alone (i.e. zero) and this parameter was varied with depth to simulate the depth effect as shown in Fig 5.8. This is indicated in Fig 5.10 by the variation in shading with depth within the rooted zones.

To determine the appropriate value of c_r' and its variation with position in the plane of failure within the continuum FE model the rooted soil zones were represented by a plane cross-section taken horizontally through model roots as illustrated in Fig 5.1(b). At a sufficient distance, r, away from the centre of the main taproot, the effect of the root reinforcement may be expected to have reduced to a negligible amount.

Limited literature (Yegian & Wright 1973) is available on the determination of the zone of the root group influence, especially for the case herein, which has variable diameter distribution. Herein, three cases are considered to investigate the influence zone of the roots: (i) the reinforcement effect is uniformly distributed along the whole slope face; (ii) influence radius r is selected based on the actual extreme boundary of the root analogues; (iii) r equal to three times the diameter of the trunk, as shown in Fig 5.1(b).

Cases (i) and (ii) represent two extreme cases, while case (iii) was established considering the group efficiency at 3D spacing to be 0.6 -0.8 for the main row in medium dense sand based on a body of literature (e.g. McVay et al. 1995; McVay et al. 1998; Rollins et al. 2005). The 2D plane strain FE model assumes that stress distribution in every longitudinal section along the length, b, of the 3-D slope geometry is equal (i.e. in the out-of-plane direction). For the rooted case considered here, two root groups were placed along the length of 3-D slope in the centrifuge, so that the equivalent (smeared) area, A, of shear plane per metre length of the slope over which the additional root strength acts is given by:

$$A = r \cdot \frac{b}{2} \qquad \textbf{Eq 5. 20}$$

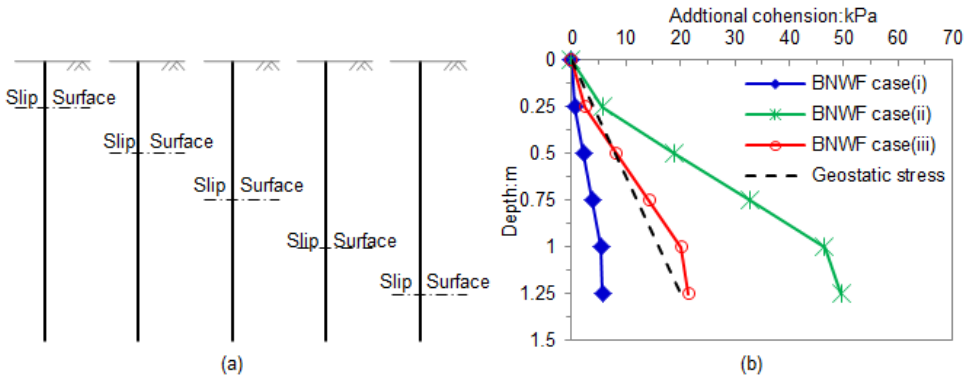

Fig 5.11 Apparent root cohesion for three cases: (a) assumed slip surface; (b) variation of root cohesion with depth;

Having evaluated the value of *A* for the rooted zone for each of the three cases (i) – (iii), BNWF simulations were run for each of the different root diameters separately considering the shear plane at different depths, with the *p-y* spring properties evaluated for the prototype effective stress conditions in the centrifuge tests (rather than the 'model scale with surcharge' simulations for the laboratory DSA tests). This is shown in Fig 5.11 (a). However, in the centrifuge, the model root groups were installed into the slope vertically, rather than perpendicular to the soil surface (as in the DSA). Modifications of the *p-y* curve due to the sloping ground effect were therefore made. The wedge-type failure mechanism only was modified as the flow-around failure has not been previously observed to be influenced by sloping ground (Reese et al. 2002). The ultimate soil resistance in this mode is therefore given by:

$$p_{us} = \gamma' x \left[\begin{array}{l} \dfrac{K_0 x \tan\phi \sin\beta}{\tan(\beta-\phi)\cos\alpha}(4t_1^3 - 3t_1^2 + 1) + \dfrac{\tan\beta}{\tan(\beta-\phi)}(Dt_2 + xt_2^2 \tan\beta \tan\alpha) \\ + K_0 x \tan\beta(\tan\phi \sin\beta - \tan\alpha)(4t_1^3 - 3t_1^2 + 1) - K_a^{'} D \end{array} \right] \quad \textbf{Eq 5. 21}$$

$$t_1 = \frac{\tan\beta \tan\theta}{1 - \tan\beta \tan\theta} \quad \textbf{Eq 5. 22}$$

$$t_2 = 1 + t_1 \quad \textbf{Eq 5. 23}$$

$$K_a^{'} = \cos\theta \frac{\cos\theta - \sqrt{\cos^2\theta - \cos^2\phi}}{\cos\theta + \sqrt{\cos^2\theta - \cos^2\phi}} \quad \textbf{Eq 5. 24}$$

Eq 5.22-Eq 5.25 replace Equations Eq 5.3 and Eq 5.7. For each shear plane depth, the additional resistive force provided by each root was added together using:

$$F_p = k\sum_{n=1}^{n}(F_r^n \cdot N_n) \qquad \textbf{Eq 5. 25}$$

where *n* is the number of distinct types/geometries of model root, reflecting the diversity of the root diameter and *N* is the quantity of the model roots of a given type (see Table 5.1). For the particular distribution of roots used in the centrifuge tests, a group-effect reduction factor was required to model root-soil-root interaction; this parameter is represented by *k* in Eq 5.26. Further DSA tests, which were arranged exactly the same as the centrifuge tests, were performed. Through comparing the additional resistive force in these tests with the 'widely spaced roots' case reported previously, a value of k = 0.78 was found. This value was then applied to the BNWF analyses for the centrifuge simulations.

The apparent root cohesion c'_r was determined in each of cases (i) – (iii) as the additional resistive force per area of specific shear plane at each depth, i.e.:

$$c'_r = F_p / A \qquad \textbf{Eq 5. 26}$$

The resulting variations of c'_r with depth for cases (i) – (iii) are illustrated in Fig 5.11 (b).

The DSA test indicated a negligible change of shear stiffness of rooted soil at the largest confining stress of 12 kPa on the slip plane (this data is shown in Fig 5.12 (a)). A similar phenomenon was observed for testing at other confining stresses (not shown). Measurements made from the buried accelerometers in the centrifuge test indicated a similar result, and also demonstrated that the damping ratio for both fallow and rooted models lay on a similar trend. As a result it was assumed in the FE analysis that the effect of the roots could be incorporated as an additional cohesion only, added to the underlying properties of the HST95 sand. Fig.5.12 also shows some model from the literature (Hardin & Drnevich, 1972; Ishibashi & Zhang, 1993) for comparison.

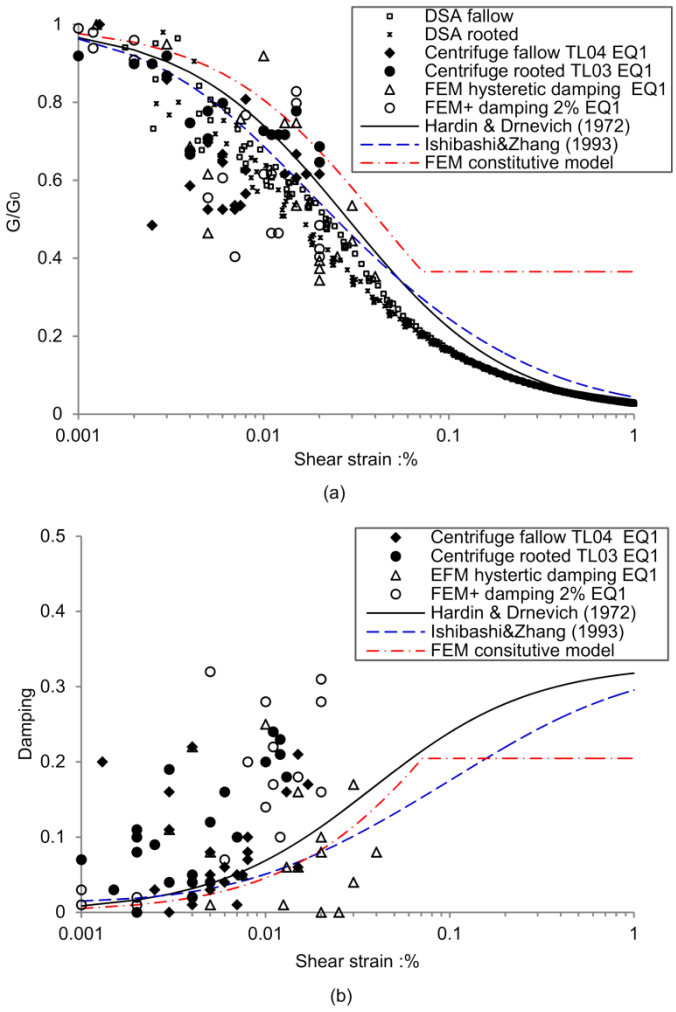

Fig 5.12 Shear modulus degradation and damping as measured in centrifuge tests, DSA tests and FEM simulations of fallow and rooted slopes, and comparison to previously published curves

5.6 Validation of FEM

The key indicators of slope performance considered herein are: (a) peak ground accelerations at the slope crest; and (b) crest settlement.

5.6.1 Fallow slope

Fig 5.13 shows a comparison of measured and simulated accelerations and settlement at the crest of the slope in the earthquake sequence of TL04. The HS small model has inherent hysteretic damping when subjected to the cyclic loading (Brinkgreve et al. 2007). But

according to Fig 5.13 (a), significant over-prediction of accelerations was observed. This appears to be associated with the increased amplification of lower frequency (<4Hz) and higher frequency (>15Hz) components, as shown in Fig 5.13 (b). Al-Defae et al. (2013) reported that additional Rayleigh damping was required to supplement the inherent hysteretic material damping to match ground accelerations when validating a similar FE model against centrifuge tests of a larger slope at 1:50 scale. Rayleigh damping was therefore added to the HS small model, where the equivalent additional viscous damping is given by:

$$\zeta_{add} = c_m\left(\frac{1}{4\pi f_n}\right) + c_k(\pi f_n) \qquad \textbf{Eq 5. 27}$$

Additional damping of approximately 2% at the frequencies of 4 Hz and 30 Hz were determined after several attempts, resulting in values of c_m = 0.8870 and c_k = 0.0001872. Al-Defae et al. (2013) proposed different parameters corresponding to 5% additional viscous damping and proposed that this was required as a result of imperfect replication of the semi-infinite boundary condition by the ESB box in the centrifuge. This would be consistent with a different required damping in this study as the stiffness of the rubber inter-layers in the ESB is normal-stress dependent and so will vary with g-level (Bertalot 2013), and so the container will necessarily perform differently at different values of *N*. Both the crest accelerations and permanent settlement with the additional damping simultaneously gave a good match between the FE simulation and the centrifuge test.

Fig 5.14 shows the accumulated shear strain at the end of the eight earthquakes from the fallow FE model. This indicates that the failure mechanism intersected the slope crest within the boundaries of the ESB container and that it also passed through the toe of the slope, therefore avoiding any potential restraint to motion of the container wall on both sides. This supports the initial decisions regarding optimising the geometry of the slope within the constraints provided by the low scaling factor.

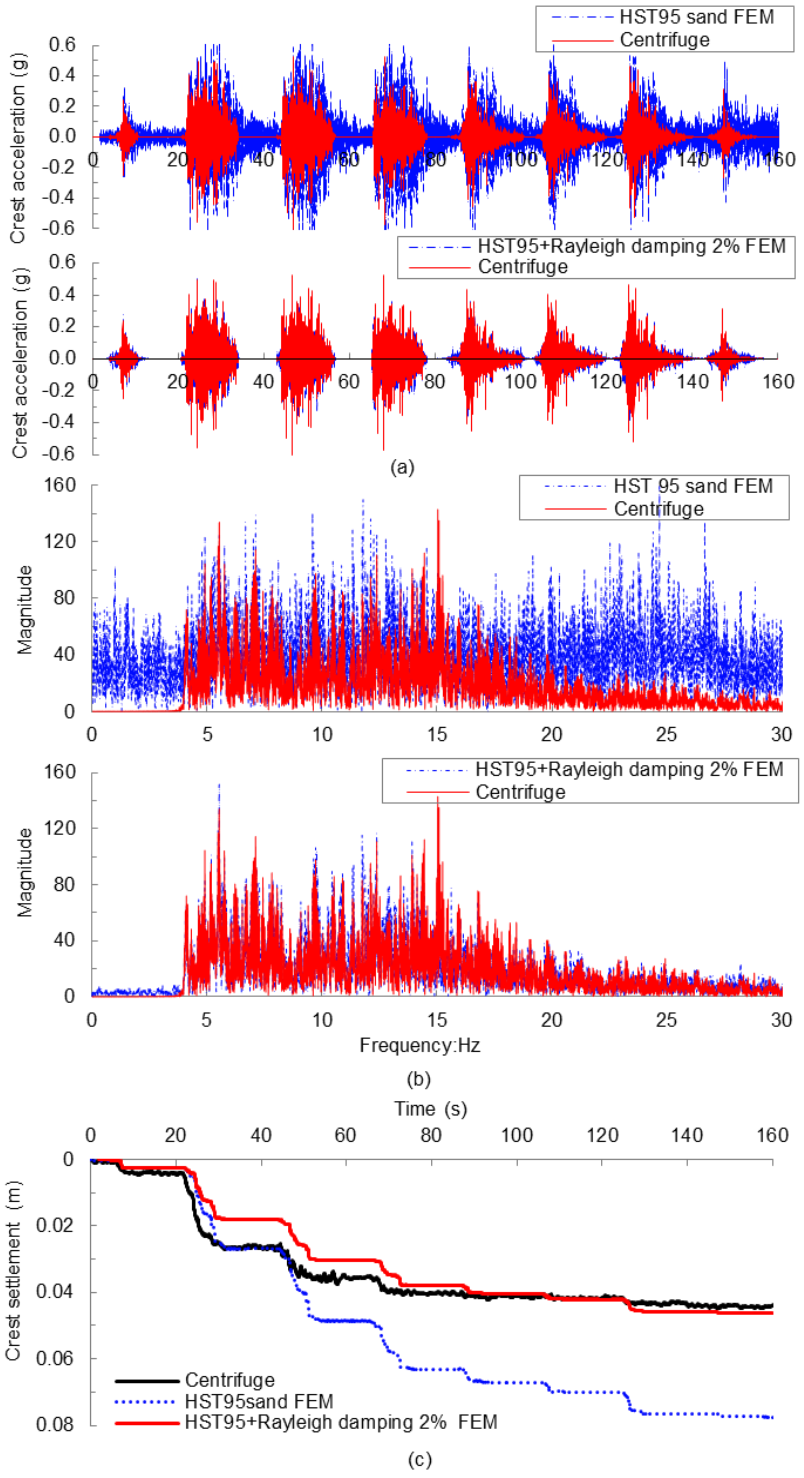

Fig 5.13 Comparison of measured and predicted acceleration and settlement at crest of fallow slope during test TL04: (a) time domain; (b) frequency domain; (c) settlement

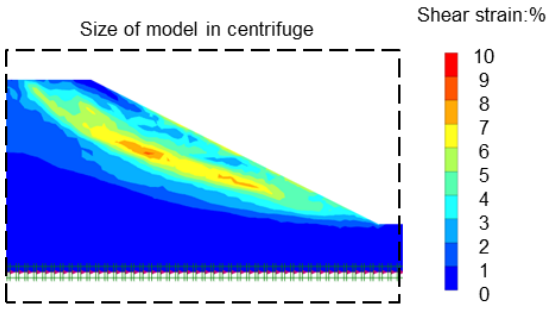

Fig 5.14 Shear strain distribution within fallow FE model (end of simulation)

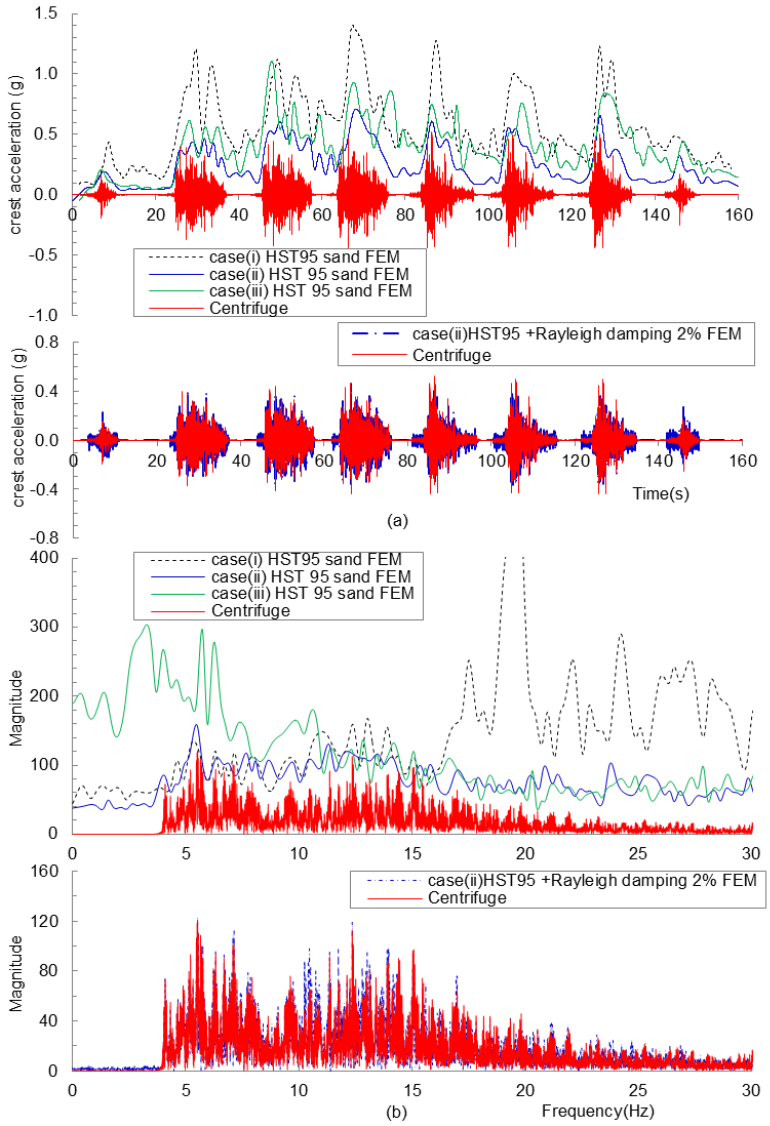

Fig 5.15 Comparison of measured and predicted acceleration for three cases at crest of rooted slope during test TL03: (a) time domain; (b) frequency domain

5.6.2 Rooted slope

The simulated accelerations for the three cases at the crest of slope (instrument 12), compared with those measured from TL03, are shown in Fig 5.15(a) and Fig 5.15(b), in both time and frequency domains, respectively. The accelerations without any additional damping in the three cases for root modelling are shown in terms of the envelope of peak values and generally demonstrate significant over-prediction. It seems that there are some effects of the variation of soil cohesion spatial distribution on the ground motion propagation, as significant differences were observed between the three cases. When Rayleigh damping was added to the model, a good match was observed for all three cases, but case (ii) with damping ratio of 2% appeared to give the best match. This damping ratio corresponds to that in the unreinforced slope, and suggests that the root analogues do not add additional damping to the soil. Case (ii) is illustrated in the figure to show the agreements.

Fig 5.16 (a) presents a comparison of the permanent crest settlement for the three root modelling cases against the centrifuge test measurements. In contrast with cases (i) and (iii), case (ii) successfully captures the pattern of settlement, specifically the root strength mobilisation in the first two motions and the re-grading effect in the subsequent motions, and this case also shows the best match simultaneously to the crest acceleration (Fig 5.15 (b)). This suggests that the root soil interaction observed from the BNWF macro-element modelling is consistent with the global dynamic behaviour of the rooted slope. It also suggests that it is important in modelling the boundary value problem not to distribute additional resistance uniformly across the slope (as in case (i)), but to know the boundaries of the zone where the roots are. Fig 5.16 (b) shows the accumulated shear strain in case (ii) for comparison with the fallow case (Fig 5.14). It can again be seen that the failure mechanism is well fitted to the size of the centrifuge model and also interestingly shows how the rooted zones act to buttress the slope, almost acting like soft retaining walls. This fundamental change in mechanism may explain why the crest settlement is so sensitive to the spatial distribution of the root reinforcement (i.e. case (i), (ii) or (iii)).

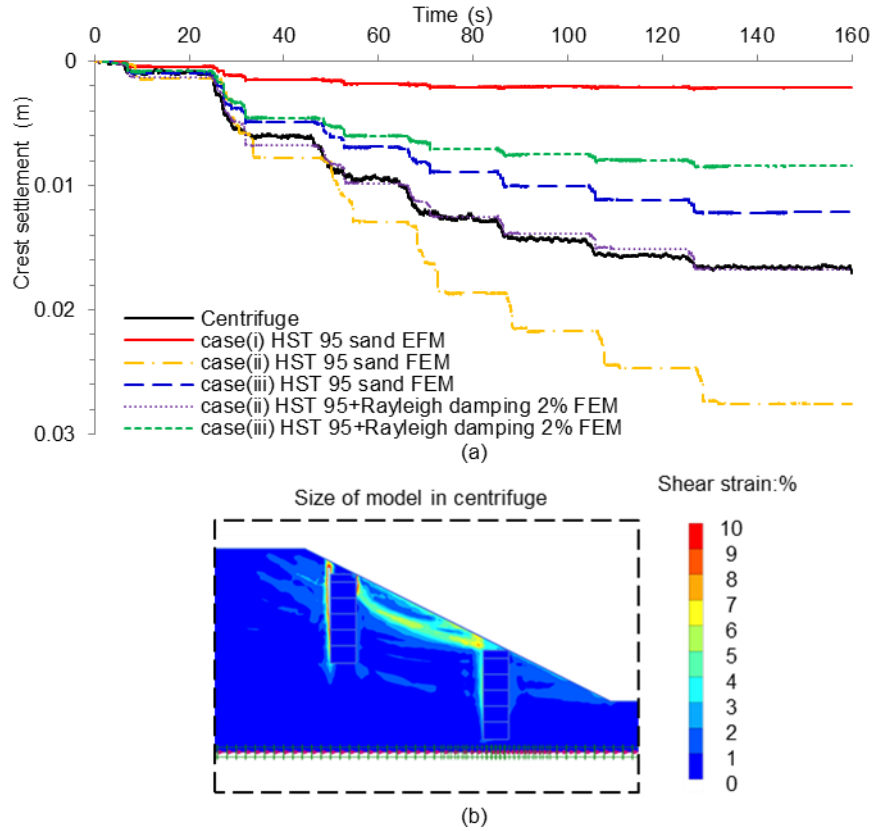

Fig 5.16 (a) Comparison of measured and predicted permanent crest settlement for three cases of root modelling during test TL03; (b) Shear strain distribution within rooted FE model (end of simulation, case ii)

5.7 Conclusions

Dynamic centrifuge testing has been performed to investigate the performance of slopes containing root analogues under a sequence of earthquake motions. 3-D printing of layered ABS plastic was used to produce repeatable root analogues which are highly representative of the mechanical behaviour of real roots. The observed slope behaviour has been simulated using a two-stage approach in which a BNWF approach using existing *p-y* curves was employed to evaluate individual root-soil interaction, and this information was then used to evaluate equivalent smeared properties for use in plane strain continuum Finite Element Analysis (FEA). The whole numerical simulation approach was validated against the centrifuge test data. The following principal conclusions can be drawn from the study:

1) Reduction of up to 61% in permanent crest settlement was observed for the small height prototype slope (1:2 slope, height 2.4 m) considered herein which was 'planted' with root analogues. The reduction mainly occurs in the first two motions (which cause the largest amounts of slip) due to the mobilisation of the root-soil interaction.
2) The BNWF macro element approach gave comparable prediction of the performance of the particular soil-root analogue system considered when undergoing monotonic shear loading. The root behaviour appeared to be dominated by transverse bending rather than axial tension when subjected to lateral soil movement. This suggests that the measurement of root material properties for slope stability analyses should therefore take into account this mode of deformation, and root-soil interaction models based on axial response may underestimate the available mechanical soil reinforcement from roots.
3) Continuum FEA using appropriately-sized zones of smeared rooted soil properties derived from the BNWF macro elements was validated to be effective at simulating the global dynamic performance of the slope reinforced with root analogues that was considered in the study. The influence zone of root groups is complex, but when simplified to the boundary geometry that the root group actually occupies, it appears to provide a very reasonable simulation.
4) Consistency was observed between dynamic acceleration and permanent soil movements in the FE simulations. A small amount of additional viscous damping was required to achieve the best match to the centrifuge data.
5) The root analogues tested added additional shear strength to the soil, but did not have an appreciable effect on modifying the soil stiffness or damping.

Chapter 6 Evaluation of the seismic performance of rooted slopes using centrifuge modelling

6.1 Introduction

This chapter will give further insight into the seismic performance of rooted slope. A series of centrifuge tests will be performed at different scales (1:10 and 1:30) and corresponding centrifugal acceleration fields (10-g and 30-g, respectively) under a sequence of earthquake ground motions. Input motion frequency content and slope height, which are often considered to be the key factors influencing the seismic behaviour of slopes are studied. The boundary effect in the ESB container will also be presented. Following this, the potential benefit of roots on slope performance will then be further discussed.

6.2 Dynamic centrifuge modelling

6.2.1 Model preparation

Five tests with varied g level and motion frequency (as indicated in Table 6.1) are compared in this chapter. All values presented herein are given at prototype scale, unless specifically noted otherwise. Typical model layouts are shown in Fig 6.1 for model TL 06 and TL 07. More details about model preparation and soil properties can be found in Chapter 3.

Table 6.1 Summary of Centrifuge models tested

Test identification number	Test scale	Slope height (m)	Root type	root cluster quantity	Motion frequency content (Hz)
TL 04	1:10	2.4	Fallow	0	4-30
TL 05	1:30	7.2	Fallow	0	1.33-10
TL 06	1:30	7.2	1:30 scale root cluster	36	1.33-10
TL 07	1:10	2.4	1:10 scale root cluster	4	4-30
TL 08	1:30	7.2	Fallow	0	4-10

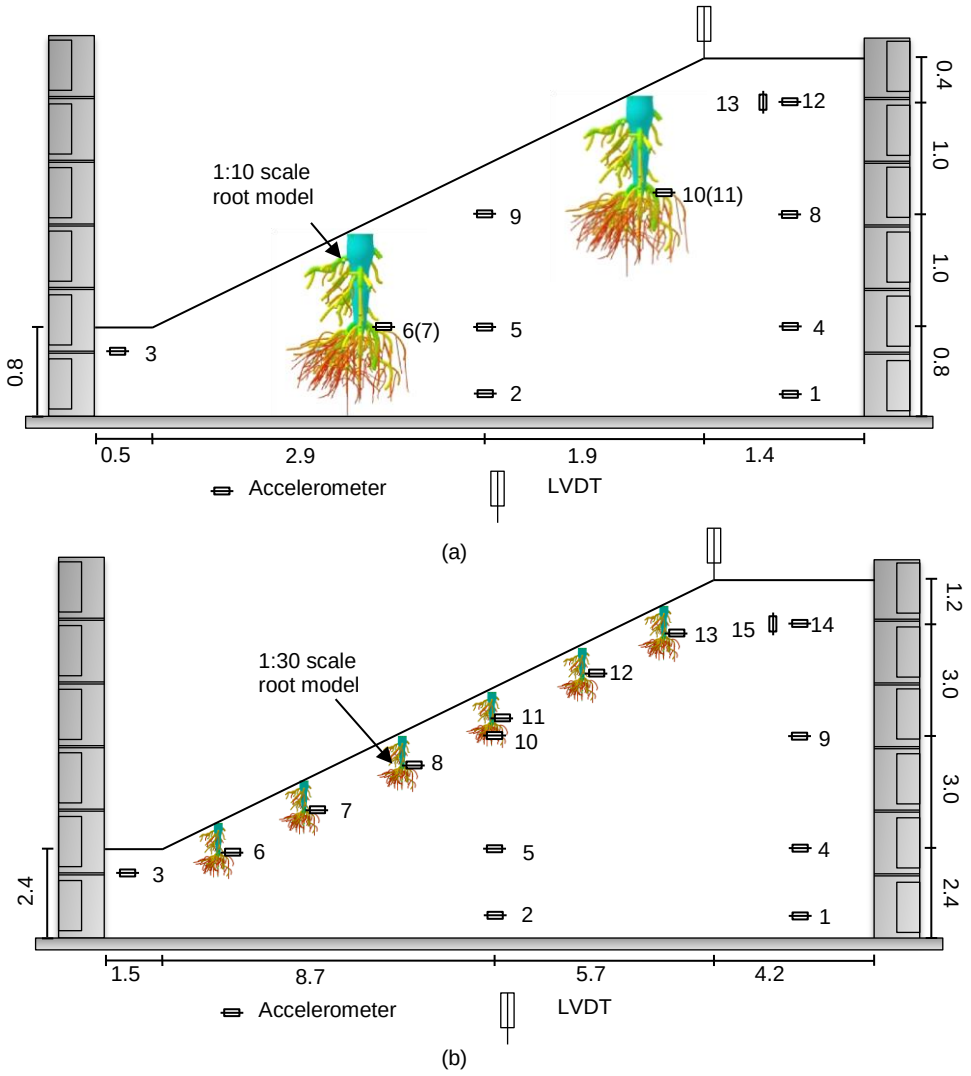

Fig 6.1 Schematic of centrifuge model geometry, instrumentation and position of root analogues: (a) 1:10 scale model; (b) 1:30 scale mode (Dimensions at prototype scale in meters)

6.2.2 Model tree roots

A simplified 3-D root model cluster (Fig 6.2) with root area ratio (RAR), root distribution and root length representative of a 1:10 and 1:30 geometrically-scaled tree root cluster consisting of a tap-root system was modelled and idealised. Further details relating to the design of this model can be found in Chapter 4. All of the roots except the tap root were simplified into circular curved bars and classified into different types (after Watson et al. 1995) based on their diameter, as shown in Table 6.2.

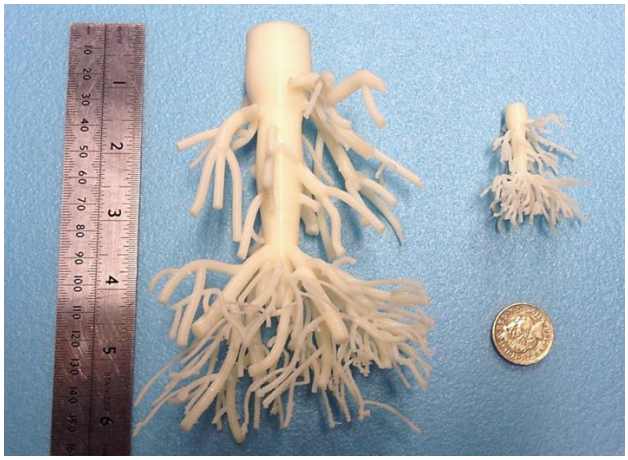

Fig 6.2 ABS plastic root model from 3D printer showing the size difference between 1:10 scale and 1:30 scale

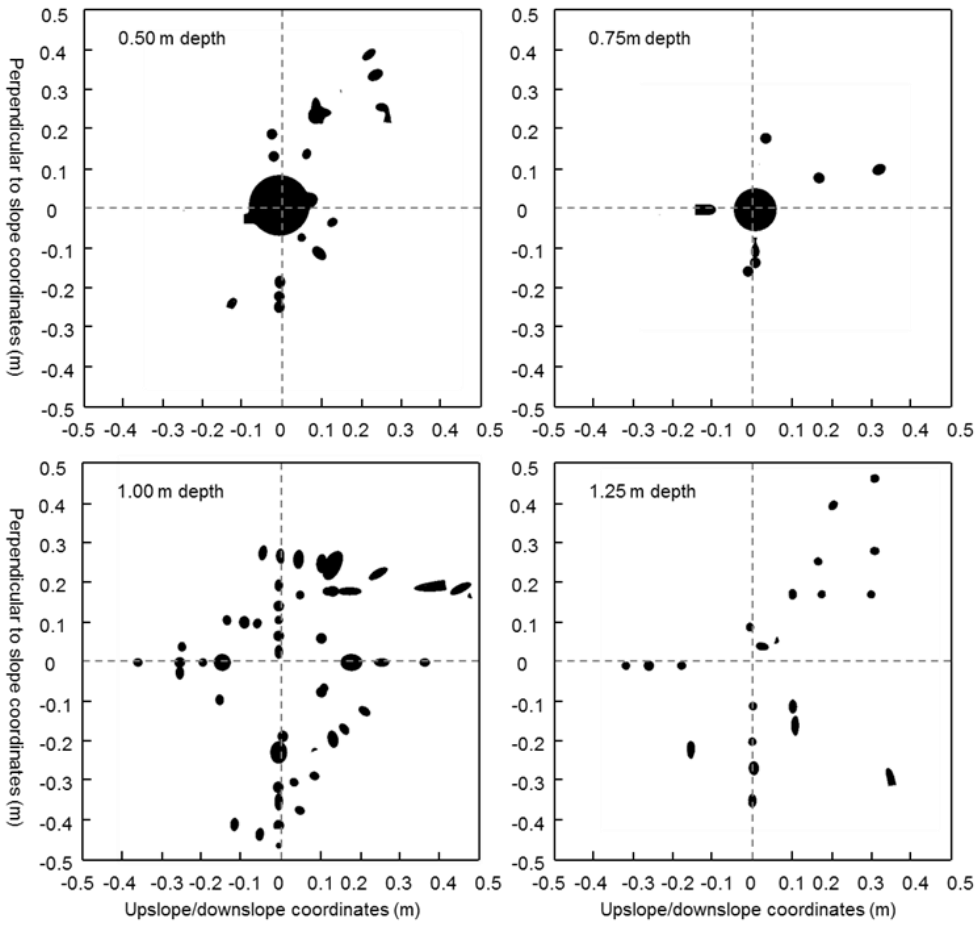

Fig 6.3 Multiple 2D distribution of roots intersecting four planes at different depths below the ground surface for 1:30 scale 3D root models at prototype scale (downslope positive)

Table 6. 2 Root diameter class for medium and structural roots (not including tap root)

Diameter at 1:10 model scale(mm)	Diameter at1:30 model scale(mm)	Diameter range at prototype scale(mm)	Root class at prototype scale (after Watson et al. 1995)
-		<5	fine
0.8	-	5-10	small
1.6	0.8	10-20	medium
3	1	20-40	large
5	1.6	>40	coarse

The model roots were fabricated using the Stratesys Inc. uPrint SE Acrylonitrile Butadiene Styrene (ABS) prototyper (also known as 3D printer) at the University of Dundee following the procedures outlined in Liang et al. (2014). Compared with the 1:10 scale root cluster, the type "small" roots were eliminated in 1:30 scale root cluster due to the threshold minimum manufacturing size in the 3D printer (0.75mm). The corresponding difference of root distribution at prototype scale is shown in Fig 6.3. The 3D printing technique can generate a uni-directionally layered structure, which can successfully simulate the fibrous structure of tree roots. The layered ABS plastic root analogues were validated to be highly representative of the mechanical behaviour of real roots after a series of element tests, which is described in more detail in Chapter 4 and Chapter 5.

The mean particle size of the sand used was 0.16 mm, while the minimum diameter of root segments modelled was 0.8 mm, which is only $5D_{50}$. Ovesen (1979) proposed that there was some deviation from continuum behaviour in centrifuge models when the ratio of foundation diameter to grain size was less than approximately 15. To verify what the impact of potential scale effects might be, a series of direct shear tests were conducted in a large direct shear apparatus (DSA) . The same 3D root cluster and density of soil as used in the centrifuge tests were used in the large DSA. The varied confining stress for different potential slip plane locations in the centrifuge test was simulated in the DSA through altering the surcharge weight. However, it should be noted that the same confining stress with position along the root in the centrifuge tests could not truly be simulated, as shown in Fig 6.4(a). The DSA tests did verify that the additional shear strength for both 1:30 and 1:10 scale root clusters were of the same order of magnitude, as shown in Fig 6.4(b). Here the difference of root cohesion between 1:30 and 1:10 scale root cluster can been considered as an evidence of particle size effect due to the change in the ratio of root diameter to grain size.

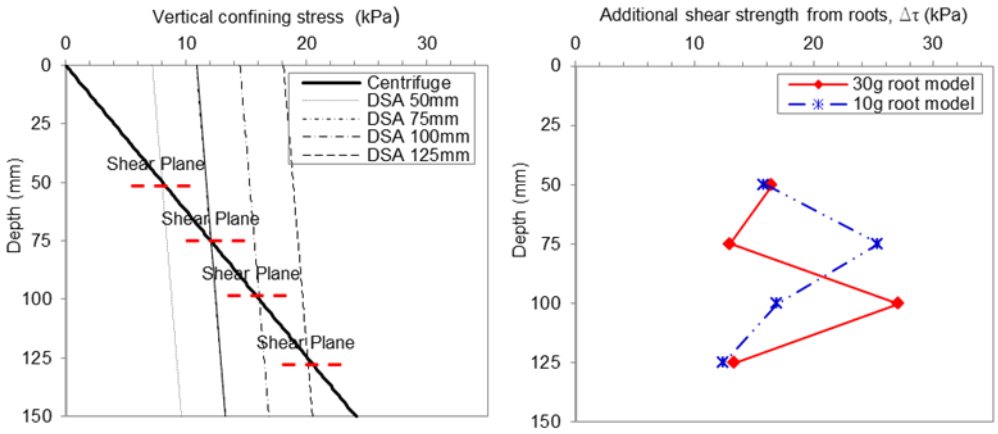

Fig 6.4 Comparison of DSA tests of 1:10 and 1:30 scale root clusters: (a) variation of confining stress (b) additional shear strength provided by roots

6.2.3 Earthquake events

Each slope model was subjected to eight successive earthquake motions, full details about these motions are presented in Chapter 3, The motions were each band-pass filtered using 512 point filter to obtain demand motions (see Fig 6.5) which were within the controllable range (40-300Hz at model scale) of the EQS. At 1:10 scale this range is between 4Hz and 30Hz, while at 1:30 scale this range is between 1.33Hz and 10Hz. Significant differences in the seismic performance of slopes between these two scales may be expected due to the combined effects of different slope height and input motion frequency. A reduced range of 4-10Hz at 1:30 scale was therefore also introduced to provide both 1:10 scale and 1:30 scale models with the same amount of low frequency motion (<4Hz) filtered out in each case, so that a comparison could be made where only the slope height was different in the fallow case. All motions were initially calibrated on a dummy slope identical to Fig 6.1, but without instrumentation before formal testing to obtain repeatable achieved motions as close as possible to the filtered demand motions.

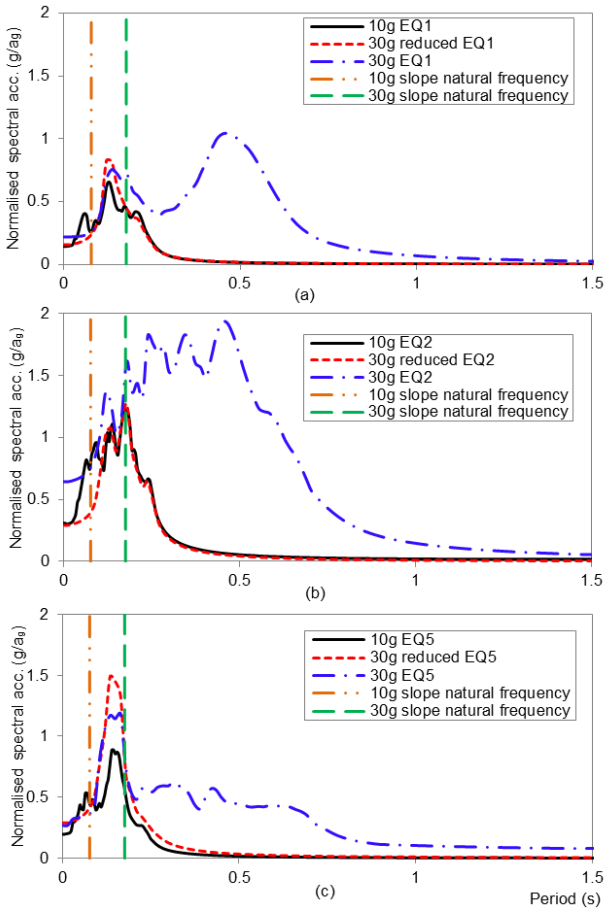

Fig 6.5 Input motions for different models: (a) Aegion; (b) Northridge; (c) L'Aquila

6.2.4 Natural frequency of the model slopes

The natural frequency (f_0) of the model slopes was estimated using:

$$f_0 = V_s / kH \qquad \textbf{Eq 6. 1}$$

where V_s is the shear wave velocity, H is the soil layer height and k is a coefficient for the shape of the soil layer (k = 4 for a half-infinite horizontal layer; k = 2.61 for a triangular shaped layer (Gazetas & Dakoulas 1992)). In this study, no resonant column (RC) tests were performed, but the shear wave velocity can be related to the maximum shear modulus (G_0) at small strain below the elastic threshold,

$$G_0 = \rho V_s^2 \quad \textbf{Eq 6. 2}$$

where ρ is density of the soil. Given the angular grained sand particles of HST 95 sand used in this study, G_0 was estimated using the relationship based on void ratio (e) proposed by Hardin & Drnevich (1972):

$$G_0 = 3230 \frac{(2.97-e)^2}{1+e} \cdot \sqrt{p_0^{'}} \quad \textbf{Eq 6. 3}$$

where $p_0^{'}$ is the initial mean effective confining stress ,which can be expressed as:

$$p_0^{'} = \frac{(1+2K_0)\sigma_v^{'}}{3} \quad \textbf{Eq 6. 4}$$

where $\sigma_v^{'}$ is the vertical effective stress and K_0 is the earth pressure coefficient at rest, which was estimated using:

$$K_0 = 1-\sin\phi^{'} \quad \textbf{Eq 6. 5}$$

where $\phi^{'}$ is effective angle of friction. A value of $\phi^{'}$=32° was reported by Al-Defae et al. (2013) for HST 95 sand.

According to Eq 6.1- Eq 6.5, the average natural frequency of the slope for 1:10 and 1:30 scale were estimated to be 12.9 Hz (0.08 s period) and 5.7 Hz (0.18 s period), respectively, and these values are shown in Fig 6.5.

6.3 Seismic performance of fallow slopes

The seismic response of the fallow slopes under sequences of strong motion will firstly be discussed. This will provide a benchmark to subsequently assess the comparative performance of the rooted slopes.

6.3.1 Dynamic response – effect of input motion frequency content

Comparing the 1:30 scale fallow models at reduced frequency range (TL-08) and at 'full' frequency range (TL-05) allows the same slope profile at prototype scale to be considered with the only difference being in the amount of low frequency signal content in the ground motion. Comparison of the seismic performance of these two models is important to determine what the implications of a lack of low frequency content will be on slope behaviour, such as was necessitated by the scaling factor used in the 1:10 scale tests.

A comparison of the peak acceleration amplification factor (S_{pk_amp} = peak acceleration at a given depth divided by the peak acceleration of the input motion in the centrifuge tests) as a function of normalised elevation (z/H) of models TL 05 and TL08 is shown in Fig 6.6. Here, the first motion of each type was selected (i.e. EQ1, EQ2 and EQ5). Values estimated from Eurocode 8, Part 5 (BSI, 2005b) for the crest (z/H = 1), are also included for comparison, where:

$$S_{pk\_amp} = S \cdot S_T \qquad \textbf{Eq 6. 6}$$

where S is a soil factor describing the site effect (= 1.4 for the 'ground type E ' soil in this study, as classified using Eurocode 8, Part 1 (BSI,2005a)) and S_T is a topographic amplification factor (≥ 1.2 for shallow slopes). The overall minimum amplification factor is then 1.7.

The response in the deeper soil (z/H < 0.2) was very similar in each case and included a limited amount of attenuation for EQ2 and EQ5 with the higher peak input motion, as previously observed by Ha et al. (2014). Towards the crest of the slope, the reduced motions generally result in smaller peak accelerations, with the exception of EQ2 – this is broadly in agreement with Fig.6.5, given the natural frequency of the 1:30 scale slope. Fig 6.7 shows a comparison of the spectral amplification factor (S_{amp}, given by dividing the crest spectral ordinates by those of input motion) between the same two models and shows that the motion which gives the highest S_{pk_amp} in each case is the one with the highest S_{amp} at periods below the natural period of the slope. This is perhaps to be expected as $S_{amp}(0) = S_{pk\_amp}$. Therefore, filtering out the low frequency (high period) components of the motion, such as was

necessitated by the low scaling factor in the 1:10 tests, will not have such a significant impact on dynamic amplification within the slope. It is also apparent from Fig 6.7(c) that the L'Aquila motion (EQ5-EQ7) is highly suitable for use in tests where different scaling factors are applied. The same is likely to be true of other motions with only limited low frequency (high period) content (see Fig 6.5).

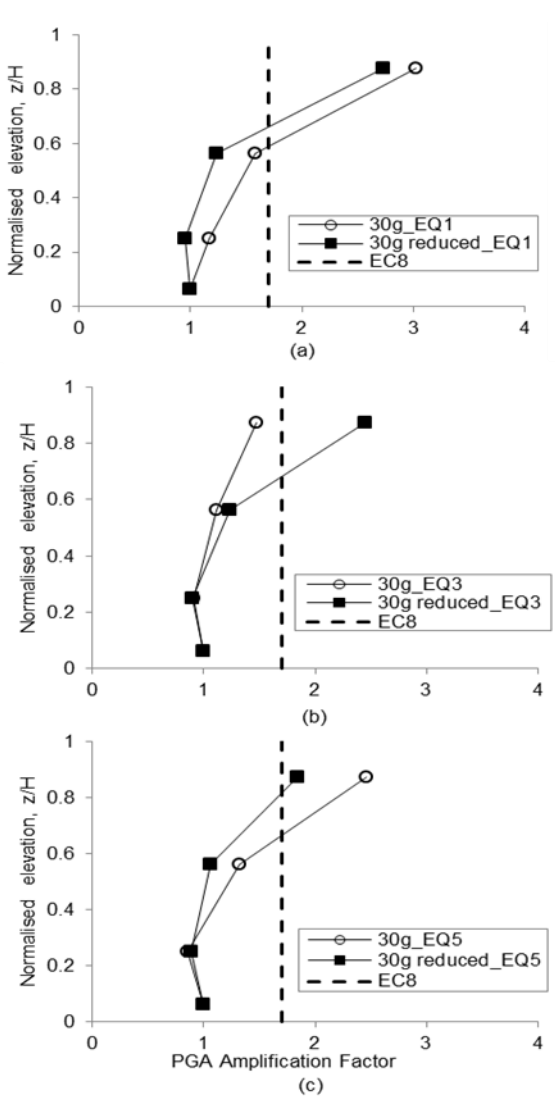

Fig 6.6 Comparison of peak acceleration amplification behaviour between 1:30 scale model at 'full' and reduced frequency content: (a) in EQ 1; (b) in EQ 2; (c) in EQ5

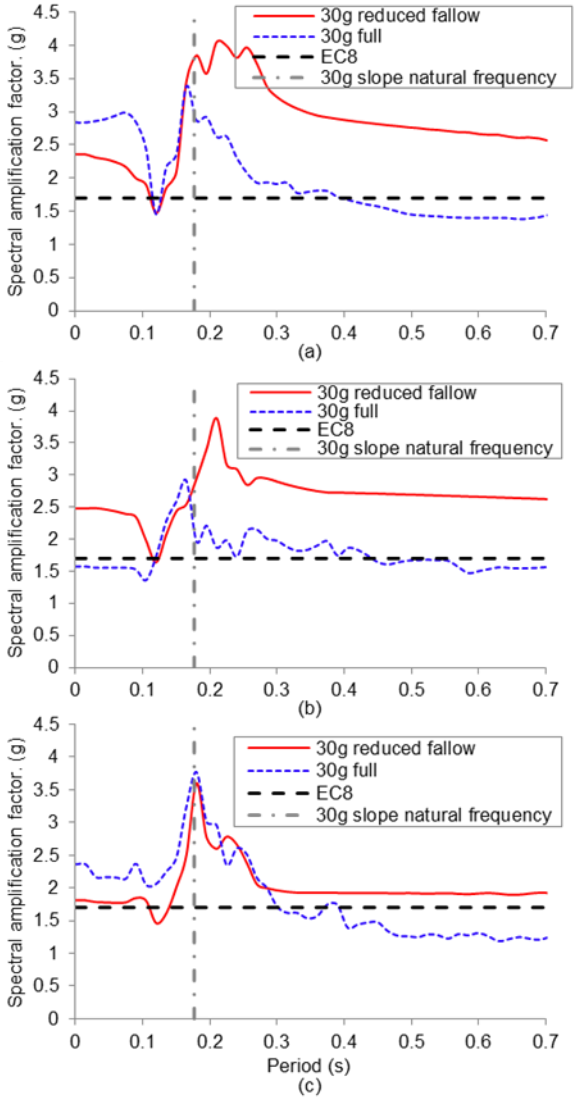

Fig 6.7 Comparison of ARS amplification factor between 1:30 scale models at 'full' and reduced frequency content: (a) in EQ 1; (b) in EQ 2; (c) in EQ5

It should also be noted that in almost all cases shown in Fig 6.7, S_{amp} is significantly higher than the constant minimum value proposed by a modern design code such as EC8. This suggests that a full site response analysis including topographical effects is important, particularly for cases where there is short period infrastructure sited at (or near) the crest of the slope which is sensitive to accelerations (e.g. low-rise masonry and other brittle structures).

6.3.2 Dynamic response – effect of slope height

Having ascertained the impact of the input motion frequency content, a comparison of tests TL-04 and TL-08 allows a comparison of two 1:2 slopes of different heights, namely 2.4 m and 7.2 m, respectively, in each case with the same low frequency cut-off in the input motion (4 Hz).

The ground motion at the crest for model TL 08 was observed to be generally larger than that of TL-04 for the same peak acceleration of the input motion. The variation of peak acceleration amplification factor with normalised elevation for these cases is shown in Fig 6.8. In two out of the three motions considered (EQ1 and EQ2 as shown in Fig 6.8), the taller slope shows increased amplification compared to the shorter slope, up to or beyond 2.5 × the input motion peak. In all cases the amplification at the crest is significantly larger than the value of 1.7 suggested by EC8. These observations would suggest that topographic amplification factors should be substantially increased, particularly in taller slopes.

6.3.3 Dynamic response – effect of aftershocks/preshocks

Fig 6.9 shows the recorded S_{pk_amp} for the first and last earthquake of similar type in test TL05 (i.e. for the tallest slope with 'full' frequency content). In this way it is possible to observe what the effect of previous strong ground motions is on the dynamic response of the slope in a subsequent event (i.e. in a strong aftershock). Generally the dynamic response of the ground was found to be insensitive to previous shaking, though comparing each pair, a small amount of additional amplification can be seen in the later motion (e.g. compare EQ4 to EQ2 or EQ7 to EQ5). The effect is most apparent comparing EQ8 to EQ1 – these are both nominally the same motion, but EQ8 occurs after a significant amount of strong shaking. These observed

small increases in amplification during later motions are presumably a result of densification of the soil during previous strong shaking.

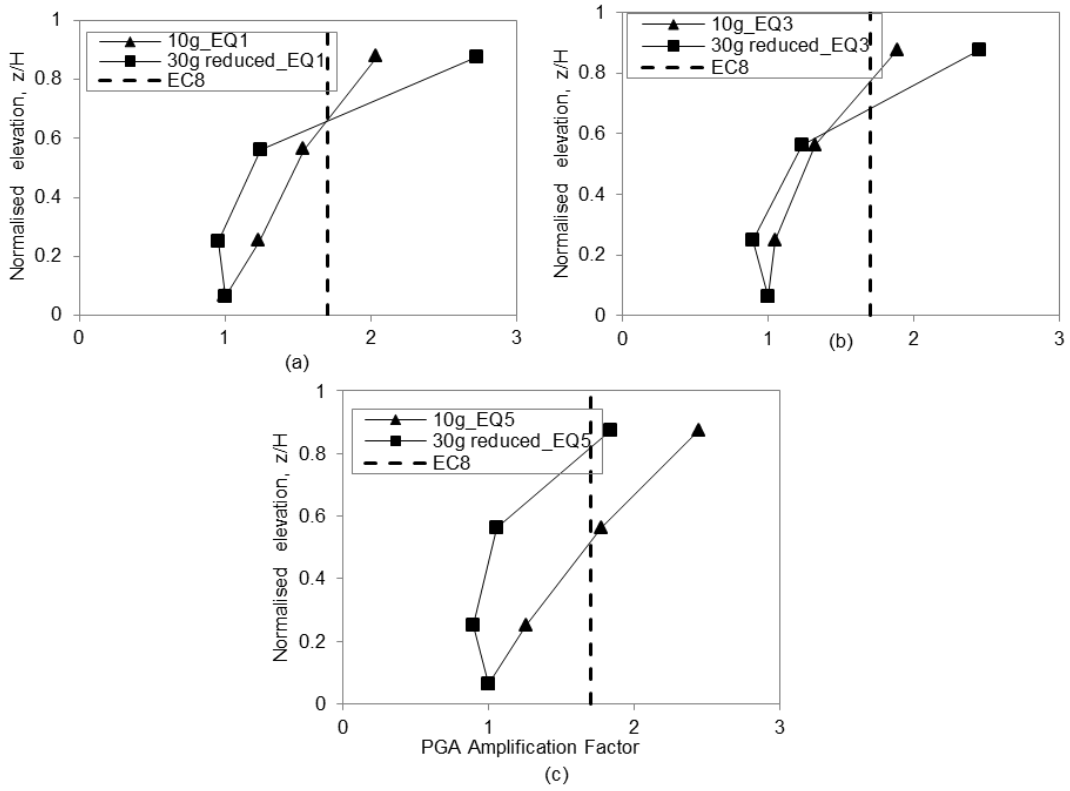

Fig 6.8 Effect of slope height on peak acceleration amplification: (a) in EQ 1; (b) in EQ 2; (c) in EQ5

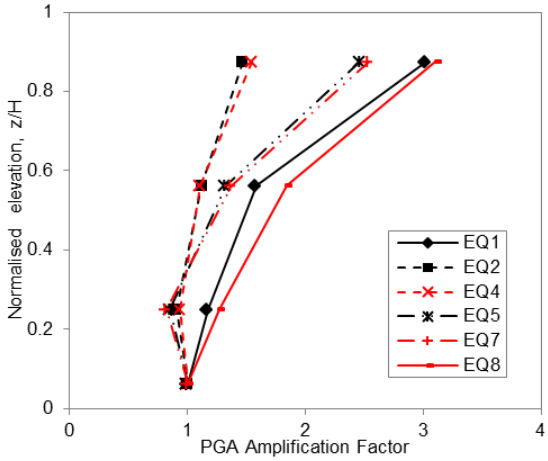

Fig 6.9 Increased peak ground motion amplification in aftershocks, 1:30 scale fallow model (TL 05) shown

6.3.4 Permanent deformations

Fig 6.10 shows a comparison of the permanent crest settlement across the eight earthquakes for model TL-05 and TL-08. It is found that in contrast to the dynamic motions (Fig.6.6) the effect of removing the low frequency content of the input motion is significant on the permanent settlement at the crest. A reduction of 60% on permanent slope settlement was observed when the low frequency content between 1.33Hz – 4Hz was removed. Considering the response in terms of a Newmark sliding block analysis, such components, having longer periods, would result in greater slip when they exceed the yield acceleration of the slope compared to higher frequency components of the same peak ground acceleration, due to the generation of larger slip velocity and hence, displacement. As a result, it is to be expected that these components will contribute significantly to (the greater part of) the accumulated slip.

A comparison of the permanent crest settlement across the eight earthquakes for models TL-04 and TL-08 (i.e. different height slopes) is shown in Fig.6.10. A reduction of approximate 57% on permanent slope settlement was observed when the height of the slope changed from 7.2m to 2.4m. This ratio is broadly consistent with the reduction in peak ground accelerations near the surface of the soil (the likely sliding mass) in the smaller slopes (Fig 6.8) and can again be understood through consideration as a Newmark sliding system. If the two slopes, because of their identical slope angle, will both yield through the formation of a mechanism close to an infinite slope, then their yield acceleration will be the same. However, the larger size of the ground motions will mean that yield will be exceeded more often and with increased slip velocity (and hence, displacement) on each occasion, resulting in increased slip.

As Fig 6.10 also shows the deformations due to the full sequence of eight earthquake motions in each case, it may also be used to compare response in preshocks and aftershocks. As previously observed for fallow slopes by Al-Defae et al. (2013), the permanent slip in subsequent nominally identical ground motions reduces due to re-grading (geometric hardening through a reduction in slope angle). This same effect can be observed in Fig 6.10 particularly comparing EQ2-EQ4 and EQ5-EQ7.

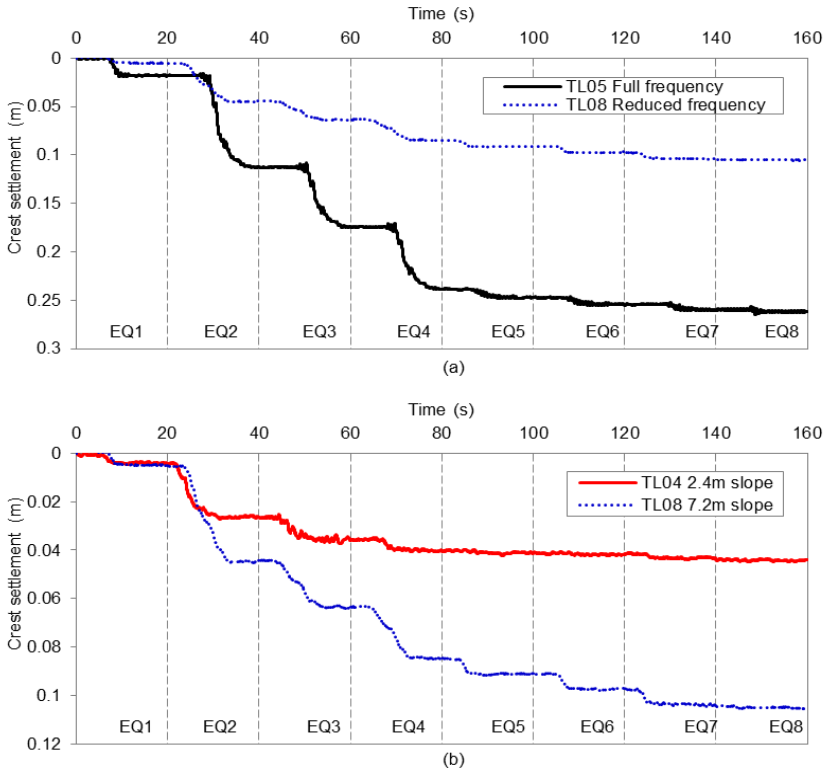

Fig 6.10 Comparison of permanent settlement at the crest in fallow slopes: (a) 1:30 scale models – input motion frequency content effect; (b) 1:10 and 1:30 scale models – slope height effect.

6.4 Seismic performance of rooted slopes

6.4.1 Boundary effect of ESB container

Three external LVDTs were located in the centre of the model (position I) as well as 50 mm (position II, model scale) and 20 mm (position III, model scale) away from the walls of the container along the centreline at the crest of the slope. The permanent crest settlement measured during the seismic events for three positions of model TL06 is shown in Fig 6.11. It was found that permanent deformation at the boundary of the ESB container is 17% higher than that at the centre of the container, and this kept accordance with the boundary acceleration amplification reported by Teymur & Madabhushi (2003). The other models presented the similar behaviour and is summarised in Table 6.4. It should be noted here the crest settlements used later are measured in the centre of the slope model, unless specific noted otherwise, to eliminate the boundary effect as suggested by Zeng & Schofield (1996).

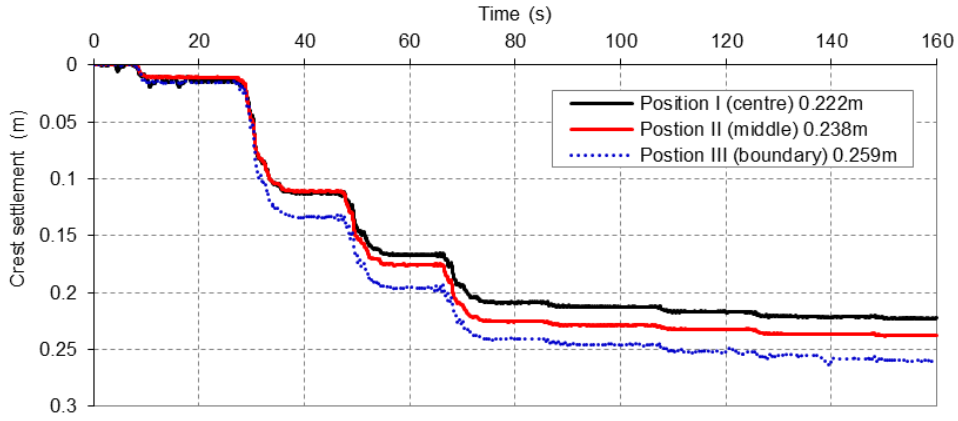

Fig 6.11 Comparison of crest settlement measured at different positions away from the ESB container boundary

Table 6.3 Normalised crest settlement at different positions away from the boundary of ES B container

Test ID	Position I	Position II	Position III
TL4	100%	84%	101%
TL5	100%	100%	110%
TL6	100%	107%	116%
TL7	100%	117%	138%
TL8	100%	108%	130%

6.4.2 Dynamic shear modulus and damping

A comparison of shear modulus and damping as functions of cyclic shear strain within rooted slopes and fallow slopes is shown in Fig 6.12. The data points were determined from second-order estimates using the accelerometer data, following the method proposed by Brennan et al. (2005). The shear modulus at a given cyclic shear strain illustrated a good match between rooted slopes and fallow slopes. This may suggest that the presence of root had quite limited effect on the stiffness of the soil. But for the damping ratio of the soil, the opposite phenomena were observed, that is, 1:10 scale rooted model showed a generally higher value than that of fallow model while a generally lower value was found in 1:30 scale rooted model. Furthermore, it is worth noting here that the 1:30 scale model at full frequency showed a much larger shear strain than the other two cases, which could be related to the magnitude of the motion.

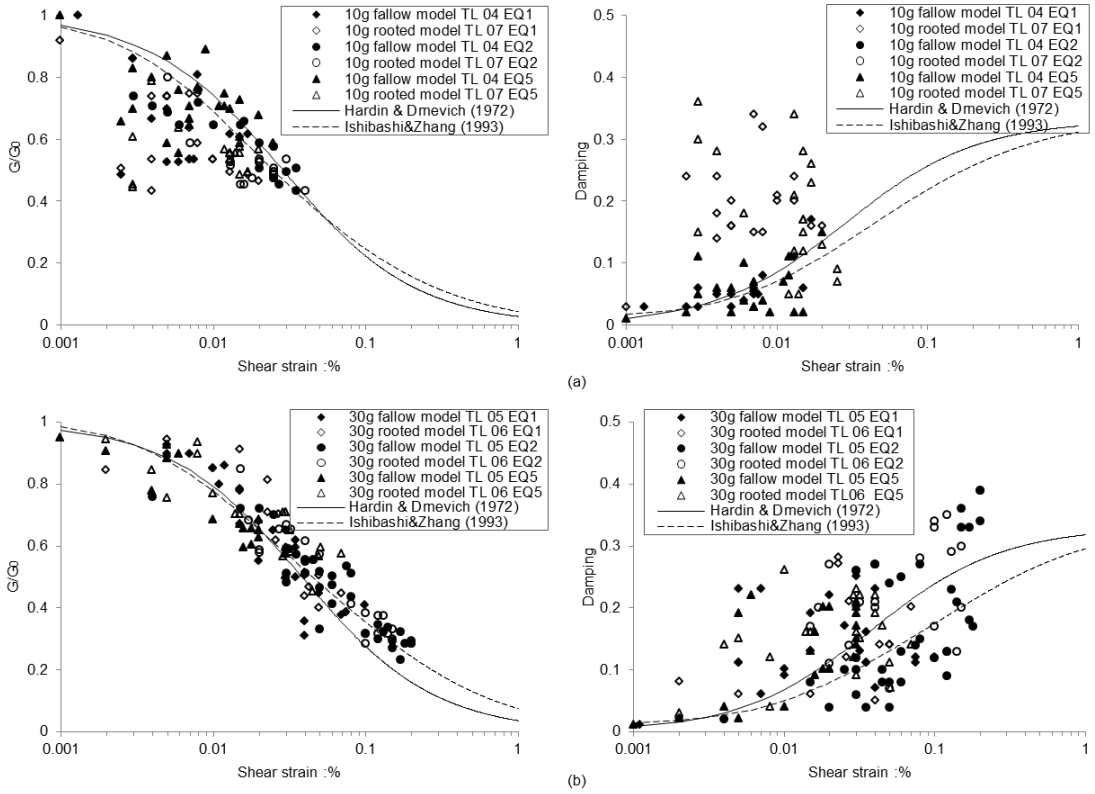

Fig 6.12 Comparison of shear modulus degradation and damping between fallow and root reinforced slopes: (a) 1:10 scale model; (b) 1:30 scale model at full frequency content;

6.4.3 Dynamic response

The ratios of peak acceleration at the crest of root-reinforced slopes to those of fallow slopes for 1:10 scale (instrument 12, Fig 6.1) and 1:30 scale (instrument 14) are shown in Fig 6.13(a). The acceleration for the root-reinforced slope was generally similar to or larger than that of the fallow slope and no significant reductions due to the root presence were observed in any of the three distinct motions (with the exception of three instances, two in EQ5 and one for 1:10 scale in EQ8. This indicates that the presence of the model roots had a very limited influence on the general propagation and amplification of earthquake motion from the toe of the slope to the crest of the slope. Chapter 4 has reported that some reduction in acceleration response was observed in the near-field of root analogues for the 1:10 scale slope; comparative measurements for the wider set of tests reported herein are given in Fig 6.13(b).

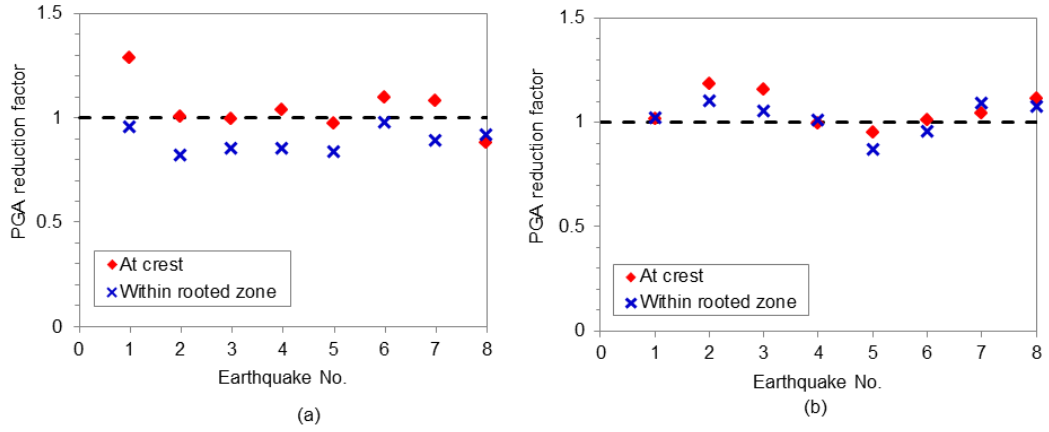

Fig 6.13 Reduction in peak acceleration due to the presence of roots: (a) 1:10 scale model; (b) 1:30 scale model

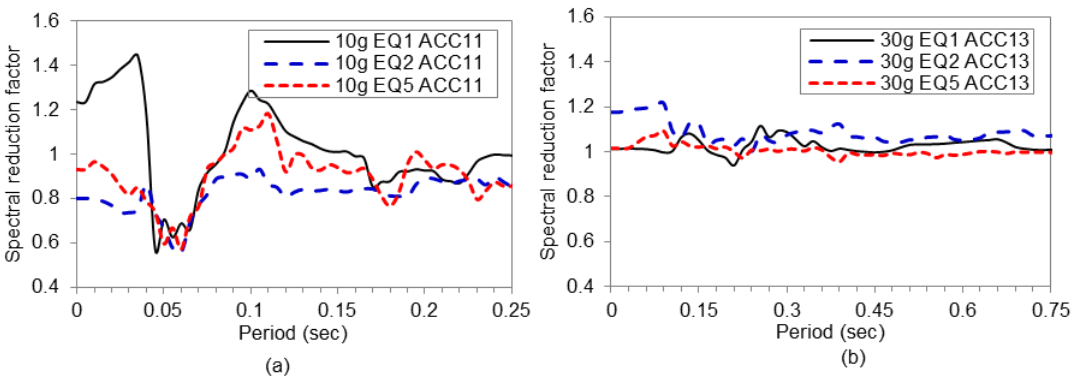

Fig 6.14 Reduction in ARS magnitude due to the presence of roots at the location of a root analogue: (a) 1:10 scale model; (b) 1:30 scale model

It is therefore apparent that although root systems may locally reduce acceleration magnitudes, the effect on the overall slope dynamic motions is still small. To further understand the effect of the roots a spectral reduction factor (S_{red_ARS}) was obtained by dividing the rooted case spectral ordinates at the crest by those for the comparative unreinforced slope, and the resulting data is shown in Fig 6.14. For the 1:30 scale slope, (Fig 6.14(b)), S_{red_ARS} was very close to 1.0, implying a negligible effect of the roots on the dynamic response of the slope. This was not the case for the 1:10 scale slope. Such a difference may be related to the relative size of the root cluster to the slope, particularly in terms of their depth, relative to the slope height. The tree root systems, which have the same 1.5 m prototype depth in each case,

influenced the 1:10 scale slope to a relatively greater depth (1.5/2.4 = 0.63*H*), but only a comparatively smaller proportion of 1:30 scale slope (1.5/7.2 = 0.21*H*).

6.4.4 Permanent deformations

Fig 6.15 shows a comparison of the permanent settlement at the crest of the slope between rooted and fallow cases. As observed for the fallow cases (Fig 6.10), a decreasing trend of settlement was observed in the rooted slopes when subjected to successive strong motions (e.g. aftershocks) attributable to the aforementioned slope geometry change (re-grading). Reductions by 85% and 15% of the permanent fallow slope movement were observed due to the presence of the roots, for the 1:10 scale model and 1:30 scale model, respectively. The majority of this reduction was observed in the first two motions (EQ1 and EQ2) for the 1:10 scale models which is consistent with observations of the straight root analogue case (plate / heart type) previously reported in Chapter 5 and attributable to the rapid mobilization of root-soil interaction due to the initial soil slip under dynamic loading. After the initial rapid mobilization, the additional resistive force of the root was largely constant after the initial mobilization.

With root analogues which had similar strengthening effects on the soil over the upper 1.5 m, given the unavoidable particle size effects (Fig 6.4), the 1:30 scale rooted model experienced a much lower reduction of crest settlement compared with 1:10 scale rooted model. The improvement also only became apparent in the later earthquakes. To understand this behaviour, the Newmark sliding block framework can again be used. Within this framework, the presence of the roots may reduce permanent slip in two ways: (i) by increasing the yield acceleration of the slope; (ii) via a reduction of the dynamic motions within the slope (specifically near the surface in the sliding mass). It has already been shown that the change in acceleration response is small or slightly increasing for both 1:10 and 1:30 cases (Fig 6.13). This leaves increasing the yield acceleration of the slope.

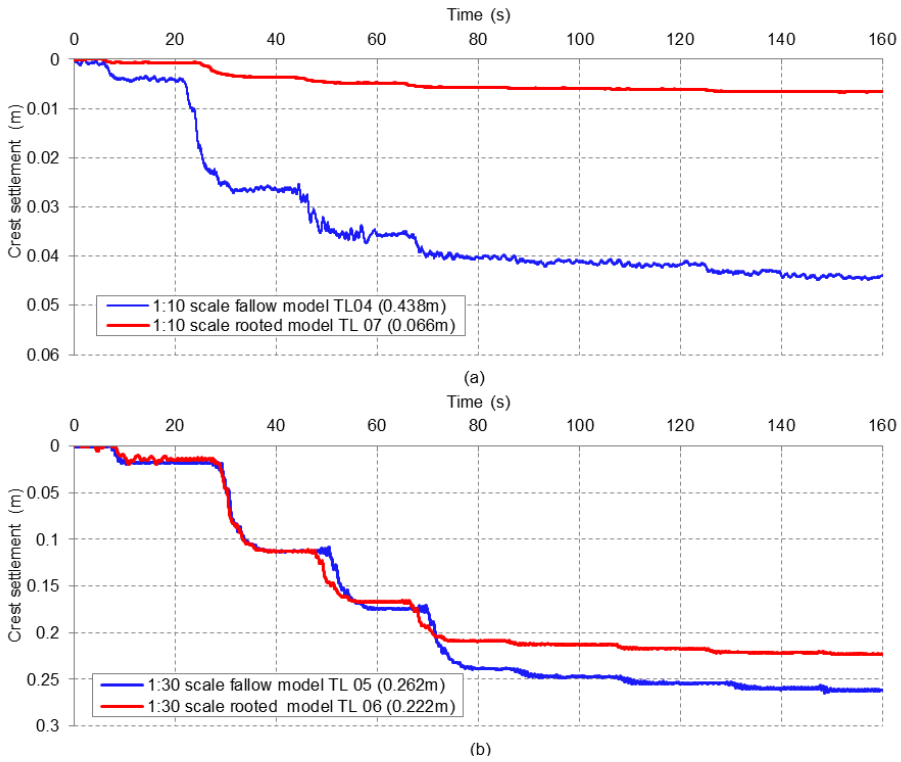

Fig 6.15 Reduction in ARS magnitude due to the presence of roots at the location of a root analogue: (a) 1:10 scale model; (b) 1:30 scale model

Fig 6.4 has shown that in both cases the root models add significant additional shear strength within their zone of influence, especially considering the low confining stresses within the soil over the top 1.5 m. Previously Al-Defae et al. (2013) determined that the shear plane in a fallow 1:2 slope in the same soil at the same relative density and for a similar height (H = 8 m, compared to H = 7.2 m for the 1:30 slope in this study) was at a depth of approximately 0.5 m and was of the translational/infinite type. Therefore it may be inferred that a translational failure will also be critical and at a similar depth in the smaller fallow 1:10 slope. The roots always have a positive contribution to shear strength at whatever depth the shear plane is, until close to their tips, at which point the soil strength reverts to soil only. Therefore it is highly likely that the shear plane over the central (majority) part of the slope will be pushed deeper, as it will be easier to shear through the unreinforced soil below the root tips, rather than through the rooted (reinforced) zone. In the case of the 1:10 scale slope, this would result in significant changes to the geometry of the slip plane at the toe of the slope to form a kinematically admissible mechanism (refer to Fig 6.1). Such changes to the mechanism

geometry would be less severe in the case of the 1:30 slope and so it is likely that the yield acceleration of the smaller (1:10 scale) slope will be increased by more than the taller (1:30 scale) slope. This may explain why the roots are apparently more effective at reducing slip in the shorter slope, however, such a mechanism requires further investigation. This mechanism, and the centrifuge observations from this study, also potentially suggest that there may be a limiting height of slope beyond which other forms of reducing slip (e.g. discretely spaced pile rows, Al-Defae & Knappett, 2014) may be more effective, but also that for slopes of modest height (e.g. small embankments) tree roots may be a very effective seismic slope stabilisation method.

6.5 Conclusion

A series of centrifuge tests has been performed at different scales (1:10 and 1:30) and corresponding centrifugal acceleration fields (10-g and 30-g, respectively) to investigate the performance of slopes containing root analogues under a sequence of earthquake motions under a sequence of earthquake ground motions. The key factors that may influence the seismic behaviour of slopes were studied. The following principal conclusions can be drawn from the study:

1) The crest amplification factors for all cases were observed to be significantly larger than the value of 1.7 suggested by EC8. These observations would suggest that topographic amplification factors should be substantially increased, particularly in taller slopes.
2) Filtering out the low frequency (high period) component of the motion, will have a significant effect on slope deformation response, but will not have a significant impact on dynamic amplification within the slope.
3) Seismic performance of the slope was found to be highly influenced by the slope height; the reason for this is due to the change of the natural frequency of the slope hence a distinct resonance response.
4) The dynamic response of the ground was found to be insensitive to previous shaking.
5) The stiffness of the soil for the overall slope was found to be insensitive to the presence of roots, but this would not be the case for the damping of the soil.

6) The influence of roots on the seismic performance of roots varies with the size of the slope. In this study, for the slope reinforced with similar tree roots, the small size slope performed much better than the large size slope, both in the acceleration response and permanent slope movement.

Chapter 7 Development of FEM-based tools for determine seismic performance of vegetated slope

7. 1 Introduction

The two-part numerical modelling approach developed in Chapter 5 is validated to be effective for plate / heart root systems of shrubs and trees, of which most of the individual roots behave independently. However, for the deep tap root system, it may not be the case given the fact that the main tap root penetrated into the soil to significant depth and mobilised other roots to resist soil movement. Experimental evidence of the distinct behaviours between such a tap root system (3D root cluster) and the plate / heart root type (straight root group) with the same distribution at a given shear plane during shear loading has been illustrated in Chapter 4. Hence, the modelling approach which can be used for a tap-root system will be developed in this chapter and validated against the centrifuge tests data reported in Chapter 6. Following validation, a parametric study was conducted to investigate the influence of different potential characteristics of rooted soil on the overall seismic performance of slope with different size.

7.2 Finite element modelling

The two–dimensional numerical simulations were conducted using the commercial finite element program PLAXIS 2D. The numerical models of TL 06 and TL 07 are shown in Fig 7.1. The dimensions of the slope were established based on the prototype size of the centrifuge with extensions at the left and right boundary to simulate semi-infinite soil conditions as closely as possible the boundary performance in the ESB container using adjacent soil. Full details of the boundary conditions can be found in Chapter 5. Input earthquake loading was applied in time domain along the bottom of the model (indicated by the arrows in Fig 7.1). The waveform used in each case was the acceleration record measured at instrument ACC2 in the centrifuge tests. Before input, the motions were band-pass filtered

using an 8th order Butterworth filter defined by a zero phase filtering method. Through this way, any steady-state offset and noise content outsider the demand frequency content in accelerometer recording could be eliminated.

The ESB container used in this study was designed to match the dynamic stiffness of the soil subject to 2010 Maule earthquake (PGA =0.4g) under an acceleration filed of 50g (Bertalot 2013). However, during earthquake, the stiffness of the soil, which depends on the void ratio, effective stress and shear strain, will change while the stiffness of the container is fixed (Madabhushi & Teymur 2003). Unwanted boundary effect will be generated due to the different g level and input earthquake motions compared with the design cases. The boundary effect along the crest was observed and demonstrated in Chapter 6. So crest settlements used in analysis were measured in the centre of the slope model as suggested by Zeng & Schofield (1996) to avoid the boundary effect. However, whether this point stands for no boundary effect or not is still uncertainty and requires further identification given the fact that the crest located very near to the ESB container wall (1.4m at prototype) at 1:10 scale slope.

In Chapter 5, the semi-infinite soil condition rather than the real case with ESB container was established with the aim to highly reduce (more than 80% for the same global coarseness) the computational time and physical memory requirement. But such condition was based on the assumption of good performance of ESB container and relative small effect on slope performance from ESB container wall. This assumption will be identified through comparing the seismic performance of semi-infinite soil condition case and ESB container case.

7.2.1 Soil constitutive models

All soil materials were simulated using the Hardening Soil constitutive model with small-stain stiffness (HS small, Schanz et al. 1999). This stress and strain dependent elastic part of the model was originally derived from the strain dependent stiffness model proposed by Hardin & Drnevich (1972):

$$\frac{G}{G_0} = \frac{1}{1+\left|\frac{\gamma}{\gamma_r}\right|} \qquad \textbf{Eq 7. 1}$$

where the threshold shear strain γ_r is quantified as :

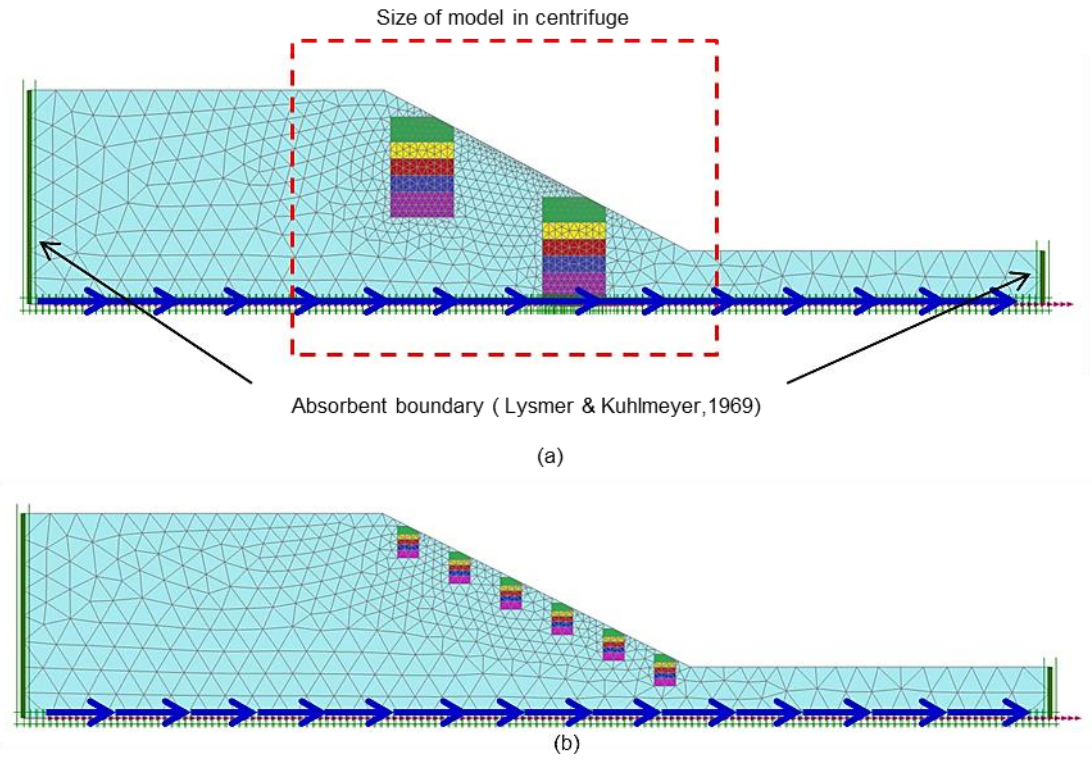

Fig 7.1 Finite element mesh, showing boundary conditions: (a) 1:10 scale model (b) 1:30 scale model

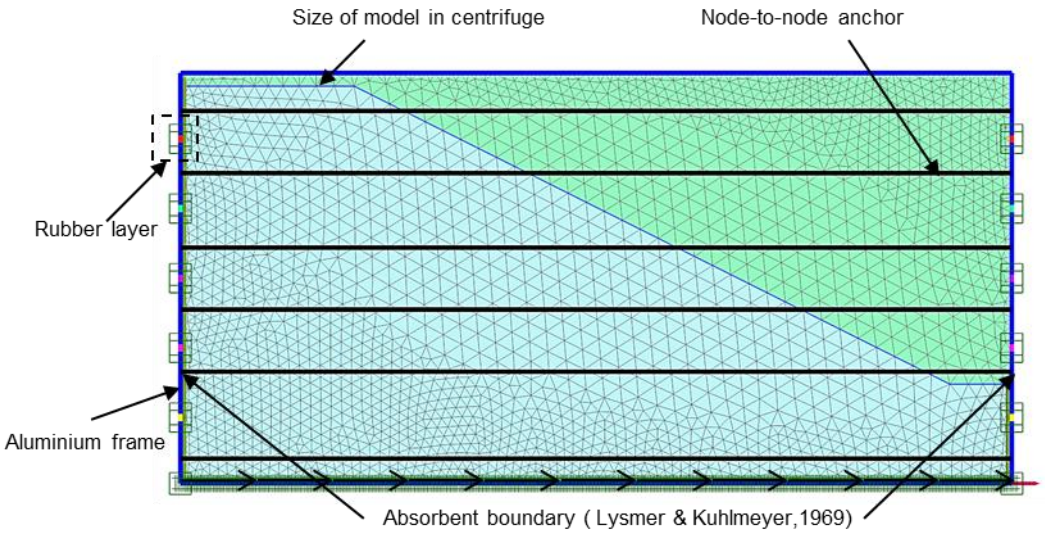

Fig 7.2 Finite element mesh of ESB boundary model (1:10 & 1:30 fallow model)

$$\gamma_r = \frac{\tau_{\max}}{G_0} \quad \textbf{Eq 7. 2}$$

with $\tau_{\max}$ being the shear stress at failure. Santos & Correia (2001) proposed that the use of a smaller threshold shear strain could reduce errors within the model and suggested the shear strain $\gamma_r = \gamma_{0.7}$ at which the secant shear modulus *G* is reduced to about 70% of its initial value:

$$\frac{G}{G_0} = \frac{1}{1 + 0.385\left|\frac{\gamma}{\gamma_{0.7}}\right|} \quad \textbf{Eq 7. 3}$$

Plastic failure is modelled using a cap-type yield surface combined with the Mohr-Coulomb failure criterion in this model. This model can successfully capture the strain hardening and small strain stiffness behaviour of soil during dynamic loading. However, strain softening behaviour is not modelled. Al-Defae et al. (2013) suggested using the critical state strength ($\phi' = \phi'_{crit}$) to model large strain slope behaviour. Such suggestion was employed in Chapter 5 and illustrated a good predication of seismic performance for 1:10 scale model. The reason for this is due to the non-significant softening behaviour resulting from the small earthquake loadings, further discussion of this will be given in Chapter 8. Hence, in this chapter, the critical state strength will still be used during modelling the 1:10 scale model. However, this may be ideal, especially for slopes subject to large cyclic loadings such as the 1:30 scale model in this study, the failure of the slope is governed by the strain softening behaviour (Bolton & Take 2011). To approximate such behaviour within a hardening soil model, the value of ϕ' used in modelling (Knappett et al. 2006) was modified from ϕ'_{crit} to ϕ^* as suggested in Detournay & Drescher (1993) and given by:

$$\phi^* = \tan^{-1}\left(\frac{\cos\psi' \sin\phi_{pk}'}{1 - \sin\psi' \sin\phi_{pk}'}\right) \quad \textbf{Eq 7. 4}$$

where ϕ_{pk}' is the peak friction angle and can be written in terms of dilation angle ψ' as

$$\phi_{pk}^{'} = \phi_{cs}^{'} + 0.8\psi^{'} \quad \textbf{Eq 7. 5}$$

for plane strain conditions (Eichhorn & Drechsler 2010); $\phi_{pk}^{'}$ can also be given as a function of the relative dilation index I_R (Bolton 1986) ,

$$\phi_{pk}^{'} - \phi_{cs} = AI_R \quad \textbf{Eq 7. 6}$$

where *A* is dimensionless factor to account for strain type, *A*= 3 for tri-axial strain, *A*=5 for plane strain; I_R is given by

$$I_R = I_D(10 - \ln p') - 1 \quad \textbf{Eq 7. 7}$$

where I_D is the relative density, 55%-60%, varied depended on the model here; $p_0^{'}$ is the mean confining stress at failure, which can be expressed as the vertical and horizontal effective stresses,

$$p_0^{'} = \frac{1}{3}(\sigma_v^{'} + \sigma_h^{'}) = \frac{1}{3}(\sigma_v^{'} + 2K_0\sigma_v^{'}) \quad \textbf{Eq 7. 8}$$

where $\sigma_v^{'}$ is the vertical effective stress, $\sigma_h^{'}$ is the horizontal effective stress, and K_0 is the earth pressure coefficient at rest , which is estimated using:

$$K_0 = 1 - \sin\phi^{'} \quad \textbf{Eq 7. 9}$$

According to Eq 7.5 to Eq 7.9, the mean peak friction angle $\phi_{pk}^{'}$ and equivalent friction angle ϕ^* are 44° and 39°, for the 7.2m slope. The corresponding dilation angle $\psi^{'}$ is 9°. All of the other input parameters (see Table 5.3) apart from the cohesion c' and damping ratio ζ_{add} for the HST 95 sand used in this study have been previously reported by Al-Defae et al. (2013) and validated to be effective in Chapter 5 and will not be further discussed in the following sections. Damping will be discussed further during validation against the centrifuge test data for the fallow slopes.

7.2.2 Root-soil matrix modelling

Initially a highly simplified model of the rooted soil zones within the slope models was considered, in which this soil was assumed to be a 'smeared' zone having the same mechanical characteristics as the surrounding soil, but with additional 'root cohesion' (apparent cohesion due to roots) added to the aforementioned HS-small soil properties. The variation of smeared properties with depth (see Fig 6.4) was determined for the centrifuge models by performing direct shear tests. Full details about this can be found in Chapter 6. The influence zone of the root systems was complex, but as found in Chapter 5, when the influence zone was simplified to the boundary geometry that the root system actually occupied, highly accurate simulations could be achieved. This approach was employed here in defining the dimension of smeared rooted zone, which are shown in Fig 7.1.

7.2.3 Modelling ESB container

7.2.3.1 General consideration

A typical layout of numerical model of TL04 and TL05 with ESB boundary is shown in Fig 7.2. Here the dimensions of the slope were established based on the prototype size of the centrifuge model. All soil materials were simulated using the Hardening Soil constitutive model with small-strain stiffness. Full details about the soil models can be found in the preceding section. The ESB container was simulated using 5-nodes plate element following the layered structure of ESB container composited of 6 aluminium frames and 5 rubber inter-layers. The plate element is based on Mindlin's theory (Bathe & Saunders 1984), which allows for plate deflections due to shearing as well as bending. For each node, three degrees of freedom are defined, that is, two translational degree of freedom (u_x, u_y) and one rational degree of freedom (rotation in the *x*-*y* plane). It should be noted that the top and bottom horizontal plates are dummy plates with the aim of establishing the whole system. During construction, these two plates should not be activated in case of any wrong amplification of earthquake motions. Rotational fixity was then applied to the base of each plate to fix the rotational degree of freedom around the *z* axis. Nodes to nodes anchors were connected between aluminium frame plates to make them behave as a whole system as in reality. Interfaces were assigned between soil model and ESB container wall to simulate the

interaction between them, here the factor of interface was taken as 1.0 to guarantee that the end wall had the same friction as the adjacent soil as proposed by Zeng & Schofield (1996). An absorbent boundary was applied on the end wall to minimize the unwanted *P* waves (Milsom 2007) generated by aluminium frames to accurate simulate the function of shear beam.

Here aluminium and rubber were considered to be isotropic and elastic material, 6 input parameters are required: two stiffness parameters, axial stiffness *EA* and bending stiffness *EI*; specific weight *w*; Poisson ratio *v*; and two viscous damping ratio parameter c_m and c_k. All the plate parameters used in the analyses are summarised in Table 7.1. The determination of these parameters will be discussed later. As indicted by Zeng & Schofield (1996), the dynamic behaviour of the ESB container is defined by the lateral stiffness of the rubber layers and by the mass of the aluminium frames, so the accuracy of simulation is highly dependent on the accuracy of rubber stiffness properties and aluminium frames mass properties.

Table 7.1 Key parameters and properties of ESB container wall

	Parameter	Bottom rubber layer	2nd rubber layer	3rd rubber layer	4th rubber layer	Top rubber layer	Aluminium frame
	EA (kN/m)	2268	2124	1979	1835	1690	25.88e6
	EI (kN m^2/m)	26.58	24.89	23.19	21.50	19.81	0.303e6
1:10	*w* (kN /m/m)	0	0	0	0	0	19.23
Scale	*v*	0.5	0.5	0.5	0.5	0.5	0.334
model	ζ (%)	5	5	5	5	5	0.04
	c_m	2.218	2.218	2.218	2.218	2.218	0.01774
	c_k	0.4681e-3	0.4681e-3	0.4681e-3	0.4681e-3	0.4681e-3	3.745e-6
	EA (kN/m)	11.13e3	9838	8538	7237	5937	77.63e6
	EI (kN m^2/m)	1175	1038	900.5	763.3	626.2	8.187e6
1:30	*w* (kN /m/m)	0	0	0	0	0	57.69
scale	*v*	0.5	0.5	0.5	0.5	0.5	0.334
model	ζ (%)	5	5	5	5	5	0.04
	c_m	0.7228	0.7228	0.7228	0.7228	0.7228	5.783e-3
	c_k	1.408e-3	1.408e-3	1.408e-3	1.408e-3	1.408e-3	0.0112e-3

7.2.3.2 Properties of rubber layer

The shear modulus G_r (kPa) of rubber layer used in this study as a function of vertical confining stress σ_v (kPa) was given by Bertalot (2013) based on the conventional shear box testing,

$$G_r = 1374 + 14.6 \cdot \sigma_v \quad \textbf{Eq 7. 10}$$

where σ_v is induced by the weight of aluminium frame rather than the soil model, and will vary with working *g* level. Young's modulus E_r (kPa) of the rubber can then derived from the following equation,

$$E_r = 2G_r(1+\upsilon_r) \quad \textbf{Eq 7. 11}$$

where $v_r=0.5$ for rubber (Mott & Roland 2010). For plane stain model, the value of *EA* (kN/m) relates to stiffness per unit width in the out-of-direction, and can be calculated by:

$$E_r A = E_r \cdot d_{eq} \cdot 1m \quad \textbf{Eq 7. 12}$$

where d_{eq} is the equivalent thickness of the plate, for solid layer used in this study, the real width of rubber sheet (0.375 m at prototype) is taken.

The flexural rigidity *EI* (kN m^2/m) can then be calculated as a function of *EA* and d_{eq},

$$d_{eq} = \sqrt{12\frac{E_r I}{E_r A}} \quad \textbf{Eq 7. 13}$$

The weight of rubber is considered to have limited effect on the dynamic performance of ESB container and is taken as 0 for simplicity. The standard dynamic damping of rubber is 5% according to Orban (2011) and applied as Rayleigh damping at the frequency of 4 Hz and 30 Hz to calculate the corresponding damping coefficient.

7.2.3.3 Properties of aluminium frame

The Young's modulus E_{Al} and Poison ratio v_{Al} of aluminium are given by Euro code 9 . The corresponding stiffness properties can then be determined following the Eq 7.12 and Eq 7.13. For the anchor connecting the two sides of walls, only axial stiffness and length is required for input. Here the length of anchor taken as 1 m, and the corresponding axial stiffness is then the same with aluminium plate.

The weight w_{Al} of the aluminium frame plate is obtained by multiplying the unit weight of plate material by the thickness of the plate d_{eq}. It should be mentioned that the calculated unit

weight of the aluminium frames should be less than the real unit weight of aluminium material due to the hallow slots on the outer sides of aluminium frames to achieve the design mass requirement as reported by Bertalot (2013). The dynamic damping of aluminium is taken as 0.04% after Orban (2011).

7.3 Validation of numerical model

7.3.1 Dynamic shear modulus and damping

A comparison of shear modulus and damping in EQ1 as functions of cyclic shear strain within both centrifuge models and the corresponding numerical simulations are shown in Fig 7.3 and Fig 7.4, for unreinforced model TL 05 and root reinforced model TL06, respectively. It was found that material hysteretic damping within the numerical model was generally smaller than that inferred from the centrifuge tests. This indicated that a small amount of additional damping was required for the soil model to accurately simulate the seismic behaviour of the HST95 sand in the tests. Rayleigh damping, which allows additional mass and stiffness-proportional damping to be modelled, was included in the simulation, full details about the determination of Rayleigh damping is given in Chapter 5.

The additional damping required so that the numerical simulations presented a good match to the centrifuge seismic performance (in terms of shear modulus, damping, accelerations and crest deformation) are illustrated in Table 7.2. It was found that for the 1:30 scale slope model a higher additional damping ratio (3.5%) was required compared to the 1:10 slope model (2%). This is not surprising given the fact that the hysteretic damping ratio is bounded by an upper limit corresponding to the lower limit of shear modulus in the HS small model (see Fig 7.3). However, during centrifuge tests, large motions were observed to illustrate higher damping than that of small motions because of the high mobilised shear strain (see Chapter 6). Hence a higher additional Rayleigh damping is essential to eliminate the gap between the 'real' damping and the material hysteretic damping for large magnitude motions. It is worth noting that the same damping ratios were used for both rooted and fallow zones within the simulations, though the effect of this will be further discussed later. The reason for this was due to the difficulties on quantifying two variations (root cohesion and damping ratio) at the

same time. It should also be noted that the increases in additional viscous damping with scaling factor are consistent with the 5% additional damping suggested for 1:50 scale tests by Al-Defae et al. (2013).

Table 7.2 Additional Rayleigh damping ratio used in different model

Model ID	Additional Rayleigh damping ratio	Motion frequency(Hz)	c_m	c_k
TL 04	2%	4-30	0.8870	0.1872E-3
TL 05	3.5%	1.33-10	0.5163	0.9833E-3
TL 06	3.5%	1.33-10	0.5163	0.9833E-3
TL 07	2%	4-30	0.8870	0.1872E-3
TL 08	2%	4-10	0.7181	0.4547E-3

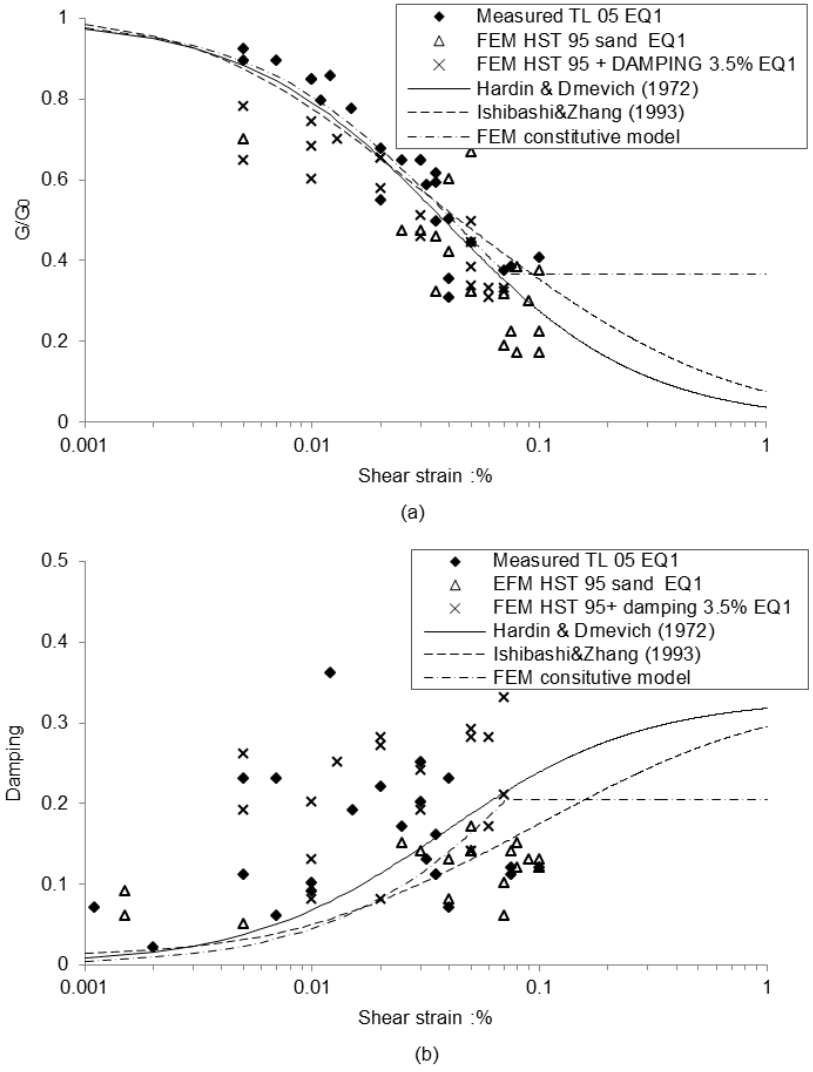

Fig 7.3 Comparison of shear modulus degradation and damping in centrifuge tests and FE simulation for 1:30 scale fallow model

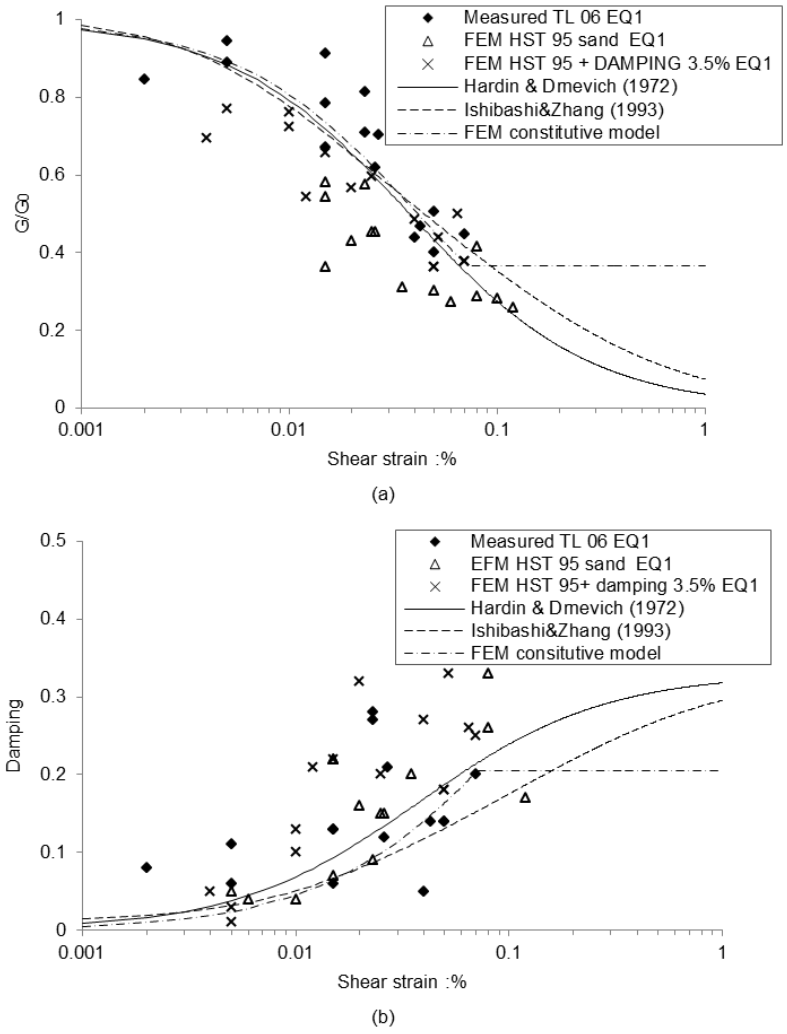

Fig 7.4 Comparison of shear modulus degradation and damping in centrifuge tests and FE simulation for 1:30 scale rooted model

7.3.2 Acceleration responses

A comparison of the measured and simulated accelerations at the crest of the slope (ACC14) for model TL 06 in both the time and frequency domains is shown in Fig 7.5. The accelerations without any additional damping in terms of the envelope of the peak values demonstrated significant over prediction, while those with additional viscous damping of 3.5% presented a good match with the recordings from the centrifuge tests. The amplification behaviour within the soil of peak accelerations at particular levels was also extracted from the simulations and compared with the measured response in Fig 7.6.

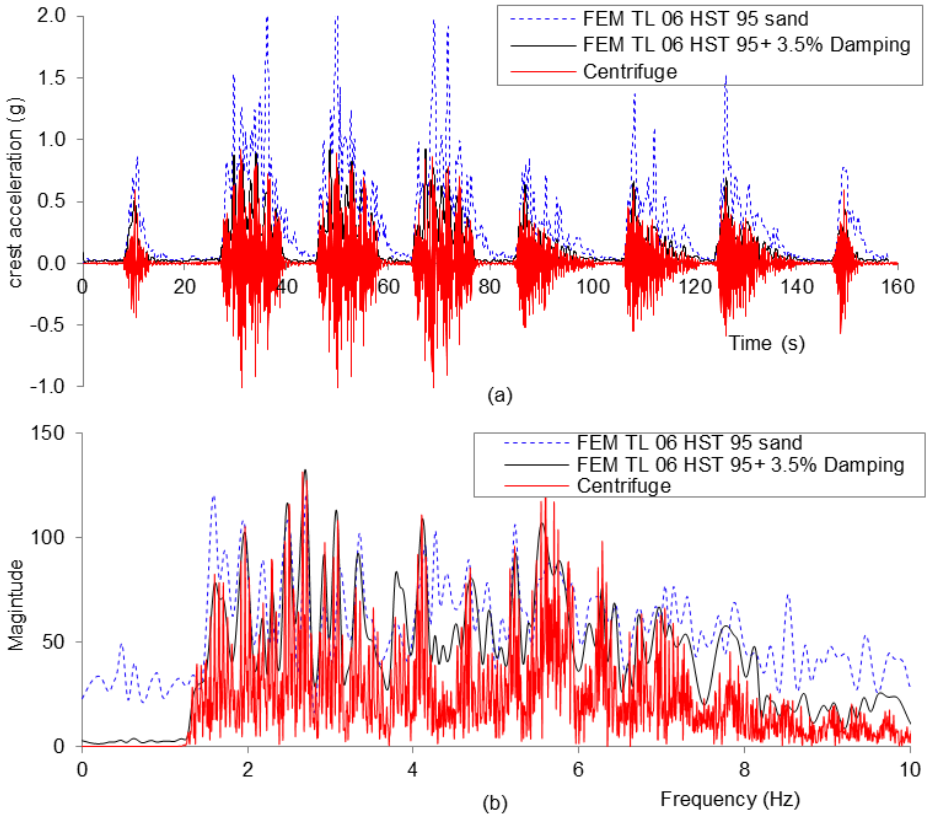

Fig 7.5 Comparison of measured and predicted acceleration (in terms of the envelope of the peak values): (a) in the time domain; (b) in the frequency domain

It can be seen that the simulated slope broadly captures the general characteristics of acceleration amplification behaviour, such as the attenuation at deeper levels and higher amplification factors around the slope crest; however, the FEM generally under-predicts the magnitude of the amplification factor, particularly in EQ1 and EQ2. Considering the hazard posed to infrastructure at the crest is more usefully represented by a response spectrum, Fig 7.7 presents a comparison of the normalised ARS at the crest of the slope for 5% nominal structural damping from FEM and measured data from the centrifuge tests. The FEM including additional Rayleigh damping showed a good match of ARS to the centrifuge data for EQ2 and EQ5, but under predicts the resonance response around the period of 0.17s of EQ1. In consideration of such under-prediction of amplification factor and resonance response to EQ1, the predicted slope height and input motion effects will show different behaviour with centrifuge models and will not be discussed later.

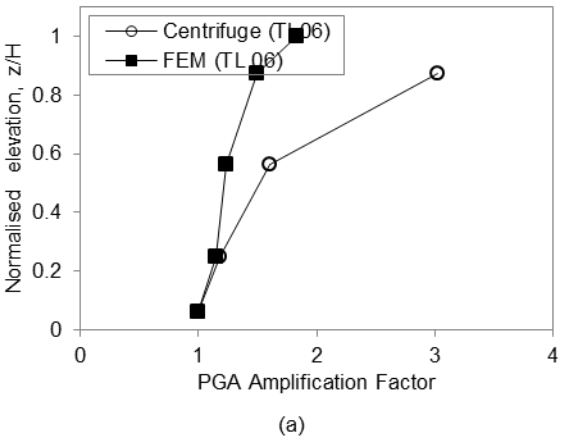

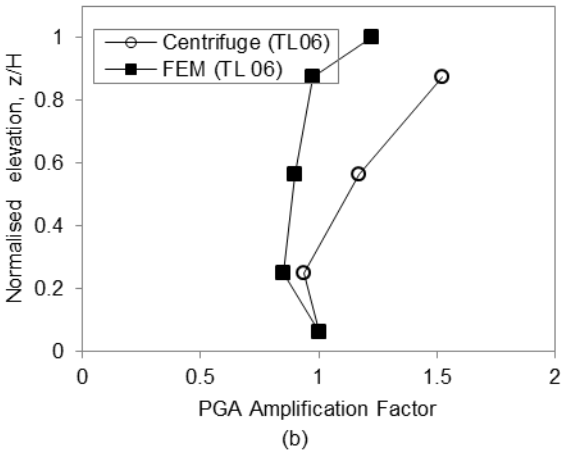

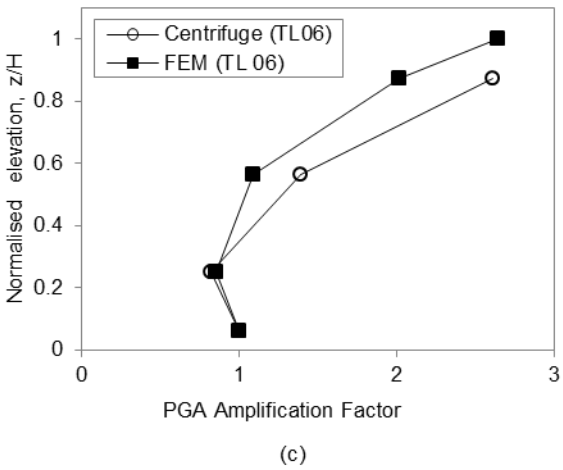

Fig 7.6 Comparison of simulated and measured peak acceleration amplification: (a) in EQ1; (b) in EQ2; (c) in EQ5

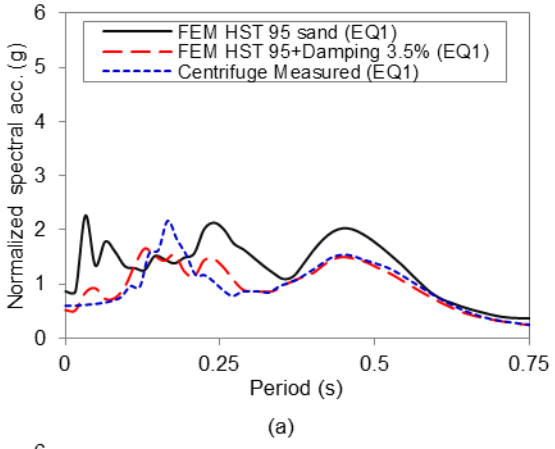

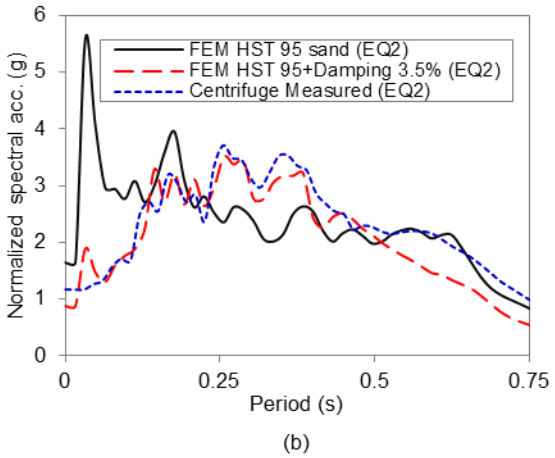

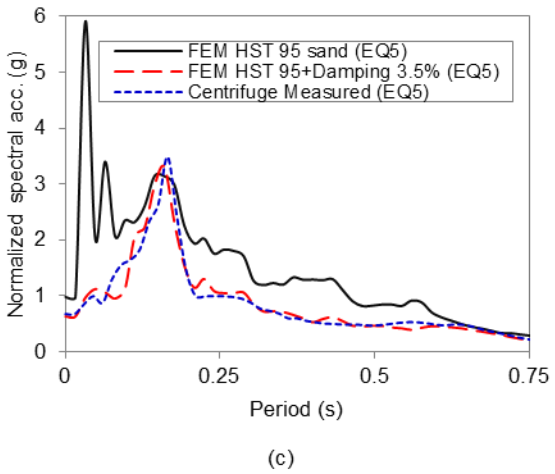

Fig 7.7 Comparison of ARS in centrifuge tests and FE simulation: (a) in EQ1; (b) in EQ2; (c) in EQ5

7.3.3 Permanent deformation

A comparison of the permanent crest settlement in the 1:10 and 1:30 scale rooted slopes across the eight earthquakes as predicted by FEM and as measured in the centrifuge is shown in Fig 7.8. It is clear that the HS small model with appropriate additional Rayleigh damping can provide a very good simulation of the permanent crest settlement. This highlights the importance of determining an accurate amount of soil damping for FE simulations.

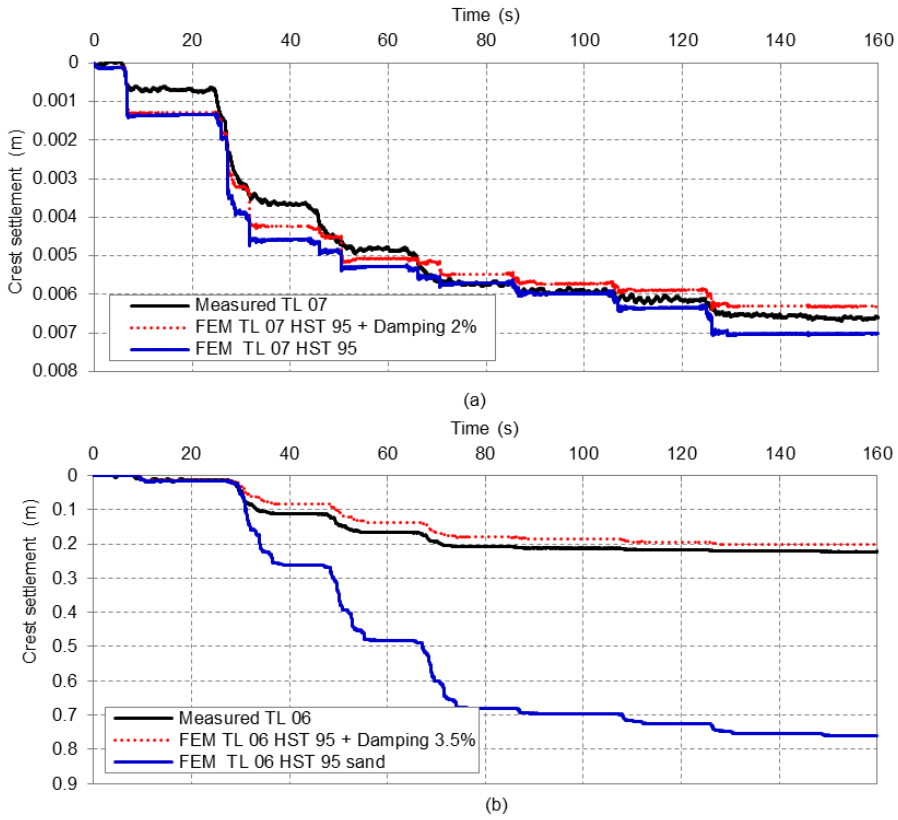

Fig 7.8 Comparison of permanent settlement at the crest in centrifuge tests and FE simulations: (a) 1:10 scale rooted slope; (b) 1:30 scale rooted slope

7.3.4 ESB container Boundary effect

Fig 7.9 shows a comparison of permanent settlement between semi-infinite soil conditions case and ESB container case at the crest of the slope (ACC14) for 2.4 m slope (model TL 04) and 7.2 m slope (model TL 05), respectively. It can be found that there was non-significant disturbance on seismic response of soil model due to the proximity to the container end wall.

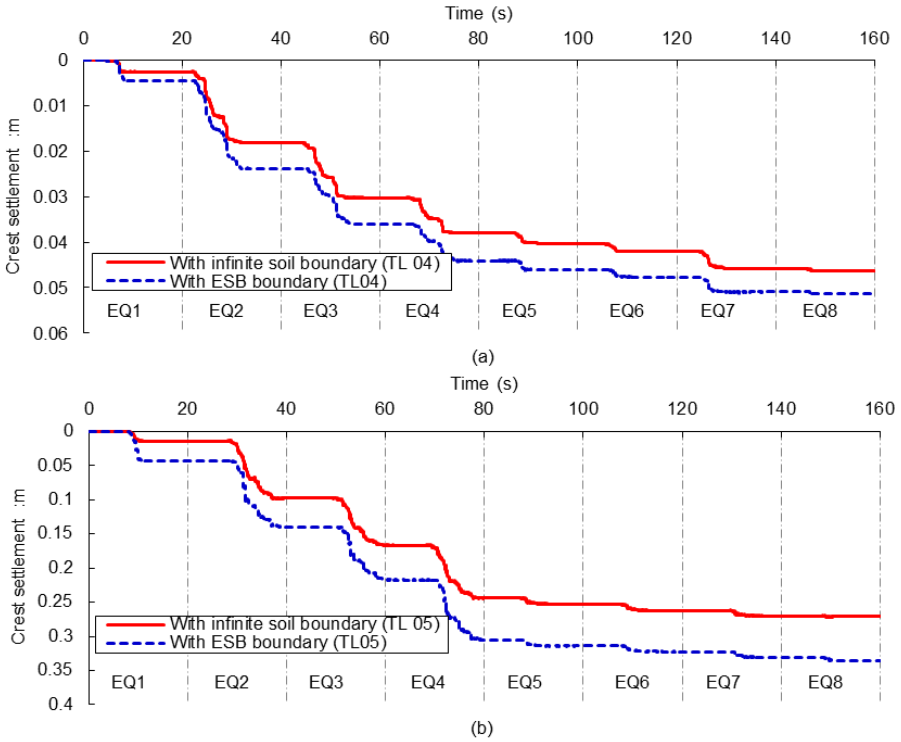

Fig 7.9 Comparison of permanent settlement between semi-infinite soil conditions case and ESB container case

Model with ESB boundary presents a slightly higher deformation (10.9% and 23.9% for 2.4 m slope and 7.2 m slope, respectively) than that for model with semi-infinite soil condition, especially for the first two motions. The reason for this is mainly associated with the relative stiffness between ESB container and soil layer as suggested by Zeng & Schofield (1996). The shear stiffness of the soil layer is significantly higher than that of the end wall at very small strain (EQ1 and EQ2). As a result, the deformation of soil induced by the base shaking is less than that of end wall. Under such conditions, the model container will drive the soil to deform further and hence a higher crest settlement. During the following motions, with the accumulation of shear strain, the shear stiffness of the soil drops very close to that of the end wall, a consistent deformation is presented between the end wall and the soil layer. However, considering the non-significant difference for the overall deformation between these two cases, it will be suitable to use semi-infinite soil conditions to represent the ESB boundary with the objective of highly reducing the computational time and physical memory requirement for engineering application.

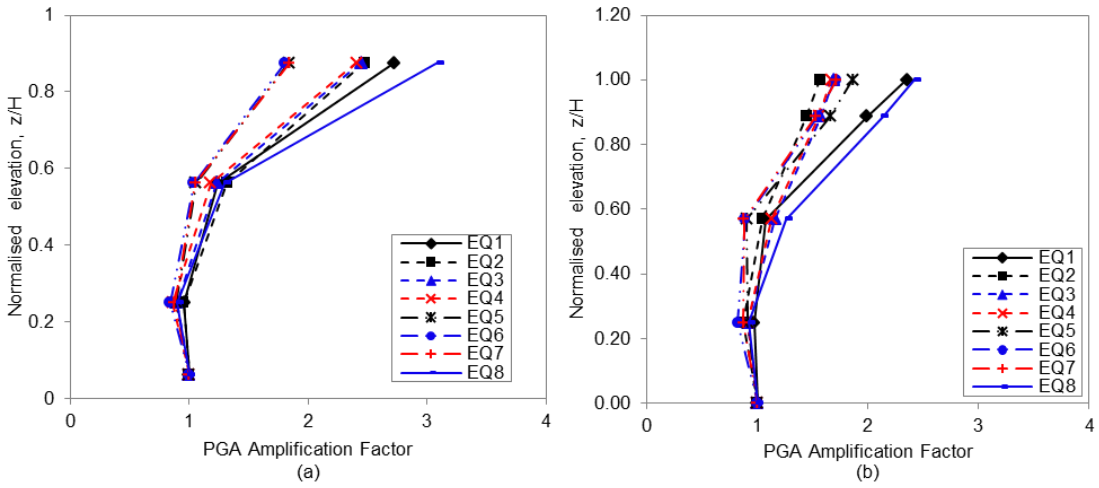

Fig 7.10 Predicted peak acceleration amplification for 1:30 scale model at reduced frequency: (a) measured data for fallow model; (b) simulated data for rooted model

7.4 Implication for slope seismic performance prediction

The seismic performance of 1:30 scale rooted slope subject to motions at reduced frequency content (4-10 Hz at prototype) was predicated. The amplification response of acceleration and crest settlement for this model are shown in Fig 7.10 and Fig 7.11, respectively. Here the additional Rayleigh damping ratio of 2% was used to keep insistent with the fallow case. The horizontal acceleration response with depth is very similar between simulated rooted case (Fig 7.10 (b)) and measured fallow case (Fig 7.10 (a)), and is insensitive to prior shaking, but highly dependent on the motion type.

For the crest settlement prediction, two cases were considered: (i) root cohesion with depth derived from 1:30 scale root cluster DSA tests; (ii) root cohesion with depth derived from 1:10 scale root cluster DSA tests. No more than 0.6% difference was observed between the two cases, suggesting that any particle size effects apparent in the root cohesion from the DSA tests (Fig 6.4 (b)) do not have a significant influence on the overall slip of the slope. This may indicate that the slip plane is moved deeper within the soil, below the rooted zone, due to the presence of the roots – i.e. that in each case the root cluster is strong enough (particularly at 1.25 m prototype depth) to result in the same position of the slip plane in rooted tests, such that the mass of slipping soil to the depths of the roots translates as a rigid block.

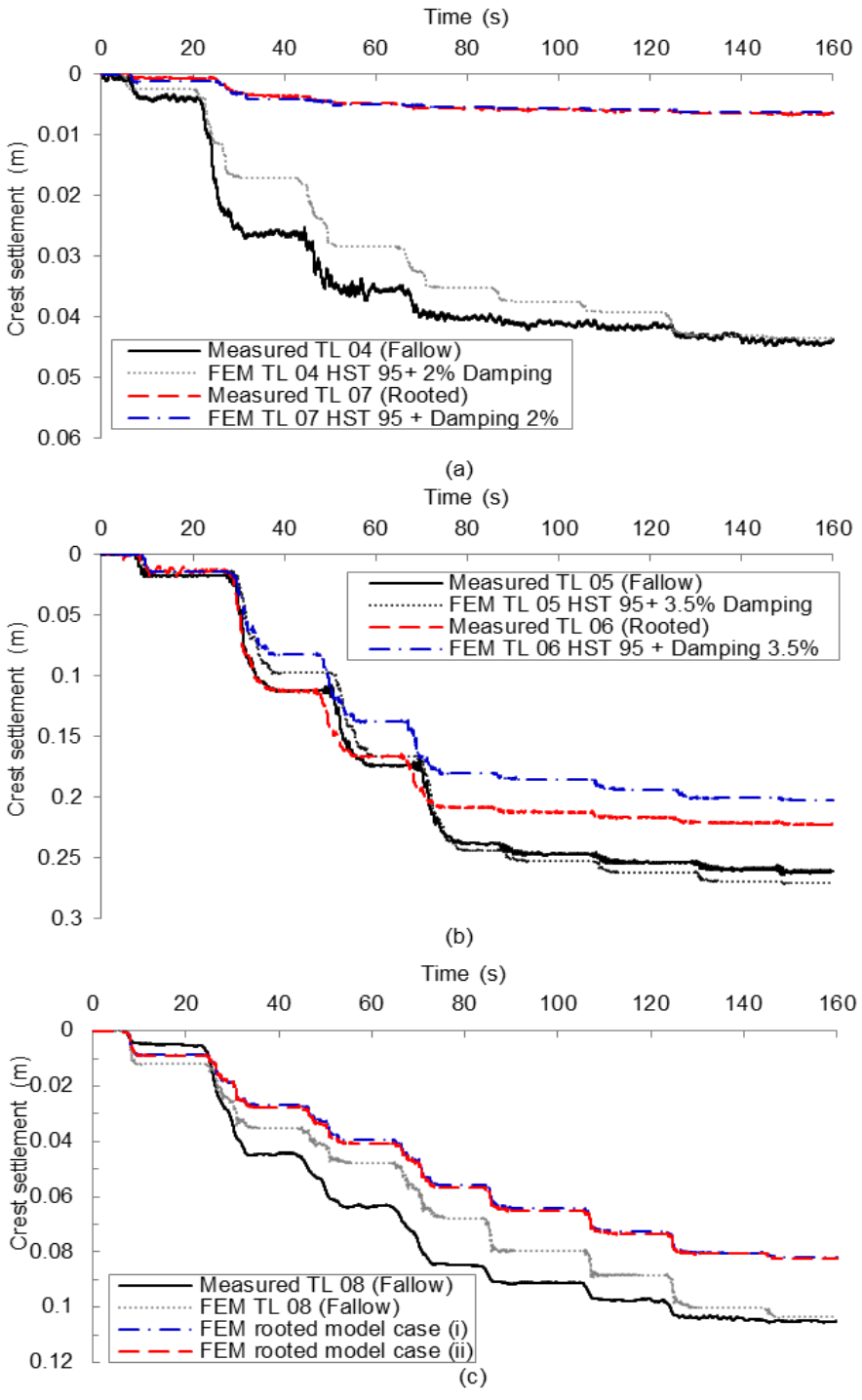

Fig 7.11 Predicted and measured permanent settlement at the crest between rooted model and fallow model: (a) 1:10 scale model; (b) 1:30 scale model at full frequency; (c) 1:30 scale model at reduced frequency

Fig 7.11 (c) also shows that a reduction of 23% of permanent deformation at crest due to the presence of roots. This is of a similar order of magnitude to the 15% reduction (Fig 7.11 (b))

observed in the centrifuge tests at 1:30 scale (7.2 m tall) slope with full frequency, implying that the reduction in low frequency content, while in general reducing the amount of slip, does not significantly affect the soil-root interaction. It is however much less than the 85% reduction (Fig 7.11 (a)) in the 1:10 scale (2.4 m tall) slope with the same reduced low frequency content, indicating that roots are a more effective stabilisation measure in shorter slopes.

7.5 Future insights into rooted slope behaviour

In this section, root modelling assumptions that may influence the seismic performance of rooted slopes that cannot be achieved within a centrifuge model will be identified through a parametric study. 1:10 scale rooted slope and 1:30 scale rooted slope performance subject to motions at full frequency content will be considered and compared to show these influences.

Fig 7.12 shows the results of a parametric study investigating the effects of (a) the magnitude of the root cohesion; (b) the ratio of rooted zone to soil damping; (c) the ratio of rooted zone to soil stiffness; and (d) the width of the zone over which the root cohesion acts. In each case, the ratio of rooted slope displacement to fallow slope displacement is shown, i.e. the lower this value, the more improved the rooted slope is.

7.5.1 Influence of rooted zone strength (root cohesion) on response

The variation of permanent settlement with the decay of root cohesion is shown in Fig 7.12 (a). To obtain these results, the distributions of root cohesion in Fig 6.4 (b) were uniformly reduced at all depths by the reduction factor shown on the *x*-axis of Fig 7.12 (a). Therefore, the values at 100% represent the magnitude of reduction, and are of the similar order of magnitude but not the same with the 85% and 15% reduction (Fig 7.11) observed in the centrifuge tests for the 1:10 and 1:30 scale slopes respectively. This is because there was no 100% match between centrifuge and simulated models (see Fig 7.11). The input motions for parametric studies are all from the rooted case rather than the individual motions between rooted case and fallow case during validation work.

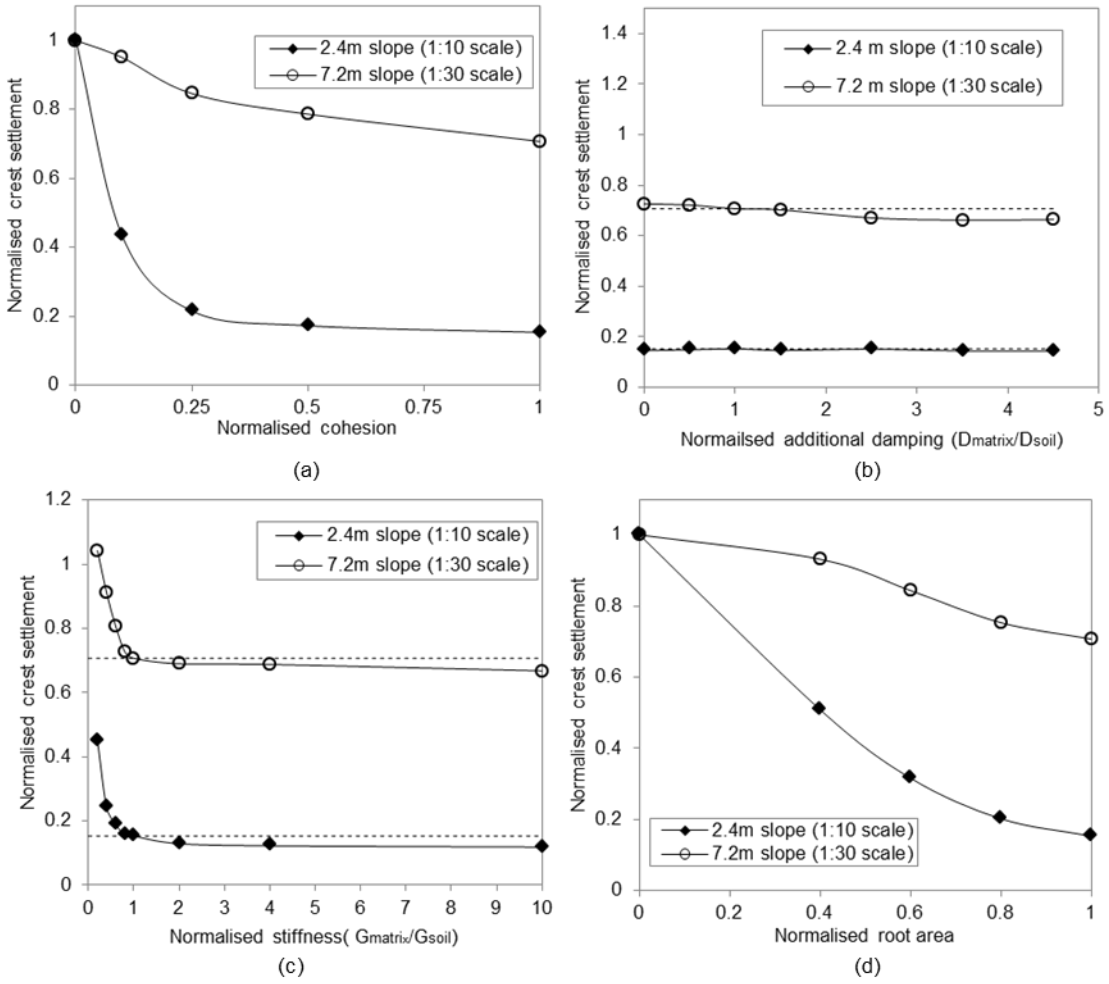

Fig 7.12 Influence of slope parameters on deformation response at the crest according to FE simulation: (a) root cohesion; (b) additional Rayleigh damping; (c) size of rooted zone; (d) root-soil matrix stiffness

The results here are of great potential application and value in the long term management of vegetated slopes because the strength of tree roots decays gradually, rather than instantly dropping to zero, when a tree dies (Coppion & Richards 1990). It can be seen in Fig 7.12 (a) that the 1:10 scale slope and 1:30 scale slope show quite different behaviour. For the small slope (1:10), the reduction in soil slip due to the roots remains significant and almost undiminished until the root cohesion decreases to 25% (approximately 4 kPa of root cohesion within the rooted zone) of its initial strength. The mechanisms of such behaviour can be associated with development of a deeper position of the slip plane due to the presence of roots, as mentioned previously. This would imply that when root cohesion is less than 4 kPa, it becomes more critical if the slip plane passes through the rooted zone, rather than taking up a

position below the rooted zone. In terms of the larger slope (1:30), the contribution of roots to slope stability decreases gradually with the decay of root cohesion. Considering the non-significant difference between case (i) and case (ii) distributions of root cohesion in Fig 7.12 (c), this suggests that the slip plane remains closer to the 'fallow' position in this case where the rooted zone is smaller relative to the slope height, resulting in a gradual reduction in effectiveness of the roots as the cohesion is reduced.

7.5.2Influence of additional damping on response

The previous comparisons on acceleration response and permanent crest settlement between soil models with and without additional damping have shown the effect of overall global (soil) damping on seismic performance of the slope. Here, the additional damping within the rooted zone was varied (keeping the surrounding soil damping as before) to understand how sensitive the slope performance was to this parameter. The variation of permanent settlement with altering the damping ratio is shown in Fig 7.12 (b). It can be found that the crest deformation response of the slope is insensitive to the variation of the damping within the rooted zone. Such response is significantly different with the case of changing overall global (soil) damping, the main reason for this should be associated with the propagation of the earthquake motions. The vibration of soil in the horizontal direction is generated mainly by vertically propagated by *S* waves (Zeng & Schofield 1996). Therefore the variation of damping within rooted zone will have very limited effect on the motions propagated into the crest hence limited effect on crest deformation. And it can be predicted here that significant difference on crest deformation response will be observed if damping of the soil underneath the crest changes.

7.5.3 Influence of matrix stiffness on response

Traditionally, the effects of roots on geotechnical system performance have been limited to adding additional strength (root cohesion). While this may be suitable for static stability problems, dynamic performance (accelerations) is more likely to be affected by stiffness. For the cases modelled in this paper, the stiffness of the rooted zone does not appear to have a significant effect on slope performance (see Chapter 6). However, other root systems may exist which have locally higher stiffness. The variation of permanent settlement due to

increases in the stiffness of the rooted zone altering the stiffness of structure-soil matrix is shown in Fig 7.12 (c). Here the stiffness was normalised by dividing the initial soil stiffness. The ratio of 10 times for the stiffness of reinforced soil is believed to cover all range of material used in geo-technical engineering. When the stiffness of the rooted zone is higher than that of the surrounding soil, the slope performance is found to be insensitive to the variation of the stiffness. For 1:10 scale rooted model, tree roots take a large portion of the slope entity, but the reduction of the crest settlement is no more than 4% when the stiffness of reinforced soil was 10 times of the fallow soil stiffness. The 1:30 scale rooted model, of which roots take a relative small portion, illustrates an even smaller reduction as expected. However, if the stiffness of the rooted zone is lower than that of the surrounding soil, the deformation of the slope is observed to be highly influenced by the variation of stiffness. Such observation indicates that the slides may initiate on weak layers, as suggested by Dan et al. (2009). Special attention should be given on remediation of such weak layers during slope management.

7.5.4 Influence of rooted zone on response

Chapter 5 has highlighted the effect of rooted zone on the seismic performance of rooted slope, but the focus in that chapter was to find the optimum size of zone that could successfully simulate the seismic performance of a rooted slope with a plate/heart type system. For different trees of the same species, the lateral extent of the root system of established tress may vary, and this parameter will also increase after new trees are planted as they establish a mature root system progressively. Better understanding the influence of the size of the rooted zone can therefore help to inform forest management and also provide a guide for the selection of species with a propensity for lateral spread in engineering application. The variation of permanent settlement with smaller rooted zones extending horizontally from the main tap root is shown in Fig 7.12 (c). It should be noted here that the root cohesion keeps the same for different rooted zones to more realistically simulate the growing process of new roots. As before, the root area of 100% represents the case modelled in the centrifuge tests. The slope performance is shown to be significantly influenced by the dimension of rooted zone for both 2.4 m slope and 7.2 m slope. Given the fact that the slip plane appears to be transferred below the rooted area due to the high root cohesion, the

horizontal extension of the root system can generate a larger influence zone and further influence the geometry of the slip plane.

7.6 Conclusion

Based on the numerical procedure developed in Chapter 5, FE models which can be used for a tap-root system was developed in this chapter and validated against the centrifuge tests data reported in Chapter 6. The possible disturbance on seismic response of slope crest due to the proximity to the container end wall was also identified. Following this, a parametric study was conducted to investigate the influence of different potential characteristics of rooted soil on the overall seismic performance of slope with different size. The following principal conclusions can be drawn from the study:

1) FE approach using appropriately-sized zones of smeared rooted soil properties derived from the large direct shear tests was validated to be effective simulating the acceleration response and deformation response of rooted slope in centrifuge modelling, however, this model could not accurately simulate the resonance response of the slope.
2) Soil model with assumed absorbent ESB boundary could successfully simulate the seismic response of soil model with infinite lateral extent and finite depth. The possible disturbance on seismic response of soil model due to the proximity to the container end wall was mainly induced by the difference of stiffness between soil model and ESB container end wall.
3) The slope performance was found to vary with the height of the slope compared to the depth of the roots. For taller slope, the slope performance was found to be significantly influenced by the horizontal extension of root system and the variation of the root cohesion, and this was associated with forcing the slip plane deeper than its optimal position. While for slopes of modest height, performance is significantly affected by the lateral and vertical extent of root system, but insensitive to the continuous increase of root cohesion.

4) The variation of key soil dynamic properties (stiffness and damping) within the rooted zone was found to be insensitive to the seismic performance of rooted slope. However, weak soil layer in the slope is a hazardous threat to the slope stability.

Chapter 8 Newmark sliding block model for predicting seismic performance of vegetated slopes

8.1 Introduction

The finite-element method (FEM) developed in Chapter 5 and Chapter 7 has been shown to be effective in predicting the seismic performance of vegetated slopes through validation against centrifuge test data and can be used in the detailed study of the seismic hazard posed to such slopes and any infrastructure located at the slope crest. However, given the computational expense of FEM, a complimentary simplified procedure would be highly useful in preliminary design, particularly for identifying key configurations for further detailed study via FEM. Such a two-level approach has been previously applied to fallow slopes and slopes reinforced with discrete piling. In this chapter, an improved sliding-block procedure is developed to predict the seismic performance of vegetated slopes. The procedure consists of two components. Firstly, an analysis using Discontinuity Layout Optimisation (DLO) is used to detect the slope failure mechanism (i.e. find the lowest upper-bound mechanism using a virtual work approach) and predict the yield acceleration of a given slope configuration, accounting for the presence of the roots. The derived yield acceleration from DLO will then be incorporated into a modified limit equilibrium formulation for sliding block to further account for the geometric hardening of the slope as it flattens with slip allowing the permanent settlement at the crest of the slope to be estimated. The procedure is then validated against the centrifuge test results reported in Chapter 6 which will reveal further insights into the seismic behaviour of vegetated slopes.

8.2 Discontinuity Layout Optimisation

8.2.1 Fundamental theory

Discontinuity Layout Optimisation (Smith & Gilbert 2007) is a recently developed numerical limit analysis procedure which can be applied to a wide range of geotechnical stability problems involving cohesive and/or frictional soils. Compared with the more traditional finite element limit analysis (FELA) technique which requires discretising the problem into solid (finite) elements, DLO employs rigorous mathematical optimisation techniques to identify a critical layout of lines of discontinuity which form at failure. These lines of discontinuity are typically 'slip-lines' in planar geotechnical stability problems and define the boundaries between moving rigid blocks of material which make up the mechanism of collapse. Associated with this mechanism is a collapse load factor, determined via the principle of virtual work, which is an upper bound on the 'exact' load factor according to formal plasticity theory.

The primal kinematic problem formulation for the plane strain analysis of a quasi-statically loaded, perfectly plastic cohesive-frictional body discretised using *m* nodal connections (slip-line discontinuities), *n* nodes and a single load case can be given by:

$$\min \lambda \mathbf{f}_L^T \mathbf{d} = -\mathbf{f}_D^T \mathbf{d} + \mathbf{g}^T \mathbf{p} \qquad \textbf{Eq 8. 1}$$

subject to

$$\mathbf{B}\mathbf{d} = \mathbf{0} \qquad \textbf{Eq 8. 2}$$

$$\mathbf{N}\mathbf{p} - \mathbf{d} = \mathbf{0} \qquad \textbf{Eq 8. 3}$$

$$\mathbf{f}_L^T \mathbf{d} = 1 \qquad \textbf{Eq 8. 4}$$

$$\mathbf{p} \geq \mathbf{0} \qquad \textbf{Eq 8. 5}$$

where $\mathbf{f}_D$ and $\mathbf{f}_L$ are vectors containing respectively specified dead and live loads, $\mathbf{d}$ contains displacements along the discontinuities, where $\mathbf{d}^T = \{s_1, n_1, s_2, n_2, \cdots, n_m\}$ and s_i and n_i are

the relative shear and normal displacements between blocks at discontinuity i ; $\mathbf{d}^T = \{c_1 l_1, c_2 l_2, \cdots, c_m l_m\}$, where l_i and c_i are respectively the length and cohesive shear strength of discontinuity i. $\mathbf{B}$ is a suitable ($2n \times 2m$) compatibility matrix , $\mathbf{N}$ is a suitable ($2m \times 2m$) flow matrix and $\mathbf{p}$ is a ($2m$) vector of plastic multipliers. The discontinuity displacement in $\mathbf{d}$ and the plastic multipliers in $\mathbf{p}$ are the linear programing variables.

For seismic problems (Smith & Cubrinovski 2011), pseudo-static theory may be employed. The imposition of horizontal and vertical seismic acceleration within the system results in additional work terms in the governing equation that are analogous to that for self- weight. Here, the contribution made by discontinuity i to the $\mathbf{f}_D^T \mathbf{d}$ term in Eq.(1) can be written as

$$\mathbf{f}_{Di}^T \mathbf{d}_i = \{(1-k_v)[-W_i \chi_i \quad -W_i \alpha_i] + k_h [-W_i \alpha_i \quad W_i \chi_i]\} \begin{bmatrix} s_i \\ n_i \end{bmatrix} \qquad \textbf{Eq 8. 6}$$

where k_v and k_h are the vertical and horizontal pseudo-static acceleration coefficients, respectively; W_i is the total weight of the strip of material laying vertically above discontinuity i, and α_i and χ_i are the horizontal and vertical direction cosines of the discontinuity in question.

The DLO method finds the optimal collapse mechanism for the problem studied. This is achieved through increasing loading within the system until collapse is achieved, by applying what is termed an 'adequacy factor' to a given load. In the case of seismic loading, this factor is applied to the horizontal or vertical acceleration. To apply live loading to the horizontal and vertical acceleration, the $\mathbf{f}_D^T \mathbf{d}$ term in Eq 8.1 is not modified ,instead modification is performed on the $\mathbf{f}_L^T \mathbf{d}$ terms, and given by

$$\mathbf{f}_{Li}^T \mathbf{d}_i = \{k_v [-W_i \beta_i \quad -W_i \alpha_i] + k_h [-W_i \alpha_i \quad W_i \beta_i]\} \begin{bmatrix} s_i \\ n_i \end{bmatrix} \qquad \textbf{Eq 8. 7}$$

8.2.2 Constitutive modelling

DLO calculations were carried out using the software Limit State: Geo 3.1, which involves an adaptive solution procedure described by Gilbert & Tyas (2003) to significantly reduce memory requirements and the time (no more than 5 minutes for one case) to reach an optimised solution. The DLO models used in this study are shown in Fig.1. The geometry of the DLO models is identical with that of the FE models in Chapter 7. The root-soil matrix was modelled using a smeared zone with additional representative shear strength (here incorporated as additional cohesion) as in the FE modelling. Further details can be found in Chapter 7 (section 7.2.2).

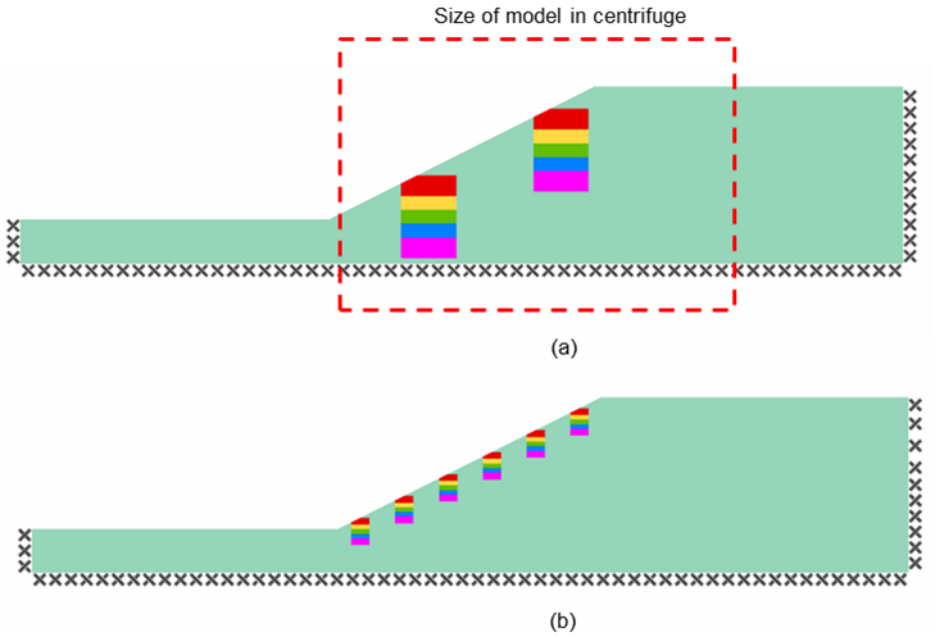

Fig 8.1 Discontinuity Layout Optimisation (DLO) model layout: (a) 2.4m high rooted model; (b) 7.2m high rooted model

The current implementation of DLO uses a rigid-plastic material model based on the Mohr–Coulomb model with an associative flow rule for frictional materials, and this was used in the modelling presented herein. Four soil input parameters were required, namely: unit weights under saturated and dry condition and two measurable effective stress strength parameters, ϕ' and c'. Although associative flow is implicitly assumed in this model, such an assumption will overestimate the yield acceleration compared to the true non-associate behaviour due to

an overestimation of the amount of dilation, and therefore potentially overestimate the yield acceleration resulting in an under-prediction of seismic slip. Hence non-associative flow should be considered pre-input (Michalowski & Shi 1995). As such a limit analysis approach is also rigid plastic, if the strength is defined by the peak friction angle it will imply that slip will not occur until peak strength is exceeded, even though the soil may be substantially into its non-linear deformation range below this level, and be able to accrue small permanent displacements with repetitive cyclic loading. To overcome these limitations an approximate procedure is proposed below (and validated against centrifuge data later on) to account for non-associativity via an equivalent associative analysis, and to determine a mobilised friction angle (ϕ'_{mob}) and corresponding mobilised yield acceleration for cases where the induced seismic shear stress is less than the peak shear strength of the soil to allow improved predictions of small amounts of permanent displacement in smaller earthquakes. This latter feature will be particularly important in predicting the behaviour of the 1:10 scale slopes.

Here, non-associative flow was modelled by adjusting the value of $\phi' = \phi'_{mob}$ used in the analyses from the actual value for the true non-associative behaviour to an equivalent associative value ϕ^* as suggested in Detournay & Drescher (1993) and used for other seismic limit analysis problems (e.g. Knappett et al. 2006), given by:

$$\phi^* = \tan^{-1}\left(\frac{\cos\psi' \sin\phi'_{mob}}{1-\sin\psi' \sin\phi'_{mob}}\right) \qquad \textbf{Eq 8. 8}$$

where ϕ'_{mob} is the mobilised friction angle which takes a value between a lower bound of ϕ'_{cs} at critical state and an upper bound of ϕ'_{pk} if the seismically induced shear stresses would be sufficient to exceed the peak soil strength. Considering the limiting case of $\phi'_{mob} = \phi'_{pk}$, ϕ'_{pk} can be written in terms of dilation angle ψ', further details on the determination of ϕ'_{pk} can be found in Chapter 7 (Eq 7.5 - 7.9).

According to Eq 7.5 to Eq 7.9, peak friction angle may be evaluated with depth in the two slope models shown in Fig.1 and averaged over the depth to obtain mean peak friction angles of 47° and 44°, for the 2.4 m and 7.2 m slopes, respectively. The dilation angle utilised by this approach is the maximum dilation angle, corresponding to the cap yield surface. The state

of the soil is very strongly dependent on its stress history (Schofield & Wroth 1968; Wood 1990), and the shape of the yield surface is determined by the maximum stress the soil has ever experienced. For smaller earthquake motions, the magnitude of the induced shear stresses may not be sufficient to push the soil to the cap yield surface, though there may be accumulation of plastic strains due to the inelasticity of the soil pre-failure. This may be represented by a yield surface (described by ϕ'_{mob}) for the non-associative soil which the induced shear stresses will just reach. This can then be modelled within an equivalent associative analysis through the use of Eq 8.1. When a motion is large enough to push the yield surface to the cap yield surface the soil will dilate to the maximum condition and any further increase in ground acceleration and seismically induced shear stress will not further change the shape of yield surface. Therefore Eq. 7.5 - 7.9 are accurate for large motions, but for small motions, over-predictions of yield acceleration (under predictions of slip) would be realised through the blunt use of peak friction angle as measured in laboratory tests and a new approach is required.

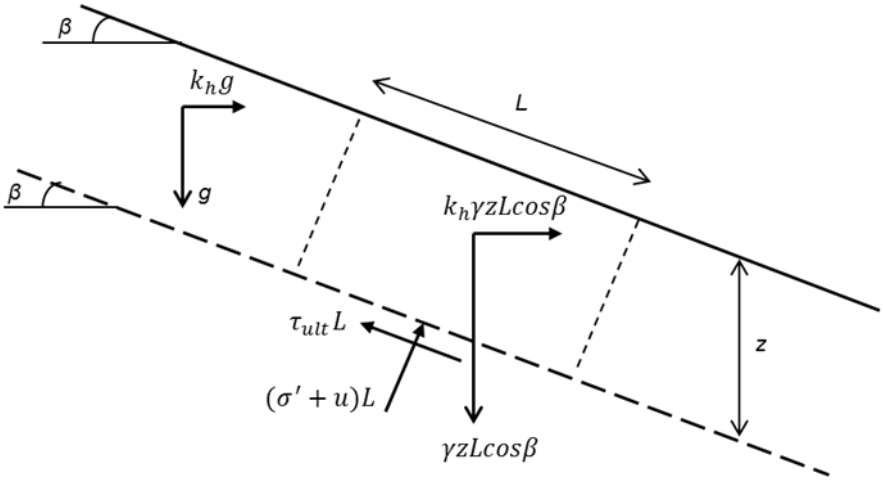

Fig 8.2 Failure mechanism of a shallow translational (infinite) slip under horizontal shaking

The first stage in this method is to determine the equivalent mean mobilised friction angle ϕ' which is consistent with the expected magnitude of the seismically induced shear stresses (i.e. the strength of the input motion). For a slope plane at depth z beneath the slope surface under uniaxial horizontal shaking (plane strain – see Fig 8.2), the applied down slope shear stress is:

$$\tau_{applied} = \gamma z \sin\beta \cos\beta + k_h \gamma z \cos^2\beta \qquad \textbf{Eq 8. 9}$$

where the first term relates to the static shear stress due to the ground slope, and the second term relates to the additional peak dynamic shear stress induced by the earthquake. The mean effective confining stress on the same slip plane is:

$$\sigma' = \gamma z \cos^2\beta - k_h \gamma z \sin\beta \cos\beta \qquad \textbf{Eq 8. 10}$$

Then, the mobilised friction angle (for a cohesionless soil) may be estimated as:

$$\tan\phi'_{mob} = \frac{\tau_h}{\sigma'} = \frac{\gamma z \sin\beta \cos\beta + k_h \gamma z \cos^2\beta}{\gamma z \cos^2\beta - k_h \gamma z \sin\beta \cos\beta} = \frac{\tan\beta + k_h}{1 - k_h \tan\beta} = \tan[\beta + \tan^{-1}(k_h)] \qquad \textbf{Eq 8. 11}$$

or alternatively,

$$\phi'_{mob} = \beta + \tan^{-1}(k_h) \qquad \textbf{Eq 8. 12}$$

Eq.8.12 is applicable while $\phi'_{mob} < \phi'_{pk}$, and is bounded by $\phi'_{mob} = \phi'_{pk}$. This is plotted in Fig 8.3, which can be used to estimate the mobilised friction angle compatible with the strength of the input motion. The strengths of the earthquake motions used in the centrifuge tests, as recorded at the base (ACC2), are also indicated on Fig 8.3.

Considering first the shorter slope the recorded peak acceleration is 0.124 g, which corresponds to a yield surface with ϕ'_{mob} of 34° (case i). Compared with that of the following motions, the peak acceleration of EQ1 is relatively small. A new, expanded yield surface will be generated for the following motions. Use of the corresponding ϕ'_{mob} for all earthquakes will be shown later on to lead to a reasonable estimation of the settlements induced by EQ1 but a significant over-prediction of the following deformations, hence an overall over-prediction. A mobilised friction angle of 38° (case ii) can be determined for EQ2. Given the fact that the peak acceleration of the following motions is not higher than that of this motion, the maximum mobilised dilation has been achieved during this motion, and no further change in mobilised friction angle would be observed for the following motions. Use of the corresponding ϕ^* derived from 38° will lead to an accurate prediction of the settlement

induced by the last six motions but an under prediction of the first two motions considering the wide range of high magnitude contents before peak acceleration for EQ2, hence an overall under prediction of crest settlement.

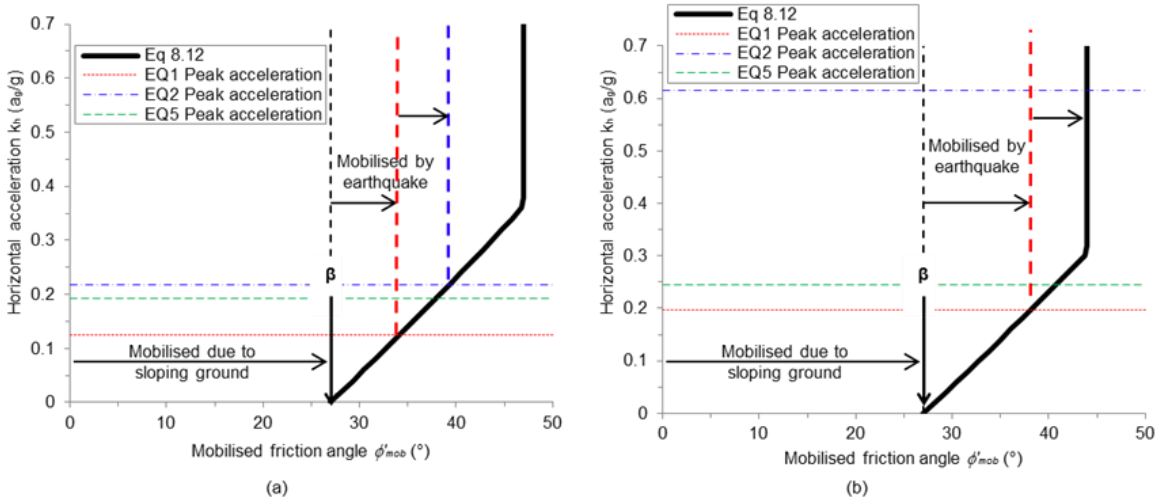

Fig 8.3 Estimation of mobilised friction angle using based on earthquake strength: (a) 2.4m slope; (b) 7.2m slope

In terms of taller slope which is subject to larger motions, the recorded peak acceleration is 0.61 g (EQ2), which is significantly higher than 0.31 g (acceleration for cap yield surface when $\phi'_{mob} = \phi'_{pk}$), so all cases will mobilise the full peak friction angle of the soil.

The soil used was cohesionless, and so the aforementioned procedure is sufficient to define the mobilised strength of unvegetated soil (i.e. $c' = 0$). For the rooted soil, the additional strength contribution from the roots used within the smeared rooted zones (see Fig 8.1) were input for the 3D root clusters (see Fig 6.4 (b)) based on the results of the large DSA tests for consistency with the FE simulations. A fine nodal density (1000 nodes) was used in all DLO calculations to accurately describe the geometry of the failure mechanism.

8.2.3 Effect of roots on slope failure mechanism (slip plane depth)

A comparison of the failure mechanisms determined for the fallow and vegetated slopes is shown in Fig 8.4. It is clear that, the 1:2 fallow slopes fail in a shallow translational

mechanism, with a shear plane located at the depth of 0.25 m and 0.70 m, for the 2.4 m and 7.2 m slope, respectively. This is consistent with the visual observations from the centrifuge tests. For the vegetated cases, different failure mechanisms are illustrated between the larger slope (7.2 m) and the smaller slope (2.4 m). The slip plane is observed to transferring from through the rooted zone to below the rooted zone for the 7.2 m slope. As for the 2.4 m slope, it is subject to a much shallower (0.09 m) slip failure between the rooted zones. The difference is not surprising given the fact that roots penetrate into the 2.4 m slope so deep and almost touch the base of the slope, as a result, roots stabilise the whole slope very well and cannot find a slip surface in the deep soil.

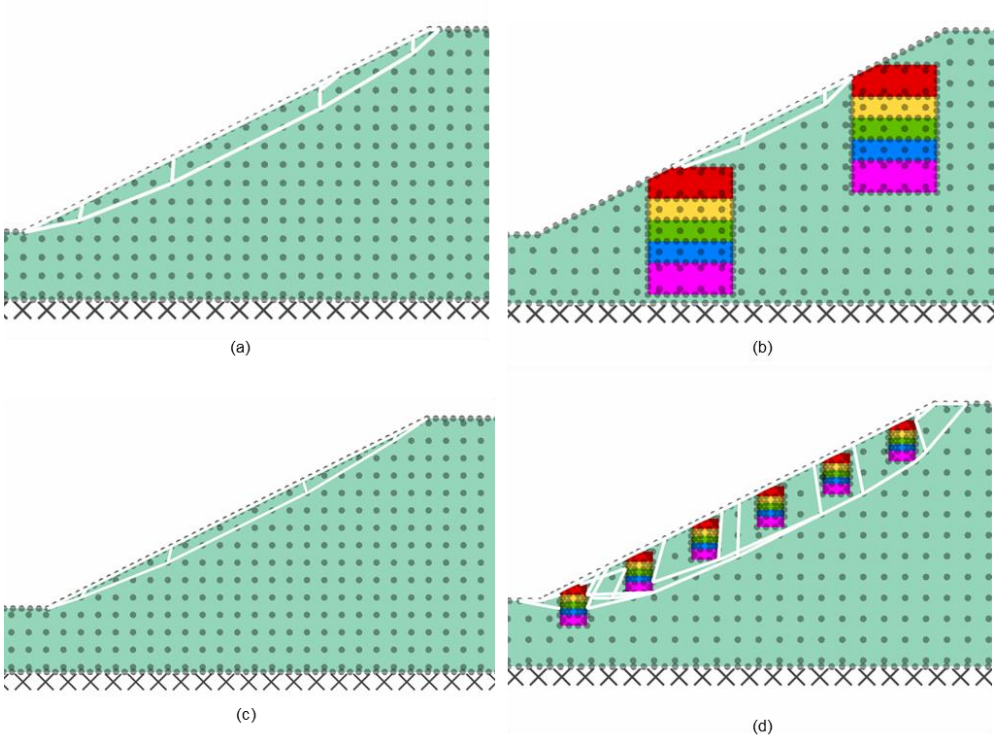

Fig 8.4 Failure mechanism computed from DLO : (a) 2.4 m fallow slope; (b) 2.4 m rooted slope; (c) 7.2 m fallow slope; (d) 7.2 m rooted slope

In other words, the shallower slip behaviour between rooted zones for 2.4 m slope implies the deep slip failure mechanism as depicted by 7.2 m slope. It is also worth noting here that the tree system acts in the same manner as toe stabilising piles in 2.4 m slope, further retraining the down-hill movement of the slope. Such observation will be employed in establishing the analytical model and will be revisited later.

8.2.4 Effect of roots on yield acceleration

Table 8.1 shows a summary of the static factor of safety (F_s) and the yield acceleration for all cases as determine by DLO, alongside the values for the yield acceleration of fallow slopes calculated using the approximate analytical infinite slope model described in Al-Defae et al. (2013). These latter results confirm that a reasonable estimation of k_{hy} is made using DLO for the fallow cases. The presence of roots is found to improve slope stability both in the static and dynamic condition (in the former case, through an increase in F_s and in the latter, via an increase in k_{hy}). An improvement of approximately 6-7% and 12% is observed for the static safety factor, for the 2.4 m and 7.2 m high slopes, respectively. In the dynamic condition, the yield acceleration for slippage is increased by 7-11% and 13%, for 2.4 m and 7.2 m slope, respectively. It is clear therefore that the presence of plant roots increases slope stability and will reduce seismic slip (due to increased yield acceleration).

However, considering Fig 8.4, it is apparent that the mechanism by which the roots achieve this stabilising effect is by forcing the slip plane below the root tips, which is clearly a sub-optimal failure mechanism compared to fallow slope conditions. Historically, the contribution of roots within slope stability has been considered through an additional shear strength component acting at the unaltered position of the slip plane (e.g. Norris *et al.* 2008; Sonnenberg *et al.* 2011; Mao *et al.* 2014). The results shown here suggest that knowing the root shear strength contribution is still important, but that (i) it is important to understand how this varies with position (particularly depth) in the soil, rather than just conducting shear box tests of rooted soil block samples at a single depth and (ii) once the roots provide a strong enough contribution to force the slip plane to pass beneath them, there will be little point in achieving further root strength.

This suggests that if planting trees to improve slope performance, it may not always be necessary to limit species choice to the strongest rooting species, and that selection from a wider range may be possible, so long as a minimum amount of root shear strength contribution can be achieved. This will be explored further in a later section.

Table 8.1. Static and dynamic slope stability data

Test ID	Slope type	Slope height	ϕ'_{mob}	ϕ^*	F_s (DLO)	z_{silp}	k_{hy} (DLO)	k_{hy} (Al-Defae et al. 2013)
TL04	Fallow	2.4m	34°	29.8°	1.264	0.38m	0.057g	0.049g
TL07	Rooted	2.4m	34°	29.8°	1.340	0.15m	0.063g	/
TL04	Fallow	2.4m	38°	33.6°	1.435	0.26m	0.124g	0.115g
TL07	Rooted	2.4m	38°	33.6°	1.532	0.15m	0.132g	/
TL05	Fallow	7.2m	44°	39.3°	1.691	0.70m	0.227g	0.203g
TL06	Rooted	7.2m	44°	39.3°	1.889	1.50m	0.257g	/

8.3 Development of an improved sliding-block method

In the forgoing section, DLO has been used to determine the critical failure mechanism and corresponding yield acceleration in vegetated slopes. While this is useful, one drawback of the DLO procedure is that it does not immediately yield to a direct measure of slope performance (e.g. seismically-induced slip) and it only provides an instantaneous yield acceleration at the initial slippage, and cannot account for the increase of acceleration due to geometric hardening of slope with slip (Al-Defae et al. 2013) without performing many repeat analyses on cases with reduced slope angle. In this section the sliding block method introduced by Newmark (1965) and modified by Al-Defae et al. (2013) to allow for geometric hardening is further developed to predict the permanent deformation response of vegetated slopes, utilising the yield accelerations derived from DLO.

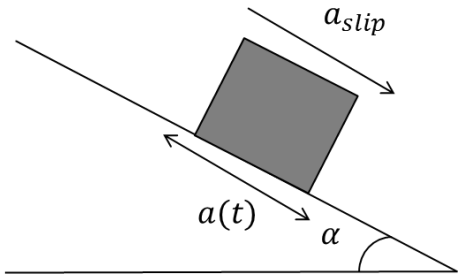

Fig 8.5 Schematic of Newmark sliding-block model

8.3.1 Formulation

The mechanism of earthquake induced slope displacement is the sliding of an essentially rigid block (given the shallow thickness, Fig 8.5) along a well-defined slip surface, which from Fig

8.5 may be approximated as largely translational, rather than rotational. From Newmark's original method, sliding occurs when the shaking induced acceleration exceeds the yield acceleration (Fig 8.5):

$$a_{slip} = a(t) - k_{hy} \quad \textbf{Eq 8. 13}$$

where k_{hy} is the horizontal yield acceleration ,which represents the acceleration required to overcome the sliding resistance along the slip plane and thus initiate sliding. Those portions of the recorded acceleration that exceed yield acceleration are integrated to obtain the cumulative displacement history of the block, *s(t)*, using the following equations:

$$v(t) = \begin{cases} \int_{t_1}^{t_2} \left(a(t) - k_{hy}\right) dt, t \in [t_1, t_2] \\ 0, otherwise \end{cases} \quad \textbf{Eq 8. 14}$$

$$\Delta s = \int_{t_1}^{t_2} v(t) dt, t \in [t_1, t_2] \quad \textbf{Eq 8. 15}$$

$$s = \sum \Delta s \quad \textbf{Eq 8. 16}$$

Aside from the DLO approach mentioned above, the horizontal yield acceleration of a shallow translational slip in fallow soil can be estimated using standard limit equilibrium techniques, incorporating pseudo–static acceleration components due to the seismic ground motion, as shown previously in Fig 8.2 (Sarma 1973; Bray & Rathje 1998;Bray & Travasarou 2007). Full details about the derivation of the yield acceleration in fallow soil can be found in Chapter 2 (Eq 2.6 – 2.9).

In a vegetated slope, the mechanism is more complicated given that the profile is now non-homogenous (rooted zone and non-rooted zone, as shown in Fig 8.1). Initial attempts, considering a rooted cohesionless slope to consist of a homogenised ϕ' (from the soil) and c' (from the roots) across the whole slope face (i.e. assuming that the additional resisting force provided by the roots was uniformly distributed among the slope plane), were presented in Chapter 5 and it was found that this assumption highly over predicted the effect of roots on

slope performance. However, Eq 2.8 can be divided into two parts, a part attributed to the fallow slope and the other part attributable to the mobilisation of root resistance, that is:

$$k_{hy(rooted)} = \frac{\cos\beta\tan\phi' - \sin\beta}{\cos\beta + \sin\beta\tan\phi'} + \frac{c'}{\gamma z\cos^2\beta + \gamma z\sin\beta\cos\beta\tan\phi'} \quad \textbf{Eq 8. 17}$$

$$k_{hy(rooted)} = \frac{\cos\beta\tan\phi' - \sin\beta}{\cos\beta + \sin\beta\tan\phi'} + \Delta k_{hy} \quad \textbf{Eq 8. 18}$$

where Δk_{hy} is the increase of yield acceleration due to the presence of roots. This increase can be determined directly from DLO:

$$\Delta k_{hy} = k_{hy(rooted)}^{DLO} - k_{hy(fallow)}^{DLO} \quad \textbf{Eq 8. 19}$$

It should be noted that the initial yield accelerations for the fallow slope component calculated by Eq 2.9 and DLO are a little different (see Table 8.1), so a modification is required to keep consistency between the two approaches which will be described later.

In a standard sliding block analysis (Kim & Sitar 2004), β and ϕ' are constant, but in reality, strain hardening (SH) and strain softening (SS) behaviour is always observed for dense soil. In a strong earthquake, a single cycle usually causes sufficient strain/slip to reach the critical state condition and so the effect of SH and SS behaviour on crest settlement is relatively limited and can be overlooked. But for small to moderate earthquakes whose peak ground acceleration magnitude is close to (larger than) k_{hy}, it may be not the case. SS behaviour has been reported to have a dramatic effect on computed slope displacements in some cases (Matasovic et al. 1997) . To account for SS behaviour, Al-Defae et al. (2013) suggested using the strain-softening model proposed by Matasovic et al. (1997) (see Fig 8.6), in which case ϕ' is highly depended on the magnitude of shear strain. Before calculation, an estimated thickness of the shear band along the slip plane is required to estimate shear strain. This makes the problem more complicated and limits its practical use. Here a much simpler but effective model based on ϕ^* is used (see Eq 8.8).

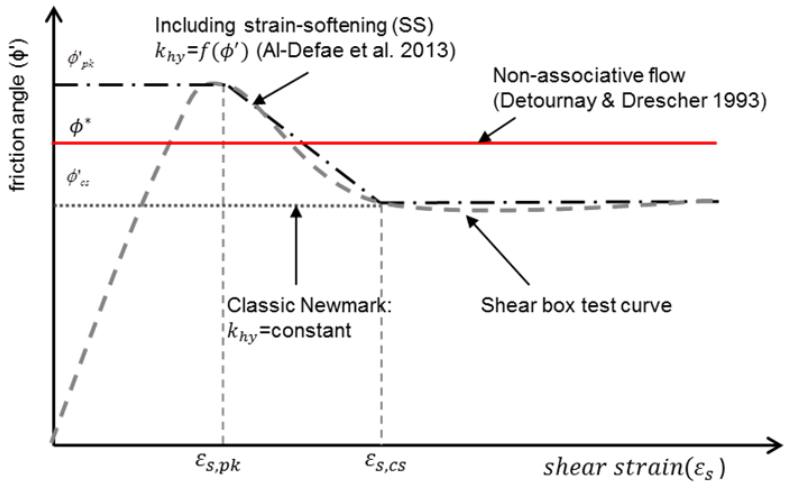

Fig 8.6 Schematic of strain hardening and strain softening in new sliding-block model along with other models

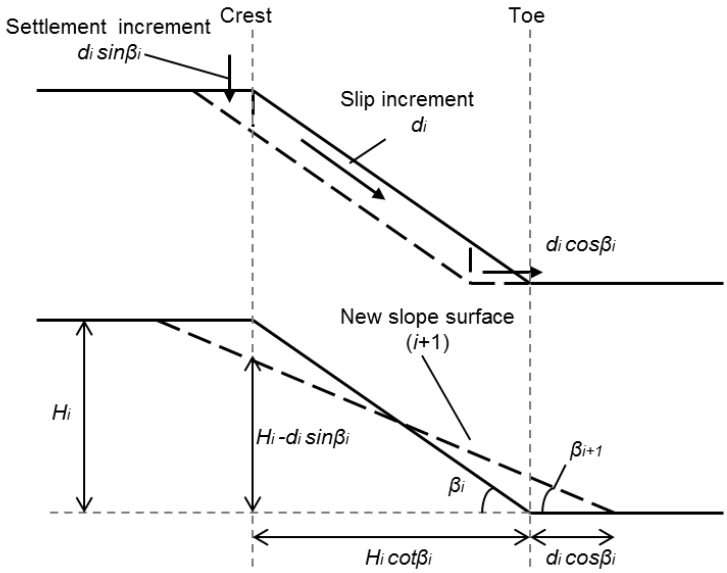

Fig 8.7 Schematic of geometric hardening (re-grading) incorporated in the sliding-block model

In terms of the slope angle, it will decrease with slippage as crest settlements make the slope shallower, which is called re-grading (RG). A simplified model for re-grading is shown schematically in Fig 8.7 after Al-Defae et al. (2013). The instantaneous slope angle β_{i+1} can be estimated by the following equation,

$$\beta_{i+1} = \tan^{-1}\left(\frac{H_i - d_i \sin\beta_i}{H_i \cot\beta_i + d_i \cos\beta_i}\right) \qquad \textbf{Eq 8. 20}$$

where H_i is the height of the slope at the previous time step of the Newmark analysis and d_i is an increment of slip in this time step. For the initial time step, d_0=0, H_i=H and β_i=β_0 (initial slope angle). It is assumed here that once the slope has deformed to a new, small value of β, the failure mechanism will continue to be of the translational type, with a new slip surface parallel to the new slope surface. Then the slope angle can be re-calculated at each time step to account for the regarding of the slope based on the increment of slip occurring in the last step using Eq 8.20.

Understanding the re-grading behaviour of slope, Eq 8.18 can then be modified to incorporate this in the unreinforced component; the difference between the DLO and analytically computed versions of this component can also be incorporated by multiplying the DLO version by a reduction factor from the analytical model:

$$k_{hy(rooted)} = \frac{k_{hy(fallow)}^{DLO}\left(\cos\beta\tan\phi' - \sin\beta\right)\left(\cos\beta_0 + \sin\beta_0\tan\phi'\right)}{\left(\cos\beta_0\tan\phi' - \sin\beta_0\right)\left(\cos\beta + \sin\beta\tan\phi'\right)} + \left(k_{hy(rooted)}^{DLO} - k_{hy(fallow)}^{DLO}\right)$$

Eq 8. 21

Eq 8.21 integrates the effects of root resistance (from DLO), SH, SS and RG behaviour into a single equation which is simple to use at each time step to calculate the instantaneous value of the yield acceleration within a Newmark sliding block analysis. The effectiveness of this equation in quantifying the performance of rooted slopes will be validated against the centrifuge data in the following section.

8.4 Validation of sliding block model

Sliding-block analyses were subsequently conducted for each of the centrifuge tests. The input earthquake loading used was the acceleration record measured at instrument ACC2 in each case, as previously used in the FEM. The effect of root resistance, geometric re-grading (change in β) and strain softening on the yield acceleration compared to the fallow slope using the mobilised friction angles for EQ1(small earthquake) and EQ2 (large earthquake) of

TL 06 is shown in Fig 8.8 as an example. Only the positive (downslope) accelerations have been shown for clarity.

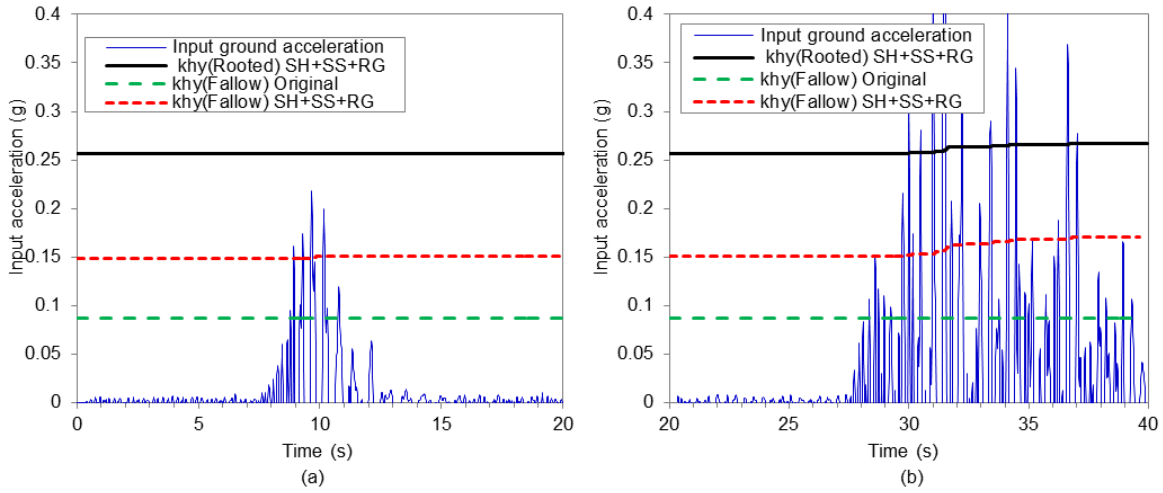

Fig 8.8 Application of new sliding-block model to 7.2 m high slope, showing key effects: (a) EQ1; (b) EQ2.

It can be seen that the model considering strain softening via ϕ^* highly increases the initial yield acceleration compared with that based on critical state strength (SH), from 0.08 g to 0.15 g for EQ1. As a result, a large portion of EQ1 will be not considered in predicting the yield acceleration and this will strongly influence the deformation response, which will be illustrated later. It is worth noting here that the effect of root resistance on yield acceleration was constant between EQ1 and EQ2. This is clearly a simplification of the problem because the effect of root resistance will be mobilised progressively rather than instantly reaching peak resistance.

However, given that root-soil interaction will mobilise very rapidly with slip due to the small diameter of the roots (see Chapter 4 and Chapter 5), the simplification is considered to be reasonable. Geometric re-grading causes the yield acceleration to increase non-linearly throughout the remainder of the earthquake with continuing slip, leading to reduced slip velocity and hence reduced permanent slip compared with the case with no geometric hardening.

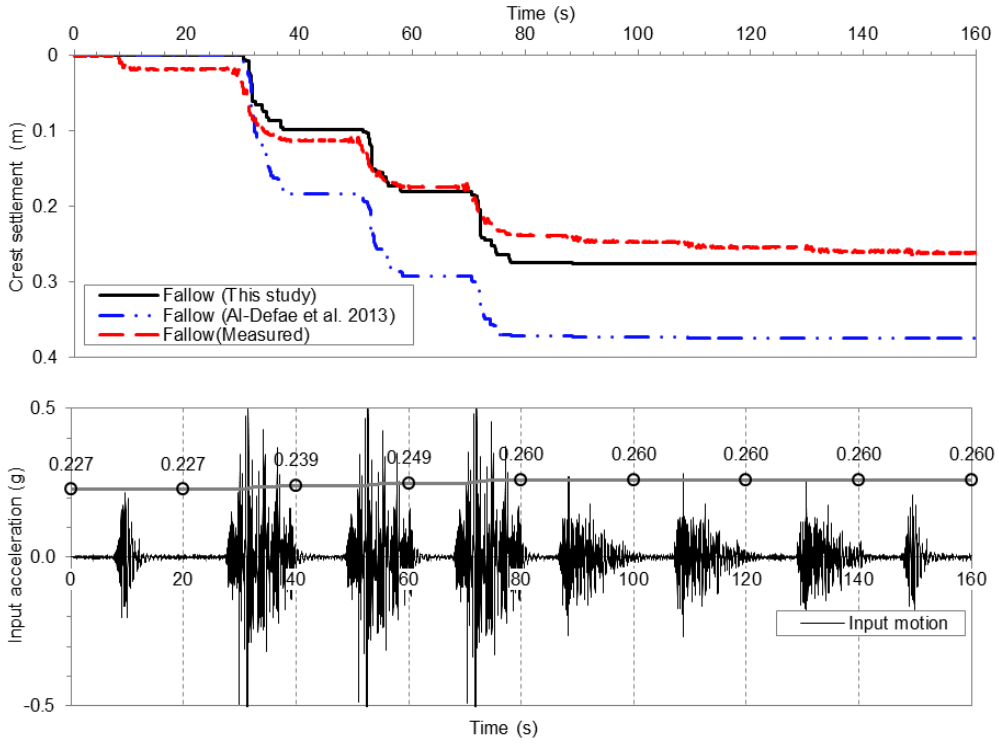

Fig 8.9 Comparison of predicted cumulative crest settlements with centrifuge test measurement for 7.2 m high fallow slope

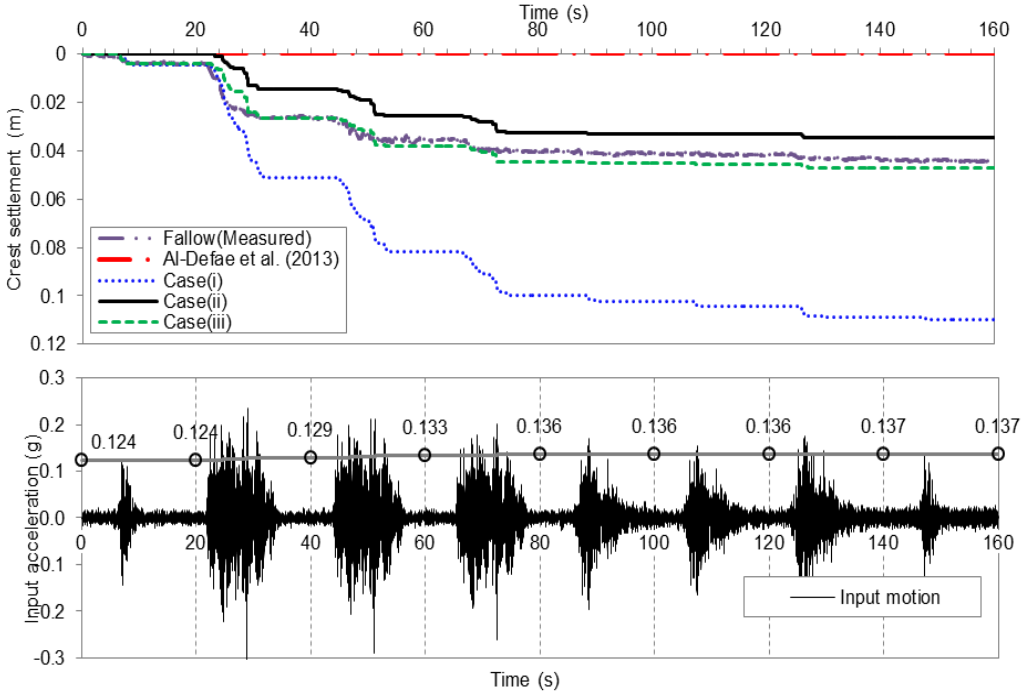

Fig 8.10 Comparison of predicted cumulative crest settlements with centrifuge test measurement for 2.4 m high fallow slope

8.4.1 Fallow slope

Fig 8.9 and Fig 8.10 shows the cumulative crest settlement across the eight earthquakes as predicted by sliding block model and compares this to the values measured in centrifuge, for the 1:30 scale (7.2 m high) slope and the 1:10 scale (2.4 m high) models, respectively. It is clear that, for both suites of earthquake motions, use of the Kim & Sitar (2004) model with critical strength hugely over-predicts settlement at the crest of fallow slope. This would lead to a significant over-prediction of the risk posed to the slope, and hence, potentially, uneconomic design. For the prediction of the large slope (7.2 m) behaviour subject to large motions the model presented by Al-Defae et al. (2013) tracks the settlement at the crest of the fallow slope reasonably closely to the centrifuge observations. However, the new model developed in this study presents an even better match.

In terms of the 2.4 m slope which is subject to smaller earthquake motions, the initial model with constant β and ϕ' shows a dramatic difference compared to the 7.2 m slope when the Al-Defae et al. (2013) model is considered. An over-estimation of 42% in crest settlement is observed for the 7.2 m slope, but for the 2.4 m slope, the slope is found to be stable without any crest deformation. This reflects the use of the full peak strength as the initial value in this model, rather than the, mobilised friction angle from Fig 8.3. The dilation and strength of sand measured in the direct shear tests are based on the cap yield surface and hence lead to an over-prediction of dilation response during small earthquake loading. Case (i) (use of mobilised friction angle of 34°) gives a good match to the displacement response of EQ1 as measured from centrifuge tests but significantly over-estimates the response of the following motions. For case (ii) (use of mobilised friction angle of 38°), under-estimations are observed for the first two motions but good matches are shown in the following six motions as described previously. To better validate the improved model and provide a reference for the rooted case, the settlement induced by each motion was also estimated separately and accumulated to obtain the overall settlement trend (case (iii)). In case (iii), three mobilised friction angles were used: 34°, 36.7° and 38°, for EQ1, EQ2 and the last six motions, respectively. The mobilised friction angle of 36.7° is derived from the first peak (0.18g) of EQ2 and shows an overall good match of the settlement for EQ2. Case (iii) presents a slight over-estimation of EQ3, the reason for this is due to the recorded peak acceleration of 0.237 g,

which is a little higher than that of EQ2 (0.22 g), but is not taken into consideration for simplicity in use.

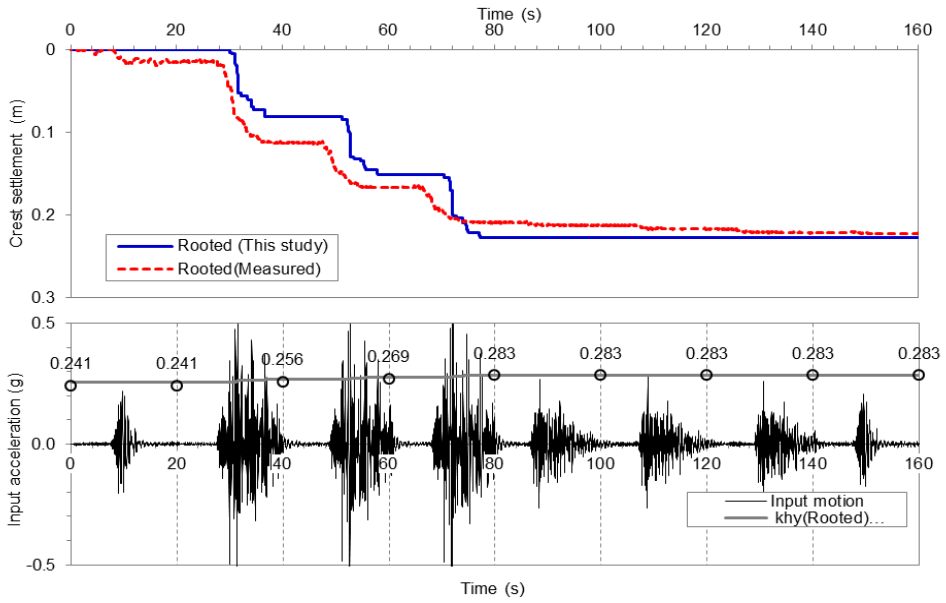

Fig 8.11 Comparison of predicted cumulative crest settlements with centrifuge test measurement for 7.2 m high fallow slope

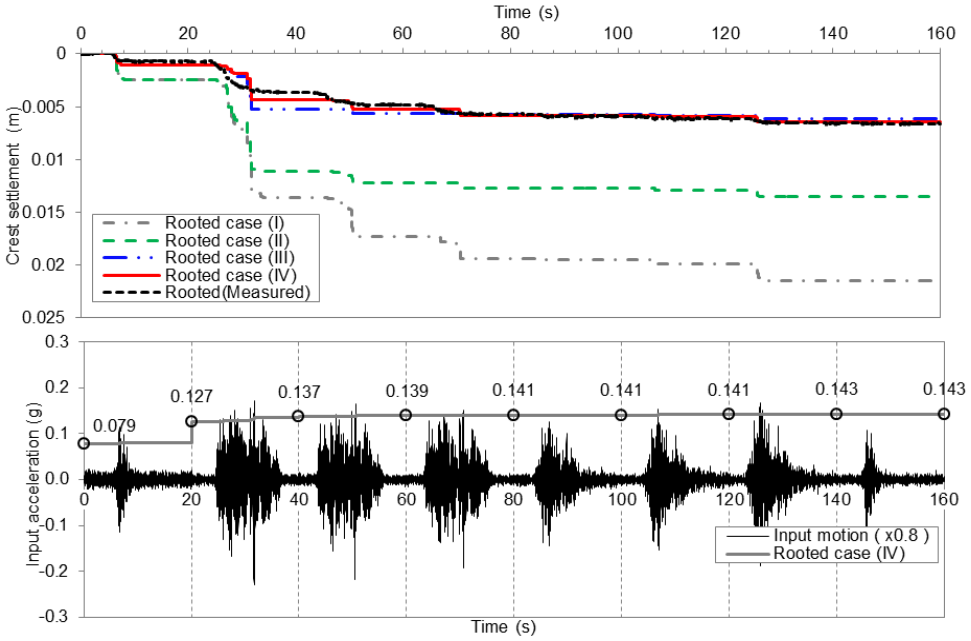

Fig 8.12 Comparison of predicted cumulative crest settlements with centrifuge test measurement for 2.4 m high fallow slope

8.4.2 Rooted slope

Fig 8.11 also shows the results of simulations of cumulative crest displacement compared with the centrifuge test data, for 7.2m rooted slope. A good match to the total measured crest settlement at the end of the test is presented. A reduction of 15% in calculated permanent crest settlement is observed after a comparison with the calculated fallow case through the modified sliding block model. This reduction is consistent with the observation from the centrifuge tests (15%). This further proves that reduction of crest settlement is mainly due to the increase of the yield acceleration for the 7.2 m slope due to the deepening of the slip plane shown in Fig 8.4 (d). However, the sliding block model does not quite capture the reduction within each motion perfectly. As observed, the root contribution is mainly mobilised in EQ4 in the centrifuge tests, but this is mobilised from EQ2 progressively in the simulated case.

The permanent crest settlement for the 2.4 m rooted slope across the eight earthquakes as estimated by the new sliding block model, with a comparison to the centrifuge results shown in Fig.8.12. Here, four cases were considered: case (a) is the standard case as used in the 7.2 m slope; case (b) is established to account for the root buttressing behaviour observed in DLO, and is achieved by adjusting the slope height from 2.4 m to 0.4 m in calculation; case (c) corresponds to the reduction (20%) of peak acceleration observed in centrifuge tests and is performed by multiplying the input motion by a factor of 0.8 as new input motion; case (d) considers the combined effect of case (b) and case (c). It can be clearly found that case (a) without consideration of the acceleration reduction effect highly under-estimates the contribution of the roots on the slope crest deformation response. The reduction of crest settlement caused by the increase of the yield acceleration, root buttressing and the reduction of peak acceleration is 54%, 37% and 71%, respectively. The overall reduction of these three effects is 90%, which is a little higher that that (85%) observed in centrifuge tests. The reason for this is associated with the fact that the contribution of roots is mainly mobilized during the first two motions and then has an apparently less significant effect for the last six motions in the centrifuge tests but the simulated case assumes that the root contribution keeps constant across the eight earthquakes. If the root contribution is ruled out for the last six motions, a very good match is presented (see Fig 8.13). Fig 8.12 also suggest that the contribution of roots on seismic performance of small slopes is mainly mobilised by the

increase of yield acceleration and decrease of peak acceleration due to the deepening of the slip plane as shown in Fig 8.4 (b).

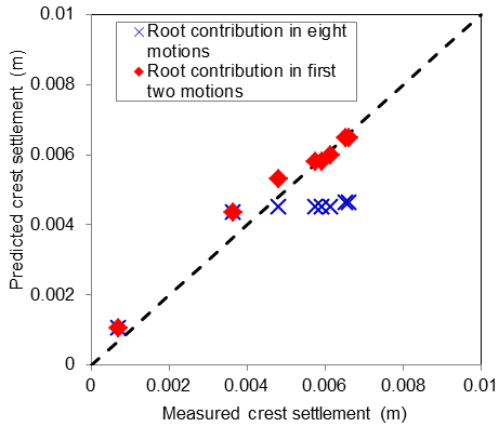

Fig 8.13 Accuracy of new sliding-block model, showing the effect of assuming the root contribution mobilised during different motions

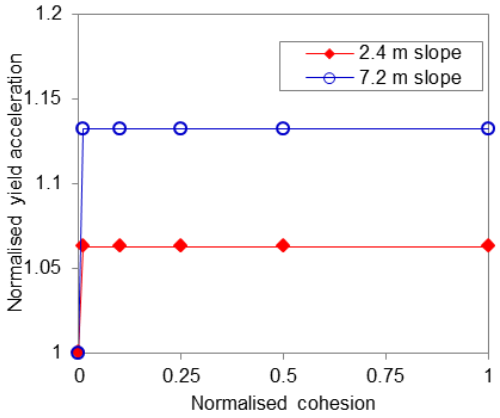

Fig 8.14 Influence of root cohesion on yield acceleration of the slope

8.5 Future insights into rooted slope behaviour

In Chapter 7, a parametric study has been conducted to investigate the influence of different potential characteristics of rooted soil on the overall seismic performance of slope with

different size using FE modelling. Here, the influence of root cohesion is further revealed using the improved sliding-block procedure.

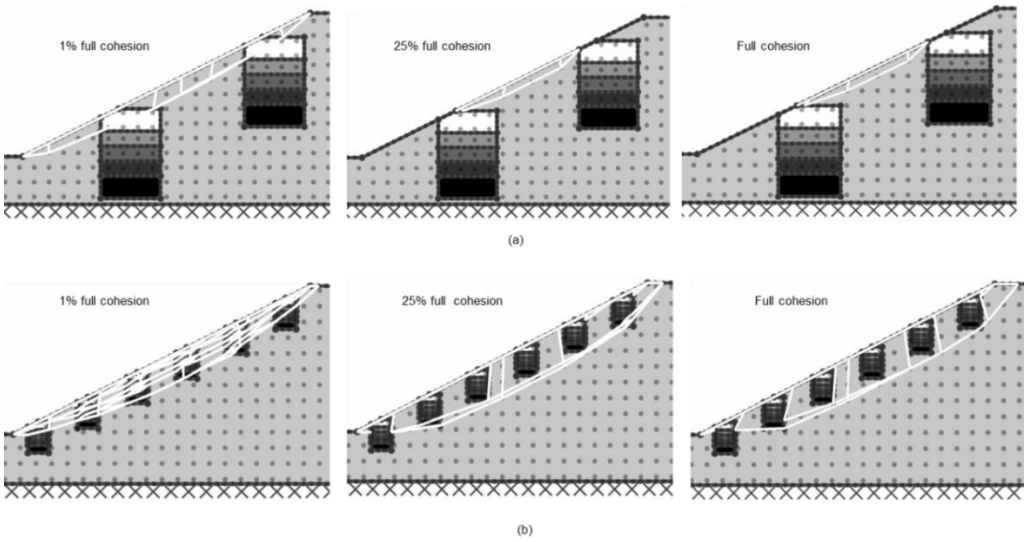

Fig 8.15 Comparison of failure mechanism for rooted slope with different cohesion: (a) 2.4m slope; (b) 7.2m slope

The variation of yield acceleration with the decay of root cohesion is shown in Fig 8.14. To obtain these results, the distributions of root cohesion in Fig 6.4 (b) were uniformly reduced at all depths by the reduction factor shown on the *x*-axis of Fig 8.14. It can be found that the yield acceleration always keeps constant even when the root cohesion decreases to 1% (approximately 0.16 kPa of root cohesion within the rooted zone) of its initial strength for 2.4 m slope. However, according to Chapter 7, when the root cohesion decreases less than 25%, the root contribution on slope performance will reduce rapidly. Such conflict was further identified by checking the depth of the slip plane for these two remarkable cases, as shown in Figure 8.15 (a). For the low root cohesion (1%) case, although the yield acceleration increases to the ultimate value, the slip plane is still passing through the rooted zone. While for the 25% strength case, the slip depth transfers from through the rooted zone to between the rooted zones as full strength case. This indicates that the rapid decrease of root contribution for 2.4 m slope reported in Chapter 7 is mainly induced by the change of slip plane rather than the decrease of yield acceleration. As for the 7.2 m slope, the slip plane shallows (see Fig 8.15 (b)) gradually with the decay of root cohesion and results in a decreasing contribution (see Fig 8.4 (b)).

8.6 Conclusion

An improved Newmark sliding-block procedure which can include the effect of roots on seismic slope performance has been developed and validated against dynamic centrifuge data. The procedure consists of two components. Firstly, DLO analysis is used to determine the seismic slope failure mechanism and estimate the corresponding yield acceleration of a given slope. The rigid perfectly plastic (Mohr–Coulomb) model with associative flow is used to model the slope, but this model overlooks the SH and SS behaviours of soil. To more realistically simulate the non-associative behaviour of cohesionless slopes, a simple modification was used to model this as an equivalent associative material and an approach for estimating mobilised friction angle as a function of earthquake strength is also incorporated. The second stage incorporates the derived yield acceleration from DLO into a modified Newmark sliding block approach to predict the permanent settlement at the crest of the slope; this also accounts for the geometric hardening response of slope with slip. This procedure is validated to be highly effective for both fallow and vegetated slopes as measured in centrifuge test and can be easily performed in preliminary design to predict the seismic performance of rooted slopes with lower computational effort than Finite Element modelling.

Some factors that may influence the seismic performance of root reinforced slopes were also revealed during the development of sliding-block model. The presence of roots deepens the slip plane depth and it is this effect which increases the yield acceleration against seismic loading hence stabilises the slope. The potential benefit of roots appears to vary with the size of the slope. For large slopes where the root depth is only a small proportion of the slope height, roots only increase the yield acceleration of slope against dynamic loading. For smaller slopes, in addition to increasing the yield acceleration in a similar way, roots also appear to decrease the magnitude of earthquake loading within the slope resulting in increased effectiveness and much reduced deformation response at the crest.

Chapter 9 Conclusions and future work

9.1 Overview

In this thesis, 3-D printing of layered ABS plastic was firstly used to produce repeatable root analogues which are highly representative of the mechanical behaviour of real roots. The printed root analogues were used in large direct shear tests and centrifuge tests to study root-soil interaction and the seismic behaviour of rooted slopes. A total of 8 identical slopes at model scale, with varied g level and motion frequency were conducted, reported and interpreted, considering fallow and root-reinforced cohesionless slopes, to provide a richer dataset concerning the dynamic response within the slope (e.g. more information on topographic amplification). This was then supported by the development of numerical modelling procedures (beam-on-a–nonlinear-Winkler-foundation (BNWF) model for root-soil interaction and finite element modelling (FEM) for global slope performance) and a modified sliding block procedure for use in design.

Tree root systems were simplified and classified into two types in this study: i) a straight root group which was designed to represent a plate / heart root system, of which most of the individual roots behave independently; ii) 1:10 and 1:30 scale root clusters which were designed to represent a tap root system. The distinct behaviour of these two types of roots were revealed and compared both in 1g large direct shear tests and 1:10 scale centrifuge tests, and this should be given particular attention when using the existing models for slope design.

Centrifuge observations and supporting analytical models illustrate that vegetated slopes perform better than the benchmark fallow slopes during earthquakes, especially in terms of the crest deformation response, which is a key parameter in performance based slope assessment and design. The benefit of vegetation to slope performance is mainly mobilised through forcing the slip plane deeper than its optimal position or buttressing the movement of the shallow soil, depending on the height of the slope compared to the depth of the roots. However, there may be a limiting height of slope beyond which other forms of reducing slip

may be more effective. The reason for this is mainly related to the shallow depth of the root system, the majority of which is concentrated within the top 2 m (Jackson et al. 1996). In other words, tree roots as an individual engineering technique for slope stabilisation will not be such an effective solution for taller slopes, where complementary hard engineering methods (e.g. piles, retaining walls) should be used. But for slopes of modest height (e.g. small embankments along transport infrastructure), tree roots may be a very effective seismic slope stabilisation method.

In practice, plant species for slope stabilisation are generally screened for their ability to establish and grow in the target environment, defined in terms of their specific physical, chemical, ecological and biological characteristics (Stokes et al. 2014). Plant traits of particular relevance to stabilising slopes, such as root morphology and root mechanical properties are highlighted in previous research (e.g. Genet *et al.* 2005;Mickovski *et al.* 2007; Sonnenberg *et al.* 2010; Ghestem *et al.* 2013). However, parametric studies reported in this thesis suggest that when vegetation is used in slopes of modest height (the most effective case), the benefit of vegetation on global slope performance is significantly affected by the lateral and vertical extent of root system, but insensitive to the continuous increase of root cohesion. So it could be better for practitioners of ecological engineering to select species with deep and extensive lateral root systems, rather than focus on cultivating species having the strongest possible root systems.

The analytical procedures developed in this thesis are recommended for use, particular in the preliminary design stages, and they could provide a quite accurate and reasonable prediction both for individual root soil interaction and global slope performance. However, it should be noted here that although the common root reinforcement models such as WWM and FBM generally over simplified the behaviour of root and soil interaction and significantly over-estimated the contribution of roots to the rooted soil shear strength, such over-estimation of root cohesion will not have a significant impact on the global slope performance (e.g. crest settlement) given the insensitivity to increasing root strength described above.

9.2 Future work

This project aimed to investigate the dynamic performance of slopes planted with tree roots from individual root-soil interaction to global slope behaviour. Specific areas for future study are described in relation to specific objectives of this:

Scale modelling of tree root system: In this study the heart/ plate roots system was simplified to be a straight root group based on previous study. Further validation of this simplification should be conducted in the future. In terms of tap root systems, only one specific 3-D root morphology (tap root system with fine roots in the deep soil) was modelled and idealised. Other root morphologies such as tap root system with extensive laterals may also be of interest. The effect of variation of root system properties with time will also be an important practical issue from the point of view of planting management.

Qualify the root and soil interaction: The root traits that may affect root and soil interaction were studied through DSA testing, but no FEM of individual roots in soil has been performed to support the testing results. Since the BNWF model gave such good simulation of individual root and soil interaction, it will be suitable to employ such a model to detect the possible factors that may affect root contribution in a computationally-efficient way. Furthermore, the root soil interaction was investigated mainly based on the root overturning behaviour; uprooting behaviour during slippage should also be considered in the future.

Improved BNWF model for root system: The BNWF model using existing *p-y* formulations was employed to simulate the individual root and soil interaction, but when it comes to the root system, a type of structure which is more complicated than pile groups, then further factors such as 3-D geometry/tortuosity will need to be investigated.

Dynamic centrifuge modelling of rooted slope: 11 centrifuge models were initially planned for the whole project. The effects of slope height, input motion frequency, and root morphology have already been investigated. However, 3 tests which were designed to investigate the effect of the subaerial component of trees (trunk) and the surrounding shallow grass root system remain. Also, the effect of different 3-D root geometries on reinforcement remains unknown and tracing the optimal structure and the widespread suitability of the analysis methods in the thesis would be an area for future research beyond this project, to

provide more detailed guidance for engineering use. Moreover, all the centrifuge tests performed in this study were conducted using dry cohesionless soil. The main reason for this was to ensure controlled parameters and avoid decouple other influences such as seismic liquefaction and root hydrological effects. Once a full understanding of the mechanical effect of roots on slope performance is obtained, the potential effects of roots on liquefaction and modifying the pore water pressure can be quantified.

Soil dilation behaviour under dynamic condition: The importance of using the mobilised friction angle in dynamic dilation analysis was highlighted in this study. Realising and determining the proper mobilised strength properties will be of great value in geo-structure design.

Numerical modelling of rooted slopes: The numerical modelling was mainly used to simulate the centrifuge modelling performed in this study. Since it could provide such a good simulation, further detailed investigation into slope site effects, slope topography effects and motion characteristic effects on seismic performance of slopes should be characterised through using varied slope geometry (e.g. slope morphology, slope angle and slope height) and varied types of earthquake motions. Furthermore, FE models with ESB container boundaries were established to investigate the effectiveness of standard FEM procedures. Further investigation into the performance of ESB containers using numerical modelling would be an area for future research.

Generalisation of the whole simulation and prediction procedure for engineering application: The improved sliding block procedure can be easily performed in preliminary design to estimate the seismic performance of rooted slopes and determine the optimal planting strategy to minimise slope deformation. However, the BNWF model developed in this study may still be difficult for engineering application due to access to the software. Implementation of a program for BNWF root-soil interaction during shear loading in a MATLAB script or Microsoft Excel spreadsheet file rather than running FE software will be more helpful.

REFERENCE

Abdi, E. 2014. Effect of Oriental beech root reinforcement on slope stability (Hyrcanian Forest,Iran). *Journal of Forest Science*. **60**(4): 166–173.

Abdi, E., Majnounian, B., Rahimi, H., Zobeiri, M., Mashayekhi, Z. & Yosefzadeh, H. 2010. A comparison of root distribution of three hardwood species grown on a hillside in the Caspian forest, Iran. *Journal of Forest Research*. **15**(2): 99–107. doi:10.1007/s10310-009-0164-2.

Abramson, L.W., Lee, T.S., Sharma, S. & Boyce, G.M. 2002. Slope stabilty and stabilization methods. *John Wiley & Sons.*

Akinnifesi, F.K., Kang, B.T. & Ladipo, D.O. 1999. Structural root form and fine root distribution of some woody species evaluated for agroforestry systems. *Agroforestry Systems*. **42**(2): 121–138. doi:10.1023/A:1006178002019.

Akl, A., Mansour, M. & Moustafa, H. 2014. Effect of changing configurations and lengths of piles on plied raft foundation behaviour. *Civil Engineering and Urban Planning*. **1**(1).

Al-Defae, A.H, Caucis, K. & Knappett, J.A 2013. Aftershocks and the whole-life seismic performance of granular slopes. *Géotechnique*. **63**(14): 1230–1244. doi:10.1680/geot. 12.P.149.

Al-Defae, A.H & Knappett, J.A 2014. Centrifuge Modeling of the Seismic Performance of Pile-Reinforced Slopes. *Journal of Geotechnical and Geoenvironmental Engineering*. **140**(6): 1–13. doi:10.1061/(ASCE)GT.1943-5606.0001105.

Al-Defae, A. H. & Knappett, J.A. 2015. Newmark sliding block model for pile-reinforced slopes under earthquake loading. *Soil Dynamics and Earthquake Engineering*. **75**: 265–278. doi:10.1016/j.soildyn.2015.04.013.

Al-Defae, A.H. 2013. Seismic performance of pile reinforced slopes. *PhD thesis,University of Dundee,UK*.

Allotey, N. & Foschi, R. 2005. Coupled P-Y T-Z Analysis of Single Piles in Cohesionless Soil Under Vertical and/or Horizontal Ground Motion. *Journal of Earthquake Engineering*. **9**(6): 755–775. doi:10.1080/13632460509350565.

Augustesen, A.H. 1901. Review of p-y relationships in cohesionless soil. *Civil Engineering*. (57).

Ausilio, E., Conte, E. & Dente, G. 2001. Stability analysis of slopes reinforced with piles. *Computers and Geotechnics*. **28**(8): 591–611. doi:10.1016/S0266-352X(01)00013-1.

Aydan, Ö., Ulusay, R., Hamada, M. & Beetham, D. 2012. Geotechnical aspects of the 2010 Darfield and 2011 Christchurch earthquakes, New Zealand, and geotechnical damage to structures and lifelines. *Bulletin of Engineering Geology and the Environment*. **71**(4): 637–662. doi:10.1007/s10064-012-0435-6.

Baker, R. 2003. Sufficient conditions for existence of physically significant solutions in limiting equilibrium slope stability analysis. *International Journal of Solids and Structures*. **40**(13-14): 3717–3735. doi:10.1016/S0020-7683(03)00075-1.

Baker, R. & Garber, M. 1978. Theoretical analysis of the stability of slopes. *Géotechnique*. **28**: 395–411. doi:10.1680/geot.1978.28.4.395.

Baker, R., Shukha, R., Operstein, V. & Frydman, S. 2006. Stability charts for pseudo-static slope stability analysis. *Soil Dynamics and Earthquake Engineering*. **26**(9): 813–823. doi:10.1016/j.soildyn.2006.01.023.

Bathe, K.J. & Saunders, H. 1984. Finite Element Procedures in Engineering Analysis. *Journal of Pressure Vessel Technology*.106 (4) p.: 421. doi:10.1115/1.3264375.

Bertalot, D. 2013. foundations on layered liquefiable soils. *PhD thesis,University of Dundee,UK*.

Bhd, P.S., Lumpur, K. & Engineer, S.G. 2004. Slope Stabilization Using Soil Nails : Design Assumptions and Construction Realities. *Malaysia-Japan Symposium on Geohazards.* : 2277–2280.

Bischetti, G.B., Chiaradia, E. A., Simonato, T., Speziali, B., Vitali, B., Vullo, P. & Zocco, A. 2005. Root strength and root area ratio of forest species in lombardy (Northern Italy). *Plant and Soil*. **278**(1-2): 11–22. doi:10.1007/s11104-005-0605-4.

Bischetti, G.B., Chiaradia, E.A., Epis, T. & Morlotti, E. 2009. Root cohesion of forest species in the Italian Alps. *Plant and Soil*. **324**(1): 71–89. doi:10.1007/s11104-009-9941-0.

Bishop, A.W. 1955. The use of the Slip Circle in the Stability Analysis of Slopes. *Géotechnique*.5 (1) pp.: 7–17. doi:10.1680/geot.1955.5.1.7.

Bolton, M.D. 1986. Discussion: The strength and dilatancy of sands. *Géotechnique*.36 (1) pp.: 65–78. doi:10.1680/geot.1987.37.4.517.

Bolton, M.D. & Take, W.A. 2011. Seasonal ratcheting and softening in clay slopes, leading to first-time failure. *Géotechnique*.61 (9) pp.: 757–769. doi:10.1680/geot.9.P.125.

Bouckovalas, G.D. & Papadimitriou, A.G. 2005. Numerical evaluation of slope topography effects on seismic ground motion. *Soil Dynamics and Earthquake Engineering*. **25**(7-10): 547–558. doi:10.1016/j.solidyn.2004.11.008.

Boulanger, R., Kutter, B. & Brandenberg, S. 2003. Pile foundations in liquefied and laterally spreading ground during earthquakes: centrifuge experiments & analyses. *Journal of Geotechnical and Geoenvironmental Engineering*. (September): 205.

Bray, J.D. & Rathje, E.M. 1998. Earthquake-Induced Displacements of Solid-Waste Landfills. *Journal of Geotechnical and Geoenvironmental Engineering*.124 (3) pp.: 242–253. doi:10.1061/(ASCE)1090-0241(1998)124:3(242).

Bray, J.D. & Travasarou, T. 2007. Simplified Procedure for Estimating Earthquake-Induced Deviatoric Slope Displacements. *Journal of Geotechnical and Geoenvironmental Engineering*.133 (4) pp.: 381–392. doi:10.1061/(ASCE)1090-0241(2007)133:4(381).

Brennan, A.J, Thusyanthan, N.I. & Madabhushi, S.P.G. 2005. Evaluation of shear modulus and damping in dynamic centrifuge tests. *Journal of Geotechnical and Geoenvironmental Engineering*. **131**(12): 1488–1497. doi:10.1061/(ASCE)1090-0241 (2005)131:12(1488).

Brennan, A.J., Knappett, J.A., Loli, M., Anastasopoulos, I. & Brown, M.J. 2014. Dynamic centrifuge modelling facilities at the University of Dundee and their application to studying seismic case histories. *ICPMG2014 – Physical Modelling in Geotechnics*. (2002): 227–233.

Brennan, A.J. & Madabhushi, S.P.G. 2009. Amplification of seismic accelerations at slope crests. *Canadian Geotechnical Journal*. **46**(5): 585–594. doi:10.1139/T09-006.

Brennan, A.J., Madabhushi, S.P.G. & Houghton, N.E. 2006. Comparing laminar and equivalent shear beam (ESB) containers for dynamic centrifuge modelling. In: *Physical modelling in geotechnics : 6th ICPMG '06*. pp. : 171–176.

Brinkgreve, R., Kappert, M. & Bonnier, P. 2007. Hysteretic damping in a small-strain stiffness model. *Numerical Models in Geomechanics*. : 737–742.

Brown, D.A., Morrison, C. & Reese, L.C. 1988. Lateral Load Behavior of Pile Group in Sand. *Journal of Geotechnical Engineering*. **114**(11): 1261–1276. doi:10.1061/(ASCE)0733-9410(1988)114:11(1261).

Brown, D.A., Reese, L.C. & O'Neill, M.W. 1987. Cyclic Lateral Loading of a Large-Scale Pile Group. *Journal of Geotechnical Engineering*. **113**(11): 1326–1343. doi:10.1061/ (ASCE)0733-9410(1987)113:11(1326).

Brown, W.J. 1991. Landslide control on North Island, New Zealand. *Geographical Review*. **81**(4): 457–472.

Buech, F., Davies, T.R. & Pettinga, J.R. 2010. The little red hill seismic experimental study: Topographic effects on ground motion at a bedrock-dominated mountain edifice. *Bulletin of the Seismological Society of America*. **100**(5 A): 2219–2229. doi:10.1785/0120090345.

Bufler, H. 1971. Theory of elasticity of a multilayered medium. *Journal of Elasticity*. **1**(2): 125–143. doi:10.1007/BF00046464.

Bush, D.I., Fernando, D.A., Cripwell, J.B. & Jones, C.J.F.P. 1991. Discussion: Reinforced earth trial stucture for dewsbury ring road. *ICE Proceedings*. **90**(2): 503–505. doi:10.1680/iicep.1991.14041.

Byway, S.C., Harris, D.E., Hill, C.H.M., Anderson, D.G., Butler, J.J., Fischer, G.S., Fellenius, B.H. & Hinman, J. 1977. Design of Pile Foundations. *Foundations*. **99**(42): 649–667. doi:10.1016/0148-9062(78)91390-6.

Cai, F. & Ugai, K. 2003. Response of flexible piles under laterally linear movement of the sliding layer in landslides. *Canadian Geotechnical Journal*. **40**(1): 46–53. doi:10.1139/t02-103.

Canadell, J., Jackson, R.B., Ehleringer, J.B., Mooney, H.A., Sala, O.E. & Schulze, E.-D. 1996. Maximum rooting depth of vegetation types at the global scale. *Oecologia*. **108**(4): 583–595. doi:10.1007/BF00329030.

Carder, D.R. 2009. Improving the stability of slopes using a spaced piling technique.

Changwei, Y., Xinmin, L. & Jianjing, Z. 2014. Analysis on mechanism of landslides under ground shaking: a typical landslide in the Wenchuan earthquake. *Environmental Earth Sciences*. **72**(9): 3457–3466.

Chen, C. & Hall, E.L. 2006. Drained and Undrained Behavior of Fiber-Reinforced Sand. *Midwest Transportation Consortium of Student Papers, Transportation Scholars Conference, Iowa State University, Ames, Iowa.* (573).

Chen, Y., Xu, L., Zhang, Y. & Du, H. 2008. *Report on the great Wenchuan earthquake source of May 12, 2008*.

Chiatante, D., Scippa, S.G., Di Iorio, A. & Sarnataro, M. 2002. The influence of steep slopes on root system development. *Journal of Plant Growth Regulation*. **21**(4): 247–260. doi:10.1007/s00344-003-0012-0.

Chok, Y. & Kaggwa, W. 2004. Modelling the effects of vegetation on stability of slopes. In: *Australia-New Zealand Conference on Geomechanics (9th: Auckland, NZ)*. 2004 pp. : 391–397.

Chu, L. & Yin, J. 2005. Comparison of interface shear strength of soil nails measured by both direct shear box tests and pullout tests. *Journal of geotechnical and geoenvironmental engineering*. **131**(9): 1097–1107.

Cima, M., Sachs, E., Fan, T. & Bredt, J. 1995. Three-dimensional printing techniques. *U.S. Patent No. 5,387,380. Washington, DC: U.S. Patent and Trademark Office.*

Coder, K. 2010. *Root Strength and Tree Anchorage*.7912 (May) p.: 88.

Collet, C., Löf, M. & Pagès, L. 2006. Root system development of oak seedlings analysed using an architectural model. Effects of competition with grass. *Plant and Soil*. **279**(1-2): 367–383. doi:10.1007/s11104-005-2419-9.

Collison, A.J.C. 2001. The distribution and strength of riparian tree roots in relation to riverbank reinforcement. *Hydrological Processes*. **15**(1): 63–79. doi:10.1002/hyp.152.

Comino, E. & Druetta, A. 2010. The effect of Poaceae roots on the shear strength of soils in the Italian alpine environment. *Soil and Tillage Research*. **106**(2): 194–201. doi:10.1016 /j.still.2009.11.006.

Coppion, N.J. & Richards, I.G. 1990. Use of vegetation in civil engineering.

Coutts, M.P., Nielsen, C.C.N. & Nicoll, B.C. 1999. The development of symmetry, rigidity and anchorage in the structural root system of conifers. *Plant and Soil*. **217**(1-2): 1–15. doi:10.1023/A:1004578032481.

Crook, M.J. & Ennos, A.R. 1998. The Increase in Anchorage with Tree Size of the Tropical Tap Rooted Tree Mallotus wrayi , King (Euphorbiaceae). *Annals of Botany*. **82**(3): 291–296. doi:10.1006/anbo.1998.0678.

Dai, F.C., Xu, C., Yao, X., Xu, L., Tu, X.B. & Gong, Q.M. 2011. Spatial distribution of landslides triggered by the 2008 Ms 8.0 Wenchuan earthquake, China. *Journal of Asian Earth Sciences*. **40**(4): 883–895. doi:10.1016/j.jseaes.2010.04.010.

Dalton, F.N. 1995. In-situ root extent measurements by electrical capacitance methods. *Plant and Soil*. **173**(1): 157–165. doi:10.1007/BF00155527.

Dan, G., Sultan, N., Savoye, B., Deverchere, J. & Yelles, K. 2009. Quantifying the role of sandy-silty sediments in generating slope failures during earthquakes: Example from the Algerian margin. *International Journal of Earth Sciences*.98 (4) pp.: 769–789. doi:10. 1007/s00531-008-0373-5.

Danjon, F., Barker, D.H., Drexhage, M. & Stokes, A. 2008. Using three-dimensional plant root architecture in models of shallow-slope stability. *Annals of Botany*. **101**(8): 1281–1293. doi:10.1093/aob/mcm199.

Danjon, F., Fourcaud, T. & Bert, D. 2005. Root architecture and wind-firmness of mature Pinus pinaster. *New Phytologist*. **168**(2): 387–400. doi:10.1111/j.1469-8137.2005. 01497.x.

Danjon, F., Khuder, H. & Stokes, A. 2013. Deep phenotyping of coarse root architecture in R. Pseudoacacia reveals that tree root system plasticity is confined within its architectural model. *PLoS ONE*. **8**(12): e83548. doi:10.1371/journal.pone.0083548.

Danjon, F. & Reubens, B. 2008. Assessing and analyzing 3D architecture of woody root systems, a review of methods and applications in tree and soil stability, resource acquisition and allocation. *Plant and Soil*. **303**(1-2): 1–34. doi:10.1007/s11104-007-9470-7.

Dannowski, M. & Block, A. 2005. Fractal geometry and root system structures of heterogeneous plant communities. *Plant and Soil*. **272**(1-2): 61–76. doi:10.1007/s11104-004-3981-2.

Davies, M.C.R. & Parry, R.H.G. 1985. Centrifuge modelling of embankments on clay foundations. *Soils and Foundations*. **25**(4): 19–36. doi:10.3208/sandf1972.25.4_19.

De Kroon, H., Hendriks, M., van Ruijven, J., Ravenek, J., Padilla, F.M., Jongejans, E., Visser, E.J.W. & Mommer, L. 2012. Root responses to nutrients and soil biota: Drivers of species coexistence and ecosystem productivity. *Journal of Ecology*. **100**(1): 6–15. doi:10.1111/j.1365-2745.2011.01906.x.

Detournay, E. & Drescher, A. 1993. Limit load in translational failure mechanisms for associative and non-associative materials. *Géotechnique*.43 (3) pp.: 443–456. doi:10.1680/geot.1993.43.3.443.

Docker, B.B. & Hubble, T.C.T. 2008. Quantifying root-reinforcement of river bank soils by four Australian tree species. *Geomorphology*. **100**(3-4): 401–418. doi:10.1016/j.geomorph.2008.01.009.

Duckett, N. 2013. Development of Improved Predictive Tools for Mechanical Soil-Root Interaction. *PhD thesis,University of Dundee,UK*.

Duncan, M. 1996. State of the art: limit equilimruim and finite-element analysis of slopes. *Journal of Geotechnical Engineering*. **122**(July): 577–596.

Dupuy, L., Fourcaud, T. & Stokes, A. 2005. A numerical investigation into the influence of soil type and root architecture on tree anchorage. *Plant and Soil*. **278**(1-2): 119–134. doi:10.1007/s11104-005-7577-2.

Eab, K., Takahashi, A. & Likitlersuang, S. 2014. Centrifuge modelling of root-reinforced soil slope subjected to rainfall infiltration. *Géotechnique Letters*. **4**(July - September): 211–216. doi:10.1680/geolett.14.00029.

Eichhorn, M. & Drechsler, M. 2010. Spatial trade-offs between wind power production and bird collision avoidance in agricultural landscapes. *Ecology and Society*. **15**(2): 10. doi: 10.

Eis, S. 1974. Root System Morphology of Western Hemlock, Western Red Cedar, and Douglas-fir. *Canadian Journal of Forest Research*. **4**(1): 28–38. doi:10.1139/x74-005.

Ennos, A.R. 1993. The Scaling of Root Anchorage. *Journal of Theoretical Biology*. **161**(1): 61–75. doi:http://dx.doi.org/10.1016/S0065-2296(00)33042-7.

Evans, S. & Bent, A. 2004. The Las Colinas landslide, Santa Tecla: A highly destructive flowslide triggered by the January 13, 2001, El Salvador earthquake. *Geological Society of America Special Papers*. **375**: 25–38.

Executive, S. 2005. Scottish road network landslides study. *Summary report*. Transport Scottland: 1–124.

Fan, C.C. & Chen, Y.W. 2010. The effect of root architecture on the shearing resistance of root-permeated soils. *Ecological Engineering*. **36**(6): 813–826. doi:10.1016/j.ecoleng. 2010.03.003.

Fan, C.C. & Lai, Y.F. 2014. Influence of the spatial layout of vegetation on the stability of slopes. *Plant and Soil*. **377**(1-2): 83–95. doi:10.1007/s11104-012-1569-9.

Fan, C.C. & Su, C.F. 2008. Role of roots in the shear strength of root-reinforced soils with high moisture content. *Ecological Engineering*. **33**(2): 157–166. doi:10.1016/j.ecoleng. 2008.02.013.

Fitter, A.H. & Stickland, T.R. 1992. Fractal Characterization of Root System Architecture. *Functional Ecology*. **6**(6): 632–635. doi:doi: 10.2307/2389956.

Fourcaud, T., Ji, J.N., Zhang, Z.Q. & Stokes, A. 2008a. Understanding the impact of root morphology on overturning mechanisms: A modelling approach. *Annals of Botany*. **101**(8): 1267–1280. doi:10.1093/aob/mcm245.

Fourcaud, T., Ji, J.N., Zhang, Z.Q. & Stokes, A. 2008b. Understanding the impact of root morphology on overturning mechanisms: A modelling approach. *Annals of Botany*. **101**(8): 1267–1280. doi:10.1093/aob/mcm245.

Frei, M., Böll, A., Graf, F., Heinimann, H. & Springman, S. 2003. Quantification of the influence of vegetation on soil stability. In: *Proceedings of the International Conference on Slope Engineering (Vol. 8, No. 10). University of Hong Kong Department of Civil Engineering*. 2003

Frydman, S. & Operstein, V. 2001. Numerical simulation of direct shear of rootreinforced soil. *Proceedings of the ICE - Ground Improvement*. **5**(1): 41–48. doi:10.1680/grim. 2001.5.1.41.

Gabet, E.J. & Mudd, S.M. 2006. The mobilization of debris flows from shallow landslides. *Geomorphology*. **74**(1-4): 207–218. doi:10.1016/j.geomorph.2005.08.013.

Gale, M.R. & Grigal, D.F. 1987. Vertical root distributions of northern tree species in relation to successional status. *Canadian Journal of Forest Research*. **17**(8): 829–834. doi:10.1139/x87-131.

Gardiner, B.A., Nicoll, B.C., Peace, A.J. & Rayner, B. 2006. Anchorage of coniferous trees relation to species, soil type and rooting depth. *Canadian Journal of Forest Research*. **36**(7): 1871–1883. doi:10.1139/x06-072.

Gassler, G. 1988. *Soil nailing-theoretical basis and practical design*.

Gazetas, G. & Dakoulas, P. 1992. Seismic analysis and design of rockfill dams: state-of-the-art. *Soil Dynamics and Earthquake Engineering*. **11**: 27–61.

Geli, L., Bard, P. & Jullien, B. 1988. The effect of topography on earthquake ground motion: a review and new results. *Bulletin of the Seismological Society of America*. **78**(1): 42–63. doi:10.1016/0148-9062(88)90024-1.

Genet, M., Kokutse, N., Stokes, A., Fourcaud, T., Cai, X., Ji, J. & Mickovski, S. 2008. Root reinforcement in plantations of Cryptomeria japonica D. Don: effect of tree age and stand structure on slope stability. *Forest Ecology and Management*. **256**(8): 1517–1526. doi:10.1016/j.foreco.2008.05.050.

Genet, M., Stokes, A., Salin, F., Mickovski, S.B., Fourcaud, T., Dumail, J.F. & Van Beek, R. 2005. The influence of cellulose content on tensile strength in tree roots. *Plant and Soil*. **278**(1-2): 1–9. doi:10.1007/s11104-005-8768-6.

Ghestem, M., Veylon, G., Bernard, A., Vanel, Q. & Stokes, A. 2013. Influence of plant root system morphology and architectural traits on soil shear resistance. *Plant and Soil*. **377** (1-2): 43–61. doi:10.1007/s11104-012-1572-1.

Gilbert, M. & Tyas, A. 2003. Layout optimization of large-scale pin-jointed frames. *Engineering Computations*. **20**(8): 1044–1064.

Gilman, E.F. 1989. Prediction root spread from trunk diameter and branch spread. *Arboricultural Journal*. **13**(1): 25–32. doi:10.1080/03071375.1989.9756398.

Giri, D. & Sengupta, A. 2009. Dynamic behavior of small scale nailed soil slopes. *Geotechnical and Geological Engineering*. **27**(6): 687–698. doi:10.1007/s10706-009-9268-x.

Goodman, A. 2001. Anchorage Mechanics of the Tap Root System of Winter-sown Oilseed Rape (Brassica napus L.). *Annals of Botany*. **87**(3): 397–404. doi:10.1006/anbo. 2000.1347.

Göttlicher, S.G., Taylor, A.F.S., Grip, H., Betson, N.R., Valinger, E., Högberg, M.N. & Högberg, P. 2008. The lateral spread of tree root systems in boreal forests: Estimates based on 15N uptake and distribution of sporocarps of ectomycorrhizal fungi. *Forest Ecology and Management*. **255**(1): 75–81. doi:10.1016/j.foreco.2007.08.032.

Graf, F., Frei, M. & Böll, A. 2009. Effects of vegetation on the angle of internal friction of a moraine. *Forest, Snow and Lanscapre Research*. **82**(1): 61–77.

Grant, R.F. 1998. Simulation in ecosys of root growth response to contrasting soil water and nitrogen. *Ecological Modelling*. **107**(2-3): 237–264. doi:10.1016/S0304-3800(97)00221-4.

Greenwood, J.R. 2006. SLIP4EX - A program for routine slope stability analysis to include the effects of vegetation, reinforcement and hydrological changes. *Geotechnical and Geological Engineering*. **24**(3): 449–465. doi:10.1007/s10706-005-4156-5.

Greenwood, J.R., Norris, J.E. & Wint, J. 2004. Assessing the contribution of vegetation to slope stability. *Proceedings of the ICE - Geotechnical Engineering*. **157**(4): 199–207. doi:10.1680/geng.2004.157.4.199.

Gregory, P.J. 2006. Roots and the Architecture of Root Systems. In: *Plant Roots: Growth, Activity and Interaction with Soils*. pp. : 18–44. doi:10.1002/9780470995563.ch2.

Guswa, A.J. 2008. The influence of climate on root depth: A carbon cost-benefit analysis. *Water Resources Research*. **44**(2). doi:10.1029/2007WR006384.

Ha, J.G., Lee, S.H., Kim, D.S. & Choo, Y.W. 2014. Simulation of soil-foundation-structure interaction of Hualien large-scale seismic test using dynamic centrifuge test. *Soil Dynamics and Earthquake Engineering*. **61-62**: 176–187. doi:10.1016/j.soildyn. 2014. 01.008.

Hales, T.C., Ford, C.R., Hwang, T., Vose, J.M. & Band, L.E. 2009. Topographic and ecologic controls on root reinforcement. *Journal of Geophysical Research: Solid Earth*. **114**(3). doi:10.1029/2008JF001168.

Hamza, O., Bengough, A.G., Bransby, M.F., Davies, M.C.R. & Hallett, P.D. 2006. Biomechanics of Plant Roots: estimating Localised Deformation with Particle Image Velocimetry. *Biosystems Engineering*. **94**(1): 119–132. doi:10.1016/j.biosystemseng. 2006.02.006.

Hardin, B.O. & Drnevich, V.P. 1972. Shear Modulus and Damping in Soils: Dsesign Equations and Curves. *Soil Mechanics and Foundations Division*. (SM7): 667–692.

Harp, E.L., Jibson, R.W. & Dart, R.L. 2013. The effect of complex fault rupture on the distribution of landslides triggered by the 12 January 2010, Haiti Earthquake. In: *Landslide Science and Practice: Complex Environment*. 2013 pp.: 157–161. doi:10. 1007/978-3-642-31427-8-20.

Hassen, G., Gueguin, M. & De Buhan, P. 2013. A homogenization approach for assessing the yield strength properties of stone column reinforced soils. *European Journal of Mechanics, A/Solids*. **37**: 266–280. doi:10.1016/j.euromechsol.2012.07.003.

He, S., Ouyang, C. & Luo, Y. 2012. Seismic stability analysis of soil nail reinforced slope using kinematic approach of limit analysis. *Environmental Earth Sciences*. **66**(1): 319–326. doi:10.1007/s12665-011-1241-3.

Hodge, A., Berta, G., Doussan, C., Merchan, F. & Crespi, M. 2009. Plant root growth, architecture and function. *Plant and Soil*.321 (1-2) pp.: 153–187. doi:10.1007/s11104-009-9929-9.

Hong, Y.-S., Chen, R.-H., Wu, C.-S. & Chen, J.-R. 2005. Shaking table tests and stability analysis of steep nailed slopes. *Canadian Geotechnical Journal*. **42**(5): 1264–1279. doi:10.1139/t05-055.

Huang, A.-B., Hsueh, C.-K., O'Neill, M.W., Chern, S. & Chen, C. 2001. Effects of Construction on Laterally Loaded Pile Groups. *Journal of Geotechnical and Geoenvironmental Engineering*.127 (5) pp.: 385–397. doi:10.1061/(ASCE)1090-0241 (2001)127:5(385).

Hynes-Griffin, M.E. & Franklin, A.G. 1984. *Rationalizing the Seismic Coefficient Method*.

Ibrahim, M., Yamin, M., Sarwar, G., Anayat, A., Habib, F., Ullah, S. & Saif-ur-Rehman 2011. Tillage and farm manure affect root growth and nutrient uptake of wheat and rice under semi-arid conditions. *Applied Geochemistry*. **26**(SUPPL.). doi:10.1016/j.apgeochem. 2011.03.102.

Di Iorio, A., Lasserre, B., Scippa, G.S. & Chiatante, D. 2005. Root system architecture of Quercus pubescens trees growing on different sloping conditions. *Annals of Botany*. **95**(2): 351–361. doi:10.1093/aob/mci033.

Jackson, R.B., Canadell, J., Ehleringer, J.R., Mooney, H. a., Sala, O.E. & Schulze, E.D. 1996. A global analysis of root distributions for terrestrial biomes. *Oecologia*. **108**(3): 389–411. doi:10.1007/BF00333714.

Jaeger, C. 1981. Slope analysis. *Engineering Geology*. **17**(1-2): 74–76. doi:10.1016/0013-7952(81)90029-6.

Jewell, R.A. & Wroth, C.P. 1987. Direct shear tests on reinforced sand. *Géotechnique*.37 (1) pp.: 53–68. doi:10.1680/geot.1987.37.1.53.

Ji, J., Kokutse, N., Genet, M., Fourcaud, T. & Zhang, Z. 2012. Effect of spatial variation of tree root characteristics on slope stability. A case study on Black Locust (Robinia pseudoacacia) and Arborvitae (Platycladus orientalis) stands on the Loess Plateau, China. *Catena*. **92**: 139–154. doi:10.1016/j.catena.2011.12.008.

Jibson, R.W. 2007. Regression models for estimating coseismic landslide displacement. *Engineering Geology*. **91**(2-4): 209–218. doi:10.1016/j.enggeo.2007.01.013.

Jibson, R.W., Harp, E.L. & Michael, J.A. 2000. A method for producing digital probabilistic seismic landslide hazard maps. *Engineering Geology*. **58**(3-4): 271–289. doi:10.1016/ S0013-7952(00)00039-9.

Johnson, G. 1999. Protecting Trees from Construction Damage: A Homeowner's Guide. *University of Minnesota–Extension service*.

Johnson, P., Card, G. & Darley, P. 2002. Soil nailing for slopes. *TRL REPORT 537*.

Jourdan, C. & Rey, H. 1997. Modelling and simulation of the architecture and development of the oil-palm (elaeis guineensis jacq.) root system: I. The model. *Plant and Soil*. **190**(2): 217–233. doi:10.1023/A:1004218030608.

Jung, J.K.H. & McCouch, S. 2013. Getting to the roots of it: Genetic and hormonal control of root architecture. *Frontiers in plant science*. **4**(June): 186. doi:10.3389/fpls.2013.00186.

Karam, G.N. 2005. Biomechanical model of the xylem vessels in vascular plants. *Annals of Botany*. **95**(7): 1179–1186. doi:10.1093/aob/mci130.

Keefer, D.K. 1984. Landslides caused by earthquakes. *Geological Society of America Bulletin*. **95**(4): 406–421. doi:10.1130/0016-7606(1984)95<406:LCBE>2.0.CO.

Khalilnejad, A., Faisal Hj. Ali & Osman, N. 2012. Contribution of the Root to Slope Stability. *Geotechnical and Geological Engineering*. **30**(2): 277–288. doi:10.1007/s10706-011-9446-5.

Khuder, H., Stokes, A., Danjon, F., Gouskou, K. & Lagane, F. 2007. Is it possible to manipulate root anchorage in young trees? *Plant and Soil*. **294**(1-2): 87–102. doi:10.1007/s11104-007-9232-6.

Kim, J. & Sitar, N. 2004. Direct Estimation of Yield Acceleration in Slope Stability Analyses. *Journal of Geotechnical and Geoenvironmental Engineering*. **130**(1): 111–115. doi:10.1061/(ASCE)1090-0241(2004)130:1(111).

Kim, Y., Lee, S. & Jeong, S. 2013. The effect of pressure-grouted soil nails on the stability of weathered soil slopes. *Computers and Geotechnics*. **49**: 253–263. doi:10.1016/j.compgeo.2012.12.003.

Kirby, J.M. & Bengough, A.G. 2002. Influence of soil strength on root growth: Experiments and analysis using a critical-state model. *European Journal of Soil Science*. **53**(1): 119–127. doi:10.1046/j.1365-2389.2002.00429.x.

Kleidon, A. 2004. Global datasets and rooting zone depth inferred from inverse methods. *Journal of Climate*. **17**(13): 2714–2722. doi:10.1175/1520-0442(2004)017 <2714:GDORZD>2.0.CO;2.

Klinge, H. 1973. Root mass estimation in lowland tropical rain forests of Central Amazonia, Brazil. II Coarse root mass of tree and palms in different height classes. *Ann. Acad. braxil. Cienc*. **45**(3/4): 595–609.

Knappett, J.A. 2012. *Craig's soil mechanics*.

Knappett, J. A., Haigh, S.K. & Madabhushi, S.P.G. 2006. Mechanisms of failure for shallow foundations under earthquake loading. *Soil Dynamics and Earthquake Engineering*. **26**(2-4 SPEC. ISS.): 91–102. doi:10.1016/j.soildyn.2004.11.021.

Knappett, J.A. & Madabhushi, S.P.G. 2009. Influence of axial load on lateral pile response in liquefiable soils. Part II: numerical modelling. *Géotechnique*. **59**(7): 583–592. doi:10.1680/geot.8.010.3750.

Koizumi, A., Oonuma, N., Sasaki, Y. & Takahashi, K. 2007. Difference in uprooting resistance among coniferous species planted in soils of volcanic origin. *Journal of Forest Research*. **12**(3): 237–242. doi:10.1007/s10310-007-0001-4.

Kokusho, T. & Ishizawa, T. 2006. Energy approach for earthquake induced slope failure evaluation. *Soil Dynamics and Earthquake Engineering*. **26**(2-4 SPEC. ISS.): 221–230. doi:10.1016/j.soildyn.2004.11.026.

Kokutse, N., Fourcaud, T., Kokou, K., Neglo, K. & Lac, P. 2006. 3D Numerical Modelling and Analysis of the Influence of Forest Structure on Hill Slopes Stability. *Disaster Mitigation of Debris Flows, Slope Failures and Landslides*. : 561–567.

Kourkoulis, R., Gelagoti, F., Anastasopoulos, I. & Gazetas, G. 2011. Slope Stabilizing Piles and Pile-Groups: Parametric Study and Design Insights. *Journal of Geotechnical and Geoenvironmental Engineering*.137 (7) pp.: 663–677. doi:10.1061/(ASCE)GT.1943-5606.0000479.

Kutter, B. 1995. Recent Advances in Centrifuge Modeling of Seismic Shaking. In: *Proceedings: Third International Conference on Recent Advances in Geotechnical Earthquake Engineering and Soil Dynamics,April 2-7, St.Louis, Missouri*. 1995

Laio, F., D'Odorico, P. & Ridolfi, L. 2006. An analytical model to relate the vertical root distribution to climate and soil properties. *Geophysical Research Letters*. **33**(18). doi:10.1029/2006GL027331.

Lal, R. 1998. Biotechnical and Soil Bioengineering Slope Stabilization: A Practical Guide for Erosion Control. *Soil Science*.163 (1) pp.: 83–85. doi:10.1097/00010694-199801000-00012.

Lauder, K. 2010. The performance of pipeline ploughs. *PhD thesis,University of Dundee,UK*.

LeBrun, B., Hatzfeld, D., Bard, P.Y. & Bouchon, M. 1999. Experimental study of the ground motion on a large scale topographic hill at Kitherion (Greece). *Journal of Seismology*. **3**(1): 1–15.

Lee, C., Hull, T. & Poulos, H. 1995. Simplified pile-slope stability analysis. *Computers and Geotechnics*. **17**(1): 1–16.

Lee, S.H., Choo, Y.W. & Kim, D.S. 2013. Performance of an equivalent shear beam (ESB) model container for dynamic geotechnical centrifuge tests. *Soil Dynamics and Earthquake Engineering*. **44**: 102–114. doi:10.1016/j.soildyn.2012.09.008.

Lees, A. 2013. Seasonal slope movements in an old clay fill embankment dam. *Canadian Geotechnical Journal*. **50**(5): 503–520. doi:10.1139/cgj-2012-0356.

Li, Y., Chen, G., Tang, C., Zhou, G. & Zheng, L. 2012. Rainfall and earthquake-induced landslide susceptibility assessment using GIS and Artificial Neural Network. *Natural Hazards and Earth System Science*. **12**(8): 2719–2729. doi:10.5194/nhess-12-2719-2012.

Liang, T., Knappett, J.A & Bengough, A.G 2014. Scale modelling of plant root systems using 3-D printing. In: *ICPMG2014–Physical Modelling in Geotechnics, Perth, Australia, 14-17 January 2014*. pp: 361–366.

Liang, T. & Knappett, J.A. 2015. Centrifuge modelling of vegetated slopes under earthquake loading. In: *6ICEGE-6th International Conference on Earthquake Geotechnical Engineering ,Christchurch, New Zealand*

Lin, D.G., Huang, B.S. & Lin, S.H. 2010. 3-D numerical investigations into the shear strength of the soil-root system of Makino bamboo and its effect on slope stability. *Ecological Engineering*. **36**(8): 992–1006. doi:10.1016/j.ecoleng.2010.04.005.

Liu, Z., Qian, J., Liu, B., Wang, Q., Ni, X. & Dong, Y. 2014. Effects of the Magnetic Resonance Imaging Contrast Agent Gd-DTPA on Plant Growth and Root Imaging in Rice. *PloS one*. **9**(6): e100246.

Loades, K.W., Bengough, A.G., Bransby, M.F. & Hallett, P.D. 2010. Planting density influence on fibrous root reinforcement of soils. *Ecological Engineering*. **36**(3): 276–284. doi:10.1016/j.ecoleng.2009.02.005.

Lundström, T., Jonas, T., Stöckli, V. & Ammann, W. 2007. Anchorage of mature conifers: resistive turning moment, root-soil plate geometry and root growth orientation. *Tree physiology*. **27**(9): 1217–1227. doi:10.1093/treephys/27.9.1217.

Lysmer, O. & Kuhlemeyer, R.L. 2008. JDRF randomized clinical trial to assess the efficacy of real-time continuous glucose monitoring in the management of type 1 diabetes: research design and methods. *Diabetes technology & therapeutics*. **10**(4): 310–321. doi:10.1089/dia.2007.0302.

Madabhushi, S.P.G. & Teymur, B. 2003. Experimental study of boundary effects in dynamic centrifuge modelling. *Géotechnique*. **53**(7): 655–663. doi:10.1680/geot.2003.53.7.655.

Malamud, B.D., Turcotte, D.L., Guzzetti, F. & Reichenbach, P. 2004. Landslides, earthquakes, and erosion. *Earth and Planetary Science Letters*. **229**(1-2): 45–59. doi:10.1016/j.epsl.2004.10.018.

Manual, E. 2003. Slope Stability. *Manual, Engineer*. **12**(877): 67–67. doi:10.1016/0148-9062(75)90139-4.

Mao, Z., Bourrier, F., Stokes, A. & Fourcaud, T. 2014. Three-dimensional modelling of slope stability in heterogeneous montane forest ecosystems. *Ecological Modelling*. **273**: 11–22. doi:10.1016/j.ecolmodel.2013.10.017.

Mao, Z., Saint-André, L., Genet, M., Mine, F.X., Jourdan, C., Rey, H., Courbaud, B. & Stokes, A. 2012. Engineering ecological protection against landslides in diverse mountain forests: Choosing cohesion models. *Ecological Engineering*. **45**: 55–69. doi:10.1016/j.ecoleng.2011.03.026.

Martin, C.M., Oliphant, J., Cathie, D., Byrne, B.W., Schupp, J. & Maconochie, A. 2013. Uplift of shallowly buried pipe sections in saturated very loose sand. *Géotechnique*. **63**(5): 382–390. doi:10.1680/geot.11.P.016A.

Martin, J. 1997. The design and installation of soil nail slope stabilization schemes using'Snail'. *Improvement Geosystems, London, 3-5 June 1997*.

Martin, Y. & Church, M. 2000. The effect of riparian tree roots on the mass-stability of riverbanks. *Earth Surface Processes and Landforms*. **25**(9): 921–937. doi:10.1002/1096-9837(200008)25:9<921::AID-ESP93>3.0.CO;2-7.

Massa, M., Lovati, S., D'Alema, E., Ferretti, G. & Bakavoli, M. 2010. An experimental approach for estimating seismic amplification effects at the top of a ridge, and the implication for ground motion predictions: The case of Narni, Central Italy. *Bulletin of the Seismological Society of America*. **100**(6): 3020–3034. doi:10.1785/0120090382.

Matasovic, N.Jr. & Kavazanjian, E. 1997. Newmark deformation analysis with degrading yield acceleration. In: *Procedings of Geosynthetics'97, Long Beach, CA, USA*. 1997 pp. : 989–1000.

McIvor, I.R., Douglas, G.B., Hurst, S.E., Hussain, Z. & Foote, a. G. 2008. Structural root growth of young Veronese poplars on erodible slopes in the southern North Island, New Zealand. *Agroforestry Systems*. **72**(1): 75–86. doi:10.1007/s10457-007-9090-5.

McVay, M., Casper, R. & Shang, T.-I. 1995. Lateral Response of Three-Row Groups in Loose to Dense Sands at 3D and 5D Pile Spacing. *Journal of Geotechnical Engineering*. **121**(5): 436–441. doi:10.1061/(ASCE)0733-9410(1995)121:5(436).

McVay, M., Zhang, L., Molnit, T. & Lai, P. 1998. Centrifuge Testing of Large Laterally Loaded Pile Groups in Sands. *Journal of Geotechnical and Geoenvironmental Engineering*. **124**(10): 1016–1026. doi:10.1061/(ASCE)1090-0241(1998)124:10(1016).

Meehan, C.L. & Vahedifard, F. 2013. Evaluation of simplified methods for predicting earthquake-induced slope displacements in earth dams and embankments. *Engineering Geology*. **152**(1): 180–193. doi:10.1016/j.enggeo.2012.10.016.

Michalowski, R. & Shi, L. 1995. Bearing capacity of footings over two-layer foundation soils. *Journal of Geotechnical Engineering*. **3**(May): 421–428.

Michalowski, R.L. & Čermák, J. 2003. Triaxial Compression of Sand Reinforced with Fibers. *Journal of Geotechnical and Geoenvironmental Engineering*. **129**(2): 125–136. doi:10.1061/(ASCE)1090-0241(2003)129:2(125).

Mickovski, S.B. & Van Beek, L.P.H. 2009. Root morphology and effects on soil reinforcement and slope stability of young vetiver (Vetiveria zizanioides) plants grown in semi-arid climate. *Plant and Soil*. **324**(1): 43–56. doi:10.1007/s11104-009-0130-y.

Mickovski, S.B., Van Beek, L.P.H. & Salin, F. 2005. Uprooting of vetiver uprooting resistance of vetiver grass (Vetiveria zizanioides). *Plant and Soil*. **278**(1-2): 33–41. doi:10.1007/s11104-005-2379-0.

Mickovski, S.B., Bengough, A. G., Bransby, M.F., Davies, M.C.R., Hallett, P.D. & Sonnenberg, R. 2007. Material stiffness, branching pattern and soil matric potential affect the pullout resistance of model root systems. *European Journal of Soil Science*. **58**(6): 1471–1481. doi:10.1111/j.1365-2389.2007.00953.x.

Mickovski, S.B., Bransby, M.F., Bengough, A.G., Davies, M.C.R. & Hallett, P.D. 2010. Resistance of simple plant root systems to uplift loads. *Canadian Geotechnical Journal*. **47**(1): 78–95. doi:10.1139/T09-076.

Mickovski, S.B. & Ennos, A.R. 2003. Anchorage and asymmetry in the root system of Pinus peuce. *Silva Fennica*. **37**(2): 161–173.

Mickovski, S.B., Hallett, P.D., Bransby, M.F., Davies, M.C.R., Sonnenberg, R. & Bengough, A.G. 2009. Mechanical Reinforcement of Soil by Willow Roots: Impacts of Root Properties and Root Failure Mechanism. *Soil Science Society of America Journal*. **73**(4): 1276–1285. doi:10.2136/sssaj2008.0172.

Mickovski, S.B., Stokes, A., van Beek, R., Ghestem, M. & Fourcaud, T. 2011. Mechanical Reinforcement of Soil by Willow Roots: Impacts of Root Properties and Root Failure Mechanism. Soil S. *Ecological Engineering*. **37**(10): 1523–1532. doi:10.1016/j.ecoleng. 2011.06.001.

Milsom, J. 2007. Field geophysics. *John Wiley and Sons*. **25**.

Miyagi, T., Higaki, D., Yagi, H., Doshida, S., Chiba, N., Umemura, J. & Satoh, G. 2011. Reconnaissance report on landslide disasters in northeast Japan following the M 9 Tōhoku earthquake. *Landslides*. **8**(3): 339–342. doi:10.1007/s10346-011-0281-9.

Mooney, S.J., Pridmore, T.P., Helliwell, J. & Bennett, M.J. 2012. Developing X-ray computed tomography to non-invasively image 3-D root systems architecture in soil. *Plant and Soil*. **352**(1-2): 1–22. doi:10.1007/s11104-011-1039-9.

Moore, J.R. 2000. Differences in maximum resistive bending moments of Pinus radiata trees grown on a range of soil types. *Forest Ecology and Management*. **135**(1-3): 63–71. doi:10.1016/S0378-1127(00)00298-X.

Mora, C.R., Schimleck, L.R., Isik, F., Mahon, J.M., Clark, A. & Daniels, R.F. 2009. trees. *Canadian Journal of Forest Research*. **39**(8): 1421–1429. doi:10.1139/X09-062.

Mott, P.H. & Roland, C.M. 2010. Response to 'Comment on paper "The bulk modulus and Poisson"s ratio of 'incompressible' materials''. *Journal of Sound and Vibration*. **329**(3): 368–369. doi:10.1016/j.jsv.2009.10.008.

Muhihaus, H.-B. & Vardoulakis, I. 1988. The thickness of shear hands in granular materials. *Géotechnique*. **38**(2): 331–331. doi:10.1680/geot.1988.38.2.331.

Newmark, N.M. 1965. Effects of Earthquakes on Dams and Embankments. *Géotechnique*. **15**(2): 139–160. doi:10.1680/geot.1965.15.2.139.

Ng, C. & Yu, R. 2014. A novel technique to model water uptake by plants in geotechnical centrifuge. *Géotechnique Letters*.

Ng, C.W.W., Zhang, L. & Nip, D.C.N. 2001. Response of Laterally Loaded Large-Diameter Bored Pile Groups. *Journal of Geotechnical and Geoenvironmental Engineering*. **127**(8): 658–669. doi:10.1061/(ASCE)1090-0241(2001)127:8(658).

Nicoll, B.C., Achim, A., Mochan, S. & Gardiner, B.A. 2005. Does steep terrain influence tree stability? A field investigation. *Canadian Journal of Forest Research*. **35**(10): 2360–2367. doi:10.1139/x05-157.

Nicoll, B.C., Berthier, S., Achim, A., Gouskou, K., Danjon, F. & Van Beek, L.P.H. 2006. The architecture of Picea sitchensis structural root systems on horizontal and sloping terrain. *Trees - Structure and Function*. **20**(6): 701–712. doi:10.1007/s00468-006-0085-z.

Nilaweera, N.S. & Nutalaya, P. 1999. Role of tree roots in slope stabilisation. *Bulletin of Engineering Geology and the Environment*. **57**(4): 337–342. doi:10.1007/ s1006400500 56

Norris, J.E., Stokes, A., Mickovski, S.B., Cammeraat, E., Van Beek, R., Nicoll, B.C. & Achim, A. 2008. Slope stability and erosion control: Ecotechnological solutions. doi:10.1007/978-1-4020-6676-4.

Oda, M. & Kazama, H. 1998. Microstructure of shear bands and its relation to the mechanisms of dilatancy and failure of dense granular soils. *Géotechnique*. **48**(4): 465–481. doi:10.1680/geot.1998.48.4.465.

Olson, G.W. 1983. Biotechnical Slope Protection and Erosion Control. 1982. *Soil Science*. **135**(2): 126. doi:10.1097/00010694-198302000-00008.

Operstein, V. & Frydman, S. 2000. The influence of vegetation on soil strength. *Proceedings of the ICE-Ground Improvement*. **4**(2): 81–89.

Orban, F. 2011. Damping of materials and members in structures. *Journal of Physics: Conference Series*. **268**: 012022. doi:10.1088/1742-6596/268/1/012022.

Osman, N., Abdullah, M. & Abdullah, C. 2011. Pull-Out and Tensile Strength Properties of Two Selected TropicalTrees. *Sains Malaysiana*. **40**(6): 577–585.

Ozier-Lafontaine, H., Lecompte, F. & Sillon, J.F. 1999. Fractal analysis of the root architecture of Gliricidia sepium for the spatial prediction of root branching, size and mass: Model development and evaluation in agroforestry. *Plant and Soil*. **209**(2): 167–180. doi:10.1023/A:1004461130561.

Pagès, L., Vercambre, G., Drouet, J.L., Lecompte, F., Collet, C. & Le Bot, J. 2004. Root Typ: A generic model to depict and analyse the root system architecture. *Plant and Soil*. **258**(1-2): 103–119. doi:10.1023/B:PLSO.0000016540.47134.03.

Paolucci, R. 2002. Amplification of earthquake ground motion by steep topographic irregularities. *Earthquake Engineering and Structural Dynamics*. **31**(10): 1831–1853. doi:10.1002/eqe.192.

Paolucci, R., Faccioli, E. & Maggio, F. 1999. 3D Response analysis of an instrumented hill at Matsuzaki, Japan, by a spectral method. *Journal of Seismology*. **3**(2): 191–209. doi:10.1023/A:1009890320625.

Parr, A. & Cameron, A.D. 2004. Effects of tree selection on strength properties and distribution of structural roots of clonal Sitka spruce. *Forest Ecology and Management*. **195**(1-2): 97–106. doi:10.1016/j.foreco.2004.02.033.

Patra, C.R. & Basudhar, P.K. 2005. Optimum design of nailed soil slopes. *Geotechnical and Geological Engineering*. **23**(3): 273–296. doi:10.1007/s10706-004-2146-7.

Pedersen, H., Lebrun, B., Hatzfeld, D., Campillo, M. & Bard, P.Y. 1994. Ground-motion amplitude across ridges. *Bulletin of the Seismological Society of America*. **84**(6): 1786–1800.

Pedley, M. 1990. The performance of soil reinforcement in bending and shear. *University of oxfored, PhD Thesis*.

Pedley, M., Brady, K., Perry, J. & Reid, M. 2003. Briefing: Embankment cuttings: condition appraisal and remedial treatment. In: *Proceedings of the ICE-Geotechnical Engineering*. 2003 pp. : 171–175. doi:10.1680/geng.2003.156.4.171.

Peltola, H.M. 2006. Mechanical stability of trees under static loads. *American Journal of Botany*. **93**(10): 1501–1511. doi:10.3732/ajb.93.10.1501.

Perdriat, J., Phillips, R., Font, J.N. & Hutin, C. 2002. Dynamically balanced broad frequency earthquake simulation systems. In: *Proc. 5th Int. Conf. on Physical Modelling in Geotechnics(ICPMG 02)*. 2002 pp. : 169–174.

Phanikanth, V.S., Choudhury, D. & Reddy, G.R. 2010. Behaviour of fixed head single pile in cohesionless soil under lateral loads. *Electronic Journal of Geotechnical Engineering*. **15 M**: 1243–1262.

Pinheiro, E.A.R., Costa, C.A.G. & De Araújo, J.C. 2013. Effective root depth of the Caatinga biome. *Journal of Arid Environments*. **89**: 1–4. doi:10.1016/j.jaridenv.2012.10.003.

Pollen, N. & Simon, A. 2005. Estimating the mechanical effects of riparian vegetation on stream bank stability using a fiber bundle model. *Water Resources Research*. **41**(7): 1–11. doi:10.1029/2004WR003801.

Poulos, H.G. 1995. Design of reinforcing piles to increase slope stability. *Canadian Geotechnical Journal*. **32**: 808–818. doi:10.1139/t95-078.

Powell, G. & Watkins, A. 1990. Improvement of marginally stable existing slopes by soil nailing in Hong Kong. In: *Proceedings of the International Reinforced Soil Conference, Glasgow, UK*. 1990

Pradhan, B., Tham, L.G., Yue, Z.Q., Junaideen, S.M. & Lee, C.F. 2006. Soil–Nail Pullout Interaction in Loose Fill Materials. *International Journal of Geomechanics*. **6**(4): 238–247. doi:10.1061/(ASCE)1532-3641(2006)6:4(238).

Rabie, M. 2014. Performance of hybrid MSE/Soil Nail walls using numerical analysis and limit equilibrium approaches. *HBRC Journal*.

Randolph, M.F. 2003. Science and empiricism in pile foundation design. *Géotechnique*. **53**(10): 847–875. doi:10.1680/geot.2003.53.10.847.

Randolph, M.F. 1981. The response of flexible piles to lateral loading. *Géotechnique*. **31**(2): 247–259. doi:10.1680/geot.1981.31.2.247.

Reddish, D.J., Ellis, E.A. & Durrani, I.K. 2010. Numerical modelling of discrete pile rows for slope stability and generic guidance for design. *Géotechnique*. **60**(3): 185–195. doi:10.1680/geot.7.00090.

Reese, L. & Van Impe, W. 2011. Single Piles and Pile Groups Under Lateral Loading (2nd Edition). *CRC Press*. : 508. doi:10.1115/1.1445326.

Reese, L., Van Impe, W. & Holtz, R. 2002. Single Piles and Pile Groups Under Lateral Loading. *Applied Mechanics Reviews*.55 p.: B9. doi:10.1115/1.1445326.

Reese, L.C., Cox, W.R. & Grubbs, B.R. 1974. Field testing of laterally loaded piles in sand. *Offshore Technology Conference*. : 459–472. doi:10.4043/2079-MS.

Refice, A. & Capolongo, D. 2002. Probabilistic modeling of uncertainties in earthquake-induced landslide hazard assessment. *Computers and Geosciences*. **28**(6): 735–749. doi:10.1016/S0098-3004(01)00104-2.

Reid, M.E., Baum, R.L., LaHusen, R.G. & Ellis, W.L. 2008. Capturing landslide dynamics and hydrologic triggers using near-real-time monitoring. In: *Landslides and Engineered Slopes. From the Past to the Future*. pp. : 179–191.

Remaud, D., Garnier, J. & Frank, R. 1998. Laterally loaded piles in dense sand: group effects. *Proc. Int. Conf. Centrifuge 98*.

Report, F. 2008. *Analysis of Laterally Loaded Long or Intermediate Drilled Shafts of Small or Large Diameter in Layered Soil*. (December).

Reubens, B., Poesen, J., Danjon, F., Geudens, G. & Muys, B. 2007. The role of fine and coarse roots in shallow slope stability and soil erosion control with a focus on root system architecture: A review. *Trees - Structure and Function*. **21**(4): 385–402. doi:10.1007/s00468-007-0132-4.

Rich, S.M. & Watt, M. 2013. Soil conditions and cereal root system architecture: Review and considerations for linking Darwin and Weaver. *Journal of Experimental Botany*.64 (5) pp.: 1193–1208. doi:10.1093/jxb/ert043.

Rodríguez, C.E., Bommer, J.J. & Chandler, R.J. 1999. Earthquake-induced landslides: 1980-1997. *Soil Dynamics and Earthquake Engineering*. **18**(5): 325–346. doi:10.1016/S0267-7261(99)00012-3.

Rollins, K. & Olsen, K. 2006. Pile spacing effects on lateral pile group behavior: Analysis. *Journal of Geotechnical and Geoenvironmental Engineering*. **132**(10): 1272–1283.

Rollins, K.M., Lane, J.D. & Gerber, T.M. 2005. Measured and Computed Lateral Response of a Pile Group in Sand. *Journal of Geotechnical and Geoenvironmental Engineering*. **131**(1): 103–114. doi:10.1061/(ASCE)1090-0241(2005)131:1(103).

Rollins, K.M., Peterson, K.T. & Weaver, T.J. 1998. Lateral Load Behavior of Full-Scale Pile Group in Clay. *Journal of Geotechnical and Geoenvironmental Engineering*. **124**(6): 468–478. doi:10.1061/(ASCE)1090-0241(1998)124:6(468).

Ruesta, P.F. & Townsend, F.C. 1997. Evaluation of Laterally Loaded Pile Group at Roosevelt Bridge. *Journal of Geotechnical and Geoenvironmental Engineering*. **123**(12): 1153–1161. doi:10.1061/(ASCE)1090-0241(1997)123:12(1153).

Saez, J., Corona, C., Stoffel, M. & Berger, F. 2014. Assessment of forested shallow lanslide movements coupling trees ring records from stems and exposed roots. *Géomorphologie*. **2**(2): 159–174.

Santos, J.A. dos & Correia, A.G. 2001. Reference threshold shear strain of soil. Its application to obtain an unique strain-dependent shear modulus curve for soil. In: *Proceedings of the Fifteenth International Conference on Soil Mechanics and Geotechnical Engineering*. 2001 pp. : 267–270.

Sarma, S.K. 1973. Stability analysis of embankments and slopes. *Géotechnique*. **23**(3): 423–433. doi:10.1680/geot.1973.23.3.423.

Schanz, T., Vermeer, A. & Bonnier, P. 1999. The hardening soil model: formulation and verification. *Beyond 2000 in Computational Geotechnics*, Balkema, Rotterdam, 281-296.

Schenk, H.J. 2008. The Shallowest Possible Water Extraction Profile: A Null Model for Global Root Distributions. *Vadose Zone Journal*. **7**(3): 1119. doi:10.2136/vzj2007.0119.

Schenk, H.J. & Jackson, R.B. 2005. Mapping the global distribution of deep roots in relation to climate and soil characteristics. *Geoderma*. **126**(1-2 SPEC. ISS.): 129–140. doi:10.1016/j.geoderma.2004.11.018.

Schenk, H.J. & Jackson, R.B. 2002a. Rooting depths, lateral root spreads and below-ground/above-ground allometries of plants in water-limited ecosystems. *Journal of Ecology*. **90**(3): 480–494. doi:10.1046/j.1365-2745.2002.00682.x.

Schenk, H.J. & Jackson, R.B. 2002b. The global biogeography of roots. *Ecological Monographs*. **72**(3): 311–328. doi:10.1890/0012-9615(2002)072[0311:TGBOR]2.0.CO;2.

Schofield, A. 1981. Dynamic and Earthquake Geotechnical Centrifuge Modelling. In: *Proceeding of International Conference on Recent Advances in Geotechnical Earthquake Engineering and Soil Dynamics*, University of Missouri-Rolla. 1981 pp. : 1081–1100.

Schofield, A. & Wroth, P. 1968a. Critical State Soil Mechanics. *Soil Use and Management*. **25**(3): 128–105. doi:10.1111/j.1475-2743.1987.tb00718.x.

Schofield, A.N. & Wroth, C.P. 1968b. Critical state soil mechanics.

Schwarz, M., Cohen, D. & Or, D. 2011. Pullout tests of root analogs and natural root bundles in soil: Experiments and modeling. *Journal of Geophysical Research: Earth Surface*. **116**(2): F02007. doi:10.1029/2010JF001753.

Schwarz, M., Lehmann, P. & Or, D. 2010. Quantifying lateral root reinforcement in steep slopes - from a bundle of roots to tree stands. *Earth Surface Processes and Landforms*. **35**(3): 354–367. doi:10.1002/esp.1927.

Schwarz, M., Preti, F., Giadrossich, F., Lehmann, P. & Or, D. 2010. Quantifying the role of vegetation in slope stability: A case study in Tuscany (Italy). *Ecological Engineering*. **36**(3): 285–291. doi:10.1016/j.ecoleng.2009.06.014.

Scott, J.M. & Loveridge, F. 2000. *Influence of climate and vegetation on railway embankments* Mott MacDonald, United Kingdom

Seed, H.B. 1979. Considerations in the earthquake-resistant design of earth and rockfill dams. *Géotechnique*. **29**(3): 215–263. doi:10.1680/geot.1979.29.3.215.

Sengupta, A. & Giri, D. 2011. Dynamic analysis of soil-nailed slope. In: *Proceedings of the ICE-Ground Improvement*. 2011 pp. : 225–234.

Sepúlveda, S. a., Murphy, W., Jibson, R.W. & Petley, D.N. 2005. Seismically induced rock slope failures resulting from topographic amplification of strong ground motions: The case of Pacoima Canyon, California. *Engineering Geology*. **80**(3-4): 336–348. doi:10.1016/j.enggeo.2005.07.004.

Shewbridge, S.E. & Sitar, N. 1989. Deformation Characteristics of Reinforced Sand in Direct Shear. *Journal of Geotechnical Engineering*. **115**(8): 1134–1147. doi:10.1061/(ASCE)0733-9410(1989)115:8(1134).

Shukha, R. & Baker, R. 2008. Design implications of the vertical pseudo-static coefficient in slope analysis. *Computers and Geotechnics*. **35**(1): 86–96. doi:10.1016/j.compgeo.2007.01.005.

Simon, A. & Collison, A.J.C. 2002. Quantifying the mechanical and hydrologic effects of riparian vegetation on streambank stability. *Earth Surface Processes and Landforms*. **27**(5): 527–546. doi:10.1002/esp.325.

Sinnett, D., Morgan, G., Williams, M. & Hutchings, T.R. 2008. Soil penetration resistance and tree root development. *Soil Use and Management*. **24**(3): 273–280. doi:10.1111/j.1475-2743.2008.00164.x.

Sivakumar Babu, G.L. & Singh, V.P. 2008. Numerical analysis of performance of soil nail walls in seismic conditions. *ISET Journal of Earthquake Technology*. **45**(1-2).

Smethurst, J., Clarke, D. & Powrie, W. 2006. Seasonal changes in pore water pressure in a grass covered cut slope in London clay. *Geotechnique*. **56**(8): 523–537. doi:10.1680/geot.2006.56.8.523.

Smith, C. & Gilbert, M. 2007. Application of discontinuity layout optimization to plane plasticity problems. In: *Proceedings of the Royal Society*. 2007 pp. : 2461–2484. doi:10.1098/rspa.2006.1788.

Smith, C.C. & Cubrinovski, M. 2011. Pseudo-static limit analysis by discontinuity layout optimization: Application to seismic analysis of retaining walls. *Soil Dynamics and Earthquake Engineering*. **31**(10): 1311–1323. doi:10.1016/j.soildyn.2011.03.014.

Smith, S. & De Smet, I. 2012. Root system architecture: insights from Arabidopsis and cereal crops. *Philosophical Transactions of the Royal Society B: Biological Sciences*.367 (1595) pp.: 1441–1452. doi:10.1098/rstb.2011.0234.

Sonnenberg, R. 2008. Centrifuge modelling of root reinforced slopes. *PhD thesis,University of Dundee,UK*. (May): 1–276.

Sonnenberg, R., Bransby, M.F., Bengough, A.G., Hallett, P.D. & Davies, M.C.R. 2011. Centrifuge modelling of soil slopes containing model plant roots. *Canadian Geotechnical Journal*. **49**(1): 1–17. doi:10.1139/T11-081.

Sonnenberg, R., Bransby, M.F., Hallett, P.D., Bengough, A.G., Mickovski, S.B. & Davies, M.C.R. 2010. Centrifuge modelling of soil slopes reinforced with vegetation. *Canadian Geotechnical Journal*. **47**(12): 1415–1430. doi:10.1139/T10-037.

Spek, L.Y. & Noordwijk, M. 1994. Proximal root diameter as predictor of total root size for fractal branching models. *Plant and Soil*. **164**(1): 119–127. doi:10.1007/BF00010117.

Spencer, E. 1968. A Method of Analysis of the Stability of Embankments Assuming Parallel Inter-Slice Forces. *Géotechnique*. **18**(3): 384–386. doi:10.1680/geot.1968.18.3.384.

Stingaciu, L., Schulz, H., Pohlmeier, A., Behnke, S., Zilken, H., Javaux, M. & Vereecken, H. 2013. In Situ Root System Architecture Extraction from Magnetic Resonance Imaging for Application to Water Uptake Modeling. *Vadose Zone Journal*. : 19. doi:10.2136/ vzj2012.0019.

Stokes, A., Atger, C., Bengough, A.G., Fourcaud, T. & Sidle, R.C. 2009. Desirable Plant root traits for protecting natural and engineered slopes against landslides. *Plant and Soil*. **324**(1): 1–30. doi:10.1007/s11104-009-0159-y.

Stokes, A., Douglas, G.B., Fourcaud, T., Giadrossich, F., Gillies, C., Hubble, T., Kim, J.H., Loades, K.W., Mao, Z., McIvor, I.R., Mickovski, S.B., Mitchell, S., Osman, N., Phillips, C., Poesen, J., Polster, D., Preti, F., Raymond, P., Rey, F., Schwarz, M. & Walker, L.R. 2014. Ecological mitigation of hillslope instability: Ten key issues facing researchers and practitioners. *Plant and Soil*. **377**(1-2): 1–23. doi:10.1007/s11104-014-2044-6.

Stokes, A. & Mattheck, C. 1996. Variation of wood strength in tree roots. *Journal of Experimental Botany*. **47**(298): 693–699. doi:10.1093/jxb/47.5.693.

Sun, H.L., Li, S.C., Xiong, W.L., Yang, Z.R., Cui, B.S. & Tao-Yang 2008. Influence of slope on root system anchorage of Pinus yunnanensis. *Ecological Engineering*. **32**(1): 60–67. doi:10.1016/j.ecoleng.2007.09.002.

Taylor, R.N. 2003. Geotechnical centrifuge technology.

Terzaghi, K. 1951. Mechanism of landslides.

Terzaghi, K. 1950. Mechanism of landslides. *Engineering Geology*. : 1–44.

Thaler, P. & Pagès, L. 1998. Modelling the influence of assimilate availability on root growth and architecture. *Plant and Soil*. **201**(2): 307–320. doi:10.1023/A:1004380021699.

Thomas, R.E. & Pollen-Bankhead, N. 2010. Modeling root-reinforcement with a fiber-bundle model and Monte Carlo simulation. *Ecological Engineering*. **36**(1): 47–61. doi:10.1016 /j.ecoleng.2009.09.008.

Tiwari, R.C., Bhandary, N.P., Yatabe, R. & Bhat, D.R. 2012. New numerical scheme in the finite element method for evaluating the root-reinforcement effect on soil slope stability. *Géotechnique*. **63**(2): 1–11. doi:10.1680/geot.11.P.039.

Tobin, B., Čermák, J., Chiatante, D., Danjon, F., Di Iorio, A., Dupuy, L., Eshel, A., Jourdan, C., Kalliokoski, T., Laiho, R., Nadezhdina, N., Nicoll, B., Pagès, L., Silva, J. & Spanos, I. 2007. Towards developmental modelling of tree root systems. *Plant Biosystems*. **141**(3): 481–501. doi:10.1080/11263500701626283.

Tofani, V., Raspini, F., Catani, F. & Casagli, N. 2013. Persistent scatterer interferometry (psi) technique for landslide characterization and monitoring. *Remote Sensing*. **5**(3): 1045–1065. doi:10.3390/rs5031045.

Toky, O.P. & Bisht, R.P. 1992. Observations on the rooting patterns of some agroforestry trees in an arid region of north-western India. *Agroforestry Systems*. doi:10.1007 /BF00 123320.

Towhata, I. 2008. Geotechnical Earthquake Engineering. Springer Series in Geomechanics and Geoengineering. Berlin, Heidelberg, Springer Berlin Heidelberg. doi:10.1007/978-3-540-35783-4.

Tripe, R., Kontoe, S. & Wong, T.K.C. 2013. Slope topography effects on ground motion in the presence of deep soil layers. *Soil Dynamics and Earthquake Engineering*. **50**: 72–84. doi:10.1016/j.soildyn.2013.02.011.

Tufenkjian, M.R. & Vucetic, M. 2000. Dynamic Failure Mechanism of Soil-Nailed Excavation Models in Centrifuge. *Journal of Geotechnical and Geoenvironmental Engineering*. **126**(3): 227–235. doi:10.1061/(ASCE)1090-0241(2000)126:3(227).

Turner, J.P. & Jensen, W.G. 2005. Landslide Stabilization Using Soil Nail and Mechanically Stabilized Earth Walls: Case Study. *Journal of Geotechnical and Geoenvironmental Engineering*. **131**(2): 141–150. doi:10.1061/(ASCE)1090-0241(2005)131:2(141).

Ueno, K. 1998. Methods of Preparation of Sand Samples. In: *Proceedings of the International Conference Centrifuge 98*. 1998 pp. : 1047–1056.

Umar, Z., Pradhan, B., Ahmad, A., Jebur, M.N. & Tehrany, M.S. 2014. Earthquake induced landslide susceptibility mapping using an integrated ensemble frequency ratio and

logistic regression models in West Sumatera Province, Indonesia. *Catena*. **118** (September 2009): 124–135. doi:10.1016/j.catena.2014.02.005.

Van Beek, L.P.H., Wint, J., Cammeraat, L.H. & Edwards, J.P. 2005. Observation and simulation of root reinforcement on abandoned mediterranean slopes. *Plant and Soil*. **278**(1-2): 55–74. doi:10.1007/s11104-005-7247-4.

Varney, G.T. & Canny, M.J. 1993. Rates of water uptake into the mature root system of maize plants. *New Phytologist*. **123**(4): 775–786. doi:10.1111/j.1469-8137.1993.tb03789.x.

Waldron, L. & Dakessian, S. 1981. Soil reinforcement by roots: calculation of increased soil shear resistance from root properties. *Soil Science*. **132**(6): 427-435.

Waldron, L.J. 1977. The Shear Resistance of Root-Permeated Homogeneous and Stratified Soil1. *Soil Science Society of America Journal*. **41**(5): 843. doi:10.2136/sssaj1977.03615995004100050005x.

Walk, T.C., Van Erp, E. & Lynch, J.P. 2004. Modelling applicability of fractal analysis to efficiency of soil exploration by roots. *Annals of Botany*. **94**(1): 119–128. doi:10.1093/aob/mch116.

Wang, H., Siopongco, J., Wade, L.J. & Yamauchi, A. 2009. Fractal analysis on root systems of rice plants in response to drought stress. *Environmental and Experimental Botany*. **65**(2-3): 338–344. doi:10.1016/j.envexpbot.2008.10.002.

Warren, E., Smith, R.G.B., Apiolaza, L.A. & Walker, J.C.F. 2009. Effect of stocking on juvenile wood stiffness for three Eucalyptus species. *New Forests*. **37**(3): 241–250. doi:10.1007/s11056-008-9120-9.

Watson, A., Marden, M. & Rowan, D. 1995. Tree Species Performance and Slope Stability. *Vegetation and Slopes, London, Thomas Telford*. : 161–171.

Wei, W.B. & Cheng, Y.M. 2009. Strength reduction analysis for slope reinforced with one row of piles. *Computers and Geotechnics*. **36**(7): 1176–1185. doi:10.1016/j.compgeo.2009.05.004.

Wells, T.C.E. 1981. Methods of studying root systems. *Biological Conservation*. **19**(2): 159. doi:10.1016/0006-3207(81)90050-1.

Won, J., You, K., Jeong, S. & Kim, S. 2005. Coupled effects in stability analysis of pile-slope systems. *Computers and Geotechnics*. **32**(4): 304–315. doi:10.1016/j.compgeo.2005.02.006.

Wood, D.M. 2003. Geotechnical modelling. Vol.1. CRC Press, 2003. doi:10.4324/9780203477977.

Wood, D.M. 1990. Soil Behaviout and Critical State Soil Mechanics. *Cambridge university press*.

Wu, T. 2013. Root reinforcement of soil: review of analytical models, test results, and applications to design. *Canadian Geotechnical Journal*. **50**(3): 259–274.

Wu, T.H. 1976. Investigation of Landslides on Prince of Wales Island, Alaska. *Geotechnical Engineering Report 5. Civil Engineering Department, Ohio State University, Columbus, Ohio, USA, 94p*.

Wu, T.H. 2007. Root reinforcement: analyses and experiments. *Eco- and Ground Bio-Engineering: The Use of Vegetation to Improve Slope Stability*. **103**: 21–30.

Wu, T.H., McKinnell III, W.P. & Swanston, D.N. 1979. Strength of tree roots and landslides on Prince of Wales Island, Alaska. *Canadian Geotechnical Journal*. **16**(1): 19–33. doi:10.1139/t79-003.

Wu, T.H. & Watson, A. 1998. Erratum: In situ shear tests of soil blocks with roots. *Canadian Geotechnical Journal*. **35**(5): 907. doi:10.1139/t98-e027.

Yanagisawa, N. & Fujita, N. 1999. Different distribution patterns of woody species on a slope in relation to vertical root distribution-and dynamics of soil moisture profiles. *Ecological Research*. **14**(2): 165–177. doi:10.1046/j.1440-1703.1999.00295.x.

Yegian, M. & Wright, S.G. 1973. Lateral soil resistance - displacement relationships for pile foundations in soft clays. In: *Offshore Technology Conference*. 1973 pp. : 663–676.

Yetimoglu, T. & Salbas, O. 2003. A study on shear strength of sands reinforced with randomly distributed discrete fibers. *Geotextiles and Geomembranes*. **21**(2): 103–110. doi:10.1016/S0266-1144(03)00003-7.

Yu, Y., Deng, L., Sun, X. & Lu, H. 2008. Centrifuge modeling of a dry sandy slope response to earthquake loading. *Bulletin of Earthquake Engineering*.

Zaimoglu, A.S. & Yetimoglu, T. 2012. Strength Behavior of Fine Grained Soil Reinforced with Randomly Distributed Polypropylene Fibers. *Geotechnical and Geological Engineering*. **30**(1): 197–203. doi:10.1007/s10706-011-9462-5.

Zeng, X. 2001. Global Vegetation Root Distribution for Land Modeling. *Journal of Hydrometeorology*. **2**(5): 525–530. doi:10.1175/1525-7541(2001)002 <0525:GVRDFL> 2.0.CO;2.

Zeng, X. & Schofield, A.N. 1996. Design and performance of an equivalent-shear-beam container for earthquake centrifuge modelling. *Géotechnique*. **46**(1): 83–102. doi:10. 1680/geot.1996.46.1.83.

Zhou, W.H. & Yin, J.H. 2008. A simple mathematical model for soil nail and soil interaction analysis. *Computers and Geotechnics*. **35**(3): 479–488. doi:10.1016/j.compgeo.2007.07.001.

APPENDICES

Appendix A Root mechanical properties

Data collected from recent studies on the relationship between root tensile strength (T_r), maximum force at breakage in tension (F_r) and Diameter (after Mao et al. 2012)

Based on Tensile strength T_r (Eq 2.3)

1–25: De Baets et al., 2008, Europe Medit., hilly; 26–47: Thomas and Pollen-Bankhead, 2010, USA Mriparian; 48–53: Genet et al., 2010, China Sichuan, montane/subalpine; 54–58: Genet et al., 2005, Europe Alps, montane; 59–61:S, Oregon and Kansas, Genet et al., 2008, China Sichuan, montane/subalpine; 62–64: Loades et al., 2010, UK experimental field; 65–69: Bischetti et al., 2009: Europe Alps, montane; 70–72: Mattia et al., 2005, Europe Medit., hilly; 73–77: Bischetti et al., 2005: Europe Alps, montane; 78: Abernethy and Rutherfurd, 2001, Australia, riparian; 79: Easson and Yarbrough, 2002, USA, riparian; 80: Abdi et al., 2009, Iran,hilly; 81: Fan and Su, 2008, China Taiwan, experimental field.

No.	Species	Functional gruop	*k*	*m*	T.S.	No.	Species	Functional gruop	*k*	*m*	T.S.
1	Atriplex halimus	Shrub	45.59	-0.56	ex situ	42	Betula nigra	Tree	45.8	-0.66	in situ
2	Salsola genistoides	Shrub	44.23	-0.51	ex situ	43	Pinus contorta	Tree	19.1	-0.65	in situ
3	Brachypodium retusum	Grass/herb	45.05	-0.61	ex situ	44	Populus spp.	Tree	18.9	-0.64	in situ
4	Thymelaea hirsuta	Shrub	33.31	-0.64	ex situ	45	Spiraea douglasii	Shurb	22.9	-0.54	in situ
5	Phragmites australis	Grass/herb	34.29	-0.78	ex situ	46	Salix geyeriana	Tree	23.3	-0.51	in situ
6	Limonium supinum	Grass/herb	33.82	-0.85	ex situ	47	Fraxinus latifolia	Tree	24.3	-0.5	in situ
7	Tamarix canariensis	Tree	31.74	-0.89	ex situ	48	Betula laminifera	Tree	79.4	-0.63	ex situ
8	Artemisia barrelieri	Shrub	30.12	-0.61	ex situ	49	Aralia elata	Tree	93.08	-0.76	ex situ
9	Stipa tenacissima	Grass/herb	24.34	-0.61	ex situ	50	Idesia polycarpa	Tree	14.34	-1.32	ex situ
10	Juncus acutus	Grass/herb	23.23	-0.89	ex situ	51	Litsea cubeba	Tree	64.36	-0.65	ex situ
11	Fumana thymifolia	Shrub	15.71	-0.66	ex situ	52	Carya cathayensis	Tree	74.28	-0.65	ex situ
12	Dorycnium pentaphyllum	Shrub	16.32	-0.62	ex situ	53	Phyllostachys nidularia	Grass/herb	34.42	-0.52	ex situ
13	Teucrium capitatum	Shrub	18.72	-0.45	ex situ	54	Pinus nigra	Tree	18.4	-0.52	ex situ
14	Dittrichia viscosa	Shrub	18.94	0.45	ex situ	55	Pinus pinaster	Tree	23.4	-0.87	ex situ
15	Thymus zygis	Shrub	19.31	-0.73	ex situ	56	Picea abies	Tree	37.86	-0.51	ex situ
16	Lygeum spartum	Grass/herb	19.28	-0.68	ex situ	57	Fagus sylvatica	Tree	63.51	-0.61	ex situ
17	Plantago albicans	Grass/herb	16.75	-0.52	ex situ	58	Castanea sativa	Tree	31.92	-0.73	ex situ
18	Rosmarinus officinalis	Shrub	12.89	-0.77	ex situ	59	Cryptomeria japonica	Tree	21.59	-0.34	ex situ
19	Helictotrichon filifolium	Grass/herb	14.51	-1.08	ex situ	60	Cryptomeria japonica	Tree	25.79	-0.37	ex situ
20	Piptatherum miliaceum	Grass/herb	11.49	-1.77	ex situ	61	Cryptomeria japonica	Tree	31.9	-0.41	ex situ
21	Avenula bromoides	Grass/herb	4.77	-1.52	ex situ	62	Hordeum vulgare	Grass/herb	2.63	-1.62	ex situ
22	Nerium oleander	Shrub	4.41	-1.75	ex situ	63	Hordeum vulgare	Grass/herb	3.03	-1.2	ex situ
23	Ononis tridentata	Shrub	9.59	n.s.	ex situ	64	Hordeum vulgare	Grass/herb	2.04	-1.27	ex situ
24	Anthyllis cytisoides	Shrub	8.43	n.s.	ex situ	65	Fagus sylvatica	Tree	41.57	-0.98	ex situ
25	Retama sphaerocarpa	Shrub	16.36	n.s.	ex situ	66	Castanea sativa	Tree	17.86	-0.53	ex situ

26	Panacum virgatum	Grass/herb	35.2	-1.78	in situ	67	Ostrya carpinifolia	Tree	21.89	-0.43	ex situ
27	Phalaris arundinacea	Grass/herb	1.7	-1.71	in situ	68	Picea abies	Tree	28.1	-0.72	ex situ
28	Lolium perenne	Grass/herb	2.1	-1.65	in situ	69	Larix decidua	Tree	33.45	-0.75	ex situ
29	Wet Meadow	Grass/herb	20.9	-1.21	in situ	70	Lygeum spartum	Grass/herb	60.7	-1.3	ex situ
30	Salix nigra	Tree	45.9	-1.1	in situ	71	Atriplex halimus	Shurb	73	-0.6	ex situ
31	Liquidamber styraciflua	Tree	52.1	-1.04	in situ	72	Pistacia lentiscus	Shurb	91.2	-0.45	ex situ
32	Tripsacum dactyloides	Grass/herb	43.1	-1	in situ	73	Salix purpurea	Tree	26.33	-0.95	ex situ
33	Elaeagnus angustifolia	Tree	22.1	-1	in situ	74	Salix caprea	Tree	34.5	-1.02	ex situ
34	Dry Meadow	Grass/herb	22.1	-0.99	in situ	75	Alnus viridis	Tree	34.76	-0.69	ex situ
35	Pinus palustris	Tree	30	-0.99	in situ	76	Corylus avellana	Tree	60.15	-0.75	ex situ
36	Plantanus occidentalis	Tree	50.5	-0.94	in situ	77	Fraxinus excelsa	Tree	35.73	-1.11	ex situ
37	Tamarix ramosissima	Shrub	23.6	-0.9	in situ	78	Melaleuca ericifolia and Eucalyptus camaldulensis	Tree	49.39	-0.77	in situ
38	Salix lemmonii	Tree	25.9	-0.86	in situ	79	Liquidamber styraciflua	Tree	23.58	-0.57	in situ
39	Alnus tenuifolia	Tree	21.6	-0.8	in situ	80	Carpinus betulus	Tree	34.24	-0.45	ex situ
40	Rubus armeniacus	Shrub	19.5	-0.69	ex situ	81	Sesbania cannabina	Shurb	60.48	-0.86	ex situ
41	Salix interior	Tree	25.2	-0.68	in situ						

Based on F_r	82–88: Nilaweera and Nutalaya, 1999, Thailand, montane; 89: Abe and Iawamoto, 1986, Japan; 90: Burroughs and Thomas, 1977, USA.										
No.	Species	Functional gruop	*k*	*m*	T.S.	No.	Species	Functional gruop	*k*	*m*	T.S.
82	Dipterocarpus alatus	Tree	54.16	1.55	ex situ	86	Ficus benjamina	Tree	31.8	1.28	ex situ
83	Hopea odorata	Tree	68.36	1.31	ex situ	87	Hevea brasiliensis	Tree	28.79	1.23	ex situ
84	Alangium kurzii	Tree	41.59	1.47	ex situ	88	Cryptomeria japonica	Tree	79.08	1.45	ex situ
85	Hibiscus macrophyllus	Tree	40.44	1.44	ex situ	89	Pseudotsuga menziesii	Tree	19.44	1.8	ex situ
85	Alstonia macrophulla	Tree	22.21	1.54	ex situ						